Volume : 1 Issue : 1 eISSN: 3059-9504
Dec. 2024

Api Journal of Science

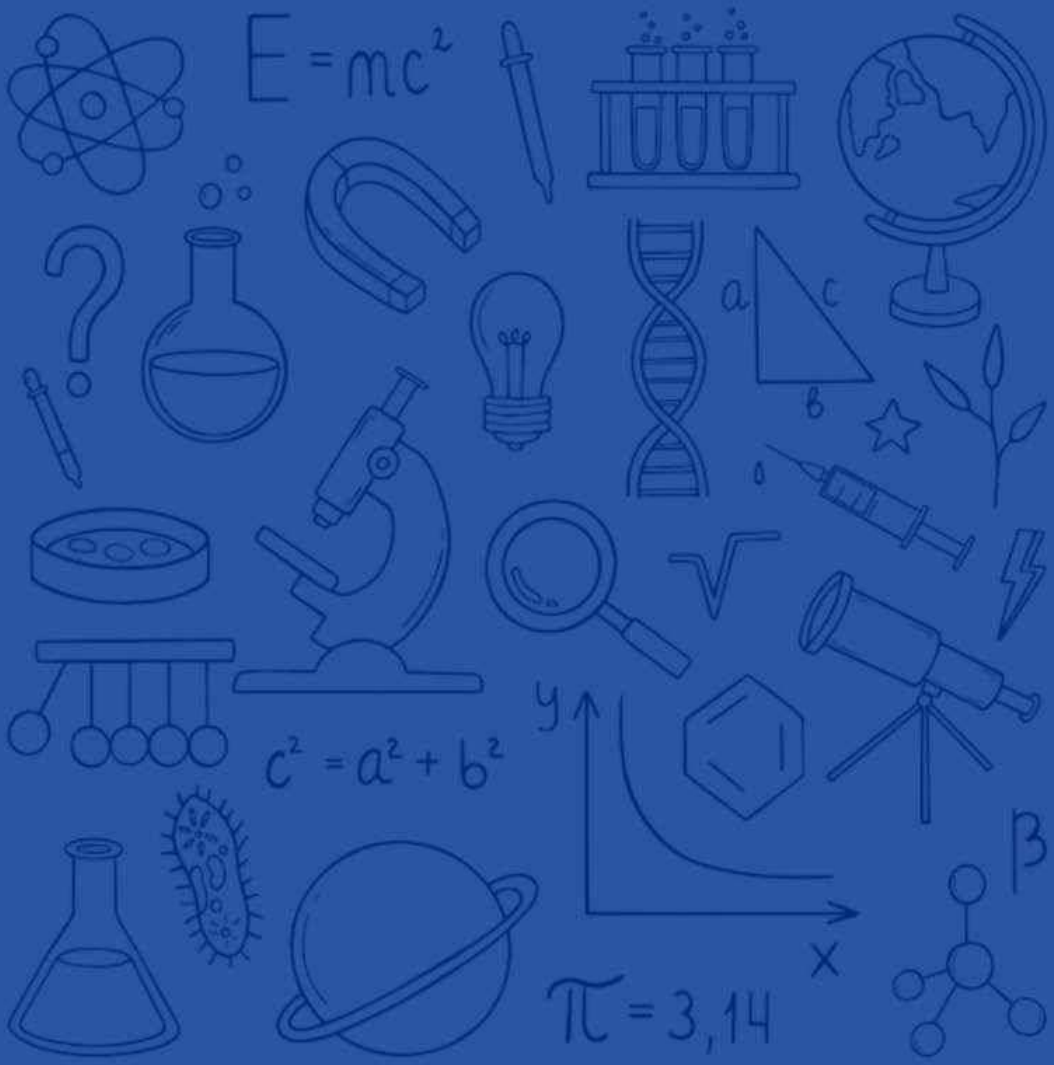

Published by:
Research Management Cell
Siddhanath Science Campus
Tribhuvan University, Nepal

Editorial Board

EDITORIAL

Research Management Cell, Siddhanath Science Campus, Tribhuvan University, is delighted to present a new issue of scientific Journal "Api Journal of Science (AJS)". AJS is a peer reviewed journal and aims to publish original research articles of all the science disciplines. We are very grateful to all the authors who have chosen to submit their manuscripts to AJS for publication. We are indebted to all the researchers and reviewers for their valuable time and effort for their rigorous evaluation process. Hard work of our editors, contributors, and esteemed supporters made it possible to reach at the publication stage.

Special thanks go to the contributors for providing their innovative research works to the readers via this regular issue of AJS. The AJS editorial team appreciates any feedback for its improvement. Finally, I appreciate your constructive feedback and further correspondence.

Editor-in-Chief

Dr. Bhawani Datt Joshi

Api Journal of Science

Content list

Pursuit of Stability, Electronic, Lattice Dynamics, and Thermoelectric Properties of Half Heusler Compound TiFeSe

Prakash Khatri[1, 2, *]

[1]Central Department of Physics, Tribhuvan University, Kirtipur 44613, Kathmandu, Nepal
[2]Department of Physics, Tribhuvan University, Siddhanath Science Campus, Mahendranagar 10406, Nepal

Research Article

ISSN: 3059-9504 (online)
Doi: xxxx

Article History

Received: October 10, 2024
Revised: November 6, 2024
Accepted: November 10, 2024
Published: December 28, 2024

Keywords

Thermoelectricity, Band structure, Phonon dispersion, Figure of merit

***Corresponding author**

Email: prakash.khatri@snsc.tu.edu.np
Phone: +977- 9848751715

ABSTRACT

Half-Heusler (HH) compounds are increasingly popular for their use as thermoelectric materials in high-temperature applications. The present work explores the electron and phonon transport properties of TiFeSe compounds to understand their thermoelectric behaviour using Density Functional Theory (DFT), semiclassical Boltzmann transport equation, and Slack's equation. The compound is thermodynamically, dynamically, and mechanically stable, exhibiting non-magnetic semiconductor behaviour with an indirect bandgap of 0.80 eV. The compound has a higher Young's modulus and bulk modulus, indicating better mechanical strength, and also has a high melting point, as calculated from the elastic constants. The lattice thermal conductivity is 24.84 $Wm^{-1}K^{-1}$ at room temperature and decreases as the temperature increases. The maximum power factor (PF) in the compound for hole doping is 182 $\mu W/cmK^2$, leading to a maximum figure of merit (zT) value of 1.45 at 1200 K. This study shows that the hole-doped TiFeSe compound is a promising candidate for high-temperature power generation in thermoelectric applications.

1. INTRODUCTION

The growing gap between the global energy demand and limited supply of non-renewable resources is pushing us toward an energy crisis. Outdated energy policies, weak regulatory standards, and lack of proper energy storage are all intensifying the crisis. To alleviate these issues, many researchers are actively working to find solutions. One way to reduce the crisis is by turning waste heat from industries, transportation vehicles etc into useful electricity using thermoelectric materials [1-4]. Nowadays, these materials are a key part of modern technology, and their conversion efficiency depends on the parameter thermodynamic figure of merit that can be expressed as [5, 6]:

$$zT = \frac{S^2\sigma T}{\kappa_{el}+\kappa_l} \quad \text{..... (i)}$$

Where S, σ, κ_{el}, κ_l, and T are the Seebeck coefficient, electrical conductivity, electronic and lattice contributions to thermal conductivity, and absolute temperature, respectively. The interdependence of S, σ, and κ_{el}, along with electron-phonon coupling in crystals, limits the zT **<** 1 in many thermoelectric materials. However, a zT > 1 is needed for better energy conversion in thermoelectric devices [7, 8].

Although skutterudites [9] and chalcogenides [10] materials are better suited for medium temperature thermoelectric applications, skutterudites face thermal stability issues at high temperatures, and chalcogenides have weaker mechanical strength [11]. Thus, the half-Heusler (hH) materials are now a major focus in recent research for high-temperature thermoelectric applications because of their tunable electronic properties, excellent thermal stability, and mechanical strength [11, 12]. They are ternary intermetallics with a cubic MgAgAs-type structure and formula XYZ, where X and Y are transition metals, and Z is a main group element. They consist of three interpenetrating face-centered cubic (fcc) sublattices, with X**,** Y**,** and Z atoms occupying Wyckoff positions 4a (0, 0, 0), 4b (1/2, 1/2, 1/2), and 4c (1/4, 1/4, 1/4) positions respectively [13, 14]. The semiconducting ground state in hH alloys necessitates a nonmagnetic ground state due to the Slater-Pauling rule, which states that magnetic moment $\mu = (N_V - 18)$, where N_V is the valence electron count (VEC) per formula unit [15]. Since the magnetic moment vanishes for compounds with 18 VEC, the search for 18-VEC compounds leads us to the TiFeSe compound. This compound is reported to have a hH phase in the material project [16]. Furthermore, Nenuwe et al. [17] reported the stability, magnetic, mechanical, and thermoelectric properties of FeTiSe, but the zT value was calculated based solely on electronic thermal conductivity (κ_{el}**)**. However, in hH compounds, lattice thermal conductivity (κ_l) is typically high due to their simple and symmetric crystal structure, as well as the fewer atoms in the primitive unit cell [18] and therefore cannot be neglected in thermal conductivity calculations. In this work, we used first-principles calculations to determine the transport parameters and their variations with chemical potential at different temperatures for both electron- and hole-doped TiFeSe compounds.

The paper is organized as follows: Section 2 covers the computational details, Section 3 includes the results and discussions, and Section 4 presents the conclusions of the study.

2. COMPUTATIONAL DETAILS

The structural, electronic, and magnetic properties were computed using density functional theory (DFT) implemented in Quantum ESPRESSO (QE) software version 7.1 [19]. Perdew, Burke, and Ernzerhof generalized gradient approximation (PBE-GGA) [20], is used to describe the exchange and correlation interactions. Ultrasoft pseudopotentials (USPP)

were used for all elements with the valence electronic configurations as: Ti: $3s^2\ 3p^6\ 3d^2\ 4s^2$, Fe: $3s^2\ 3p^6\ 3d^6\ 4s^2$, and Se: $4s^2\ 4p^4$. The geometric visualization of the optimized crystal structure is done with XcrySDen [21]. The calculations used a plane wave basis with a kinetic energy cut-off of 70 Ry and a charge density cut-off of 700 Ry. A Monkhorst-Pack [22] k-point grid of 10×10×10 in the first irreducible Brillouin zone (BZ) was used for integrating over the BZ. Diagonalization (David), a mixing beta factor (0.3), and Marzari-Vanderbilt smearing [23] (width 0.005 Ry) were used throughout the calculations. Γ → X → W → K → Γ → L → U → W → L → K is the high symmetry path in the first BZ along which sampling points are chosen. A denser k-point mesh of 20 × 20 × 20 was used to evaluate the density of states (DOS) and partial density of states (PDOS). The energy eigenvalues calculated using DFT with the same mesh were also used in the calculations within the BoltzTraP code to estimate the transport coefficients by solving the Boltzmann transport equations [24]. Phonon dispersion calculations were carried out to evaluate dynamical stability using density functional perturbation theory (DFPT) [25] within the Quantum ESPRESSO package, with a 2 × 2 × 2 q-point mesh. The mechanical properties were assessed using the thermo_pw [26] tool within QE suite, while Slack's equation [27] was used to calculate the κ_l.

3. RESULTS AND DISCUSSION

.

3.1. Structural Stability

Before studying the properties properties, it's important to ensure its stability for any hypothetical compounds. TiFeSe is a ternary hH compound that belongs to the $F\bar{4}3m$ space group and has a structure of MgAgAs prototype. In XYZ hH compounds, the Y element stays at the 4b position, while the X and Z elements can occupy in the positions 4a and 4c. We have evaluated the stability by placing Fe at the 4b site and assessed the suitability of Ti and Se by swapping their positions at the 4a and 4c sites. The labels I and II refer to the two structural configurations as in Figs.1(a) and 1(b) that differ in their atomic positions, as shown in Table 1. The energy vs. volume plots Figs.1(c) and 1(d) for the I and II structures are fitted using the Murnaghan equation of state [28] to obtain the optimized lattice parameter. After VC-relax, it results in lattice parameters of 10.60 a.u. and 10.59 a.u. for the type I and type II structures, respectively. Based on the SCF energy, the type I structure has a slightly lower total energy (−395.373480 Ry) compared to that (−395.373472 Ry) of type II structure. Although the energy difference is not significant, we have selected the slightly lower-energy structure (Type I) for our calculations, which is also reported in Ref. [17]. The calculated lattice parameter is in close agreement with the reported value of 10.62 a.u. (5.62 Å) in Ref. [17]. Therefore, all further calculations were carried out using the type I structure

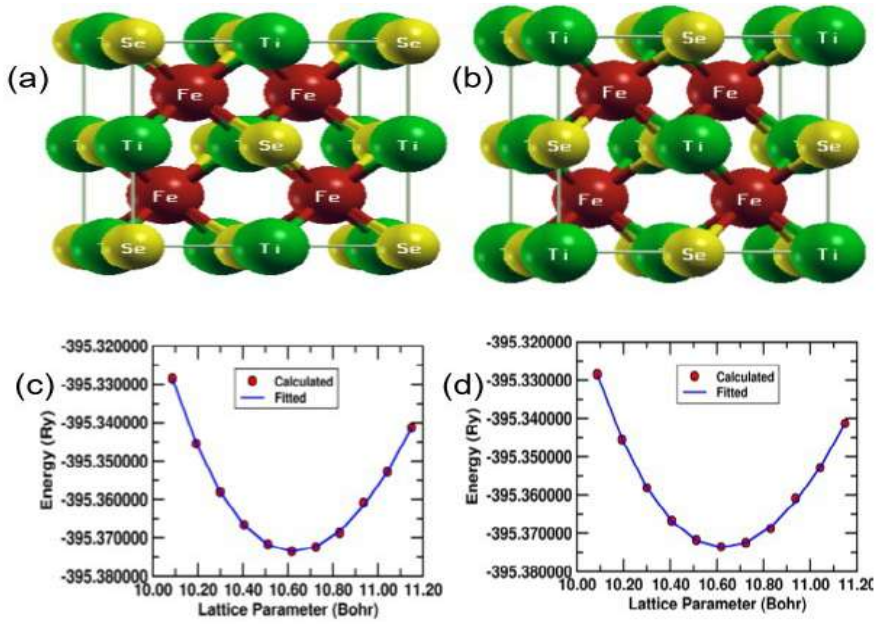

Fig. 1. (a) Conventional unit cell of TiFeSe (type-I) (b) Conventional unit cell of TiFeSe (type-II) (c) Energy (in Ry) vs. lattice parameter (in Bohr) for TiFeSe (type-I) (d) and Energy (in Ry) vs. lattice parameter (in Bohr) for TiFeSe (type-II)).

After structural optimization, we confirmed the compound's thermodynamic, dynamical, and mechanical stability by calculating the formation energy, phonon dispersion, and elastic constants, respectively. The formation energy is calculated as:

$$E_{form} = \frac{(E_{TiFeSe}) - (xE_{Ti} + yE_{Fe} + zE_{Se})}{x+y+z} \quad \text{..... (ii)}$$

Here, E_{TiFeSe}, E_{Ti}, E_{Fe}, and E_{Se} represent the total energy p.u.c. of the bulk crystal TiFeSe, bulk elements Ti, Fe, and Se, respectively, x, y, and z are the total number of Ti, Fe, and Se atoms, respectively. From our calculations, the formation energy of TiFeSe is −0.54 eV/atom. The stability of the materials against elemental segregation is suggested by this negative formation energy.

Table 1. Atomic positions, optimized lattice parameters (in a.u.) and total energy (Ry) for type (I and II) of TiFeSe.

Type	4a (X)	4b (Y)	4c (Z)	Lattice Parameter (a.u.)	Total energy (Ry)
I	0, 0,0	0.25, 0.25, 0.25	0.5, 0.5, 0.5	10.60	−395.373480
II	0.5, 0.5, 0.5	0.25, 0.25, 0.25	0, 0, 0	10.59	−395.373472

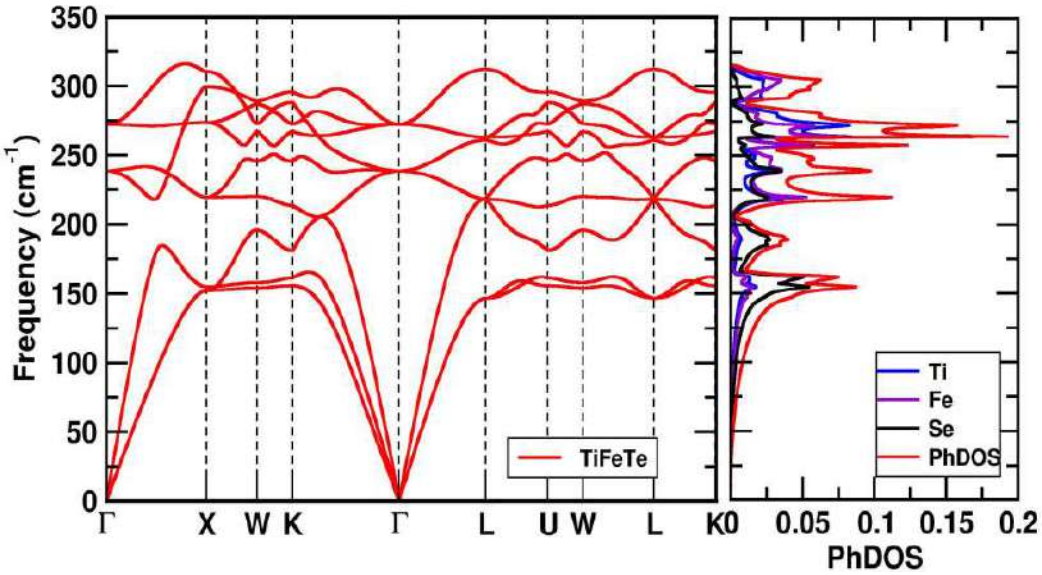

Fig. 2. Phonon dispersion plot and phonon density of states (PhDOS) of TiFeSe.

The phonon dispersion along the specified high-symmetry points is presented alongside the phonon density of states (PhDOS) in the Fig 2. This is used to check the dynamical stability of the compound. Since TiFeSe has three atoms in its primitive cell, the dispersion plot has nine vibrational modes, three low frequency acoustic modes and six high frequency optical modes. The absence of imaginary frequencies indicates dynamical stability of the compound. The acoustic branches are highly dispersive and are almost linear near the Γ point, resulting in higher group velocities, while the optical modes are flatter and have lower group velocities. This makes acoustic modes more dominant in heat transfer than optical modes. The high frequencies are mainly due to the vibration of Fe and Ti atoms having nearly similar atomic masses and the low-frequency branches are caused by the vibrations of relatively heavier Se atoms, as seen in the PhDOS. The overlap between low-frequency optical modes and high-frequency acoustic modes suggests strong phonon-phonon scattering, which affects the lattice thermal conductivity of the compound.

The mechanical stability of the compound is evaluated by calculating the elastic constants with the thermo_pw code [26] in Quantum ESPRESSO. The cubic materials have three independent elastic constants: C_{11}, C_{12}, and C_{44}, which were found to be 267.45 GPa, 101.38 GPa, and 74.77 GPa, respectively. The compound meets the Born's mechanical stability criteria [29] ($C_{11} > 0$, $C_{44} > 0$, $C_{11} - C_{12} > 0$, and $C_{11} + 2C_{12} > 0$). The Young's modulus and bulk modulus are calculated using the Voigt-Reuss-Hill approximation [30]. The ratio of stress to strain defines Young's modulus, which quantifies a material's stiffness. With a Young's modulus of 200.64 GPa, the compound exhibits the significant rigidity. The bulk modulus (B) measures how compressible a material is under pressure. TiFeSe has a high B value of 156.73 GPa, means that it resists compression and performs well under high pressure. The melting temperature (T_m) of cubic crystals can be calculated from elastic constant C_{11} using the formula [31]:

T_m = [553 K + (5.91 K / GPa) C_{11}] ± 300 K ..... (iii)

The compound's high melting point of 2133.62 K suggests it is well-suited for high-temperature applications.

3.2. Electronic and magnetic properties

The electronic band structures (EBS), along with the DOS and PDOS, computed using the optimized lattice parameters, are displayed in Fig 3. The high-symmetry path Γ → X → W → K → Γ → L → U → W → L → K is used for plotting EBS and a dashed line at 0 eV represents the Fermi energy. The valence band maximum (VBM) is located at the L point, and the conduction band minimum (CBM) at the Γ point. This indicates that TiFeSe is an indirect band gap semiconductor with a band gap of 0.80 eV. The calculated band gap value is very closer to (0.81 eV) as reported by Nenuwe et al. [17], but lower than the value (0.86 eV) found in the Materials Project [16]. Variations in band gap values may arise due to the use of different exchange-correlation functionals in the studies. Additionally, there is no experimental band gap value available for comparison.

The VBM at the L point is a doubly degenerate state with heavy-hole and light-hole bands of varying curvatures. Sharp bands with higher curvature exhibit a smaller effective mass, whereas the flat bands with lower curvature result a larger effective mass for their charge carriers. Thus, the degenerate bands at the VBM results in a higher Seebeck coefficient for hole doped compounds. There is a triply degenerate band at the Γ point, ~ 360 meV below the VBM, while the band extrema at the X point of the CB is ~290 meV higher than the CBM. These bands do not significantly contribute to the

transport properties of the compounds. The symmetrical DOS plot between the spin-up and spin-down channels indicates the non-magnetic nature of the material. The PDOS plot reveals that the Fe-3d orbitals contribute significantly the VB, while Ti-3d orbitals dominate the CB, with minimal contributions from Se-4p orbitals in both bands. TiFeSe is a non-magnetic semiconductor with zero magnetic moment 0.0 μ_B and is consistent with the Slater-Pauling rule [15], magnetic moment $\mu = (Z - 18)\ \mu_B$, based on its valence electron count Z. The suitable semiconducting EBS and non-magnetic ground state of the compound motivate us to quantify the transport parameters and thermoelectric properties.

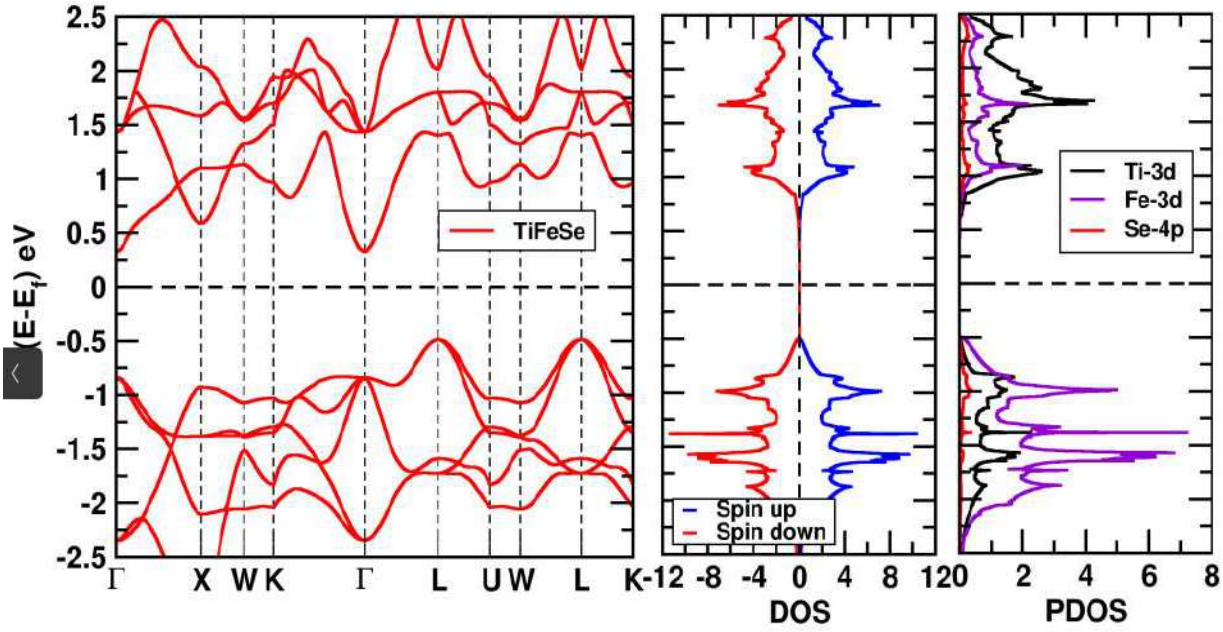

Fig. 3. The electronic band structure (EBS), total density of states (DOS), and partial density of states (PDOS) plots of TiFeSe atoms with a horizontal dotted line representing the Fermi level.

3.3. Thermoelectric Properties

The transport parameters, Seebeck coefficient (S), electrical conductivity (σ), and electronic thermal conductivity (κ_{el}) are calculated using the semi-classical Boltzmann transport theory in BoltzTraP software [24]. It relies on the rigid band approximation (RBA) and the constant relaxation time approach (CRTA). A constant relaxation time of 10^{-14} seconds chosen based on some other hH compounds, is used to evaluate the transport properties as a function of chemical potential for different temperatures, as shown in Fig. 4.

Mott's equation [32] for the Seebeck coefficient:

$$S = \frac{8\pi^2 k_B^2 m_D T}{3eh^2}\left(\frac{\pi}{3n}\right)^{1/3} \quad \text{.....(iv)}$$

shows that S depends on the DOS effective mass (m_{DOS}) and higher carrier concentration (n). The DOS effective mass $m_{DOS} = N_V^{2/3} m_b$, depends on the total band degeneracy N_v.

The Fig. 4(a) shows that for both p-type (hole doping) and n-type (electron doping) rise until they reach a peak value as the chemical potential (μ) increases. S peaks in the chemical potential (μ) range of − 0.2 eV to 0.2 eV for all temperatures. With further increases in the μ, S rapidly decreases after reaching the peak value. The peak value of S for p-type regions (hole doping) is higher than for n-type regions (electron doping) at all temperatures. The peak S is ~ 1120 μV/K for p-type regions and ~915 μV/K for n-type regions at 400 K within the observed range of μ. The higher S in the p-type region may result from the doubly degenerate band at the VBM. However, a triply degenerate band at the Γ point, ~360 meV below the VBM, does not have a significant effect on the transport parameters. The band curvature around the CBM is relatively sharper, leading to a lower S for electrons in the n-type regions. The closest band extrema to CBM is at the X point, ~ 290 meV higher than the CBM, and does not make a major contribution to the transport properties. The carrier concentration increases and hence peak value of S decreases as the temperature rises. At 1200 K, the peak values of the S are ~ 445 μV/K for p-type and ~350 μV/K for n-type TiFeSe compounds. The maximum values of S for TiFeSe in this study are comparable to those observed in LiCaX (X = As, Sb) [33], but they are lower than those reported for XFeTe (X = Ti, Hf) [34] systems at the same temperature.

The relationship between electrical conductivity (σ) and chemical potential (μ) at different temperatures is illustrated in Fig.4(b). σ exhibits a similar pattern at all temperatures. In the μ range of −0.2 to 0.2 eV, σ remains nearly zero, but it rises outside of this range for all temperatures. When the temperature increases, electrons gain thermal energy, which boosts their mobility μ_c and leads to higher electrical conductivity ($\sigma = ne\mu_c$). σ is higher for hole doping (negative μ) than for electron doping (positive μ) region, indicating that p-type doping demonstrates greater σ compared to n-type doping within the examined region. However, this trend could alter if the temperature-dependent relaxation time, calculated from the effective mass, is included in the calculation of σ. Fig.4(d) illustrates that the electronic thermal conductivity (κ_{el}), increases with rising temperature. The Wiedemann-Franz law ($\kappa_{el} = L\sigma T$, where L is the Lorentz number) relates σ to κ_{el}. κ_{el} displays a similar trend in variation with μ as σ does across different temperatures.

The change in the power factor (PF = $S^2\sigma$) with the μ at different temperatures is illustrated in Fig.4(c). The PF has very low values close to the Fermi level; however, it rises sharply with an increase in μ. There are two distinct peaks in the PF for both p-type and n-type materials. As the μ continues to increase, the PF gradually decreases, and this trend is obeyed across all temperatures. The peak PF is 53 μW/cmK² for n-type doping and 46 μW/cmK² for p-type doping at 400 K. As the temperature increases, the peak value of the PF rises due to enhanced σ, despite a decline in the S. TiFeSe exhibits its highest PF values of 182 μW/cmK² for p-type doping and 161 μW/cmK² for n-type doping at a temperature of 1200 K. p-type doping has higher PF values at all temperatures compared to n-type doping. The calculated PF values are slightly lower than those previously reported for 18 VEC hH TiIrX (X = As and Sb) at 600 K [35]. These PF values indicate better thermoelectric performance at elevated temperatures.

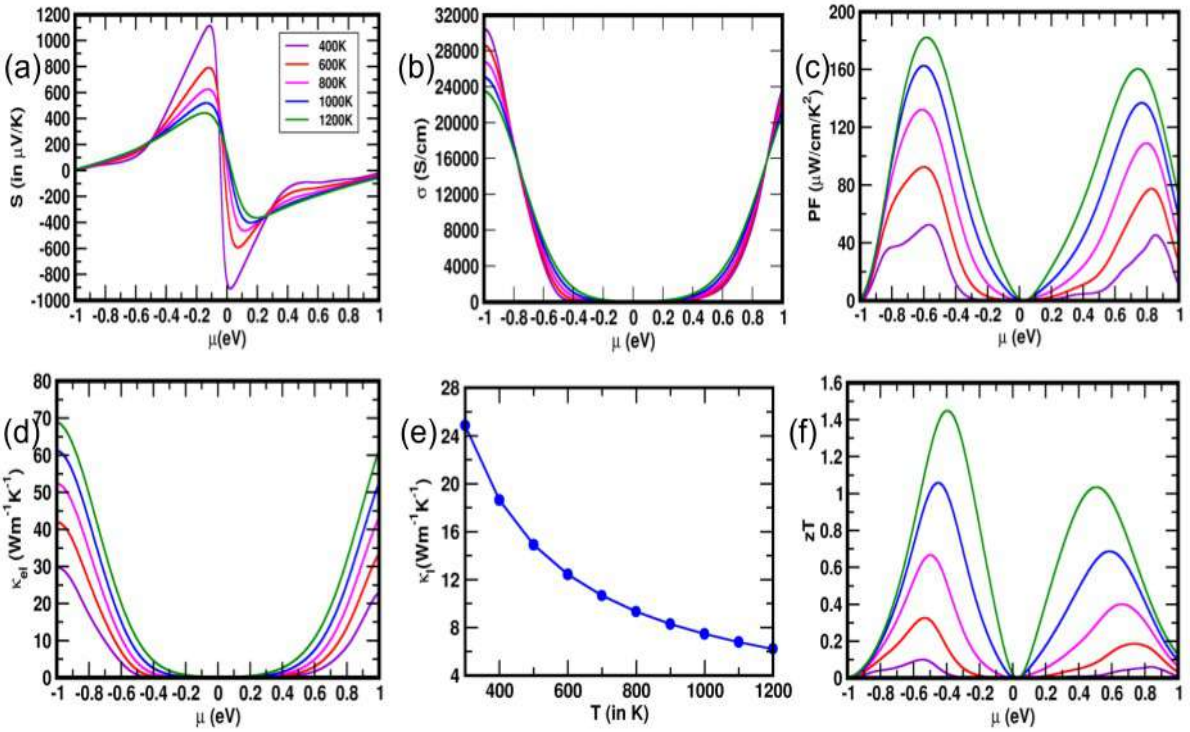

Fig. 4. Variations of (a-d) Seebeck coefficient, electrical conductivity, power factor, and electronic thermal conductivity with respect to chemical potential; (e) lattice thermal conductivity as a function of temperature; and (f) zT with chemical potential at different temperatures.

Fig.4(e) shows the calculated κ_l from Slack's equation of TiFeSe as a function of temperature. The Slack's equation is [27],

$$\kappa_l = \frac{V^{1/3} A M \theta_D^3}{\gamma^2 T n^{2/3}} \quad \text{.....(v)}$$

where, Grüneisen parameter is calculated as,

$$\gamma = \frac{9-12(v_t/v_l)^2}{2+4(v_t/v_l)^2} \quad \text{.....(vi)}$$

and dimensionless constant,

$$A = \frac{2.43\times10^{-8}}{1-0.514/\gamma+0.228/\gamma^2} \quad \text{.....(vii)}$$

M, V, and n represent the average atomic mass, the volume per cell, and the number of atoms in the primitive unit cell, respectively. The Debye temperature (456.24 K) and the Grüneisen parameter (1.69) are obtained from the longitudinal velocity (v_l) of (6158.954 m/s) and the transverse velocity (v_t) of (3368.264 m/s), which are calculated from the elastic constants using the thermo_pw code.

The κ_l at room temperature is 24.84 $Wm^{-1}K^{-1}$. Phonon generated by lattice vibrations, whose scattering increases with temperature in crystalline materials, influence the κ_l. κ_l decreases with increasing temperature, and reaches its minimum value of 6.21 $Wm^{-1}K^{-1}$ at 1200 K. The κ_l value of the compound in this study at 300 K is much higher than that of the iron-based 18 VEC hH NbFeTe [36], slightly more than NbFeSb [37], close to TiFeTe, and lower than HfFeTe [34].

The variation in the zT as a function of μ for different temperatures is displayed in the Fig.4(f). Like PF, the zT has very low values close to the Fermi level and further rises sharply with an increase in μ both sides making two distinct peaks in the zT for both hole and electron doped materials. At 400 K, the peak zT values are 0.11 for hole doped and 0.07 for electron doped compounds. As the temperature increases, the peak value of zT also rises, reaching 1.45 for the p-type region and 1.04 for the n-type region at 1200 K. Thus, the present compound shows better potential for thermoelectric applications at high temperatures in hole-doped materials compared to electron-doped ones. These zT values are significantly lower than those reported by Nenuwe et al. [17], which did not consider the lattice contribution to thermal conductivity. Thus, it indicates that the lattice contribution cannot be neglected in zT calculations for hH compounds. The zT calculated for TiFeSe is lower than that of TiFeTe [34] but higher than that of NbFeTe [36], considering the temperature-dependent relaxation time.

By utilizing the band engineering for electronic transport and phonon scattering strategies for thermal transport, the zT of

the compounds can be further enhanced.

4. CONCLUSIONS

In conclusion, this study summarizes the key findings from the theoretical investigation of TiFeSe compounds, based on density functional theory and semiclassical Boltzmann transport theory. The thermodynamic, dynamic, and mechanical stabilities of the TiFeSe compound were assessed through the evaluation of formation energy, phonon spectrum, and elastic constants, respectively. The EBS and DOS indicate that the compound exhibits non-magnetic semiconducting behaviour with indirect band gap of 0.80 eV. The κ_l calculated using Slack's equation, is 24.84 $Wm^{-1}K^{-1}$ at room temperature and was found to decrease with increasing temperature. The electronic and thermal transport properties were evaluated at various chemical potentials and temperatures. TiFeSe achieves a maximum zT value of 1.45 for hole doping and 1.04 for electron doping, respectively, at 1200 K. The high PF of the compound contributes zT > 1. The zT values suggest that TiFeSe is a strong candidate for thermoelectric performance and this study will assist in guiding experimental work.

ACKNOWLEDGMENTS

PK acknowledges with gratitude the support received from UGC Nepal's PhD grants (award no. PhD-79/80-S&T-14). PK appreciates the computational resources and valuable suggestions from Prof. Narayan Prasad Adhikari, Central Department of Physics, Tribhuvan University, Nepal.

REFERENCES

[1] S. Lv, Z. Qian, D. Hu, X. Li, W. He, A comprehensive review of strategies and approaches for enhancing the performance of thermoelectric module, *Energies*, 13 (2020) 3142. https://doi.org/10.3390/en13123142.

[2] P. Rodgers, Silicon goes thermoelectric, *Nature Nanotechnology*, 3 (2008) 76. https://doi.org/10.1038/nnano.2008.17.

[3] J. Tervo, A. Manninen, R. Ilola, H. Hänninen, State-of-the-art of thermoelectric materials processing, *VTT Technical Research Center of Finland*, Vuorimiehentie (2009).

[4] C. Gayner, K. K. Kar, Recent advances in thermoelectric materials, *Progress in Materials Science*, 83 (2016) 330-382. https://doi.org/10.1016/j.pmatsci.2016.07.002.

[5] G. J. Snyder, E. S. Toberer, Complex thermoelectric materials, *Nature Materials*, 7 (2008) 105-114. https://doi.org/10.1038/nmat2090.

[6] M. Wambach, R. Stern, S. Bhattacharya, P. Ziolkowski, E. Müller, G. K. Madsen, A. Ludwig, Unraveling self-doping effects in thermoelectric TiNiSn half-Heusler compounds by combined theory and high-throughput experiments, *Advanced Electronic Materials*, 2 (2016) 1500208. https://doi.org/10.1002/aelm.201500208.

[7] J. R. Sootsman, D. Y. Chung, M. G. Kanatzidis, New and old concepts in thermoelectric materials, *Angewandte Chemie International Edition*, 48 (2009) 8616-8639. https://doi.org/10.1002/anie.200900598.

[8] J. Wei, L. Yang, Z. Ma, P. Song, M. Zhang, J. Ma, X. Wang, Review of current high-ZT thermoelectric materials, *Journal of Materials Science*, 55 (2020) 12642-12704. https://doi.org/10.1007/s10853-020-04949-0.

[9] C. Uher, Skutterudites: Prospective novel thermoelectrics, in *Semiconductors and Semimetals*, 69 (2001) 139-253. https://doi.org/10.1016/S0080-8784(01)80151-4.

[10] Y. Shi, C. Sturm, H. Kleinke, Chalcogenides as thermoelectric materials, *Journal of Solid State Chemistry*, 270 (2019) 273-279. https://doi.org/10.1016/j.jssc.2018.10.049

[11] L. Huang, Q. Zhang, B. Yuan, X. Lai, X. Yan, Z. Ren, Recent progress in half-Heusler thermoelectric materials, *Materials Research Bulletin*, 76 (2016) 107-112. https://doi.org/10.1016/j.materresbull.2015.11.032

[12] S. J. Poon, Recent advances in thermoelectric performance of half-Heusler compounds, *Metals*, 8 (2018) 989. https://doi.org/10.3390/met8120989

[13] F. Casper, T. Graf, S. Chadov, B. Balke, C. Felser, Half-Heusler compounds: novel materials for energy and spintronic applications, *Semiconductor Science and Technology*, 27 (2012) 063001. http://dx.doi.org/10.1088/0268-1242/27/6/063001

[14] A. Page, P. F. P. Poudeu, C. Uher, A first-principles approach to half-Heusler thermoelectrics: Accelerated prediction and understanding of material properties, *Journal of Materiomics*, 2 (2016) 104-113. https://doi.org/10.1016/j.jmat.2016.04.006

[15] I. Galanakis, P. Mavropoulos, P. H. Dederichs, Electronic structure and Slater–Pauling behaviour in half-metallic Heusler alloys calculated from first principles, *Journal of Physics D: Applied Physics*, 39 (2006) doi:10.1088/0022-3727/39/5/S01

[16] Materials Project, TiFeSe (mp-961660). https://next-gen.materialsproject.org/materials/mp-961660, 2024. (accessed 08 October 2024).

[17] N. O. Nenuwe, N. O. Agbawe, Ab initio predictions of thermoelectric, mechanical, and phonon characteristics of FeTiSe half-Heusler compound, *Current Applied Physics*, 53 (2023) 132-141. https://doi.org/10.1016/j.cap.2023.06.008.

[18] S. Anand, M. Wood, Y. Xia, C. Wolverton, G. J. Snyder, Double half-Heuslers, *Joule*, 3 (2019) 1226-1238. https://doi.org/10.1016/j.joule.2019.04.003.

[19] P. Giannozzi, O. Andreussi, T. Brumme, O. Bunau, M. B. Nardelli, M. Calandra, S. Baroni, Advanced capabilities for materials modelling with Quantum ESPRESSO, *Journal of Physics: Condensed Matter*, 29 (2017) 465901. https://doi.org/10.1088/1361-648X/aa8f79.

[20] J. P. Perdew, K. Burke, M. Ernzerhof, Generalized gradient approximation made simple, *Physical Review Letters*, 77 (1996) 3865. https://doi.org/10.1103/PhysRevLett.77.3865.

[21] A. Kokalj, XCrySDen—a new program for displaying crystalline structures and electron densities, *Journal of Molecular Graphics and Modelling*, 17 (1999) 176-179. https://doi.org/10.1016/S1093-3263(99)00028-5.

[22] H. J. Monkhorst, J. D. Pack, Special points for Brillouin-zone integrations, *Physical Review B*, 13 (1976) 5188. https://doi.org/10.1103/PhysRevB.13.5188.

[23] N. Marzari, D. Vanderbilt, A. De Vita, M. C. Payne, Thermal contraction and disordering of the Al (110) surface, *Physical Review Letters*, 82 (1999) 3296. https://doi.org/10.1103/PhysRevLett.82.3296

[24] G. K. Madsen, J. Carrete, M. J. Verstraete, BoltzTraP2, a program for interpolating band structures and calculating semi-classical transport coefficients, *Computer Physics Communications*, 231 (2018) 140-145. https://doi.org/10.1016/j.cpc.2018.05.010.

[25] S. Baroni, S. De Gironcoli, A. Dal Corso, P. Giannozzi, Phonons and related crystal properties from density-functional perturbation theory, *Reviews of Modern Physics*, 73 (2001) 515. https://doi.org/10.1103/RevModPhys.73.515.

[26] A. D. Corso, thermo_pw. http://dalcorso.github.io/thermo_pw, 2024 (accessed 08 October 2024).

[27] D. T. Morelli, G. A. Slack, High lattice thermal conductivity solids, in *High Thermal Conductivity Materials*, Springer New York, 2006. (pp. 37-68).

[28] F. D. Murnaghan, The compressibility of media under extreme pressures, *Proceedings of the National Academy of Sciences*, 30 (1944) 244-247. https://doi.org/10.1073/pnas.30.9.244.

[29] M. Born, R. Fürth, The stability of crystal lattices. III: An attempt to calculate the tensile strength of a cubic lattice by purely static considerations, in Mathematical Proceedings of the Cambridge Philosophical Society, 36 (1940) 454-465. https://doi.org/10.1017/S0305004100017503.

[30] L. I. A. N. G. Zuo, M. I. C. H. E. L. Humbert, C. L. A. U. D. E. Esling, Elastic properties of polycrystals in the Voigt-Reuss-Hill approximation, *Journal of Applied Crystallography*, 25 (1992) 751-755. https://doi.org/10.1107/S0021889892004874

[31] M. E. Fine, L. D. Brown, H. L. Marcus, Elastic constants versus melting temperature in metals, *Scripta Metallurgica*, 18 (1984) 951-956. https://doi.org/10.1016/0036-9748(84)90267-9.

[32] G. Tan, L. D. Zhao, M. G. Kanatzidis, Rationally designing high-performance bulk thermoelectric materials, *Chemical Reviews*, 116 (2016) 12123-12149. https://doi.org/10.1021/acs.chemrev.6b00255.

[33] M. Singh, Augmented thermoelectric performance of LiCaX (X= As, Sb) Half Heusler compounds via carrier concentration optimization, *Journal of Physics and Chemistry of Solids,* 174 (2023) 111182. https://doi.org/10.1016/j.jpcs.2022.111182.

[34] P. Khatri, N. P. Adhikari, Mechanical and thermoelectric response of 18-valence electron half-Heusler tellurides XFeTe (X = Ti, Hf): A theoretical perspective, *Materials Today Communications,* 39 (2024) 108853. https://doi.org/10.1016/j.mtcomm.2024.108853.

[35] S. Chibani, O. Arbouche, M. Zemouli, K. Amara, Y. Benallou, Y. Azzaz, ... & M. Ameri, Ab initio prediction of the structural, electronic, elastic, and thermoelectric properties of half-Heusler ternary compounds TiIrX (X = As and Sb), *Journal of Electronic Materials*, 47 (2018) 196-204. https://doi.org/10.1007/s11664-017-5761-9.

[36] G. S. AlGhamdi, A. Saini, A. A. AlShaikhi, & R. Kumar, First-principles investigation of thermoelectric properties of half-Heusler alloy NbFeTe, *Journal of Superconductivity and Novel Magnetism,* (2021) 1-10. https://doi.org/10.1007/s10948-021-06082-8.

[37] T. Fang, S. Zheng, T. Zhou, L. Yan, & P. Zhang, Computational prediction of high thermoelectric performance in p-type half-Heusler compounds with low band effective mass, *Physical Chemistry Chemical Physics,* 19 (2017) 4411-4417. https://doi.org/10.1039/C6CP07897D

Antioxidant Activity and HR-LCMS Analysis of Phytochemicals Present in the Methanolic Extract of the Rhizomes of *Paris Polyphylla* (Satuwa)

Paurakh Magar[a], Galaxy Pokhrel[c], Sachin Silwal[a], Sabi Thapa[a], Ajaya Mahato[a], Bishisha Adhikara[a], Shiva Bagale[a], Pabitra shrestha[b], Bodhbabu Bhattarai[a*], Ganga Raj Pokhrel[a*]

[a]*Department of Chemistry, Birendra Multiple Campus, Tribhuvan University Chitwan, Nepal.*
[b]*Department of Microbiology, Birendra Multiple Campus, Tribhuvan University Chitwan, Nepal.*
[c]*Purbanchal University, Shree Medical and Technical college, Chitwan, Nepal.*

Research Article

ISSN: 3059-9504 (online)
Doi:xxxx

Article History

Received: October 21, 2024
Revised: November 18, 2024
Accepted: November 20, 2024
Published: December 28, 2024

Keywords

Paris Polyphylla, Antioxidant activity, Total phenolic content; Total flavonoid content, medicinal herb, HR-LCMS

***Corresponding author**
Email: pokhrelgangaraj1967@gmail.com (GR Pokherel), Phone: + 977-9845706727; b2bhattarai@yahoocom (B Bhatterai), Phone: +Phone no: 9845055622

ABSTRACT

Antioxidant activity and the complete High-Resolution Liquid Chromatography Mass Spectrometry (HR-LCMS) metabolomic profiling of the rhizomes of *Paris Polyphylla* is still unknown. This study mainly focused on the analysis of the phytochemicals present in the methanolic extract of the rhizomes of *P. Polyphylla*. The roots of *Paris polyphylla* is used in traditional medicine as counteragent for snake bite, remedy for insect poison, relieve for wounds, sore throat etc. Like other medicinal plants, root of *Paris polyphylla* contains numerous potential bioactive compounds. Such bioactive compounds have significant antioxidant activity. Quantative measurement of total Flavonoids, phenolics and antoxidants were carried using spectrometric technique based on quercetin, gallic acid and ascorbic acid as the standards. The total flavonoids content is calculated as 38.430.27mg QE/g dry weights. Moreover the total phenolic constitutes 41.470.53 mg GAE/g dw and the total antioxidant comprises 20.690.97 mg Ascorbic acid equivalent/g dw. HR-LCMS analysis conducted in both positive and negative ESI modes revealed the presence of 128 distinct molecules. Root of *P. Polyphylla* possesses valuable antioxidant properties for dietary and medicinal use.

1. INTRODUCTION

The majority of the people in the world use plants and plant products as a curative agent for their disease due to its negligible side effect. The unique property of medicinal plant to cure various diseases is due to the presence of different class of phytochemicals [1]. Phytochemicals are the bioactive molecules which exhibit antioxidant and anti-inflammatory activities. Some biologically active molecules of the plant have anti-carcinogenic property also. The presence of numerous phytochemicals in the medicinal plant is the cause to use plant based product as antimicrobial, antiviral, analgesic, anticancer and antioxidant activity [2, 3]. Various plant extracts are used as traditional medicine. Essential oil obtained from Lemongrass is also used in traditional medicine which showed maximum inhibition of the bacteria S. aureus at concentration of 100 percent [4]. Clinical and epidemiological research focused on fruits, vegetables, grains and other plant parts [5]**.** Phytochemicals are effective in the prevention of cardiovascular disease as well as diabetics. Phytochemicals are also effective in the treatment of bone disease, i.e. Osteoporosis. Gynecological, neurological and immunological disorder can also be addressed using the phytochemicals [6].

Antioxidants present in the plant material are potential for maintaining good health and coronary heart disease in which arteries of heart are unable to supply enough oxygenated blood to the heart. Cancer is also alarming issue in the group of scientists and food manufacturers as consumers are aware about functional food with specific health effect [7]. Antioxidants can inhibit the oxidation of lipids or other molecules by obstructing the chain initiation or propagation reaction [8]. Phenolic acids, phenolic diterpenes and flavonoids have antioxidative effects [9, 10]. Antioxidant plays important role to absorb and neutralize free radicals, decomposes peroxides and quenches singlet and triplet oxygen [11]. A large number of phytochemicals have significant antioxidant magnitude correlated with lower impermanence rates of cancer in human populations [12].

Rhizome decoction of *P. Polyphlla* is used in the treatment of ulcer, diphtheria, epidemic Japanese B encephalitis, appendicitis, lymphadenopathy, tonsillitis, parotitis, mastitis and rheumatism. It alleviates pain and relieves boils, carbuncles, sore throat, and traumatic pain. It is also used for the treatment of the liver, stomach, nose, lungs, throat and breast cancer in Chinese traditional medicine [13]. The potentialities of the phytochemicals for their use to cure various ailments must be evaluated.

Raw plant extract is the composite blend of numerous phytochemicals used to make traditional medicine. Such composite blends of phytochemicals take control to cure particular and complicated disease [14]. The appropriate screening of the phytochemicals is significant to search novel chemical compounds used for the medicine. The extraction, phytochemical screening and High Resolution Liquid Chromatography Mass spectrometry (HR-LCMS) analysis of the rhizomes extract of plant contributed to search appropriate plant species for particular disease control [15].

The preliminary analysis of the extract of rhizome gives key information about total flavonoids, total phenolic and antioxidant content. A small amount of the extract is sufficient for HR-LCMS analysis which reveals the presence of bioactive compounds such as amino acid, fatty acid, triterpenoids, flavonoids, diterpenes, lipid, phenolic compounds, sesquiterpenoids, quinolizidine alkaloid, and benzoquinone. The purpose of this study was to evaluate the rhizomes of *P. Polyphylla* as new potential source of antioxidant and phenolic compounds. Our study aims to disclose almost all phytochemicals constituents present in the rhizomes of *P. Polyphylla* using HR-LCMS.

2. MATERIALS AND METHODS

The rhizomes of the plant *P. Polyphylla* were collected from its cultivated habitat, Kherbang, Thabang (2300-2400 meter from sea level) of Jaljala area in Thabang Rular Municipality, Rolpa, Nepal. The rhizomes were excavated during flowering season (July-Aug) from 5-10 centimeter below the surface of the soil using spade. Any coarse materials adhered on the roots were removed and first washed with tap water and then with distilled water. The water present on the surface of the sample was blotted dry using blotting papers. The clean and surface dry rhizomes were stored in zipper bags. The samples were carried into the lab for further execution within 3-4 days. It was chopped into small pieces using knife and air dried in shade until it became completely dry. The air dried samples were stored in desiccators at lab temperature to avoid any moisture absorption.

All the reagents/ chemicals used were of analytical grade (Make: Merck/ Qualigens/ CDH). For qualitative analysis, the powdered sample (50g) was packed in Soxhlet extractor and subjected for continuous percolation for 72 h using 500 mL methanol as solvent. The extract was filtered using Whatman filter paper No.1. Then it was evaporated and concentrated on water bath at about 40-45℃ until it became just like curd. The protocol for the extraction was used as in Naik et al. [16]. The methanolic extract was preserved at -20℃ prior further analysis.

For quantitative analysis, 450 g of powdered sample was taken in 1000mL of round bottom flask and soaked in methanol of analytical grade (4 x 500ml) and stirred in every five minutes (about 10-12 hours) for 3-4 days. The extract thus obtained after 72 hours of cold percolation was filtered using Whatman No.1 (0.45µm) filter paper to remove the suspended materials and dried on petri plate under the high speed ceiling fan. The gummy mass of the plant extract was then placed in amber colored glass bottle, sealed using parafilm and stored at -20℃ prior further analysis. The yield of the extract was calculated using the formula:

$$\text{Yield } \% = \frac{Wt.of crude extract}{Wt.of the powdered plant sample taken} \times 100$$

Qualitative phytochemical tests: Preliminary phytochemical analysis of the methanolic extract is carried out following the method used in Naik et al. [16]. The extract was subjected for the tests of the phytochemicals such as alkaloids, flavonoids, steroids, terpenoids, glycosides, phenols, saponins, carbohydrates, and proteins.

Test for alkaloids: The extract is treated with 2N HCl and heated on water bath at 80˚C for 10 minutes. After heating, the solution was filtered and tested.

i. Mayer's test: Few drops of Mayer's reagent is added to part of the above filtered solution and observed for the formation of turbidity or dull white/ yellow cream precipitate.
ii. Wagner's test: Part of the filtrate is treated with the Wagner's reagent and observed for the formation of brown or reddish brown precipitate.

Test for flavonoids: Following tests are carried out for the screening of flavonoids.

i. Lead acetate test: The extract is treated with few drops of 10% lead acetate solution, and then observed for the formation of yellow coloration.
ii. Sulphuric acid test: The extract is used with few drops of conc. H_2SO_4 and observed for its orange color formation.
iii. NaOH test: The extract is stirred with 10% NaOH followed by 5N HCl and observed the color change from orange to yellow.

Test for terpenoids:

i. Salkowski test: 5 mg of extract is treated with 2 ml of chloroform. Then carefully added conc. H_2SO_4 and observed the brown coloured layer at the interference.

Test for saponins: About 5 mg extract is shaken with 5 ml of distilled water and observed for the formation of foam.

Test for carbohydrates: 5 mg of extract is dissolved in 5 ml of distilled water and filtered. The filtrate is used to test the carbohydrate.

i. Molisch's test: The filtrate is agitated with few drops of Molisch's reagent and shaken well. Conc. H_2SO_4 is then added along the side of the test tube and observed for the formation of red or dull violet ring at the interference.

Test for glycosides: 2 ml of the extract, 1 ml of glacial acetic acid and 1 ml of 5 % ferric chloride is added in a test tube and mixed well. Then 3 drops of conc. H_2SO_4 is added to it, shaked and observed for the formation of greenish blue color.

Test for proteins: Few drops of 0.2 % ninhydrin is mixed to 2 ml of the extract and heated to 100˚C temperature, then observed for the formation of blue color.

Test for Steroids:

i. Salkowski test: The methanolic extract of the sample is again subjected for the extraction with chloroform. Thus extracted aliquot is shaken with conc. H_2SO_4 and set aside for some time and observed the formation of red color.

Test for phenols: 1 ml of the extract, 2 ml of distilled water and 5 drops of 10% ferric chloride solution are mixed in test tube and shaken well. The formation of blue or green colour is observed.

Quantitative phytochemical analysis: The quantitative phytochemical analysis is carried out for the estimation of flavonoids and phenols as described in papers Kenneth-Obosi and Khan [17,18].

Determination of total flavonoids: Total flavonoids were determined by using aluminum chloride colorimetric assay method. In this method, quercetin was used as reference standard solution. 0.2000g standard quercetin compound was dissolved in 200 mL of methanol. From this solution, 10 ml was taken and diluted to 100 ml in the same solvent to make 100 µg/mL solutions [19]. Different concentrations (1, 2, 3, 4, 5, 6, 7, 8, 9, 10 µg/mL) of standard solutions were prepared using serial dilution technique. 35µg /mL extract solution was also prepared in the same solvent. Then 10 µl of 10% aluminum chloride solution was added in 50 µl extract solution (10µg/mL) and standard solution (different concentration) separately and incubated at room temperature for 40 minutes. The absorbance of both solutions was measured at 415 nm (maximum absorbance by blank solution) separately using UV-Visible spectrophotometer (UV-1800, Simadzu).

Determination of total phenolic compound: Total phenolic compound was determined by using gallic acid as reference standard solution. In this process, different concentrations of standard solutions of gallic acid were prepared. One mL of Follin-ciocalteu phenol reagent (10%) and 0.5 ml of 7.5% aqueous Na_2CO_3 solution was mixed with 1mL of the root extract (100 µg/mL), and reference solutions separately [20]. Solution thus prepared was then allowed to stand for about 30 min. The absorbance of the solutions was observed at 742 nm (maximum absorbance) separately using UV-Visible spectrophotometer (UV-1800, Simadzu).

Prior to measuring the absorbance of standard and sample solutions, the absorbance of the blank solution was also noted.

Evaluation of antioxidant activity: Evaluation of anti-oxidant activity was carried out using DPPH assay method [17] and Khan et al. [18]. Briefly, ascorbic acid was used as the reference standard. Different concentrations of reference solutions and extract samples solutions (100µg/mL) were prepared. 250 ml stock solution of DPPH (0.04mg/mL) was prepared in methanol. Then 15 ml of stock solution of DPPH was added in 10 ml reference solution and sample solution prepared in methanol and incubated at room temperature for 30 min. Measurement of absorbance was carried out at 515nm (maximum absorbance) using UV-Visible spectrophotometer (UV-1800, Simadzu).

HR-LCMS/MS analysis:

Methanolic extract of rhizomes (i.e. viscous, 500mg) of *P. Polyphylla* was packed in 5ml sample tube made of borosilicate glass and sent to the lab "sophisticated analytical instruments facility (SAIF), IIT, Mumbai India" by TNT courier for HR-LCMS/MS analysis. The HR-LCMS/MS analysis was carried out using (6550 iFunnel Q-TOFs) system consisting of Hip sampler, binary pump, column component, Q-TOF having dual ion source and electrospray ion generation(ESI) with Agilent Jet Stream (AJS). Q-TOF data acquisition and mass spectrometric evaluation were carried out using Agilent mass Hunter Software. The optimal running parameters of HR-LCMS, solvent condition and time table are as follows.

Table 1: Acquisition method of HR-LCMS

Parameter	Value
Ion source	Dual AJS ESI
MS Abs. threshold	200
MS/MS Abs. threshold	5
MS Min Rang(m/z)	130
MS max Rang(m/z)	10000
MS Scan Rate (spectra/sec)	1.0
MS/MS Scan Rate (spectra/sec)	1.0
Isolation Width MS/MS	Medium (~4 amu)
Max Precursors Per Cycle	10
Threshold (Abs)	10000
Target (counts/spectrum)	25000.0
Gas Temperature(^oC)	250
Gas Flow (l/min)	13
Nebulizer (psig)	35
SheathGas Temp	300
SheathGas Flow	11
Vcap	3500
Nozzle Voltage (V)	10000
Fragmentor	175
Skimmer1	65
Octopole RFPeak	750
Draw speed	100.0 µL/min
Eject speed	100.0 µL/min
Wait time after drawing	2.0 s
Sample flush out factor	5.0
Injection volume	3.0 µL
Wash Time	3.0 s
Flow	0.300mL/min
low pressure Limit	0.00 bar
high pressure Limit	1200.00 bar
Max. flow Ramp up	100.00 mL/min^2
Max. flow Ramp Down	100.00 mL/min^2
Stop time	30.00 min

Table 2: Solvent composition

	Channel	Ch.1 Solvent	Name 1	Ch2 Solvent	Selected	Used	Percent
1	A	100.0% water V.02	0.1% FA in water	100.0% water V.02	Ch. 2	Yes	95.00 %
2	B	100.0 % Acetonitrile V.02	90% ACN + 10% H_2O + 0.1% FA	100.0 % Acetonitrile V.02	Ch.2	Yes	5.00 %

Table 3: Time table

	Time	A	B	Flow	Pressure
1	1.00 min	95.00 %	5.00 %	0.300 mL/min	1200.00 bar
2	20.00 min	0.00 %	100.0 %	0.300 mL/min	1200.00 bar
3	25.00 min	0.00 %	100.0 %	0.300 mL/min	1200.00 bar
4	26.00 min	95.00 %	5.00 %	0.300 mL/min	1200.00 bar
5	30.00 min	95.00 %	5.00 %	0.300 mL/min	1200.00 bar

Statistical analysis: All experiments were performed in triplicates. Values for each sample are expressed as the mean ± standard deviation.

3. RESULTS AND DISCUSSION

The 450g of the powdered sample on percolation using Soxhlet in methanol for 72 hours yield 67.779g (15.06%) of crude extract. The preliminary phytochemical screening of the crude extract shows the following result.

Table 4: Test results of phytochemical screening of the plant extract

S. No.	Phytochemicals	Result
1	Alkaloids	
	a. Meyer's test	+
	b. Wagner's test	+
2	Flavonoids	
	a. Lead acetate test	+
	b. H_2SO_4 test	+
	c. NaOH test	+
3	Terpenoids	
	a. Salkowski test	+
4	Saponins	+
5	Carbohydrates	
	a. Molisch's test	+
6	Steroids	+
7	Proteins	+
8	Phenols	+

(+) represents the positive result

Quantitative analysis of selected phytochemicals

Flavonoids: Determination of the total flavonoids in the methanolic extract of rhizome is carried out using quercetin as reference standard and different concentrations of reference is prepared for the calibration of the instruments. The regression equation between absorbance and amount of quercetin was Y = 0.0065x (R^2 = 0.996). Similarly, 10µg/mL solution of the sample is also prepared. All samples were observed in UV-Visible spectrophotometer (UV-1800, Simadzu) at the maximum wavelength of 415nm. The TFC is estimated using the formula x (V/m) and expressed as mg QE/g of extract in dry weight. The quantity of flavonoid compounds in solution is found 2.55µg/mL sample solution. The total flavonoids compounds in the dry extract is found 38.430.27mg QE/g.

Total phenolic compounds: Gallic acid is taken as reference standard and the different concentrations of reference standard are prepared for the calibration of the instrument. The regression equation between absorbance and amount of gallic acid was Y = 0.006x+0.106 (R^2 = 0.998). Similarly, different concentrations of the sample solution in µg/mL are also measured in UV-Visible spectrophotometer (UV-1800, Simadzu) at the maximum wavelength of 742nm. The phenolic compound in solution is found to be 27.59 µg/mL sample solution. Moreover the total phenolic compounds in the dry extract constitutes 41.470.53 mg GAE/g.

Antioxidant activity test: Ascorbic acid is taken as reference standard. Different concentrations of reference standard solutions are prepared for the calibration of the instrument. The regression equation between absorbance and amount of ascorbic acid was y = -0.017x + 0.534 (R^2 = 0.989). Similarly, 100µg/mL solutions of the sample were prepared and observed in UV-Visible spectrophotometer (UV-1800, Simadzu) at the maximum wavelength of 515 nm Spectrometer (UV-1800, Simadzu) at the maximum wavelength of 515nm. The amount of antioxidant compound in sample solution is 13.76µg/mL. Furthermore, the total antioxidant compound in the dry comprises 20.69±0.97 mg ascorbic acid equivalent /g.

Total Phenolic and Flavonoids have been studied extensively because of their preventive effects against oxidative stress related diseases, several cancers, cardiovascular and neurodegenerative diseases [21]. The plenty of total phenolic and flavonoid contents in the extract be possibility of discovering new natural molecules with antioxidants, antibacterial, anticancer and anti-inflammatory properties.

Phenolic acids, flavonoids and other polyphenols are known to

contribute the antioxidant activities in plants [22, 23]. Relatively high flavonoids, phenolics and antioxidant molecules in the extracts suggest that plant phenolics significantly contribute to the free radical scavenging and reducing activity.

HRLCMS Profiling

The methanolic extract of rhizomes is subjected to HR-LCMS analysis. HR-LCMS analysis is conducted in both positive and negative modes which revealed the presence of 128 distinct compounds, out of which 106 compounds are found in the register of molecular library of HR-LCMS, whereas the remaining 22 compounds are not found in the record of molecular library and listed as unidentified molecules.

The compounds are separated using the LC column (ZORBAX EclipseC_{18} (150 × 2.1 mm, 5µm)), and subsequently analysed using mass spectrometer. The chromatograms of the molecules present in the methanolic extract and their Mass spectra capture under positive and negative modes of ionization are illustrated in figure 1 and 2 respectively. The HR-LCMS profile of the molecules along with mass/charge ratio, retention time of chromatogram and mass of the fragmented moiety is mentioned in the table 5 and 6. Some of the identified compounds are listed below.

Table 5: List of some selected identified compounds in HRLCMS profiling

S.N	Name	Molecular Formula	Retention Time (RT)	Mass	Chemical class
1	L-Carnitine	$C_7H_{16}NO_3$	1.008 (+ ESI)	162.1135	Aminoacid derivative
2	BILA 2185BS	$C_{35}H_{46}N_4O_4S$	1.184 (+ESI)	618.3219	aminoacid amide
3	Bruceantinol	$C_{30}H_{38}O_{13}$	3.185 (+ ESI)	606.2315	Quassinoids
4	MET-enkephalin	$C_{27}H_{35}N_5O_7S$	9.041 (+ ESI)	573.229	Opioid peptides
5	Moracin A	$C_{16}H_{14}O_5$	10.187 (+ ESI)	286.0846	2-arylbenzofuran flavonoids
6	Zapotin	$C_{19}H_{18}O_6$	1.039 (- ESI)	342.1126	Flavone
7	Bryostatin 1	$C_{47}H_{68}O_{17}$	9.987 (- ESI)	904.4498	cyclic macrolides
8	Dioscin	$C_{45}H_{72}O_{16}$	12.672 (- ESI)	868.4759	phytosteroid sapogenin

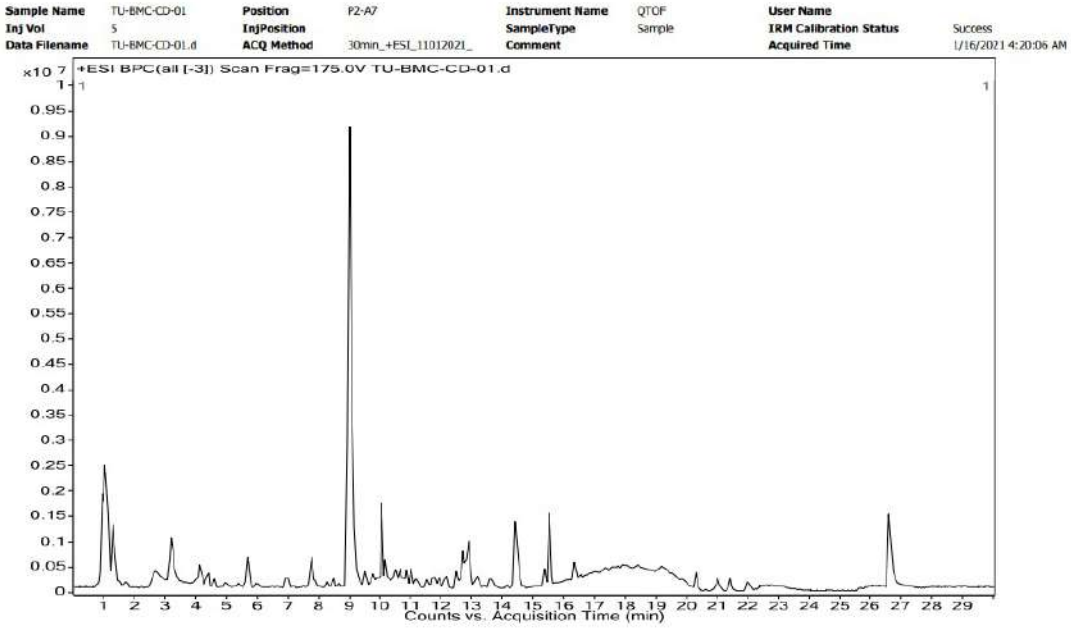

Fig. 1: LCMS chromatogram of the methanolic extract in positive ESI mode

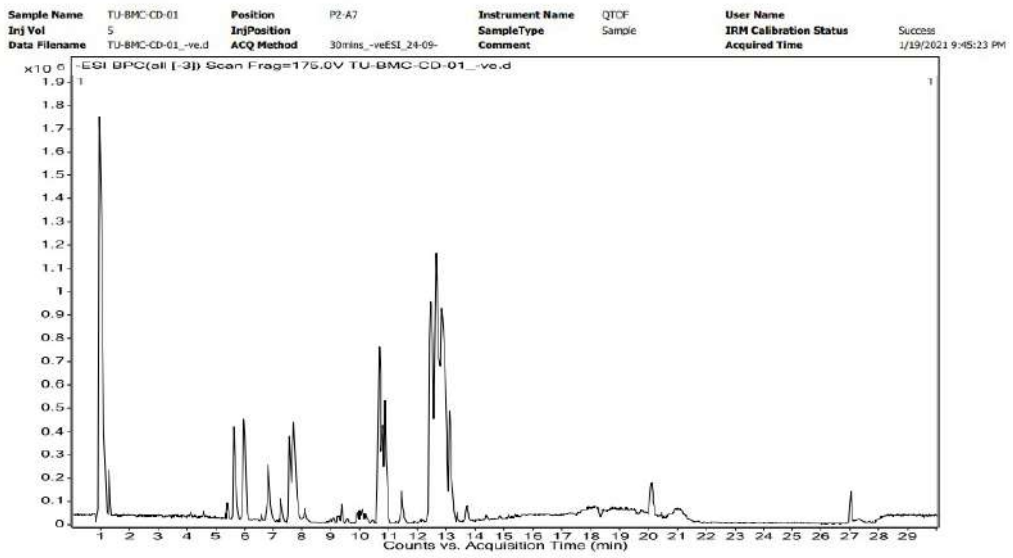

Fig. 2: LCMS chromatogram of the methanolic extract in negative ESI mode.

LCMS spectra, structure & functions of the selected phyto-compounds present in the plant.

To the best of our knowledge, this is the first validate analytical report of *P. Polyphylla* from Rolpa, Nepal. The most intense peak is obtained at retention time (RT) of 9-minute in positive ESI mode and 1min and 13 minute RT in negative ESI mode. Mass to charge ratio (m/z) of the majority of phyto-constituents lies in between100- 1000 mDa range. Out of 106 compounds that are matched in the molecular library of HR-LCMS, significant secondary metabolites are listed in the table 6. Most active secondary metabolites present in the methanolic extract are: L-Carnitine (Organic acid, m/z = 144.1024), BILA 2185BS (Peptide, m/z = 657.2856), Bruceantinol (Degraded triterpenoids, m/z = 321.1499), MET-enkephalin (Peptide, m/z = 573.2517), Moracin A (Phenylpropanoids, m/z = 286.1078), Zapotin (Polyphenols, m/z = 341.1053), Bryostatin 1 (Avermectins m/z = 949.4502/903.4449 /903.4464), Dioscin (Saponin, m/z = 913.4743) and so on.

Table 6: HR-LCMS data sheet of the chemical constituents present in the crude extract

N.	RT Min.	Mass	Ion Type	m/z	Calc m/z	Molecular Formula	Proposed Metabolites	Class of Compounds	Activity
ESI (+)									
1.	1.008	162.1135	M+ [H2O]	144.1024	144.1019	$C_7H_{16}NO_3$	L-Carnitine	Amino acid	Metabolomic Enhancer
2.	1.114	295.1595	(M+ Na) + [-H2O]	300.1383	300.1393	$C_{16}H_{25}NO_2S$	Tertatolol	Sulfonyl	Blood Pressure Depressor
3.	1.116 /1.446	217.1846 217.185	(M+K) +	256.1481 /256.1483	256.1462 /256.1462	$C_{15}H_{23}N$	Prolintane	Alkylamine	Stimulant
4.	1.184	618.3219	(M+K) +	657.2856	657.2871	$C_{35}H_{46}N_4O_4S$	BILA 2185BS	Peptide	Anti- HIV
5.	1.505	142.0204	(M+NH_4) +	160.0542	160.0539	$C_5H_6N_2OS$	Methylthiouracil	Thiazolidinone	Antithyroid reagent
6.	1.885	204.1171	(M+K) + [-H2O]	225.0697	225.0676	$C_{13}H_{16}O_2$	Isobutyl cinnamate	Aromatic Ester	Flavorant
7.	2.79	304.1109	(M+H) + [-H2O]	287.1073	287.109	$C_{11}H_{21}N_4O_2PS$	Imicyafos	Organophosphate	Nematicides
8.	3.185	606.2315 /606.2318	(M+2 (NH4))+2	321.1499 /321.1499	321.1494 /321.1494	$C_{30}H_{38}O_{13}$	Bruceantinol	Quassinoid	Antitumor activity
9.	3.856 /4.18	541.1302 /541.1302	(M+NH4) + [-H2O]	541.1534 /541.1534	541.1557 /541.1557	$C_{26}H_{21}F_6NO_5$	Acrinathrin	Fluoroquinolone	Insecticidal activity
10.	4.426	342.1472	(M+NH4) + [-H2O]	342.1706	342.17	$C_{20}H_{22}O_5$	Deoxymiroestrol	Steroidal phenol	Estrogenic
11.	5.723	480.3094	(M+H) +	481.3167	481.316	$C_{27}H_{44}O_7$	26-Hydroxy ecdysone	Steroids	Ecdysone
12.	9.01 /9.321	336.1047 /336.1053	(M+H) + [-H2O]	319.1014 /319.1022	319.0999 /319.0999	$C_{17}H_{20}O_5S$	Firocoxib	Coxibs	Anti-inflammatory drugs
13.	9.041	573.229	(M+NH4) +[-H2O]	573.2517	573.249	$C_{27}H_{35}N_5O_7S$	MET-enkephalin	Opioid peptide	Anti- cancer / Multiple

									Biological activity
14.	9.932	928.5045	(M+H)+ [-H2O]	911.5014	911.4999	$C_{47}H_{76}O_{18}$	Hoduloside IV	Triterpenoid saponin	Nutraceutical, Anti-sweet
15.	10.187	286.0846	(M+NH4)+ [-H2O]	286.1078	286.1074	$C_{16}H_{14}O_5$	Moracin A	Stilbenoid	Antioxidant &Multiple Biological Activity
16.	10.76 /11.071	430.3089 /430.3086	(M+H)+ [-H2O]	413.3058 /413.3058	413.305 /413.305	$C_{27}H_{42}O_4$	Schidigeragenin C	lignan glycosides	Nutraceutical
17.	11.6	460.3406	(M+NH4)+	478.3745	478.368	$C_{32}H_{44}O_2$	All-trans-carophyll yellow	Triterpenoids	Adjuvant, biomarker
18.	11.817	304.2775	(M+NH_4)+[-H2O]	304.3008	304.2999	$C_{21}H_{36}O$	3-Pentadecylpheno	Phenolic lipids	Multibiological
19.	12.435 /12.716	432.3246 /432.3243	(M+H) + [-H2O]	415.3214 /415.321	415.3207 /415.3207	$C_{27}H_{44}O_4$	24-Hydroxycalcitriol	Secosteroid	Osteoprotective
20.	12.919	872.4781	(M+Na)+ [-H2O]	877.4569	877.4556	$C_{44}H_{72}O_{17}$	Schidigerasaponin D1	Triterpenoid saponin	Antifungal
21.	13.566	326.3795	M+	326.379	326.3781	$C_{22}H_{48}N$	Didecyldimethylammonium	Quaternaryammonium compound (QAC)	Disinfectant
22.	14.437	520.3408	M+	520.3402	520.3398	$C_{26}H_{51}NO_7P$	1-Linoleoylglycerophosphocholin	lysophospholipid	Diagnostic
23.	15.335	358.9574	(M+NH4)+ [-H2O]	358.9805	358.9801	$C_9H_{11}Cl_2N_3O_4S_2$	Methyclothiazide	Thiazide	Diuretic
24.	18.898 /26.653	301.299 /273.2676	(M+H)+	284.2957 /274.2749	284.2948 /274.2741	$C_{16}H_{35}NO_2$	Sphinganine	Sphingolipid	Biomarker Property
25.	20.979	960.5798	(M+H)+	961.5873	961.5843	$C_{48}H_{84}N_2O_{17}$	Megalomicin C1	Macrolide	Antibiotic
26.	26.651	212.1065	(M+NH4)+	230.1403	230.14	$C_{12}H_{12}N_4$	MeIQ	Heterocyclic amine	Carcinogen
27.	26.763	241.132	(M+H)+ [-H2O]	224.1287	224.1281	$C_{12}H_{19}NO_4$	N-(3-oxo-ctanoyl)-homoserine lactone	N-acylhomoserinelactone (AHL)	Priming
ESI (-)									
28.	0.853	361.11	(M-H)-	360.1031	360.1024	$C_{17}H_{19}N_3O_4S$	Omeprazole sulfone	sulfoxides	reduce gastric acid
29.	1.031 /1.378	378.0889 / 378.0885	(M-H)-	377.0822 / 377.0817	377.0813 /377.0813	$C_{17}H_{18}N_2O_6S$	Carbenicillin	Penicillins	Bactericidal antibiotic
30.	1.039	342.1126	(M-H)-	341.1053	341.1031	$C_{19}H_{18}O_6$	Zapotin	Methoxylated flavone	Antidepressant, Anticancer, Antifungal, and Antioxidant agent.
31.	1.24	422.0782	(M+CH3COO)-	481.0913	481.0964	$C_{12}H_{23}O_{14}P$	Lactose 6-phosphate	Disaccharides	Emulsifying salt
32.	4.038	508.1298	(M+HCOO)-	553.1277	553.1231	$C_{23}H_{25}ClN_2O_9$	Clomocycline	Tetracyclines	Tetracycline antibiotic
33.	6.994	1082.4664	(M-H)-	1082.4664	1081.4497	$C_{52}H_{74}O_{24}$	Mithramycin DK	polyketides	Anti-cancer
34.	7.543	340.1749	(M+HCOO)-	385.1751	385.1769	$C_{20}H_{24}N_2O_3$	3-Hydroxyquinine	Quinoline alkaloids	12 % antimalarial
35.	9.987 /12.03 /12.847	904.4498 /904.449 /904.4514	(M+HCOO)- /(M-H)- /(M-H)-	949.4502 /903.4449 /903.4464	949.4439 /903.4384 /903.4384	$C_{47}H_{68}O_{17}$	Bryostatin 1	polyketides. macrolides	Antineoplastic / Neuroprotective
36.	10.628	436.0388	(M+HCOO)-	481.0368	481.0381	$C_{18}H_{16}N_2O_7S_2$	C.I. 14700	Xanthene dyes.	cosmetic colorant
37.	10.843	916.4596	(M-H)-	915.4524	915.4595	$C_{45}H_{72}O_{19}$	Fistuloside C	Triterpenoid Saponins	Anti-fungal
38.	12.672	868.4759	(M+HCOO)-	913.4743	913.4802	$C_{45}H_{72}O_{16}$	Dioscin	Steroidal saponins	Anti-fungal
39.	13.35	668.3472	(M+HCOO)-	713.3468	713.3449	$C_{25}H_{44}N_{14}O_8$	Capreomycin	Cyclic polypeptide	Antibiotics
40.	13.539	381.9669	(M+HCOO)-	426.9652	426.9636	$C_{14}H_8Cl_3F3N_2O$	Fluopicolide	Pyridyl-ethyl-oxazolidinones	Fungicide
41.	19.063	946.569	(M+HCOO)-	991.5697	991.5483	$C_{48}H_{82}O_{18}$	Ginsenoside Re	Ginsenosides Triterpenoid saponins	Anti-arrhythmic
42.	20.082 /20.347	564.3877 /564.3885	(M+HCOO)-	609.388 /609.388	609.3949609.3949/	$C_{40}H_{52}O_2$	Alloxanthin	Xanthophylls carotenoids	Antioxidant

L-Carnitine: It is an important amino acid. It plays a significant role to boost our body metabolism. It does this by improving mitochondrial function and increasing cellular energy. It is also used for fat loss. Besides, L-carnitine supplementation can also help with cognition and better brain functioning and its supplementation may slow down the aging process due to its effect on cellular health. It also helps in some other functions in body, such as maintaining general brain function and reduces certain risk of disorder [24].

BILA 2185BS: It is used as protease inhibitor, i.e., antiviral drug used against HIV. It interrupts HIV replication by binding and blocking HIV protease. For this purpose, the substrate analog protease inhibitor BILA 1906BS and BILA 2185BS are selected combinely [25].

Bruceantinol: It is the novel therapeutic STAT3 (Transducer and Activator of Transcription-3) inhibitor demonstrating potent antitumor activity in-vitro and in-vivo human colorectal cancer models. It also behaves as cytotoxic agent on breast cancer cells too. It effects on the growth of cell, proliferation, cell cycle, and apoptosis. It can be used either alone or in signal transducer and activator of transcriptions-3 gene which is generally associated with disease [26].

MET-enkephalin: It is synthetic form of the naturally occurring, endogenous opioid peptide, it has potential analgesic, neuromodulatory, immunomodulatory, anti-inflammatory, anti-nociceptive/analgestic, antidepressant, and anti-gastrointestinal (GI) motility modulating activity. It also mimics its endogenous ligand and targets, binds and activates the opioid receptors. These leads to an analgestic effect, inhibits neuropathic pain, and inhibits gastrointestinal (GI) muscles contractility, enhances the tissue growth and regeneration, modulates the inflammatory immune response and inhibits the secretion of pro-inflammatory cytokinines. MET-enkephalin with tridecactide is on clinical trial to evaluate the efficiency and safety of an immunomodulatory therapy for the treatment of patients with moderate to severe COVID-19 infections [27].

Moracin A: The therapeutic effect of moracins as 2-arylbenzofuran derivatives against airway inflammation. It is also cytotoxic against THP1 cell. Due to presence of benzofuranheterocycle, these are biologically active as anticancer, antimicobrial, immunomodulatory, antioxidant, and anti-inflammatory property [16].

Zapotin: The study reports the potent anticancer activity of zapotin and suggests a role for zapotin both as a chemopreventive and a chemotherapeutic agent against colon cancer [28].

Bryostatin 1: Bryostatins are potent agonists (drugs or naturally occurring substances that activate physiologic receptors) of protein kinase C. Bryostatin's anticancer activity has been proved against various cancer types [29].

Dioscin: Dioscin is a typical saponin with multiple pharmacological activities. It has demonstrated antitumor activity against many kinds of tumors such as lung cancer, esophageal cancer, gastric cancer, colon cancer, gliblastoma, cervix carcinoma, ovarian cancer, breast cancer, prostate cancer, and leukemia [30].

HR-LCMS screening indicates that root extract of *P. Polyphylla* possesses different bioactive ingredients having multi-variant activates, i.e., useful to suppress the several oxidative stress related diseases. Data shows that crude extract is enriched with significant amount of potential chemical compounds such as phenolics, flavonoids and terpenoids that exhibits correlation with numerous medicinal effects.

Phytochemical screening of the extract showed that it is rich of phytochemicals. It showed positive tests for alkaloids, flavonoids, terpenoids, proteins, phenols, saponin and steroids and carbohydrates.

Quantitative analysis of the selected phytochemicals (flavonoids, phenols and anti-oxidant molecules) suggests that the plant contains substantial amount of those analyzed photochemical. Results showed that total flavonoids compounds (TFC) is 38.43 ± 0.27 mg QE/g, total phenolic compounds (TPC) is 41.810.72 mg GAE/g and anti-oxidant active compounds is 25.750.50 mg Ascorbic acid (AA)/g concentration.

HRLCMS results showed that the plant contain various active phyto-compounds that are very useful for human. The compounds present in the plant are protease inhibitor, antiviral, anti-thyroid, antimicrobial, nematocide, STAT3 inhibitor, insecticide, analgesic, neuro-transmodulator, immunomodulatory, anti-inflammatory, analgesic, antidepressant, membrane stabilizer, cyto-toxic against TPH1 cell, anticancer or antioxidant, antifungal, antibiotic, anti-parasitic, etc. and some compounds are very useful for edema, cirrhosis, kidney disease, control of high blood pressure, boosting body metabolism, loosing fat, brain functioning, insect moulting, controlling osteoarthritis, stimulating intestinal calcium transport, urinary tract infection etc.

Plant extract not only contains beneficial molecules for human health but also contains some molecules which show hazardous effect to human health. They cause insomnia, nervousness, hallucination, psychosis, and even may cause death. Some are acute toxic to oral, dermal, eye and carcinogenic. The molecule Carbenicillin ($C_{17}H_{18}N_2O_6S$) is present in the HRLCMS profile of the extract. It is a penicillin antibiotic. This is only used to treat certain kinds of bacterial infections. Besides its use and benefits, some side effects might be seen while using this medicine. Some side effects are allergic reactions, breathing problems, discolored tongue, fever, pain or difficulty passing urine, stomach cramps, unusual bleeding, bruising, unusually weak or tired, diarrhea, headache and loss of appetite, nausea, vomiting, sore mouth or tongue, stomach upse. Because of its medicinal property MET-enkephalin with tridecactide is on clinical trial to evaluate the efficiency and safety of an immunomodulatory therapy for the treatment of patients with moderate to severe COVID-19 infections [27].

4. CONCLUSION

Methanolic extract of the rhizomes of the plant *P. Polyphylla* showed that the plant is very useful because its quantitative results showed promising amounts of total flavonoids compounds, total phenolic compounds and antioxidant active compounds. It is also rich in different phytochemical compounds like alkaloids, steroids, etc.

HRLCMS profiling shows 128 different compounds (22 unknown compounds and 106 known compounds). Among them, 40 compounds were biologically active and potent and out of 40, 36 of them have useful medicinal properties. They are very useful for treatment of different types of diseases and infections caused by gram positive and gram negative bacteria, virus, and fungus. They are also helpful in treatment of different types of cancers like in-vitro and in-vivo human colorectal cancer, advanced pancreatic cancer, advanced

head and neck cancer, lung cancer, esophageal cancer, gastric cancer, colon cancer, gliblastoma, cervix carcinoma, ovarian cancer, breast cancer, prostate cancer, leukemia etc. They are potent in treatment of high blood pressure too.
Among their benefits, the plant has some phyto-compounds like MeIQ, Prolintane, 3-Pentadecylphenol, Didecyldimethylammonium, etc. These compounds cause adverse effects on human health. These are carcinogenic, cause insomnia, nervousness and irritability. Over dosage of them may cause hallucinations, psychosis, and death. They have acute toxicity in oral ingestion too. These compounds not only cause skin and eye irritation. But also have effect on body weight, blood, bronchoalveolar lavage (BAL), and the lungs.

To sum up *P. Polyphylla* is a very potent medicinal plant. Its natural flora (indigenous native plant) is declining alarmingly. Government should initiate a campaign program to cultivate, protect and conserve its natural species. To disclose all the parameters of the root extract of the *P. Polyphylla,* further more analysis of bioactivity in different bacterial strain, isolation, purification and characterization of bioactive compound should be carried out. The unidentified molecules observed in HRLCMS data should be isolated and identified to add further medicinal importance of the plant species. HR-LCMS metabolomic analysis disclosed almost all the active molecules which are proposed to be purified in the future work & used as potential biomarkers.

DECLARATION OF COMPETING INTEREST

The authors declare that they have no known competing interests or personal relationships that could have appeared to influence the work reported in this paper.

ACKNOWLEDGEMENTS

Authors are thankful to sophisticated analytical instruments facility (SAIF), IIT, Mumbai, India for this study by providing HR-LCMS facility for the analysis of the crude extract.

REFERENCES

[1] M. Prasathkumar, S. Anisha, C. Dhrisya, R. Becky, S. Sadhasivam, Therapeutic and pharmacological efficacy of selective Indian medicinal plants - A review. *Phytomedicine plus*, 1, (2021) 100029. https://doi.org/10.1016/j.phyplu.2021.100029

[2] M.M. Pandey, S. Rastogi, A.K.S. Rawat, Indian Traditional Ayurvedic System of Medicine and Nutritional Supplementation. *Evidence-Based Complementary and Alternative Medicine*. 12 (2013) 376327. http://dx.doi.org/10.1155/2013/376327

[3] S. Parham, A. Z. Kharazi, H. R. Bakhsheshi-Rad, H. Nur, A.F. Ismail, S. Sharif, S. RamaKrishna, F. Berto, Antioxidant, Antimicrobial and Antiviral Properties of Herbal Materials. *Antioxidants*, 9 (2020) 1309. doi: 10.3390/antiox9121309

[4] P. R. Joshi, P. R. Pant, A. Bist, G. Pant, B. Pant, P.S. Saud, Assessment of the Antibacterial Activity of Lemongrass-Extracted Essential Oil. *BIBECHANA,* 20(**2023)** 290-296. https://doi.org/10.3126/bibechana.v20i3.58311

[5] Y. Huang, D. Xiao, B. M Burton-Freeman, I. Edirisinghe, Chemical Change of Bioactive Phytochemicals During Thermal Processing. *Reference Module in Food Scienc,*(2016). https://doi.org/10.1016/B978-0-08-100596-5.03055-9

[6] D.A. Bekele, G. S. Geleta, Iodometric Determination of the Ascorbic acid (Vitamin C) content of some Fruits consumed in Jimma Town Community in Ethiopia. *Research Journal of chemical science,* 5(2015) 60-63. ISSN 2231-606X

[7] J. Löliger, (1991). The use of antioxidants in foods. In: Aruoma OI, Halliwell B (eds). Free radicals and food additives. London, *Taylor and Francis* (1991) 121-150.

[8] Y.S. Velioglu, G. Mazza, L. Gao, B.D. Oomah, (1998). Antioxidant Activity and Total Phenolics in Selected Fruits, Vegetables, and Grain Products. *Journal of Agricultural Food & Chemistry*, 46 (1998) 4113–4117. doi: 10.1021/jf9801973

[9] F. Shahidi, P.K Janitha , P.D. Wanasundara, Phenolic Antioxidants. *Critical Reviews of Food Science & Nutrition*, 32 (2009) 67–103. https://doi.org/10.1080/10408399209527581

[10] P.G. Pietta, Flavonoids as Antioxidants. *Journal of natural product*, 63(2000) 1035-1042.

[11] T. Osawa, Novel Natural Antioxidants for Utilization in Food and Biological Systems. *Postharvest Biochemistry of Plant Food-Materials in the Tropics*, Japan Scientific Press, Tokyo, (1994) 241-251.

[12] Y.S. Velioglu, G. Mazza, L. Gao, B.D. Oomah, Antioxidant Activity and Total Phenolics in Selected Fruits, Vegetables, and Grain Products. *Journal of Agriculture and Food Chemistry,* 46 (1998) 4113-4117

[13] M. K.C., S. Phoboo, P.K. Jha, (2010). Ecological Study of Paris Polyphylla SM. *Ecoprint: an International Journal of Ecology,* 17 (2010) 87-93. ISSN 1024-8668

[14] H.S. Sofi, R. Rashid, T. Amna, R. Hamid, F.A. Sheikh, Recent advances in formulating electrospun naofiber membranes: Delivering active phytoconstituents. *Journal of Drug Delivery Science and Technology*, 60 (2020) 102038.

[15] D.A. Dias, O.A.H. Jones, D.J. Beale, B.A. Boughton, D. Benheim, K.A. Kouremenos, J-L. Wolfender, D.S. Wishart, Current and Future Perspectives on the Structural Identification of Small Molecules in Biological Systems. *Metabolites***,** 46 (2016). DOI: 10.3390/metabo6040046

[16] L. Naik, P. Shaym, P. Marx, S. Baskari, C. Devi, Antimicrobial Activity and Phytochemical Analysis of Ocimum tenuiflorum Leaf Extract. *International Journal of Pharm Tec Research,* 8 (2015) 88-95. ISSN: 0974-4304

[17] O.K. Kenneth-Obosi, Qualitative and Quantitative Evalution of Phytochemical Constituents of Selected Horticulture and Medicinal Plants in Nigeria. *International Journal of Homeopathy and Natural Medicines,* 3(2017)1-8. http://dx.doi.org/10.11648/j.ijhnm.20170301.11

[18] H. Khan, M. Saeed, N.M.S. Perviz, Phytochemical analysis, antibacterial, and antifungal assessment of aerial parts of *Polygonatum Verticillatum***.** *Toxicology and Industrial Health*, 32 (2013). http://dx.doi.org/10.1177/0748233713512362.

[19] C.-C. Chang, M.-H. Yang, H.-M Wen, J.-C. Chern, Estimation of total flavonoid content in propolis by two complementary colometric methods," *Journal of Food and Drug Analysis*, 10 (2002). https://doi.org/10.38212/2224-6614.2748.

[20] L. Fu, Bo-Tao Xu, X.-R. Xu, R.-Y Gan, Y. Zhang, E.-Q. Xia,

H.B. H.-B Li, (2011). Antioxidant capacities and total phenolic contents of 62 fruits. *Food Chemistry,* 129 (2011) 345–350. https://doi.org/10.1016/j.foodchem.2011.04.079

[21] D.J. Bhuyan, A. Basu, Phenolic compounds: Potential Health Benefits and Toxicity. In Q. V. Vuong (Ed.) Utilisation of Bioactive Compounds from Agricultural and Food Production Waste. (2017) 27-59, Chapter: 2 Publisher: *CRC Press, Taylor & Francis Group Editors*.

[22] C.A. Rice-Evans, N.J. Miller, G. Paganaga, Antioxidant properties of phenolic compounds. *Trends in Plant Science*, 2 (1997) 152-159. https://doi.org/10.1016/S1360-1385

[23] S. Kumar, A.K. Pandey, Chemistry and Biological Activities of Flavonoids: An Overview. Hindawi, *The Scientific World Journal*, Article ID 162750, (2013) 16 http://dx.doi.org/10.1155/2013/162750

[24] I. S. Al-Dhuayan, Biomedical role of L-carnitine in several organ systems, cellular tissues, and COVID-19. *Brazilian Journal of Biology,* 82 (2022). https://doi.org/10.1590/1519-6984.267633

[25] L. Doyon, G. Croteau, D. Thibeault, F. Poulin, L. Pilot, D. Lamarre, Second Locus Involved in Human Immunodeficiency Virus Type 1 Resistance to Protease Inhibitor. *Journal of Virology,* 70 (1996), 3763-3769. doi: 10.1128/jvi.70.6.3763-3769.1996

[26] N. Wei, J. Li, C. Fang, J. Chang, V. Xirou, N.K. Syrigos, B.J. Marks, E. Chu, J.C. Schmitz, Targeting colon cancer with the novel STAT3 inhibitor bruceantinol. *Oncogene*, 38 (2019) 1676-1687. https://doi.org/10.1038/s41388-018-0547-y

[27] D. Zho, N. Plotnikoff, N. Griffin, T. Song, F. Shan, Methionine enkephalin, its role in immunoregulation and cancer therapy. *International immunopharmacology*, 37 (2016) 59-64. https://doi.org/10.1016/j.intimp.2016.02.015

[28] G. Murillo, W.H. Hirschelman, A. lto, R.M. Moriarty, A.D. Kinghorn, J.M. Pezzuto, R. G. Mehta, Zapotin, a Phytochemical Present in a Mexican Fruit, Prevents Colon Carcinogenesis, *Nutrition and Cancer*, 57 (2007) 28-37, https://doi.org/10.1080/01635580701268097

[29] P. Kollar, J. Rajchard, Z. Balounova, Z. Pazourek, Marine Natural Product: Bryostatins in Preclinical and Clinical Studies. *Pharmaceutical Biology,* 52 (2013), 237-242. http://dx.doi.org/10.3109/13880209.2013.804100

[30] L. Yang, S. Ren, F. Xu, Z. Ma, L. Wang, Recent Advances in the Pharmacological Activity of Dioscin. *BioMed Research International,* (2019). https://doi.org/10.1155/2019/5763602

Structural, Electronic, Vibrational Properties and Molecular Docking of Paracetamol: a first-principle's Study

Kamalesh Khadayat[1], Bhawani Datt Joshi[1]*

[1]*Department of Physics, Siddhanath Science Campus, Tribhuvan University, Mahendranagar, 10400.*

Research Article

ISSN: 3059-9504 (online)
Doi: xxxx

Article History

Received: August 8, 2024
Revised: September 6, 2024
Accepted: September 13, 2024
Published: December 28, 2024

Keywords

Paracetamol, DFT, Analgesic, Vibrational spectroscopy, Molecular Docking, MEP

***Corresponding author**

Email: bhawani.joshi@snsc.tu.edu.np
Orcid: orcid.org/0000-0003-3276-9319
Phone: +977-9841580777 (BD Joshi)
Fax: +977-99521304

ABSTRACT

Aromatic compounds are known for their biological and clinical applications. The present work explores the structural, electronic, and vibrational properties of paracetamol by DFT employing B3LYP/6-31G theory using Gaussian 09 software. To examine the equilibrium geometries, vibrational spectra, molecular electrostatic potential (MEP), lowest unoccupied molecular orbital (LUMO), highest occupied molecular orbital (HOMO), and UV-Vis spectra analysis of the tittle compound were performed. Vibrational assignments based on the potential energy distribution (PED) were made using the scaled vibrational frequencies. By using the Time Dependent DFT approach the electronic characteristics are classified. The Structure Activity Relationship has been interpreted by mapping the molecular electrostatic potential (MEP) which helps in understanding how the electronic distribution affects the molecule's behavior and interactions, particularly its activity and reactivity. Visualizing the frontier molecular orbital in both the gas and solvent phases offers important information about the reactivity, stability, as well as various structural and physical characteristics of the title compound. Additionally, the determined HOMO and LUMO energy values indicate that a charge transfer happens inside the molecule. Further, AutoDock Vina was utilized to perform the molecular docking investigation of paracetamol against the protein CYP2E1(1EQG). The docking analysis shows a -6.6 kcal/mol favorable binding affinity with the CYP2E1(1EQG) receptor, indicating a robust interaction and promising pharmacological importance.

1. NTRODUCTION

Paracetamol, also known as acetaminophen, is a widely used synthesized compound with numerous clinical applications primarily as an analgesic and antipyretic [1-3]. Since 1980s, paracetamol is the top choice for managing fever and pain in children and other demographics and it is available in both single and multiple ingredient forms [3,4]. The World Health Organization (WHO) has listed paracetamol as an essential medication [5]. Its chemical structure includes one benzene ring core with a hydroxyl group and an amide group (acetamide) attached in the para position, with a molecular formula $C_8H_9NO_2$ and a molar mass of 151.165 g/mol, and with a density of 1.293 g/ml. Its melting point is 168°C with boiling points ranging from 420°C [5,6]. The presence of lone pairs on the hydroxyl oxygen, carbonyl oxygen, and nitrogen, along with the benzene pi-cloud and the p-orbital on the carbonyl carbon, results in significant conjugation in this structure, leading to high reactivity in electrophilic aromatic substitution. Two activating groups on the benzene ring enhance electron density, causing electrophiles to preferentially react at the ortho and para positions, resulting in quicker and more specific reactions [6]. From a medical perspective, paracetamol is utilized for addressing mild to moderate pain such as headaches, colds, muscle aches, sprains, back pain, menstrual cramps, arthritis pain, and toothaches [7]. It is also prescribed to pregnant women for the management of pain and fever [8]. Unlike acetanilide and acetphenetidines, paracetamol does not cause anemia or liver damage and it is preferred over aspirin for patients prone to gastric damage or those with coagulation disorders or on anticoagulants [3]. In 2005, researchers discovered that paracetamol is metabolized in the brain by the enzyme FAAH into AM404 which enhances the endocannabinoid system and pain signal transmission, suggesting that paracetamol is a pro-drug [9]. Paracetamol is generally safe when taken at recommended dose i.e., up to 4 g per day, but prolonged use of paracetamol can lead to rare side effects such as blood abnormalities, skin rashes, and pancreatitis. In case of overdose it can cause severe complications such as sweating, nausea, vomiting, liver damage, kidney failure, severe tissue death, brain swelling, blood infection, and even death [10,11].

Literature reveals that Mallah et al. [12] described a new method using transmission FTIR spectroscopy to quickly and inexpensively measure paracetamol levels in solid pharmaceutical products. Castro-Suarez et al. [13] studied on vibrational analysis of paracetamol from commercial tablets employing ATR FTIR spectroscopy, quantum cascade laser spectroscopy, and raman spectroscopy to directly detect paracetamol in pharmaceuticals. The analysis of infrared spectra was utilized through chemometrics methods such as HQI values. Habiba et al. [14], employs spectroscopy to examine paracetamol molecules and crystals, with a specific emphasis on the structure and influence of hydrogen bonds within them. Also, Oparin et al. [15], focuses on studying paracetamol polymorphic forms through controlling external parameters at the solid sample interface using SCF technology. Wang et al. [16] conducted computational systematic examinations on paracetamol and its metabolites (AM404 and NAPQI) to investigate the fundamental mechanism of paracetamol. Many research groups have studied paracetamol's clinical activity, but structural activity, including geometry optimization, MEP, HOMO-LUMO, and molecular docking studies, remains a focus of attention. This research is focused on the structure, electronic and vibrational properties including molecular docking by using density functional theory (DFT) employing B3LYP/6-31G level of

theory. The theoretical Raman and IR spectra were examined to analyze potential energy distribution. Molecular electrostatic potential surfaces (MESP) have been generated to comprehend the connection between molecular structure and biological activity. Visualization of the HOMO-LUMO plot helps in interpreting the intramolecular charge transfer feature of the molecule. Molecular docking was conducted to examine how the title molecule binds with the proteins. Figure 1(a and b) shows the crystal and optimized molecular structure of paracetamol, respectively

.

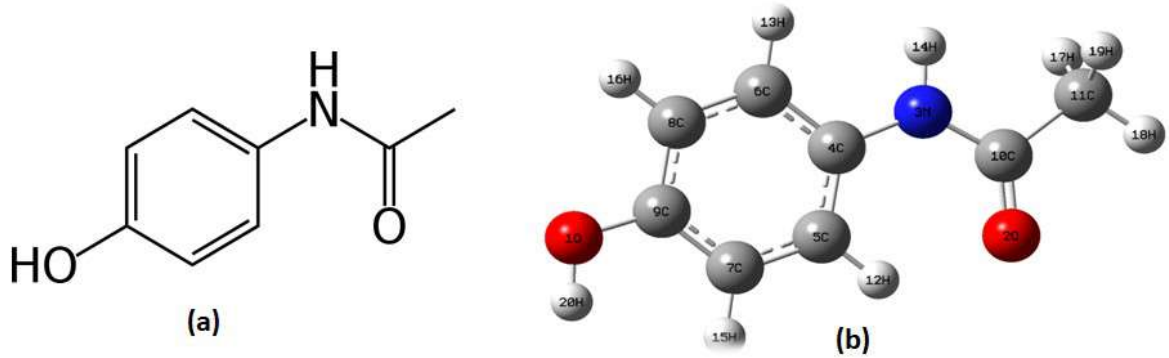

Fig. 1: (a)Molecular structure of paracetamol(Source Wikipedia) (b)Optimized geometrical structure of paracetamol.

2. MATERIALS AND METHODS

Quantum mechanical approaches are being used more frequently in computer-aidded drug design to calculate molecular orbital characteristics, dipole moments, atomic partial charges, and molecular electrostatic potential properties [17]. The initial geometry of paracetamol (PCT) was acquired from the PubChem database [18]. Using the Gaussian 09 program, the geometry was optimized employing density functional theory (DFT) at B3LYP/6-31G level without any constraints on the geometry of molecule [19] . Following geometry optimization, the vibrational frequencies of the molecule were calculated using the same level of theory. The title molecule contains 20 atoms, therefore it has 54 normal modes of vibrations based on the equation, total vibrations equal to 3N-6 [20], where N is the total number of atoms. Vibrational analysis was carried out using normal modes along with calculating potential energy distribution (PED). The calculation of potential energy distribution (PED) was done by utilizing the internal coordinates of molecular geometry with localized symmetry by Pulley's suggestion [21,22] using GAR2PED software. The Gauss-View software [23] was utilized to visually display the computed Raman and IR data. The electronic absorption wavelength was determined in solvent and gaseous phases through time-dependent density functional theory (TD-DFT) calculations [24]. AutoDock Vina [25] was used for molecular docking, while AutoDock tools [26] were utilized for preparing the ligand and protein interaction. Furthermore, Discovery Studio Visualizer was utilized for visualizing the interactions between the molecule and target protein [27].

3. RESULTS AND DISCUSSION

3.1 Geometry Optimization

The table below lists the optimal structural properties of paracetamol that were determined employing density functional theory (DFT) at B3LYP/6-31G level. It contains parameters, bond length, bond angle and dihedral angle. The number of bound electrons determines the bond length. In addition to the atoms themselves, other variables that affect the bond length between two atoms in a molecule include orbital hybridization and the electronic and steric character of the substituent. Stronger attraction between atoms and shorter bond lengths are associated with higher bond orders (number of bonded electrons).

Table 1: Optimized geometric parameters (bond length, bond angle and dihedral angles) of paracetamol.

Parameters	Bond Length (Å)	Parameters	Bond angle (˚)	Parameters	Dihedral angle (˚)
O1-C9	1.3611	C9-O1-H20	108.9008	H20-O1-C9-C7	-0.0507
O1-H20	0.9727	C4-N3-C10	128.1253	H20-O1-C9-C8	-179.973
O2-C10	1.2269	C4-N3-H14	115.2519	C10-N3-C4-C5	0.0037
N3-C4	1.3952	C10-N3-H14	116.6229	C10-N3-C4-C6	179.9847
N3-C10	1.4013	N3-C4-C5	119.9953	H4-N3-C4-C5	-179.9702
N3-H14	1.0179	N3-C4-C6	120.0026	H14-N3-C4-C6	0.0108
C4-C5	1.3948	C5-C4-C6	120.0021	C4-N3-C10-O2	0.1939
C4-C6	1.3949	C4-C5-C7	119.9939	C4-N3-C10-C11	-179.999
C5-C7	1.3949	C4-C5-H12	124.2667	H14-N3-C10-O2	-179.8325
C5-H12	1.081	C7-C5-H12	115.7394	H14-N3-C10-C11	-0.0254

C6-C8	1.3949	C4-C6-C8	119.9951	N3-C4-C5-C7	179.9953
C6-H13	1.087	C4-C6-H13	120.795	N3-C4-C5-H12	0.0061
C7-C9	1.3948	C8-C6-H13	119.2099	C6-C4-C5-C7	0.0142
C7-H15	1.0869	C5-C7-C9	120.0037	C6-C4-C5-H12	-179.975
C8-C9	1.3947	C5-C7-H15	119.351	N3-C4-C6-C8	-179.9858
C8-H16	1.0866	C9-C7-H15	120.6453	N3-C4-C6-H13	0.0085
C10-C11	1.5081	C6-C8-C9	120.0041	C5-C4-C6-C8	-0.0047
C11-H17	1.0936	C6-C8-H16	119.6573	C5-C4-C6-H13	179.9896
C11-H18	1.0935	C9-C8-H16	120.3386	C4-C5-C7-C9	0.0142
C11-H19	1.0937	O1-C9-C7	120.0023	C4-C5-C7-H15	-179.9862
		O1-C9-C8	119.9966	H12-C5-C7-C9	179.9759
		C7-C9-C8	120.0011	C12-C5-C7-H15	0.0038
		O2-C10-N3	127.4398	C4-C6-C8-C9	-0.0047
		O2-C10-C11	120.7964	C4-C6-C8-H16	179.9824
		N3-C10-C11	111.7635	H13-C6-C8-C9	-179.9991
		C10-C11-H17	109.74	H13-C6-C8-H16	-0.012
		C10-C11-H18	109.8233	C5-C7-C9-O1	-179.9176
		C10-C11-H19	109.8423	C5-C7-C9-C8	0.0047
		H17-C11-H18	108.9843	H15-C7-C9-O1	0.0541
		H17-C11-H19	109.5378	H15-C7-C9-C8	179.9764
		H18-C11-H19	108.893	C6-C8-C9-O1	179.9271
				C6-C8-C9-C7	0.0047
				H16-C8-C9-O1	-0.0599
				H16-C8-C9-C7	-179.9823
				O2-C10-C11-H17	118.0931
				O2-C10-C11-H18	-1.6917
				O2-C10-C11-H19	-121.4278
				N3-C10-C11-H17	-61.7287
				N3-C10-C11-H18	178.4865
				N3-C10-C11-H19	58.7504

The improved geometric characteristics of paracetamol, identified through the 6-31G basis set and DFT/B3LYP method, offer valuable information about the molecule's configuration. The bond lengths for the O1-H20 bond is 0.9727 Å. The length of a carbon-carbon bond can vary between 1.20 and 1.54 Å, contingent upon the chemical bonding type [28]. In the study , the longest C-C bond was present between C10-C11 and shortest between C8-C9 with 1.5081 Å and 1.3947 Å respectively. Significantly, the C-O bonds lengths (1.3893 Å at O1-C9 and 1.2414 Å at O2-C10) emphasize the importance of the carbonyl and hydroxyl functional groups in the molecule's pharmacological effects. In hybridization, the bond angle rises with the s character of the s hybrid bond and falls by around 2.5% as the lone pair of electrons increase. The C4-N3-C10 has the highest angle of 128.1253° indicates a planar arrangement around the nitrogen atom, which is commonly seen in amide bonds, revealing additional structural information. The angle of 119.9939° between carbons C4, C5, and C7 demonstrates the benzene ring's aromatic nature, preserving its hexagonal shape. These geometric factors highlight how the electronic and steric factors of paracetamol interact to determine its molecular shape, affecting its reactivity and its ability to bind to biological targets. Having this comprehensive structural data is crucial in comprehending how paracetamol behaves in different chemical and biological scenarios, which helps in developing pharmaceutical agents that are more efficient.

3.2 Mulliken Atomic Charges

that refers to an estimation of electron density distribution within molecules. This concept originates from Mulliken population analysis, which allocates electron density based on molecular orbital coefficients derived from quantum chemical calculations. These charges offer valuable insights into amolecule's electron distribution and partial charges, aiding in the understanding of chemical reactivity, polarity, and intermolecular interactions. However, the results can be influenced by the selected basis set and the level of theory oxygen atoms are negatively charged and hydrogen atoms are positively charged. As was observed in the molecular docking section, the net negative charge on oxygen atoms (electron

Mulliken atomic charge is a term in computational chemistry applied in the quantum chemical calculations [29]. Mulliken charges for paracetamol are listed below in the Table 3. Carbon C10 atom with the most positive charge and is therefore expected to be the site of nucleophilic attack in the compound's title. On the other hand, nitrogen N3 has the highest negative charge and is expected to be the site for electrophilic attack. Regarding the hydrogen atoms, the majority of the Mulliken charges are concentrated at H20. Additionally,

donor) and the positive charge on hydrogen atoms play a major role in intermolecular hydrogen bonding. The figure 2 below shows the graph of Mulliken charge against atoms.

Table 3: Mulliken Atomic Charges of paracetamol .

Label number	Symbol	Mulliken Atomic Charge	Label number	Symbol	Mulliken Atomic Charge
1	O	-0.603637	12	H	0.236887
2	O	-0.485140	13	H	0.174675
3	N	-0.831400	14	H	0.320455
4	C	0.321729	15	H	0.179464
5	C	-0.202183			
6	C	-0.204216	16	H	0.201739
7	C	-0.221731	17	H	0.215088
8	C	-0.184311	18	H	0.236429
9	C	0.280226	19	H	0.213324
10	C	0.641953	20	H	0.352767
11	C	-0.642116			

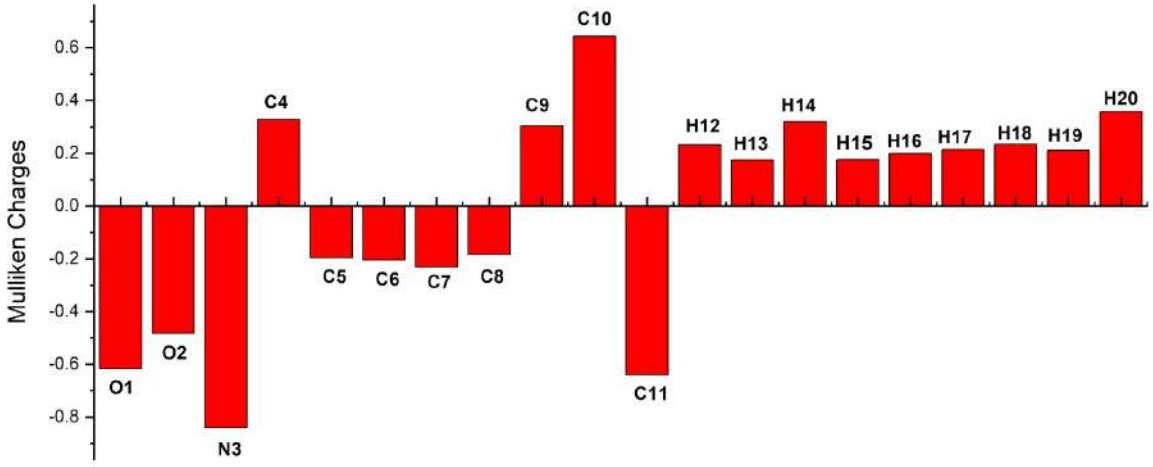

Fig. 2: Calculated Mulliken Charges of Paracetamol.

3.3 UV-Vis Spectral Analysis

The UV-Vis spectral range shows transitions between various electronic energy levels, which give rise to the absorption bands that are found there. When the frequency of incoming electromagnetic radiation coincides with the difference in energy between two electronic states, an electron is stimulated.

The electronic structure of the molecule and its surroundings control the energy fluctuation. Charge dislocation and adherence to specific regulations, such as the Laporte selection rule, spin multiplicity selection rule, and coupling interaction with neighbour cations, are necessary for a transition to happen after radiation absorption [30]. TD-DFT

calculations were carried out in both the gaseous phase and a solvent (water) environment to investigate electronic transitions in terms of energies and oscillator strength. The energies, absorption wavelength, and oscillator strength of paracetamol were theoretically calculated using TD DFT, along with an examination of the chemical reactivity are represented in table 4. The calculated UV-Vis absorption spectra in solvent and gaseous phases are shown in the figures 3 and 4 respectively.

Table 4: Calculated absorption wavelength, energies and oscillator strength of paracetamol using DFT.

S.N	Transition States(Gas/Solvent)	Wavelength (nm)	Energy(eV)	Oscillator Strength	Type of transition
1	H→L+1/ H→L+1	255.28/260.79	4.8568/4.7542	0.0301/0.0415	π → π
2	H→L/ H→L	245.31/248.32	5.0541/4.9928	0.3706/0.4585	π → π
3	H-1→L/ H-2→L	243.46/235.86	5.0926/5.2567	0.0008/0.0007	π → π
4	H→L+2/ H→L+2	197.98/198.37	6.2624/6.2501	0.0361/0.0138	π → π
5	H−2→L/ H−1→L	194.84/195.99	6.3634/6.3261	0.0741/0.1304	π → π
6	H−2→L+ 1/ H−1→L+ 1	192.35/183.72	6.9020/6.7485	0.3303/0.4469	π → π
7	H−3→L+1/ H−3→L+1	177.33/179.06	6.9918/6.9242	0.0013/0.0051	π → π

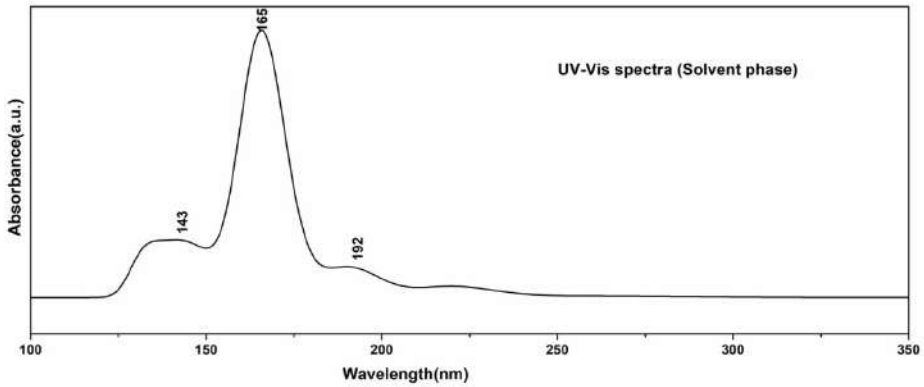

Fig. 3: UV plot of paracetamol in solvent phase between the ranges 100-350 nm.

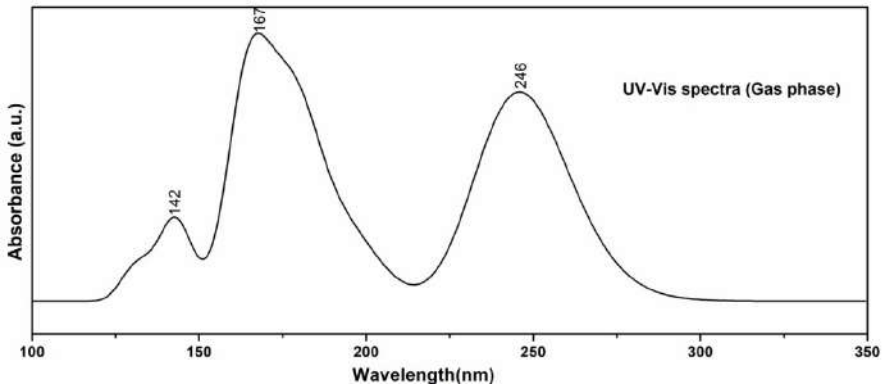

Fig. 4: UV plot of paracetamol in gas phase between the range 100-350 nm.

The prediction of electric and optical properties relies heavily on HOMO and LUMO; the bigger the energy gap, the more stable the molecules are, and vice versa. A molecule with a narrow frontier gap typically has higher conductivity and higher reactivity in chemical reactions [31], is more optically polarizable, and is kinetically less stable. The electronic transition with a high oscillatory strength (f), as well as its absorption wavelength (λ), excitation energy, and dipole moment (μ), were calculated by DFT employing B3LYP/6-31G level of theory and are shown in table 4.

The first allowed transition H→L in gas phase was calculated as 245.31nm with oscillator strength 0.3706 and in solvent phase it was at 248.32nm with oscillator strength 0.4585. The other main transitions in the gas phase were calculated at 255.28 nm (H→L+1), 243.46 nm (H-1→L), 197.98 nm (H→L+2), 194.84 nm (H–2→L), 192.35 nm (H–2→L+1) and

177.53 nm (H–3→L+1) with oscillator strengths 0.0301, 0.0008, 0.0361,0.0741, 0.3303 and 0.0013 respectively. Similarly, in the solvent phase the main transition were at 260.79 nm (H→L+1), 235.86 nm (H-2→L),198.37 nm (H→L+2), 195.99 nm (H–1→L), 183.72 nm (H–1→L+1) and 179.06 nm (H–3→L+1) with oscillator strengths 0.0415, 0.0007, 0.0138, 0.4469 and 0.0051 respectively. The mainly transition which is observed in the UV-Vis spectrum is π → π*.

Similarly, the energy difference (ΔE = E_{LUMO}–E_{HOMO}) between the two molecular orbital was 5.594 eV and 5.566 eV, respectively in the gas and solvent phases. Figure 5 shows HOMO-LUMO plot for the different molecular orbitals taking part in the charge accumulation process in the solvent and gaseous phase.

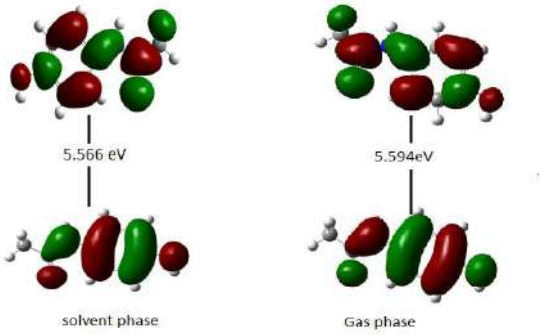

Fig. 5: HOMO-LUMO plot in gas and solvent phases.

3.4 Vibrational Assignment

The Vibrational frequency calculations were performed using the improved structural parameters to describe all of the stationary locations as minima. For every normal mode, the computed PED, IR intensity, Raman activity, and vibrational wave numbers are shown in table 5. The PED assignments were assigned using the internal coordinate system that Pulay et al. recommended. Figures 6 and 7 show the theoretically anticipated infrared and raman spectra, respectively.

Table 5: Vibrational wave numbers, Raman activity, IR intensity and Potential energy distribution [DFT/B3LYP/6- 31G] .

Wavelength		IR Intensity	Raman Activity	Potential Energy Distribution(PED)(≥5%)
unscaled	scaled			
58	58	3.560	0.594	τ(CC)(49)+τ(C10N)(15)+ρ'(C=O)(13)+[ρ(11)+ρ'(4)](CH3)[ρ(11)
77	77	0.528	1.284	[τ((43)+R[δoop(6)](C4N)+δoop(NCH)(14)+τ(C10N)(10)+R[τa](10)+R[δoop](CH)(8)
92	93	5.939	0.482	[τ(36)+R[δoop](4)](C4N)+τ(CC)(34)+R[τa](6)+ τ(C10N)(6)
165	166	9.178	0.432	γ(NCH)(36)+R[δin](C4N)(35)+ρ(C=O)(14)+ R[δin](CO)(6)
190	191	0.082	0.055	R[τa](53)+τ(C10N)(19)+τ(C4N)(6)+δoop(NCH)(6)+R[δoop](CH)(6) τ(C4N)(6)
320	321	0.778	1.579	R[δin](C4N)(25)+[δ(18)+ρ(16)](C=O)+R[δin](CO) (15)+γ(NCH)(13)
322	323	0.323	5.140	ρ(C=O)(24)+R[δa(20)+(υ(12)+δin(5))(C4N)]+ γ(NCH)(12) υ(C10N)(8)
359	360	147.646	5.271	τ(OC)(98)
399	400	5.840	2.028	R[puck](29)+R[δoop](CO)(22)+R[δoop](C4N) (18)+τ(C10N)(8)R[δoop](CH)(9)
425	425	9.235	1.715	R[δin](CO)(49)+R[δin](C4N)(19)+R[δa'](14)+δ (C=O)(9)
452	453	0.136	0.079	R[τa'](82)+R[δoop](CH)(7)
507	507	20.686	3.819	R[δa (33)+ρ'(7)](CH3)+[ρ(35)+δ(9)](C=O)
553	553	26.216	0.495	R[δoop]R[δa (CO)(31)+R[τa](30) + R[δoop](C4N)(24) + R[δoop](CH)(3)
622	622	7.216	0.920	ρ'(C=O)(58) + τ(C10N)(14)+[ρ(12)+ρ'(4)](CH3)+τ(C4N)(6)
635	633	1.405	4.147	υ(CC)(24)+R[δa]+R[δa](15)+γ(NCH)(7)+R[υ(C4N)(6) (6)+υ(CO)(6)+[δ(3)+δ(18)](C=O)](15)+γ(NCH)(7)
652	651	72.284	4.414	δoop(NCH)(53)+τ(C10N)(16)+τ(C4N)(8)+ ρ'(C=O)(6)+R[δoop](CH)(5)
680	678	0.036	6.368	R[δa'](77)
784	781	0.152	1.092	R[puck](65)+R[δoop](C4N)(17)+R[δoop](CO)(15)
804	800	16.570	21.076	υ(CO)(20)+R[δtrig](18)+υ(CC)(12)+γ(NCH)(11)+ R[υ(CC)](12)R[υ(C4N)](6)

859	854	11.865	6.248	R[δoop](CH)(86)+R[δoop](C4N)(5)+R[puck](5)
861	856	9.201	16.330	R[δa](17)+R[υ(CC)](45)+R[υ(C4N)](11)+ υ(CO)(8)+γ(NCH)(5)
895	890	97.961	0.517	R[δoop](CH)(68)+ R[δoop](C4N)(5) +R[δoop] +(CO)(13)+R[τa](11)
948	942	5.360	4.355	υ(CC)(27)+γ(NCH)(22)+[δ(22)+ υ(6)](C=O)+ υ(C10N)(10)+R[υ(CC)](5)
1002	994	0.086	2.497	R[δoop](CH)(76)+R[puck](16)
1035	1027	43.044	7.226	[[ρ'(44)+ρ(13)+δa'(3)](CH3)+υ(C10N)(16)+R[δtrig] (5)
1049	1041	0.175	0.898	R[δtrig](48)+R[υ(CC)](41)
1070	1061	5.250	1.778	R[δoop](CH)(81)+R[puck](12)
1085	1075	13.819	0.154	[[ρ](57)+[ρ'](18)+[δa(6)]](CH3)+ρ'(C=O)(15)
1149	1137	113.726	5.347	(CH)(6)+R[δin](C4N)(6)+R[υ(CC)](15)
1191	1179	199.916	7.408	δ(CHO)(34)+υ(CO)(17)+R[δin](CH)(20)+ R[υ(CC)](17)
1238	1224	3.061	24.856	R[δin](CH)(71)+R[υ(CC)](13)+R[υ(C4N)](5)
1243	1229	51.029	0.196	υ(C10N)(22)+υ(CC)(16)+R[υ(C4N)](9)+ [ρ'](CH3)(8)+R[υ(CC)](7)+[δ(9)+ρ(6)+υ(4)] (C=O)
1277	1261	150.492	40.547	R[υ(C4N)](20)+R[υ(CC)](32)+R[δtrig](11)+ R[δin](CH)(7)+υ(CO)(5)+υ(C10N)(5)+ρ](NCH)(5)
1316	1299	3.147	33.666	υ(CO)(33)+R[υ(CC)](27)+R[δin](CH)(13)+ υ(C4N)](6)
1343	1326	87.494	56.237	R[υ(CC)](59)+R[δin](CH)(8)+R[υ(C4N)](8)+υ(C10N)(6)+ δ (CHO)(5)
1396	1376	55.570	1.565	R[δin](CH)(56)+δ(CHO)(11)+R[υ(CC)](11)
1431	1411	24.853	21.476	[δs](CH3)(94)+υ(CC)(5)
1464	1442	27.238	6.096	R[δin] (CH)(35)+R[υ(CC)](26)+[ρ](NCH)(10)+δ (CHO)(7)
1526	1501	62.302	16.837	[δa'](CH3)(58)+[δa](CH3)(21)
1554	1529	11.784	28.949	[δa](CH3)(69)+[δa'](CH3)(23)+[ρ](CH3)(5)
1559	1533	403.544	40.544	R[δin](CH)(33)+R[υ(CC)](24)+[ρ](NCH)(14)+ R[υ(C4N)](9)
1581	1554	10.886	2.579	R[δin](CH)(26)+[ρ](NCH)(23)+R[υ(CC)](23)+ υ(C10N)(5)
1629	1600	28.157	15.459	R[υ(CC)](50)+[ρ](NCH)(15)+R[δa'] (7)+ R[δin](C4N)(5)
1661	1631	6.753	140.844	R[υ(CC)](56)+R[δin](CH)(21)+R[δa](11)+υ(CO)(3)
1733	1699	120.412	14.936	[υ(68)+ρ(4)](C=O)+[ρ(8)+γ(3)](NCH)+υ(C10N)(5)
3058	2932	4.232	133.539	υ(CH3)(100)
3113	2982	10.092	66.045	υ(CH3)(100)
3178	3041	4.347	72.984	R[υ(CC)](89)+υ(CH3)(10)
3181	3044	29.260	3.019	R[υ(CH)](98)
3184	3046	0.035	149.151	R[υ(CH)](97)
3234	3091	3.591	116.848	R[υ(CH)](96)
3281	3134	9.980	38.393	R[υ(CH)](99)
3524	3352	22.764	179.141	υ(OH)(100)
3540	3366	17.627	78.198	υ(NH)(99)

Proposed assignments and potential energy distribution (PED) for vibrational normal modes.
Types of vibration: ν, stretching; δ, deformation (bending); δ_{in}, in-plane bending; δ_{oop}, out-of-plane bending; ρ, rocking; τ, torsion. Potential energy distribution (contribution ≥ 5).

Vibration of Benzene ring

The frequency range of the ring carbon–carbon stretching vibrations is 1625–1430 cm^{-1} [32]. The bands exhibit variability in strength and are often observed at wavenumber of ranges 1625–1590, 1590–1575, 1540–1470, 1465–1430, and1380–1280 cm^{-1} for the five bands in the region, as provided by Varsanyi [32]. In this study, the C-C stretching vibrations were computed at 1533 and 1554 cm^{-1}. The carbon hydrogen stretching vibration give rise to bands in the region 3100 and 3000 cm^{-1} [33,34]. In this study, the virtually

pure C-H stretching vibrations at a wavelength of 3044 cm^{-1} were calculated using IR intensity and Raman activity of 29.260 and 3.019 a.u, respectively. The other C-H stretching with bigger PED contributions in the scaled frequency was computed in the 3091 cm^{-1} to 3134 cm^{-1} range.

O-H Vibration

The vibrations of the hydroxyl group are expected to be the most sensitive to the environment, whether free or hydrogen-bonded. Hydrogen-bonded species cause significant variations in spectral band characteristics, including intensity, shape, and frequency location of peaks. The free hydroxyl group absorbs heavily in the 3600-3550 cm^{-1} region, but hydrogen bonds can drop the O-H stretching wavenumber to the 3550-3200 cm^{-1} area with an increase in IR intensity and breadth [35]. The study computed the pure mode (100% contribution in PED) in O-H stretching at 3352 cm^{-1}, with Raman activity and IR intensity of 179.141 and 22.764 a.u., respectively.

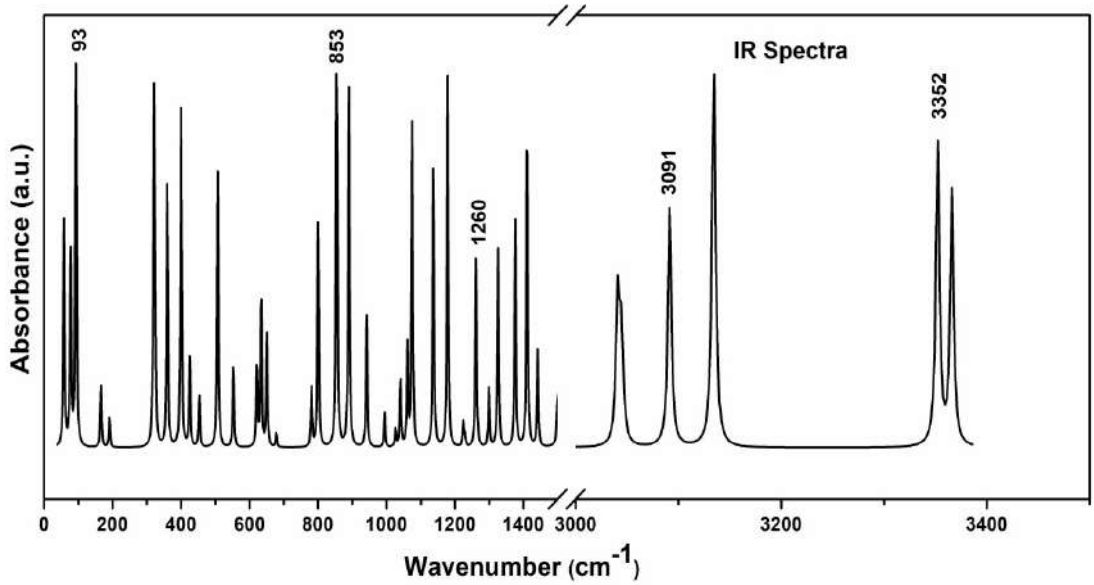

Fig. 6: IR Spectra of paracetamol between the range 0 – 3500cm^{-1} (Intensities of selected characteristics modes are assigned).

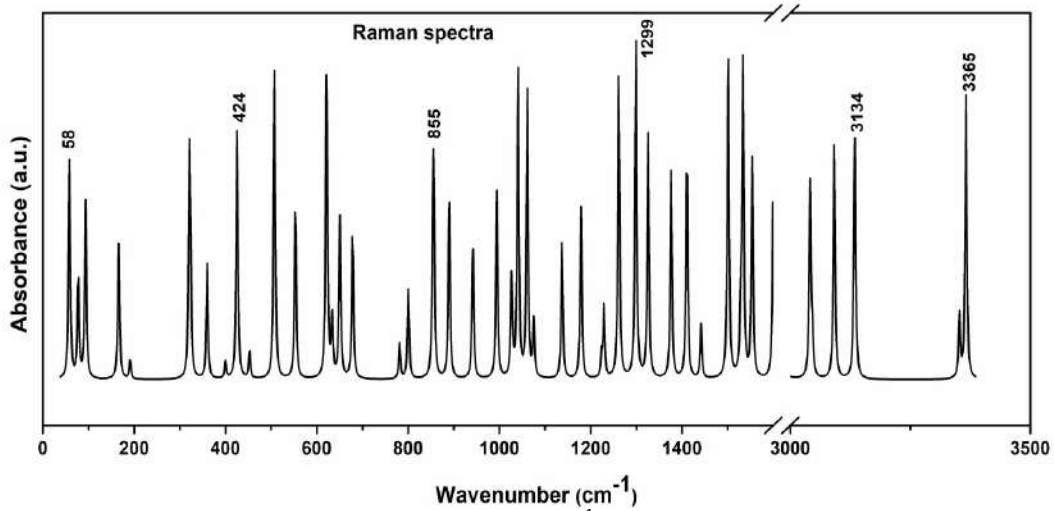

Fig. 7: Raman spectra of paracetamol between the ranges 0 -3500 cm^{-1}. Intensities of selected characteristic modes are assigned.

N-HVibration

This mode is due to the N-H bond in the amide group, which can exhibit coupling with nearby vibrations depending on the hydrogen bonding interactions. The N-H stretching absorption occurs in the range 3500-3220 cm^{-1} and is a characteristic peak that can be used to identify the presence of NH functional group in a molecule [15,36]. In this study, pure N-H stretching mode were recorded at 3366 cm^{-1} with IR intensity 17.627 and Raman intensity 78.198 respectively.

C=O Vibration

The C=O vibrations have been most widely studied by infrared spectroscopy. This multiple-bonded group is highly polar and gives rise to an intense infrared absorption band [37]. An essential spectroscopic characteristic of paracetamol is the C=O vibration, which sheds light on the molecular makeup and bonding characteristics of the substance. The C=O stretching vibration often shows in the range of 1670–1820 cm^{-1} [38]. In

the present study, C=O vibration were recorded at 1699 cm^{-1} with IR intensity and Raman activity of 120.412 and 14.936 units respectively in scaled DFT.

3.5 Molecular Electrostatic Potential (MEP) surface

The MEP at a point r in the space around a molecule (in atomic units) can be expressed as [39]:

$$V(r) = \sum_A \frac{z_A}{\left|\vec{R}_A - \vec{r}\right|} - \int \frac{\rho\left(\vec{r}_1{}'\right) dr'}{\left|\vec{r}' - \vec{r}\right|}$$

where ρ (r′) is the molecule's electronic density function and Z_A is the charge on nucleus A, which is situated at R_A. The contributions of nuclei and electrons to the potential are denoted by the first and second terms, respectively. The resultant, or V(r), is the net electrostatic impact that the molecule's nuclei and electrons create at each location r. The MEP is a valuable measure for elucidating the structure–activity connection, hydrogen bonding, and reactivity of compounds, including pharmaceuticals and biomolecules [40]. The dipole moment, electronegativity, partial charges, and chemical reactivity site of a molecule are all correlated with the total chargedistribution [41]. In the MEP, the green zone denotes the neutral region, while the red and blue regions relate to the electron-rich and electron-poor regions.

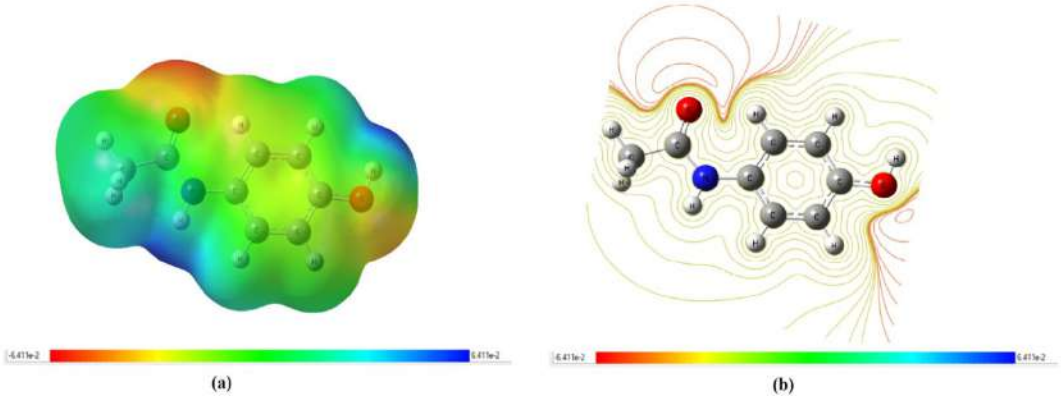

Fig. 8: (a) Molecular electrostatic potential map, and (b) Contour plot of molecular electrostatic potential surface of paracetamol.

Using the computer program GaussView, the MEP for paracetamol was plotted using the 6-31G basis set in order to estimate the reactive sites of the molecule. Figure 8 displays MEP surfaces for paracetamol. The MEP (Figure 8) for paracetamol demonstrates that the O atom of the C=O group of the molecule has a visible negative electrostatic potential surface, making it amenable to electrophilic assault. The positive charge is localised on the H atom attached to the hydroxyl group. Potential rises in red, orange, yellow, green, and blue order [42]. The proton's attraction is caused by the negative region of MEP.

3.6 Molecular Docking

Molecular docking is a potent computer method at the forefront of molecular biology and contemporary drug development. It is essential to comprehending how small molecules like possible therapeutic compounds interact with their target biomolecules, which are usually proteins or nucleic acids. Molecular docking offers important insights into the binding affinities, binding modes, and structural dynamics that control the formation of these crucial molecular complexes by emulating the binding process between these molecules in silico [43]. The protein structure for protein CYP2E1 (1EQG), which is used to dock paracetamol, was retrieved from the Protein Data Bank (PDB). In order to optimize the geometry for accurate binding simulations, the structure was cleaned by removing excess water molecules, adding any missing polar hydrogen atoms, and adjusting charge assignments and force fields. Similarly, using tools such as pyMol, the ligand paracetamol was produced in PDB format from SDF format. AutodockTools defines docking parameters and specifies PDBQT (Protein Data Bank, partial charge Q and type T) files for ligand paracetamol and receptor protein CYP2E1(1EQG). Using available literature or binding site prediction tools, the binding site on CYP2E1 (1EQG) was located. A grid box was then constructed around the binding site to provide targeted docking simulation on the active site with the highest interaction potential.

The docking simulation was carried out using programs such as AutoDock, AutoDock Vina [25,26], Glide by modifying settings including grid box dimensions 40Å× 40Å× 40Å, search strategy, and scoring function. The grid box is set at x-axis, y-axis and z-axis at 46.985, 33.471 and 187.492 directions respectively with spacing of 0.375Å. By comparing the docking scores, which indicate binding and visually inspecting significant chemical interactions such hydrogen bonding, pi-pi stacking, and hydrophobic contacts, the results were assessed to determine the optimal binding configuration for paracetamol. In order to visualize the binding interactions and significant residues, the protein-ligand complex with the top docking posture was imported into BIOVIA Discovery Studio [27] and 2D and 3D interaction maps were created. Detailed reports that highlighted the interaction details, examined the binding site structure, and assessed paracetamol's potential as a modulator of CYP2E1 (1EQG)'s function were produced using these graphics. To sum up, the outcomes were documented by keeping photos and notes for further analysis and reporting. n 1963, Ramachandran et al. presented the [phi(ϕ),psi(Ψ)] angles as a way to represent the protein backbone.

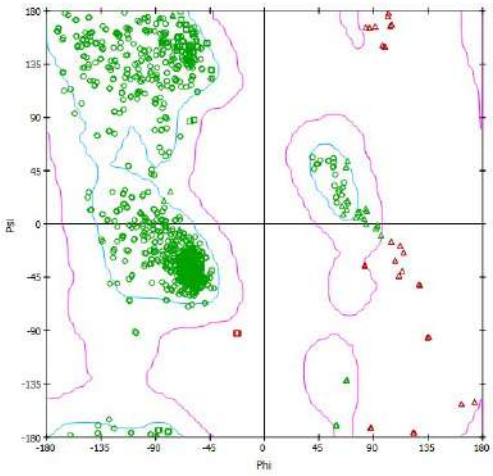

Fig. 9: Ramachandran plot of protein 1EQG.

Ramachandran plot, is widely employed in protein structure determination and secondary structure definition. Ramachandran et al. created a steric map of the Ramachandran plot based on analyzing local hard-sphere repulsions between atoms that are third neighbors (1-4 interactions), which forecasted the usual permissible regions: the α_R , α_L, and β-regions. The steric map shown in Figure 9 is now widely accepted as the typical way to interpret the Ramachandran plot, as established by Richardson in 1981. Mandel and colleagues were the first to pinpoint the precise steric clashes that establish the limits of this standard steric map [44] .The figure shows heavy residue in the alpha helix region ($\alpha_{R)}$ suggesting the significant secondary structure.

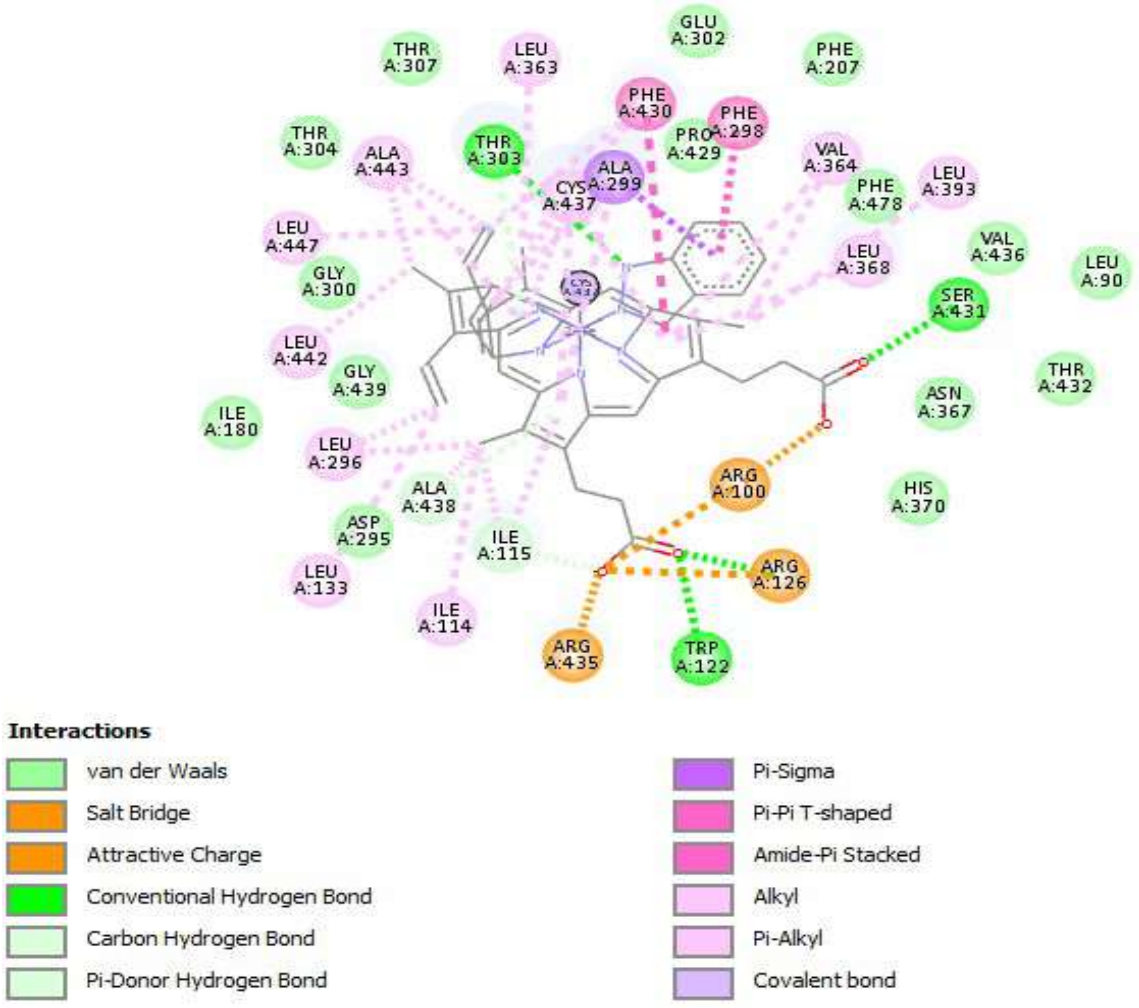

Fig. 10: 2D- ligand intraction diagram of paracetamol with CYP2E1(1EQG)

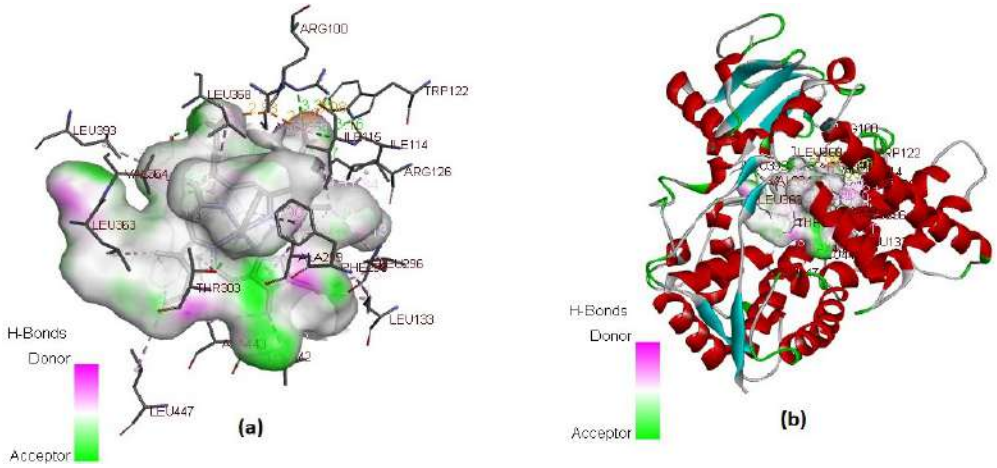

Fig. 11: (a**)** Docked structure showing binding pocket in terms of H-bond (b) Docked 3D structure showing binding pocket in terms of H-bond with receptor.

4. CONCLUSION

An analysis of the structural, electronic, and vibrational characteristics of paracetamol was carried out through DFT, alongside a molecular docking investigation with AutoDock Vina, to study the molecular structure, vibrational frequencies, MEP, HOMO-LUMO analysis, and molecular docking of the compound. It was observed that all the calculated vibrational modes were active in both IR and Raman spectroscopy. Information on the title molecule's size, shape, charge density distribution, and chemical reactivity sites has been gathered through MEP mapping. Negative potential is situated close to the O atom of the C=O group of the molecule, while positive potential is situated near the hydrogen atom of the hydroxyl group. Additionally, the pale yellow area within the benzene structure was forecasted to be a transitional phase. Using the TD-DFT/B3LYP/6-31G basis set, the electronic transition has been calculated in both the gas phase and the aqueous environment (water), illustrating the charge transfer within the molecule. The role of charge transfer between the acceptor and donor groups was made extremely evident by HOMO-LUMO. The HOMO-LUMO analysis indicated an energy gap of 5.594 eV in the gas phase and 5.566 eV in solvent, highlighting the molecule's chemical reactivity and stability. This shows that paracetamol is somewhat more reactive in a solution, which is crucial for its interaction with biological systems. Moreover, predictions have been made regarding the binding locations of the protein matrix and the title molecule. The protein CYP2E1(1EQG) molecule complex was estimated to have a binding affinity of -6.6 kcal/mol. Therefore, the title molecule has a good binding potential against the protein CYP2E1(1EQG), as theoretically demonstrated by the molecular docking studies demonstrating the significance in the fields of medicinal chemistry, title molecular chemical biology, pharmacology,and drug design in the creation of novel medications and materials. This study highlights the importance of computational chemistry in drug discovery and development, promoting its continuous use and integration in the field.

AUTOR CONTRIBUTIONS

K. Khadayat: Writing-original draft, investigation, and Formal analysis; B.D. Joshi: Methodology, Writing-review and editing, Conceptualization, and supervision

CONFLICTS OF INTEREST

There are no conflicts to declare.

ACKNOWLEDGEMENTS

B.D Joshi would like to acknowledge University Grants Commission, Nepal for partial financial support under Faculty Research Grant (FRG--79&80-S&T-05).

REFERENCES

[1] H.N. Morse, Ueber eine neue Darstellungsmethode der Acetylamidophenole, *European Journal of Inorganic Chemistry,* **11** (1878) 232-233. https://doi.org/10.1002/cber.18780110151

[2] M.J. Smilkstein, G.L. Knapp, K.W. Kulig, B.H. Rumack, Efficacy of oral N-acetylcysteine in the treatment of acetaminophen overdose: analysis of the national multicenter study (1976 to 1985), *The New England Journal of Medicine,* **319** (1988) 1557–1562. https://doi.org/10.1056/NEJM198812153192401

[3] A. Bertolini, A. Ferrari, A. Ottani, S. Guerzoni, R. Tacchi, S. Leone, Paracetamol: New vistas of an old drug, *CNS Drug Reviews,* **12** (2006) 250–275. https://doi.org/10.1111/j.1527-3458.2006.00250.x

[4] L.O. Ahmed, R.A. Omer, Computational study on paracetamol drug, *Journal of Physical Chemistry and Functional Materials,* **3** (2020) 9-13.

[5] O.O. Oloyede, Z.O. Alabi, A.O. Akinyemi, S.F. Oyelere, B.O. Amuwaolorun, B.C.D. Owoyemi, Comparative evaluation of acetaminophen form (I) in commercialized paracetamol brands, *Scientific African,* **19** (2023) e01537. https://doi.org/10.1016/j.sciaf.2022.e01537

[6] U. Freo, C. Ruocco, A. Valerio, I. Scagnol, E. Nisoli, Paracetamol: A review of guideline recommendations, *Journal of Clinical Medicine,* **10** (2021) 3420. https://doi.org/10.3390/jcm10153420

[7] O. Airaksinen, J.I. Brox, C. Cedraschi, J. Hildebrandt, J. Klaber-Moffett, F. Kovacs, A.F. Mannion, S. Reis, J.B. Staal, H. Ursin, G. Zanoli, European guidelines

[8] for the management of chronic nonspecific low back pain, *European Spine Journal,* **15** (2006) S192–S300. https://doi.org/10.1007/s00586-006-1072-1

[9] A. Lupattelli, O. Spigset, M.J. Twigg, K. Zagorodnikova, A.C. Mårdby, M.E. Moretti, M. Drozd, A. Panchaud, K. Hämeen-Anttila, A. Rieutord, R.G. Juraski, M. Odalovic, D. Kennedy, G. Rudolf, H. Juch, A. Passier, I. Björnsdóttir, H. Nordeng, Medication use in pregnancy: A cross-sectional, multinational web-based study, *BMJ Open,* **4** (2014) e004365. https://doi.org/10.1136/bmjopen-2013-004365

[10] E.D. Hogestatt, B.A.G. Jönsson, A. Ermund, et al., Conversion of acetaminophen to the bioactive N-acylphenolamine AM404 via fatty acid amide hydrolase-dependent arachidonic acid conjugation in the nervous system, *Journal of Biological Chemistry,* **280** (2005) 31405–31412. https://doi.org/10.1074/jbc.M501489200

[11] J.L. Finnan, R.E. Lisa, D.N. Schmidt, Process for preparing spray dried acetaminophen powder and the powder prepared thereby, (U.S. Patent No. 4,710,519), *U.S. Patent and Trademark Office,* http://www.t3db.ca/toxins/t3d2571, 1975.

[12] S.Shiffman, D.R. Battista, J.P. Kelly, M.K. Malone, R.B. Weinstein, D.W. Kaufman, Prevalence of exceeding maximum daily dose of paracetamol, and seasonal variations in cold-flu season, *British Journal of Clinical Pharmacology,* **84** (2018) 1250–1257. https://doi.org/10.1111/bcp.13551

[13] M.A. Mallah, S.T. Sherazi, M.I. Bhanger, S.A. Mahesar, M.A. Bajeer, A rapid Fourier-transform infrared (FTIR) spectroscopic method for direct quantification of paracetamol content in solid pharmaceutical formulations, *Spectrochimica Acta Part A: Molecular and Biomolecular Spectroscopy,* **141** (2015) 64–70. https://doi.org/10.1016/j.saa.2015.01.036J.

[14] R. Castro-Suarez, M. Vásquez-Osorio, S.P. Hernandez-Rivera, A.A. Pájaro-Payares, Vibrational analysis of acetaminophen from commercial tablets, *IOP Conference Series: Materials Science and Engineering,* **519** (2019) 012006. https://doi.org/10.1088/1757-899X/519/1/012006

[15] U. Habiba, A. Alam, S.U.D. Rahman, S. Piya, IR spectra of paracetamol, *Bangladesh Journal of Scientific and Industrial Research,* **56** (2021) 255-262. https://doi.org/10.3329/bjsir.v56i4.57197

[16] R.D. Oparin, M. Moreau, I. De Walle, M. Paolantoni, A. Idrissi, M.G. Kiselev, The interplay between the paracetamol polymorphism and its molecular structures dissolved in supercritical CO2 in contact with the solid phase: In situ vibration spectroscopy and molecular dynamics simulation analysis, *European Journal of Pharmaceutical Sciences,* **77** (2015) 48–59. https://doi.org/10.1016/j.ejps.2015.05.016

[17] Y. Wang, W. Lin, N. Wu, X. He, J. Wang, Z. Feng, X.-Q. Xie, An insight into paracetamol and its metabolites using molecular docking and molecular dynamics simulation, *Journal of Molecular Modeling,* **24** (2018) 243. https://doi.org/10.1007/s00894-018-3790-9

[18] M.P. Gleeson, D. Gleeson, QM/MM calculations in drug discovery: A useful method for studying binding phenomena? *Journal of Chemical Information and Modeling,* **49** (2009) 670–677. https://doi.org/10.1021/ci800419j

[19] H.E. Pence, A. Williams, ChemSpider: an online chemical information resource, *Journal of Chemical Education,* **87** (2010) 1123–1124. https://doi.org/10.1021/ed100697w

[20] C. Lee, W. Yang, R.G. Parr, Development of the Colle-Salvetti correlation-energy formula into a functional of the electron density, *Physical Review B,* **37** (1988) 785–789.https://doi.org/10.1103/PhysRevB.37.785R. Mishra, B.D. Joshi, A. Srivastava, P. Tandon, S. Jain, Quantum chemical and experimental studies on the structure and vibrational spectra of an alkaloid—Corlumine, *Spectrochimica Acta Part A: Molecular and Biomolecular Spectroscopy,* **118** (2014) 470–480. https://doi.org/10.1016/j.saa.2013.09.015

[21] P. Pulay, G. Fogarasi, F. Pang, J.E. Boggs, Systematic ab initio gradient calculation of molecular geometries, force constants, and dipole moment derivatives, *Journal of the American Chemical Society,* **101** (1979) 2550-2560. https://doi.org/10.1021/ja00504a009

[22] G. Fogarasi, X. Zhou, P.W. Taylor, P. Pulay, The calculation of ab initio molecular geometries: Efficient optimization by natural internal coordinates and empirical correction by offset forces, *Journal of the American Chemical Society,* **114** (1992) 8191-8201. https://doi.org/10.1021/ja00047a032

[23] A. Frisch, A.B. Nielson, A.J. Holder, *GaussView User Manual,* Gaussian Inc., Pittsburgh, P.A. https://www.scirp.org/reference/referencespapers? Reference id :1525346,2000.

[24] M.E. Casida, K.C. Casida, D.R. Salahub, Excited-state potential energy curves from time-dependent density-functional theory: A cross section of formaldehyde's 1 A1 manifold, *International Journal of Quantum Chemistry,* **70** (1998) 933–941. https://doi.org/10.1002/(SICI)1097-461X(1998)70:4/5<933::AID-QUA39>3.0.CO;2-Z

[25] O Trott, A.J. Olson, AutoDock Vina: improving the speed and accuracy of docking with a new scoring function, efficient optimization, and multithreading, *Journal of Computational Chemistry,* **31** (2010) 455–461. https://doi.org/10.1002/jcc.21334

[26] G.M. Morris, R. Huey, W. Lindstrom, M.F. Sanner, R.K. Belew, D.S. Goodsell, A.J. Olson, AutoDock4 and AutoDockTools4: Automated docking with selective receptor flexibility, *Journal of Computational Chemistry*, **30** (2009) 2785–2791. https://doi.org/10.1002/jcc.21256.

[27] Dassault Systèmes, BIOVIA Discovery Studio, Dassault Systèmes, https://www.3ds.com/products/biovia/discovery-studio, 2016.

[28] C. Corminboeuf, F. Tran, J. Weber, The role of density functional theory in chemistry: Some historical landmarks and applications to zeolites, *Journal of Molecular Structure: THEOCHEM*, **762** (2006) 1–7. https://doi.org/10.1016/j.theochem.2005.07.03.

[29] R.S. Mulliken, Electronic Population Analysis on LCAO–MO Molecular Wave Functions. I, *The Journal of Chemical Physics*, **23** (1955) 1833–1840. https://doi.org/10.1063/1.1740588.

[30] M. Picollo, M. Aceto, T. Vitorino, UV-Vis spectroscopy, *Physical Sciences Reviews*, **08** (2018) 1-14. https://doi.org/10.1515/psr-2018-0008.

[31] D. Lewis, C. Ioannides, D. Parke, Interaction of a series of nitriles with the alcohol-inducible isoform of P450: Computer analysis of structure—activity relationships, *Xenobiotica*, **24** (1994) 401–408. https://doi.org/10.3109/00498259409043243.

[32] G. Varsanyi, Assignments for Vibrational Spectra of Seven Hundred Benzene Derivatives, Wiley, New York, 1974.

[33] V.K. Rastogi, M. Alcolea Palafox, R.P. Tanwar, L. Mittal, 3,5-Difluorobenzonitrile: ab initio calculations, FTIR and Raman spectra, *Spectrochimica Acta Part A: Molecular and Biomolecular Spectroscopy*, **58** (2002) 1987–2004. https://doi.org/10.1016/s1386-1425(01)00650-3.

[34] M. Karaback, et al., An experimental and theoretical study of molecular structure and vibrational spectra of 2-chloronicotinic acid by density functional theory and ab initio Hartree-Fock calculations, *Journal of Molecular Structure*, **885** (2008) 28–35. https://doi.org/10.1016/j.molstruc.2007.10.004.

[35] N.B. Clothup, L.H. Daly, S.E. Wiberley, Introduction to infrared and Raman spectroscopy, Academic Press, 1990.

[36] B.D. Joshi, G. Thakur, M.K. Chaudhary, Molecular Structure, Homo-Lumo and Vibrational Analysis of Ergoline by Density Functional Theory, *Scientific World*, **14** (2021) 21–30. https://doi.org/10.3126/sw.v14i14.34978.

[43] aristolochic acid II using density functional theory, *BIBECHANA*, **12** (2014). https://doi.org/10.3126/bibechana.v12i0.11702.

[44] B. Jacobs, P. Ir, M. Bigdeli, P.L. Annear, W. Van Damme, Addressing access barriers to health services: An analytical framework for selecting appropriate interventions in low-income Asian countries, *Health*

[37] G. Socrates, Infrared and Raman Characteristic Group Frequencies, Tables and Charts, 3rd ed., Wiley, Chichester, 2001.

[38] A. Prabakaran, S. Muthu, Normal Coordinate Analysis and Vibrational Spectroscopy (FT-IR and FT-Raman) Studies of (2S)-2-Amino-3-(3,4- Dihydroxyphenyl)-2-ethylpropnoic Acid Using ab Initio HF and DFT Method, *Spectrochim. Acta Part A*: *Molecular and Biomolecular Spectroscopy*, **99** (2012) 90–96. https://doi.org/10.1016/j.saa.2012.09.014

[39] R. Parthasarathi, J. Padmanabhan, U. Sarkar, et al., Toxicity analysis of benzidine through chemical reactivity and selectivity profiles: A DFT approach, *Internet Electronic Journal of Molecular Design*, **2** (2003) 798–813.

[40] S. Chidangil, P. Mishra, Structure-activity relationship for some 2',3'-dideoxynucleoside anti-HIV drugs using molecular electrostatic potential mapping, *Journal of Molecular Medicine*, **3** (1997) 172–181. https://doi.org/10.1007/s008940050029.

[41] B.D. Joshi, P.N. Chaudhary, Molecular structure, MESP, HOMO-LUMO, and vibrational analysis of β-Asarone using density functional theory, *Kathmandu University Journal of Science, Engineering and Technology*, **9** (2013) 1–14. https://doi.org/10.3126/kuset.v9i2.63714.

[42] J.B. Khadka, B.D. Joshi, Molecular electrostatic potential, HOMO-LUMO and vibrational study of *Policy and Planning*, **27** (2012) 288–300. https://doi.org/10.1093/heapol/czr038.

[45] B.K. Ho, A. Thomas, R. Brasseur, Revisiting the Ramachandran plot: Hard-sphere repulsion, electrostatics, and H-bonding in the α-helix, *Protein Science*, **12** (2009) 2508–2522. https://doi.org/10.1110/ps.03235203

Assessment of Invasive Alien Plant Species in Buffer zone and Indo-Nepal Border Area and their Impact on Native Biodiversity in Kanchanpur, Nepal

Divya Bhatt[1], Roshani Saud[2], Dhiraj Dhami[3], Bimala Shakya[4] and Man Dev Bhatt[5*]

[1]Department of Botany, Siddhanath Science Campus, Tribhuvan University, Mahendranagar, Nepal
[2]Department of Botany, Siddhanath Science Campus, Tribhuvan University, Mahendranagar, Nepal
[3]Department of Botany, Siddhanath Science Campus, Tribhuvan University, Mahendranagar, Nepal
[4]Department of Natural History Museum, Kathmandu, Nepal
[5]Department of Botany, Siddhanath Science Campus, Tribhuvan University, Mahendranagar, Nepal

Research Article

ISSN: 3059-9504 (online)
Doi:xxxx

Article History

Received: October 21, 2024
Revised: November 18, 2024
Accepted: November 20, 2024
Published: December 28, 2024

Keywords

Buffer zone, Dominant, IAPS, IVI, Kanchanpur.

***Corresponding author**

Email: bhattmdrp@gmail.com (M.D. Bhatt)
Phone: + 977-984872189

ABSTRACT

IAPS are already a huge worldwide environmental issue, endangering biodiversity, altering ecosystems, and disrupting socioeconomic systems. The current study aimed to assess the distribution, diversity, and effect of IAPS in the Indo-Nepal buffer zones of Kanchanpur District, Nepal, with a focus on Bhimdatta and Dodharachadani Municipality. Between September 2023 and July 2024, a comprehensive field survey was undertaken at the research sites. Using quadrat sampling and herbarium identification, 21 plant species were identified. These species belonged to 11 families of which Asteraceae family was dominant in all study sites; holding 8 species. On the basis of IVI, 10 invasive plant species were recorded as dominant in all study sites. Of these, the highest importance value index of dominant invasive alien plant species at site 1 was recorded by *Partheniun hysterophorus* (41.39) and lowest by *Mimosa pudica* (2), whereas among dominant invasive alien plant species of site 2 the highest IVI was of *Lantana camara* (56.46) and lowest by *Argemone maxicana* (3.82). At site 3, the highest importance value index of dominant invasive alien plant species was recorded by *Parthenium hysterophorus* (28.35) and lowest by *Bidens pilosa* (2.85). The study's findings could have ecological and economic implications, such as loss of biodiversity, soil degradation, and health dangers. Furthermore, the study revealed the adaptive reproductive tactics of IAPS, such as allelopathy and seed viability, which increase their invasive nature. The findings highlight the critical need for focused management techniques to minimize the growing threat of IAPS, particularly in buffer zones where conservation efforts are currently underexplored.

1. INTRODUCTION

The word 'invasive' comes from the word 'invasion' which means to invade and the word 'alien' means foreigner or migratory. Invasive alien species refers to those plant and animal that have been moved or imported either intentionally or unintentionally by human, from their native habitat to new environment [1]. The spread of IAS is recognized as one of the significant threats to the biodiversity often leading to the loss of native species and altering ecosystem [2,3]. The issue of IAS is a global concern, affecting both developed and developing countries like Nepal, where the resources of their management are limited [4]. IAPS can drastically change species composition and reduce biodiversity, thereby threatening global biodiversity [5,6].

The invasive alien plant species (IAPS) are characterized by their fast growth and extensive spread, causing significant damage to native species and habitats globally [7]. Invasion of habitats by these species is a global problem impacting ecological, economic and social system [8]. One-sixth of the world's land surface is highly vulnerable to invasion including developing countries and biodiversity hotspots [9]. The risks of invasions are increasing due to expanding transportation networks, technological advancements, landscape transformations, climate change, and geopolitical events such as warfare and migration [10]. For example, territories occupied by the IAPS in South Africa increased by 50% between 2000 and 2016 [11].

Over several generations, the IAPS are capable of adapting to their introduced habitat [12]. This adaptability is often facilitated by their ability to adjust to new climatic condition [13], which can further exacerbate their negative impacts on the ecosystem [14,15]. For instance, some IAPS, such as *Parthenium,* exhibit allelopathic effects due to the presence of water-soluble phenolic and sesquiterpene lactones like parthenin [16]. This compound inhibits the growth of other plants through soil contamination [17,18], allowing IAPS to dominate in their introduced habitat [19].

Banerji conducted the first survey of invasive alien species (IAS) in Nepal in 1958, focused on the invasion of *Eupatorium glandulosum* in Eastern Nepal [20]. Subsequent IUCN research revealed 21 distinct IAS in the country [21], which increased to 25 in Shrestha's 2016 study and 26 according to the Department of Plant Resources in 2020 [20]. This reflects an

alarming rise in the rate of invasions by IAS over the last couple of decades.

Previous research is focused on ecological studies within wetlands and protected areas [22]. Limited studies have been done or emphasis laid on buffer zones and the bordering regions. A buffer zone-also known as a multiple use or transitional zone-is a relatively new concept, while the notion has been used for some time [23]. The buffer zone concept, introduced by UNESCO, aims to integrate conservation goals with local development by encouraging sustainable resource use and active community participation [24,25]. In Nepal, buffer zones serve as a strategy to reduce conflicts between protected areas and neighboring communities by supporting wildlife conservation while addressing the immediate needs of local residents [26]. These zones improve ecological conditions as well as increase the ranges of wildlife habitats. Buffer zones are regarded as critical for protecting biologically valuable places while meeting developmental objectives [23]. Long-standing cultural bonds and shared resources have in the past been the base of cross-border relations on the 1,751 km open India-Nepal border. In recent times, problems of human and drug trafficking, illegal trade, and environmental degradation have cropped up to put pressure on coordinated, sustainable management of biodiversity and security concerns as a challenge [27]. According to [28], a border region is an area, and a border is a line that divides the territories of different states. As noted by [29], all such regions display differences in spatial planning and subsidy and tariff policies, in social and tax legislation, economic intercourse, standards and levels of living, purchasing power, and wage rates. Over the years, various IAS have emerged to threat local biodiversity by inhibiting the regrowth of native species. However, no systematic assessment of IAS has been conducted outside the protected areas mainly in buffer zones. The present study focuses on Indo- Nepal border areas and Suklaphanta National Park buffer zone of Kanchanpur district and focuses more precisely on Bhimdatta and Dodharachadani Municipality in order to assess the status regarding IAS. This research represents the current situation of IAPs in these transitional locations and gives an overview of their diversity, implications, and management option.

2. MATERIALS AND METHODS

2.1. Study area

The study was conducted in Kanchanpur District, Nepal, particularly in buffer zone of Shuklaphant National Park (SNP) in Bhimdatta Municipality and Indo-Nepal border areas of Bhimdatta Municipality and Dodhara Chandani Municipality. Kanchanpur district of Far western Nepal, Sudurpaschim Province, has the total area of 1,610 sq.km. Topographically the district was divided into three regions; Churia hills, Bhabar range and Terai plains. The climate of Kanchanpur district is dry tropical type with rainy summer and dry winter climate. The area is situated in tropical zone having an average 1775mm annual rainfall with maximum temperature 42^{o}C during summer and minimum temperature 6^{o}C during winter. The relative humidity is in the range of 84-87%. The average annual rainfall estimated approximately 1575mm [30].The study area is biologically rich and ecologically fragile; hence, it comes within the critical zone for assessing the spread and impact of invasive plant species.

The geographic and ecological context of the Bhimdatta Municipality area spans 171 square kilometers with diverse landscapes, ranging from 60 meters to 1,528 meters above sea level. It borders the globally important biodiversity hotspot of Shuklaphanta National Park, with its urban settlements, agricultural fields, and forest buffer zones. A highway, the Bhramadev Highway, bisects this Municipality, thus providing a pathway that may help in the dispersal of invasive species. Similarly, the Dodhara Chandani Municipality Municipality covers the area of 56.84 sq. km and has been situated in the western frontiers of Nepal bordering the Mahakali River and the Indian State of Uttarakhand. A riverine landscape, regions of forests, and pieces of agriculture have elevations ranging from 60-300 meters, which are seriously vulnerable to the invasion and proliferation of alien plant species through human activities and cross-border relationship.

2.1.1. Study Locations: For capturing the distribution and dynamics of the IAPs the key sites were selected as;

Border Area of Dodhara Chandani Municipality (Site 1): This site focuses on areas in the vicinity of the Mahakali River and the edge of the forest. These are areas where disturbance due to human activities like agriculture and grazing favors the proliferation of invasive plants.

Shuklaphanta Buffer Zone and Border Area (Gaddachauki to Bhramadev) (Site 2): This site provides a focus on the park's peripheral areas and also the westernmost border of Nepal, starting from the busy Gaddachauki checkpoint right down to the ecologically significant Bhramadev region. Anthropogenic activities like trade, road construction, and the expansion of agriculture are leading causes for the introduction and propagation of invasive species in the region.

Bhramdev Highway (Bhasi to Jhilmila Lake) (Site 3): This stretch of highway connects Bhasi to the Jhilmila Lake area and serves as a critical dispersal corridor for invasive species. Roadside vegetation and nearby agricultural lands were surveyed to assess the prevalence of invasive species along this key transportation route.

These sites have been selected to represent both natural and anthropogenic landscapes, in which invasive species thrive in areas with disturbances like road construction, cross-border trade, and agricultural activities. Their proximity to Shuklaphanta National Park presents another layer of complexity due to the invasion of native ecosystems by invasive species, thus posing a threat to biodiversity. The study area indicates its strategic value in understanding the distribution, pathways, and ecological impacts of invasive species in Kanchanpur District (**Figure 1**).

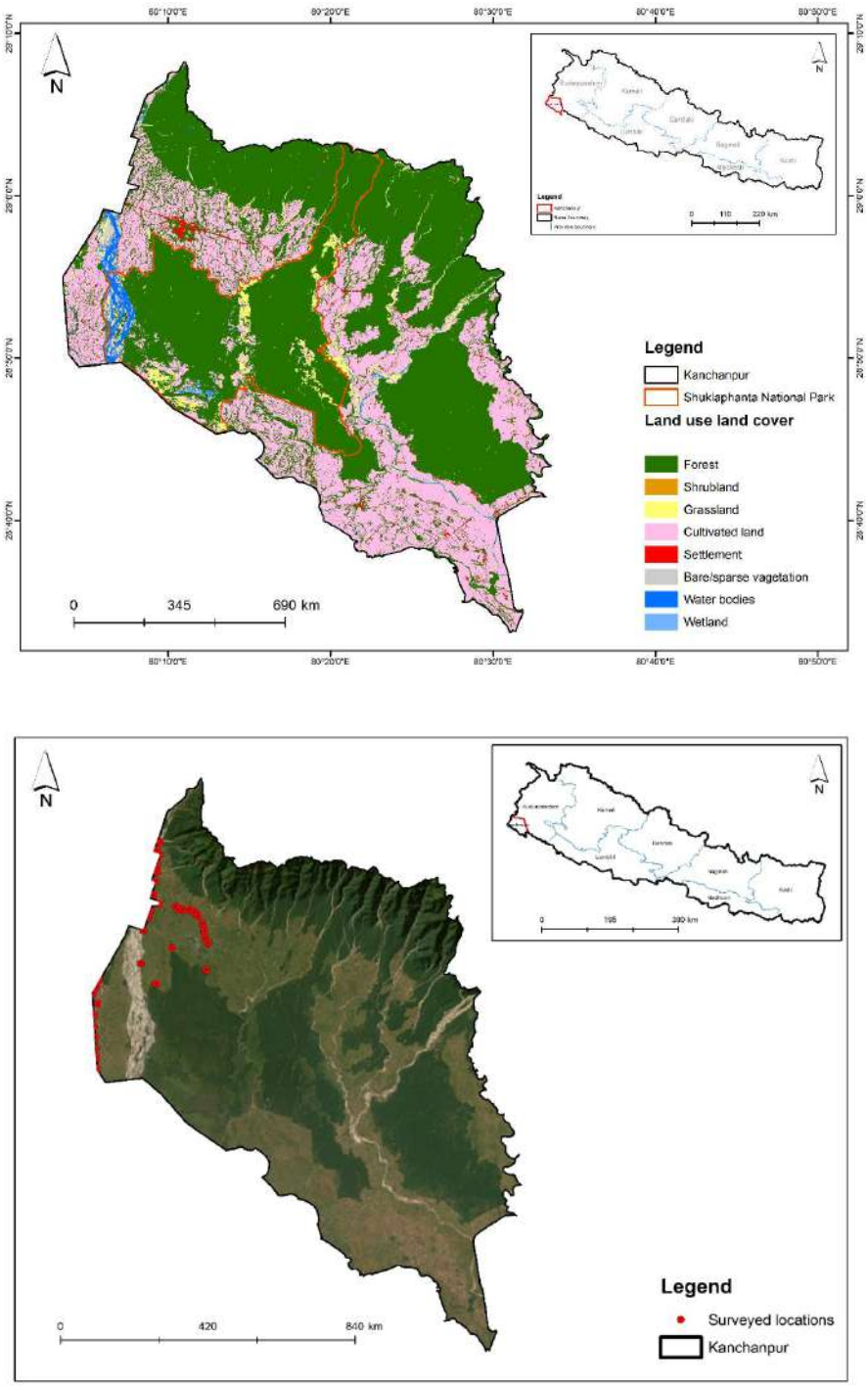

Fig. 1: Maps of study area.

The survey, which runs from September 2023 to July 2024, include systematic monthly visits to study plant species' growth forms, phenology, and status, as well as the collection of samples for morphological investigations. A quadrat sampling approach (5×5 m) was used to calculate density, frequency, coverage, and the Importance Value Index (IVI) using [31] and [32] methodologies. The plant species referred to be invasive by respondents were collected, pressed, dried, mounted and preserved based on standard methods as given by [33]. Before preservation all the collected vouchers were examined and identified with the help literature [34,35,36]. Furthermore, the species were confirmed by comparing with herbarium specimens deposited at KATH (National Herbarium and Plant Laboratories, Godawori, Lalitpur, Nepal), TUCH (Tribhuvan University Herbarium, Department of Botany, Kirtipur, Kathmandu), and Department of Botanty, Siddhanath

Science Campus, Mahendranagar. All voucher specimens were deposited at Department of Botany, Siddhanath Science Campus, Mahendranagar. Scientific name of plants and their families were verified with referring to the plant list (http://www.theplantlist.org/). The reproductive biology of dominant invasive species was evaluated, including seed weight, size, shape, and germination tests, with field activities captured through photography. The collected data was recorded in notebooks and evaluated on a computer to provide thorough study results.

3. RESULTS AND DISCUSSION

3.1. Floristic composition and Diversity pattern of plant species

A total of 21 plant species were reported at three study sites, including 16 species at site 1, 18 at site 2, and 20 at site 3. *Ageratum houstonianum, Alt-ernanthera philoxeroides, Bidens pilosa, Calotropis gigantean, Echhornia crassipes, Galinsoga quadriradiata, Hyptis suaveolens, Imperata cylindrica, Ipomoea carnea, Lantana camara, Mimosa pudica, Parthenium hysterophorus, Senna alata, Senna occidentalis, Senna tora,* and *Xanthium strumarium* are among the plant species found at site 1 (**Table 1**). At site 2, there are also *Ageratum houstonianum, Ageratina adenophora, Amaranthus spinosus, Argemone maxicana, Bidens pilosa, Calotropis gigantean, Chromolaena odorata, Galinsoga quadriradiata, Hyptis suaveolens, Ipomoea carnea, Lantana camara, Mimosa pudica, Parthenium hysterophorus, Senna occidentalis, Senna tora, and Xanthium strumarium* **(Table 1).** Similarly, site 3 contains *Alternanthera philoxeroides, Ageratum conyzoid, Ageratum houstonianum, Ageratina adenophora, Amaranthus spinosus, Argemone maxicana, Bidens pilosa, Calotropis gigantean, Chromolaena odorata, Galinsoga quadriradiata, Hyptis suaveolens, Ipomoea carnea, Lantana camara, Mimosa pudica, Parthenium hysterophorus, Senna alata, Senna occidentalis, Senna tora,* and *Xanthium strumarium. Ageratum haustoniaum, Bidens pilosa, Calotropis gigantean, Gallinsoga quadradiata, Hyptis suaveolens, Ipomoea carnea, Imperata cylindrica, Lantana camara, Parthenium hysterophorus, Senna occidentalis, Senna alata, Senna tora,* and *Xanthium strumarium* are the prevalent species found in all three locations. The distribution of invasive species in reference to Nepal was studied by [21,37,38].

These species are classified into 11 families (**Figure 2**): Asteraceae (8), Amaranthaceae (2), Apocynaceae (1), Convolvulaceae (1), Fabaceae (2), Lamiaceae (1), Mimosaceae (1), Papaveraceae (1), Pontederiaceae (2), Poaceae (1), and Vebenaceae (1). The major family at our study site was Asteraceae. The present investigation of dominant family correlates with the study of [39]. The dominant family was Asteraceae due to its vast seed output and efficient seed and pollen grain dissemination. The majority of IAPS are now widespread, although a few are limited to a specific geographical area. They're invading a vast amount of country. The most prevalent invasive alien plant in forests and shrublands is *Lantana camara*, while the least common is *Hyptis suaveolens*. *Parthenium hysterophorus* is the most prevalent in grasslands and residential areas; *Senna alata* is the least common. *Parthenium hysterophorus* is the most frequent in agroecosystems, and *Ageratum houstonianum* is the least common. *Eichhornia crassipes* is the most frequent in wetlands, whereas *Alternanthera philoxeroides* was the least common [40].

Table 1: Floristic composition, density and IVI of Plant Species in different study sites

Name of IAPs	Common Name	Local Name	Family	Site1 (D1)	Site2 (D2)	Site3 (D3)	IVI
Ageratum conyzoid L.	Billygoat weed	Gandhe	Asteraceae	-	-	3	11.84
Ageratum houstonianum Mill.	Blue billigoat weed	Nilo Gandhe	Asteraceae	12.64	17.86	8.88	31.84
Ageretena adenophora L.	Crofton weed	Kalo Banmara	Asteraceae	-	1.14	5.25	12.26
Alternanthera philoxeroides (Mart.) Griseb.	Alligator weed	Jalajambhu	Amaranthaceae	1.55	-	6.63	15.68
Amaranthus spinosus L.	Spiny pigweed	Kande lude	Pontederiaceae	-	2.86	0.63	8.3
Argemone maxicana L.	Mexican poppy	Thakal	Papaveraceae		0.43	0.38	3.62
Bidens pilosa L.	Black jack	Kalokuro	Asteraceae	1.18	0.43	0.25	4.64
Calotropis gigantean	Milk weed	Aank	Apocynaceae	0.55	1.43	2.13	7.52
Chromolaena odorata (Spreng.) King andRobinson	Siam weed	Setobanmara	Asteraceae	-	3.14	8.25	17.4
Eichhornia crassipes (Mart.) Solms.	Water hyacinth	JalaKumbhi	Pontederiaceae	0.64	-	-	5.19

Galinsoga quadriradiata Ruiz & Pav.	Shaggy soldier	Jhusechirlanga	Asteraceae	4.09	0.43	2	9.98
Hyptis suaveolens (L.) Poit.	Bushmint	Tulsijhar	Lamiaceae	9.09	2.43	7.88	19.5
Imperata cylindrica (P. Beauv. and Rubus ellipticus Sm.)	Cogongrass	Siru	Poaceae	1.82	11.86	4.38	18.07
Ipomoea carnea Jacq.	Pink morning glory	Beshram	Convolvulaceae	2.36	4.57	8.88	17.05
Lantana camara L.	Lantana	Kirnekanda	Vebenaceae	6.45	30.14	11.25	34.68
Mimosa pudica L.	Sensitive plant	Lajjawati	Mimosaceae	0.18	0.43	1.38	4.36
Parthenium hysterophorus L.	Parthenium	Patijhar	Asteraceae	11.09	6.57	11.25	29.32
Senna alata	Candle bush	Alu Pate Jhar	Fabaceae	0.27	1.14	0.38	4.77
Senna occidentalis (L.) Link	Coffee senna	Panwar	Fabaceae	1	1.86	1.63	7.78
Senna tora (L.)	Sickle pod senna	Tapre	Amaranthaceae	12.27	14.14	8.38	31.58
Xanthium strumarium L.	Rough cockle bur	Bhedekuro	Asteraceae	7.18	6.71	5.75	19.68

Note: D1= Density at Site 1, D2= Density at site2 & D3= Density at site 3.

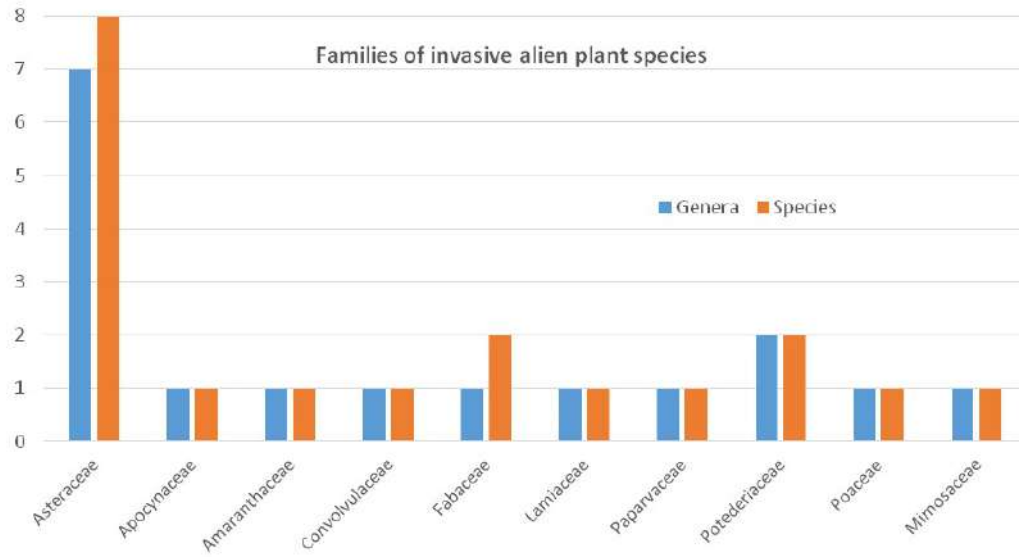

Fig. 2: Families of invasive alien plant species

The scatter plot graph of composition of different genera and species of IAPs, refers to the density of invasive alien plant species across three different sites, whereby D1, D2, and D3 corresponds to measurement across Site 1, Site 2, and Site 3, respectively. Most data points across the three sites lie at the lowest part of the y-axis. Hence, most of the species have low densities irrespective of the sites. However, a few species were high-density outliers, such as *Lantana camara,* which had a D2 value of 30.14 in Site 2, and *Imperata cylindrica*, which had a D2 value of 11.86 also in Site 2, indicating higher invasiveness in the site. The overall downward trend of the scatter plot suggests that the densities are somewhat lower in Site 3, which may reflect environmental or ecological differences among the sites. This distribution underlines the fact that, while the majority of species remain at low density across all sites, a few high-density species have to be taken care of through focused management in Site 2, where the density level is more pronounced **(Figure 3)**.

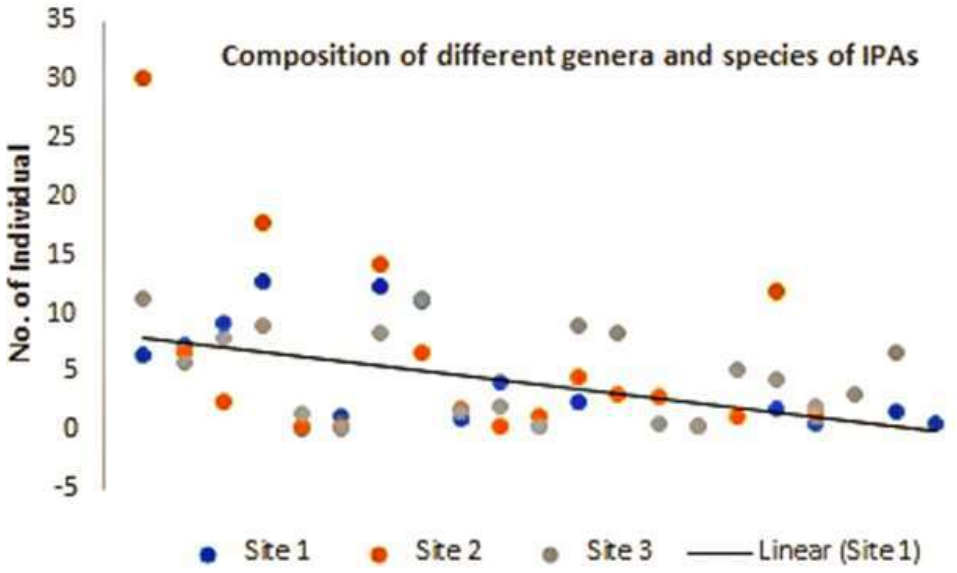

Fig. 3: Composition of different genera and species of IAPs in the study sites.

3.1 Top Dominating Invasive Plant Species

Ten plant species were identified as top dominating (IVI > 15.68) throughout all study sites based on the Importance Value Index (IVI). Of these, *Parthenium hysterophorus* had the highest importance value index (IVI) of the dominant invasive alien plant species at site 1, while *Mimosa pudica* had the lowest (2). In contrast, *Lantana camara* had the highest IVI of the dominant invasive alien plant species at site 2, while *Argemone maxicana* had the lowest (3.82). *Parthenium hysterophorus* had the highest important value index of dominating invasive alien plant species at site 3 (28.35), while *Bidens pilosa* had the lowest (2.85) (**Figure 4**). The present findings were more or less similar with the findings of [41]. Of the reported top dominating IAPs, three of them-*Lantana camara, Chromolaena odorata*, and *Eichhornia crassipes*-are listed among the top 100 invasive alien species worldwide [42].

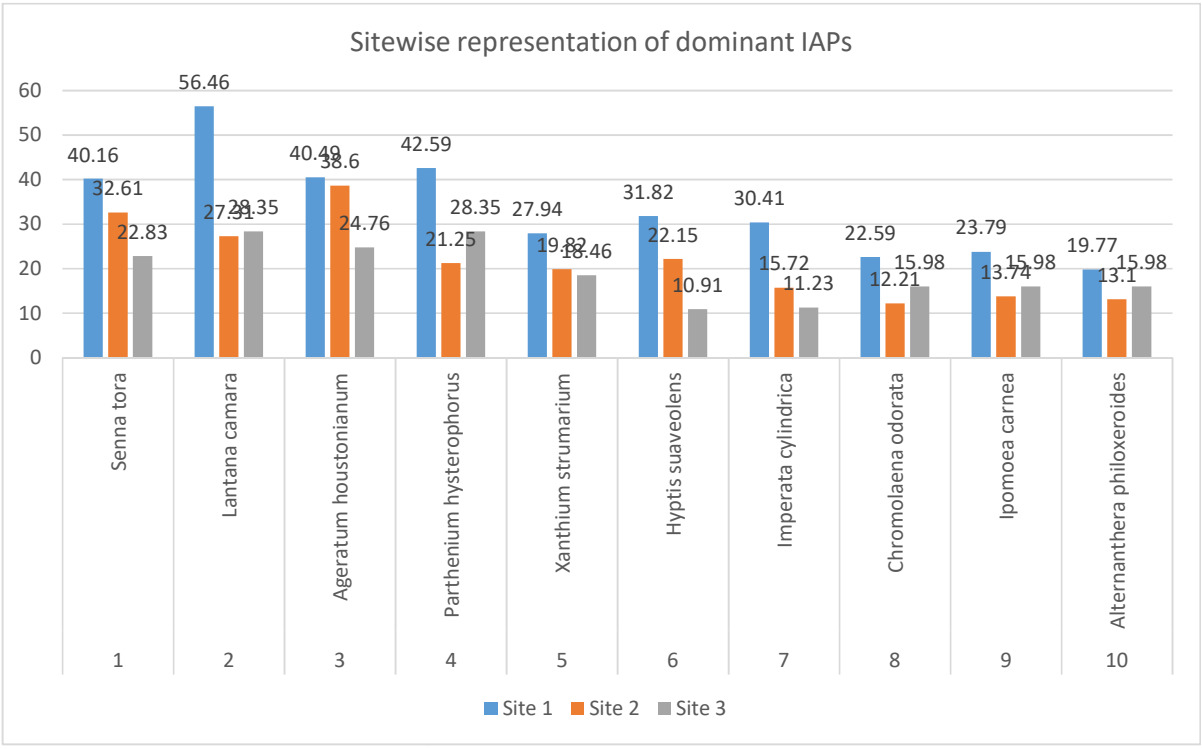

Fig. 4: Site wise representation of dominant IAPs

The plot graph (**Figure 5**) shows the average density of various the values of average density that range from close to 50 down to approximately 8, an indication of the extent different species dominates the ecosystem. The x-axis has to refer to the species index from the table, going from highest ranked in density to lowest ranked. Every point in this plot is an average density of some species, and the overall trend is captured by a downward sloping trend line. The slope in this line is steep-it reflects a very strong negative correlation; moving from the first species to the last, average density systematically drops. This is in agreement with the values in the table, which shows that *Lantana camara* has the highest average density, being 47.85, followed by *Ageratum houstonianum* with an average of 39.37, while species like *Chromolaena odorata* and *Alternanthera philoxeroides* are at the lower extreme, with densities of 11.39 and 8.17, respectively. In some ways, this hierarchy of density is reinforced by the plot and table alignment, and it would only be expected that species at the top of such a list may be more common and hence have a stronger effect on the ecosystem. This visual and numerical ranking underlines the dominance of such species as *Lantana camara* and *Ageratum houstonianum*, which can possibly have greater threats to local biodiversity because of their extensive spread. The downward trend in this plot indicates the lesser spread and perhaps lower competitive ability of the species towards the bottom, like *Alternanthera philoxeroides*.

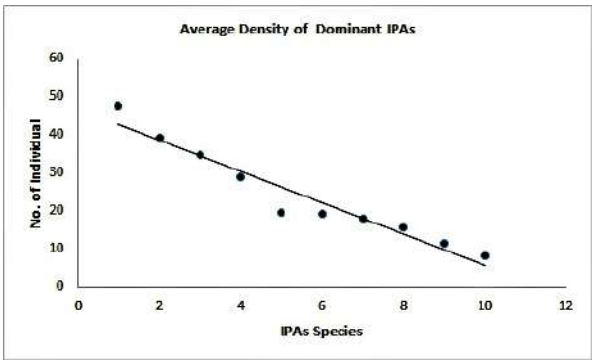

Fig. 5: Average density of dominant IAPs

3.3. Impacts of IAPS

Invasive alien plant species (IAPS) pose a substantial danger to global biodiversity by disrupting ecosystem functioning and services while also contributing to climate change. IAPS is widely recognized as the second biggest driver of biodiversity loss [43,44]. On average, IAPS diminish native plant fitness and growth by 41.7% and 22.1%, respectively, causing severe changes in local-ecosystems [14]. IAPS can also cause "invasion meltdowns," in which one invasive species promotes the invasion of another, exacerbating ecological damage [45]. These species flourish in nutrient-rich settings and changed fire regimes, which increase their dominance and damage local flora and fauna [46,47].

The repercussions of IAPS go beyond biodiversity loss. They can impair water sources and destabilize soils, causing erosion and increasing water scarcity problems [48,49]. Furthermore, top dominating invasive alien plant species. The y-axis shows IAPS might restrict water transportation and reduce recreational and tourism opportunities, causing economic losses [50]. While some IAPS may provide aesthetic and recreational benefits, they frequently degrade the ecosystems they invade, resulting in the loss of regulatory services such as biological pest control, pollination, and climate regulation, all of which are essential for agriculture and forestry [49, 51].

The effect of IAPS on human health is multifaceted. Some species, such as *Lantana camara*, are useful for repelling mosquitos [52,53]. Others, like as *Parthenium hysterophorus*, pose serious health dangers by serving as vectors for diseases like malaria and causing allergies, respiratory issues, and skin ailments. Furthermore*, Parthenium* has been shown to transmit phytoplasmas that are damaging to crops [54].

3.3 Reproductive behavior of dominant IAPs

In Nepal very few studies have been conducted on the IAPs, especially their reproductive biology, whereas in developed countries considerable literature is available on the biology of IAPs including characteristics, phenology and life cycle of many species. Only a few works on reproductive biology are available in tropical weeds [55] and temperate weeds [56,57]. The knowledge of reproductive biology is essential for proper management of IAPs.

The current study investigated the reproductive biology of dominant invasive alien plant species across sites. From which 10 species reported as dominant species of which nine terrestrial species were selected for reproductive biological analysis. One species, *Alternanthera philoxeroides,* also known as alligator weed, was not subjected to reproduction measurement in detail, as being aquatic in nature required a different methodology. So, reproductive biology of nine major IAPs identified on the basis of IVI. The seed germination was generally high above 70% in *Lantana camara, Parthenium hysterophorus*, *Senna tora*, *Hyptis suaveolens*, *Senna occidentalis* and low 30% in *Xanthium strumarium* (**Table 3**). The germination data obtained from our study were in their raw form. However, we have tried to make the data clear and valid with the support of the findings of [55,56,57] that correspond with our study. There is a correlation between the seeds and their weight. In the present study the IAPs with lighter seeds produced higher number of seeds which are believed to be a feature of soil seed banks. [58] stated that small seeds have a better chance to enter into the soil easily than the bigger ones. IAPs differ greatly in seed production, seed size, physical conditions of crop fields, competition with the crop and production level factors play important role. In the present study highest seed weight 2.40 gm was recorded in *Xanthium strumarium* species and lowest seed weight 0.03 gm in *Hyptis suaveolens* species.

Table 3: Reproductive behaviours of dominant IAPs.

Parameters	*A. houstonianum*	*Chromolaena odorata*	*Lantana camara*	*Parthenium hysterophorus*	*Senna tora*	*Senna occidentalis*	*Xanthium strumarium*	*Galinsoga quadriradiata*	*Hyptis suaveolens*
Flower colour	Blue, white, Pink	Whitish Blue	Mix red, orange, yellow or purple, white	Whitish cream like	Yellow	Yellow	Yellowish Green	Golden Yellow	Purple, blue
Agent of pollination	Insect, Butterflies	Insect	Insect, Butterflies, Bees	Wind, water, insect	Bees	Beetles	Wind	Insect	Bees
Number of seeds/fruit	40,000 seed per plant	80,000 to 90,000 per plant	1 to 20 seeds on each flower	4-5 seed per flower	20 to 40 seeds per pod	30 to 40 seeds	2 seed per fruit	7,500 seed per plant	Up to 3,000 seed per plant
Life span	Annual	Perennial	Annual	Annual	Annual	Annual or perennial	Annual	Annual	annual
Seed colour	Brown to black	Blackish	Blue black	Black	Greenish	Brown with pale band	Green yellow, Brown	Brownish black	Shiny black
Seed shape	Slender	Elongated	Rounded	Wedge shaped	Cylindrical	Flat	Oval	Cylinder or oval	Shield shaped
Seed size (mm)	0.62mm	0.03mm^2	3.233mm^2	0.04mm^2	1.987mm^2	1.573mm^2	5.85mm^2	0.13mm^2	1.02mm
10 seed weight (g)	0.014		0.18		0.15	0.18	2.40	0.033	0.03
Method of dispersal	Wind, animal, human, water	Wind	Wind, animal, bird	Wind, animal, water	Agricultural tool, animal dung, animal, water	Agricultural tools, animal, human, seed,water	Animal, human, water	Animal	Animal, human, water
Time for 1st seed to germinate (days)	3 - 5 days	7 - 9 days	3 - 4 days	6 - 7th days	7 days	8 - 14 days	7 days	9 - 10 days	10 - 12 days
Germination (%)	48 - 50	50 - 80	50 - 80	60 – 90	70 - 90	50 - 80	30 - 40	70 - 90	50 - 80
Reproductive means	Seed	Seed	Seed	Seed	Seed	Seed	Seed	Seed	Seed

4. CONCLUSION

Invasive alien plant species (IAPs) are the species of plant that are non-native, non-indigenous, exotic and foreign and or introduced to an ecosystem other than its natural home by direct or indirect involvement of humans knowingly or unknowingly. Invasive plants usually possess traits that make them effective invaders such as a short life cycle, high growth rate, and large number of seeds with good dispersal ability and good colonizing capacity. A total of 21 species were recorded in three sites of study area of which 16 species were present at site1, 18 species at site 2 and 20 species at site 3 indicate the area was suitable for invasive species. All the investigated species were belonged to 11 families. Of these the maximum importance value index of dominant plant species was recorded by *Lantana camara* (34.68) and minimum by *Alternanthera*

philoxeroides (15.68). Of the reported species *Lantana camara*, *Chromolaena odorata* and *Eichhornia crassipes* were included in world's 100 worst invasive alien plant species [42]. In the present findings, agriculture, ecosystem services, climate, human health and animal and economy were highly affected by IAPs. IAPs destroy the quality and quantity of natural scenario, soil, crops and thus cause loss in country's economy. As per the [59], management of these alien species, the Strategy has included a number of activities such as nation-wide distribution survey of five most problematic IAPS, development of atlas for the identification and early detection of invasive species, enhancement of the capacity of custom and quarantine offices, use of appropriate biological control agents, and public education and community participation.

5. Recommendations

Invasive alien species are already widespread with wide ranging ecological and socioeconomic impacts which are most likely to increase continuously in future under business-as-usual scenarios. For the proper managements would be applied to conduct initiation of biological control program, education and awareness among all stakeholders including policy makers, community participation, institution and Governance, integration with responses to other components of global environmental changes, particularly the climate change, and land use and land cover change, National Strategy of Invasive Alien Species Management. The integrated approach to IAPS management will includes long-term prevention, border phytosanitary measures, and public awareness for early infestation detection and control. Mechanical removal of the species, pesticide use, and iological means of introducing predators following rigorous risk sessments, as well as restoration of native vegetation by replanting and buffer zone formation, will be used as control approaches. IAPS demands community participation through sustainable livelihoods, and its design, implementation, and monitoring are all done with community input. Strategic management is improved by IAPS biology research, a centralized database, and policy development at all levels, including cross-border cooperation.

ACKNOWLEDGEMENTS

The authors are thankful to the Campus Chief, Siddhanath Science Campus (TU), Mahendranagar, Nepal for providing laboratory facilities. First and second authors are grateful to the Bhimdatta Municipalty for their financial support and also thankful to the friend Sagar Kunwar for his support during field visits and also thankful to the related personals for the help during data collection and analysis.

REFERENCES

[1] R. SousaP. Morais, E. Dias, C. Antunes, Biological invasions and ecosystem functioning: Time to merge. *Biological Invasions,* **13** (2011) 1055–1058.

[2] Ricciardi, R. J. Neves, J. B Rasmussen, Impending extinctions of North American freshwater mussels (Unionoida) following the zebra mussel (Dreissena polymorpha) invasion. *Journal of Animal Ecology,* **67**(4) (1998) 613–619.

[3] R.K. Kohli, K.S. Dogra, D.R. Batish, H.P. Singh, Impact of invasive plants on the structure and composition of natural vegetation of northwestern Indian Himalayas. *Weed Technology*, **18** (2004) 1296-1300.

[4] Convention on Biological Diversity. United Nations Environment Programme. Convention on Biological Diversity (CBD). Retrieved May **17** (1992) 2014, from http://www.biodiv.org

[5] M.A. Davis, J.P. Grime, K. hompson, Fluctuating resources in plant communities: A general theory of invasibility. *Journal of Ecology*, **88** (2011) 528-534.

[6] P. Pyšek, A global assessment of invasive plant impacts on resident species, communities, and ecosystems: The interaction of impact measures, invading species' traits, and environment. *Global Change Biology*, **18** (2012) 1725-1737.

[7] G. Howard, S. Matindi, *Invasive species in Africa's wetlands: Alien threats and solutions*. IUCN Eastern African Regional Program (2017).

[8] H. Dutta, Insights into the phenomenon of alien plant invasion and its synergistic interlinkage with three current ecological issues. *Journal of Asia Pacific Biodiversity*, **11(2)** (2018) 188-198.

[9] R. Early, B.A. Bradley, J.S. Dukes, J.J. Lawler, J.D. Olden, D.M. Blumenthal, P. Gonzalez, E.D. Grosholz, I. Ibañez, L.P. Miller, C.J. Sorte, Global threats from invasive alien species in the twenty-first century and national response capacities. *Nature Communications*, **7(1)** (2016) 1-9.

[10] A. Ricciardi, T.M. Blackburn, J.T. Carlton, P.E. Dick, Hulme, J.C. Iacarella, D.C. Aldridge, Invasion science: A horizon scan of emerging challenges and opportunities. *Trends in Ecology & Evolution,* **32(6)** (2017) 464–474.

[11] L. Henderson, J.R. Wilson, Changes in the composition and distribution of alien plants in South Africa: An update from the Southern African Plant Invaders Atlas. *Bothalia-African Biodiversity & Conservation*, **47(2)** (2017) 1-26.

[12] H.G. Baker, Patterns of plant invasion in North America. In H.A. Mooney & J.A. Drake (Eds.), *Ecology of biological invasions of North America and Hawaii* (1986) (pp. 44-57) Springer.

[13] J.J. Hellmann, J.E. Byers, B.G. Bierwagen, J.S.Dukes, Five potential consequences of climate change for invasive species. *Conservation Biology***, 22(3)** (2008) 534-543.

[14] M. Vilà, J.L. Espinar, M. Hejda, Ecological impacts of invasive alien plants: A meta-analysis of their effects on species, communities, and ecosystems. *Ecology Letters,* **14** (2011) 702–708.

[15] B.B. Shrestha, K.K. Shrestha, Invasions of alien plant species in Nepal: Patterns and process. In T. Pullaiah & M. R. Ielmini (Eds.), *Invasive alien species: Observations and issues from around the world*. John Wiley & Sons Ltd. (In press) (2021)

[16] B. Timsina, B.B. Shrestha, M.B. Rokaya, Z. Munzbergova, Impact of *Parthenium hysterophorus* L. invasion on plant species composition and soil properties of grassland communities in Nepal. *Flor Morphology, Distribution, Functional Ecology of Plants,* **206(3)** (2011) 233–240.

[17] R.G. Belz, C.F. Reinhardt, L.C. Foxcroft, K. Hurle, Residue allelopathy in *Parthenium hysterophorus* L.: Does parthenin play a leading role? *Crop Protection*, **26(3)** (2007) 237-245

[18] H. Rashid, M.A. Khan, A. Amin, K. Nawab, N. Hussain, P.K. Bhowmik, Effect of *Parthenium hysterophorus* L. root extracts on seed germination and growth of maize and barley. *American Journal of Plant Science and*

Biotechnology, **2(2)** (2008) 51–55.

[19] L. Khaniya, B.B. Shrestha, Forest regrowth reduces richness and abundance of invasive alien plant species in community-managed *Shorea robusta* forests of central Nepal. *Journal of Ecology and Environment*, **44(1)** (2020) 1-8.

[20] M.D. Ghimire, K. Sharma (Dhakal), D.S. Saud, Invasive alien species of Nepal. Ministry of Forest and Environment, Department of Plant Resources, Government of Nepal, (2020).

[21] S. Tiwari, B. Adhikari, M. Siwakoti, K. Subedi, *An inventory and assessment of invasive alien plant species of Nepal*. IUCN Nepal, (2005).

[22] M. Pandey, K.B. Thapa-Magar, B.S. Poudel, T.S. Davis, B.B. Shrestha, Plant invasion research in Nepal: A review of recent national trends. *Weeds – Journal of Asian Pacific Weed Science Society,* **2(2)** (2020) 16-33.

[23] A. Ebregt, P. De Greve, Buffer zones and their management (Theme Studies Series 5). *Forests, Forestry and Biological Diversity Support Group, National Reference Centre for Nature Management (EC-LNV), International Agricultural Centre (IAC)* (2020).

[24] L. Bajracharya, *Biodiversity Conservation in Buffer Zone-Problems and Opportunities: Conservation Practices, Buffer Zone Vegetation and Livelihood Needs in Pithauli VDC, Chitwan National Park, Nepal.* Unpublished master's degree dissertation. Tribhuvan University, Kathmandu, Nepal, (2009).

[25] M. Wells, K. Brandon, The principles and practice of buffer zones and local participation in biodiversity conservation. *Ambio,* **22(2/3)** (1993) 157–162.

[26] Department of National Parks and Wildlife Conservation (DNPWC). *Buffer Zone Management Rules*. Kathmandu: Department of National Parks and Wildlife Conservation, Nepal, (1996).

[27] M.J. Pulami, Introducing the idea of Border Governance for Nepal-India open border. *Journal of Political Science*, **23** (2023) 77-97.

[28] J.R.V. Prescott, *The geography of frontiers and boundaries*. London: Methuen, (1965).

[29] P. Meusburger, The impact of the Austrian-Swiss border on the economic and population structure of the two halves of the Rhine Valley. *Bulletin of the Austrian Geographical Society,* **117** (1975) 303.

[30] District Development Committee, Kanchanpur. *Fact sheet Kanchanpur information, research and publication unit* Mahendranagar, Farwest Region of Nepal, (2008).

[31] R. Misra, *Ecology workbook*. Oxford and IBH Publishing Company and Ltd, (1968).

[32] J.T. Curtis, R.P. McIntosh, An upland forest continuum in the prairie-forest border region of Wisconsin. *Ecology*, **32(3)** (1951) 476-496.

[33] L. Forman, D. Bridson, *The herbarium handbook*. Royal Botanic Gardens, Kew, (1989).

[34] H. Hara, W.T. Stearn,L.H.J. Williams, *An enumeration of the flowering plants of Nepal; a joint project of the British Museum (Natural History) and the University of Tokyo,* (Vol. 1) (1978). British Museum of Natural History.

[35] A.J. Grierson, D.J. Long, *Flora of Bhutan, including a record of plants from Sikkim*. Vol. 1, Parts 1 and 2. Royal Botanic Garden, (1983).

[36] J.R. Press, K.K. Shrestha, D.A. Sutton, *Annotated checklist of the flowering plants of Nepal*. The Natural History Museum, London, (2000).

[37] K.R. Bhattarai, I.E. Maren, S.C. Subedi, Biodiversity and invasibility: Distribution patterns of invasive plant species in the Himalayas, Nepal. *Journal of Mountain Science*, **11** (2014) 688-696.

[38] M. Siwakoti, B.B. Shrestha, An overview of legal instruments to manage invasive alien species in Nepal. In *Proceedings of the International Conference on Invasive Alien Species Management*, (2014) (pp. 25–27). Chitwan, Nepal.

[39] T. Belbase, S. Ghimire, Status of invasive alien plant species (IAPS) in Shreenagar Hill of Tansen, Palpa, Nepal. *Acta Scientific Agriculture*, **5(5)** (2021) 103-109.

[40] B.B. Shrestha, P.B. Budha, S. Pagad, L.J. Wong, Global register of introduced and invasive species - Nepal. *Invasive Species Specialist Group ISSG*, (2017)Checklist Dataset.

[41] K. Pandey, G. Paudel, A. Neupane, K.R. Acharya, S. Adhikari, Status of invasive alien plant species in urban forests of Hetauda, Nepal. *Forestry Journal of Institute of Forestry, Nepal,* **18** (2021) 107-118.

[42] S. Lowe, M. Browne, S. Boudjelas, M. DePoorter, *100 of the world's worst invasive alien species: A selection from the Global Invasive Species Database*. The Invasive Species Specialist Group (ISSG), Species Survival Commission (SSC), World Conservation Union (IUCN), (2000) New Zealand.

[43] J. Gurevitch, D.K. Padilla, Are invasive species a major cause of extinctions? *Trends in Ecology & Evolution*, 19(9) (2004) 470-474.

[44] D.F. Sax, S.D. Gaines, Species invasions and extinction: The future of native biodiversity on islands. *Proceedings of the National Academy of Sciences, **105*** (Supplement 1) (2008) 11490–11497.

[45] D. Simberloff, B. Von Holle, Positive interaction of nonindigenous species: Invasional meltdown? *Biological Invasions,* **1** (1999) 21–32.

[46] C.M. D'Antonio, P.M. Vitousek, Biological invasions by exotic grasses, the grass/fire cycle, and global change. *Annual Review of Ecology and Systematics*, **23** (1992) 63-87.

[47] J.C. Chambers, What makes Great Basin sagebrush ecosystems invasible by *Bromus tectorum*? *Ecological Monographs*, **77** (2007) 117-145.

[48] R.T. Shackleton, A.B.R. Witt, F.M. Piroris, B.W. van Wilgen, Distribution and socio-ecological impacts of the invasive alien cactus *Opuntia stricta* in eastern Africa. *Biological Invasions,* **19** (2017) 2427–2441.

[49] L. Pejchar, H.A. Mooney, Invasive species, ecosystem services, and human well-being. *Trends in Ecology & Evolution*, **24(9)** (2009) 497-504.

[50] M.E. Eiswerth, Input-output modeling, outdoor recreation, and the economic impact of weeds. *Weed Science*, **53** (2005) 130-137.

[51] R.I. Colautti, Characterized and projected costs of nonindigenous species in Canada. *Biological Invasions*, **8** (2006) 45-59.

[52] F.C. Mng'ong'o, J.J. Sambali, E. Sabas, J. Rubanga, J. Magoma, A.J. Ntamatungiro, Repellent plants provide affordable natural screening to prevent mosquito house entry in tropical rural settings: Results from a pilot efficacy study. *PLoS ONE*, **6(10)** (2011).

[53] P.K. Rai, Mercury pollution from a chloralkali source in a tropical lake and its biomagnification in aquatic biota: Link between chemical pollution, biomarkers, and human health concern. *Human and Ecological Risk Assessment: An International Journal,* **14(6)** (2008). 1318–1329.

[54] H. Cai, Evidence for the role of an invasive weed in widespread occurrence of phytoplasma diseases in diverse vegetable crops: Implications from lineage-specific molecular markers. *Crop Protection*, **89** (2016) 193-201.

[55] F.T. Shiew, A.N. Rao, Y. Wee, Reproductive biology of weeds in Singapore. *Journal of the Singapore National Academy of Science,* **17**(1988) 74–101.

[56] C.B. Thapa, P.K. Jha, Reproductive biology of four dominant weeds of paddy fields in Pokhara, Nepal. *Scientific World,* **2** (2004) 34–39.

[57] M.D. Bhatt, S.P. Singh, Reproductive biology of dominant weeds of paddy fields in upland areas of Far Western Nepal. *Geobios*, **37**(2010) 217-222.

[58] J.P. Grime, G. Manson, A.V. Curtis, J. Rodman, S.R. Band, M.A.G. Mowforth, A.M. Neal, S.A. Shaw, A comparative study of germination characteristics in a local flora. *Journal of Ecology*, **69**(1981) 1017-1059.

[59] B.B. Shrestha, (2016). Invasive alien plant species in Nepal. In P. K. Jha, M. Siwakoti, & S. Rajbhandary (Eds.), *Frontiers of Botany* (pp. 269–284). Central Department of Botany, Tribhuvan University.

Diversity, Abundance, and Threats to Birds in Bhimdatta Municipality, Kanchanpur, Nepal

Shreyashi Bista[1] Priyanka Joshi[2] Mahadev Bista[2*]

[1]National Biodiversity Strategy and Action Plan Secretariat, United Nations Development Program, Thapathali, Kathmandu
[2]Department of Zoology, Siddhanath Science campus, Mahendranagar; Kathmandu University, School of Science

Research Article

ISSN: 3059-9504 (online)
Doi: xxxx

Article History

Received: October 25, 2024
Revised: November 12, 2024
Accepted: November 20, 2024
Published: December 28, 2024

Keywords

Poaching, Avifauna, Threats, Diversity, Passeriformes, Ciconiiformes

***Corresponding author**

Email: mahadevbista2026@gmail.com (M Bsta),
Phone: + 977-984852357

ABSTRACT

The avifaunal survey was conducted in Wards 15, 18, and 19 of Bhimdatta Municipality, Kanchanpur, Nepal, from February 2022 to May 2023 using the Point Count Method. Fixed observation points were established across croplands, rangelands, and urban areas, where birds were recorded within a 50-meter radius during a 10-minute observation period at each point. Bird identification was carried out with the assistance of experts from Bird Conservation Nepal (BCN) and using the revised edition of Birds of Nepal (2022) as a reference. Data were systematically documented, including species, and threats characteristics. This study recorded 29 bird species across 11 orders and 23 families. The order Passeriformes exhibited the highest species richness, with 15 species from 11 families, followed by Galliformes and Coraciiformes, each with four species. Psittaciformes, Accipitriformes, Ciconiiformes, Pelecaniformes, and Strigiformes were the least represented orders, with only one species each. The Black-necked Stork was the sole near-threatened species identified, while the remaining 28 species were classified as least concern according to the IUCN Red List. Threats to avifauna, including habitat loss, urban expansion, and poaching, were identified through field observations and consultations with local stakeholders, emphasising the need for targeted conservation interventions.

1. INTRODUCTION

Birds play a vital role in maintaining ecological balance. The highest concentrations of bird species are found in the tropical and subtropical forests of Southeast Asia, with a gradual decline towards the poles [1]. Birds serve as reliable indicators of environmental health, influencing agricultural productivity and contributing to soil formation [2,3,4] However, global declines in avian diversity and abundance, driven by habitat destruction, climate change, and anthropogenic pressures, pose significant concerns for biodiversity conservation [5] These declines threaten avian populations and disrupt critical ecological processes, upon which both human and natural systems depend.

At a global scale, habitat loss due to deforestation, agricultural expansion, and urbanization remains the most significant driver of avian population declines [6] emerging infectious diseases, such as avian influenza and Newcastle Disease Virus (NDV), exacerbate population declines by causing substantial mortality among bird species [7].

Nepal is fortunate to harbour an extraordinary diversity of bird species. This richness is primarily attributed to the country's unique climatic and topographical variations, which have fostered the development of diverse forest ecosystems and habitats [8]. Despite its small size, Nepal's birdlife is among the richest in Asia [9], largely due to its varied physiographic zones, which support a high diversity of fauna and flora [10]. Furthermore, due to its location at the biogeographical intersection of the Palearctic and Oriental regions, it is globally recognized for its remarkable avian diversity, with approximately 892 recorded species [11]. The country's strategic location along the Central Asian migratory flyway further enhances this diversity, attracting migratory species from Siberia, China, and Southeast Asia [12]. Despite this rich biodiversity, Nepal faces considerable conservation hallenges. The country has identified 37 Important Bird and Biodiversity Areas (IBAs), with 19 located within protected areas, while the remaining IBAs lie outside formal conservation networks [13]. Among the bird species, 42 bird species are classified as globally threatened and 168 species are listed as nationally threatened, including 67 critically endangered, 39 endangered, and 62 vulnerable species [14]. Nearly one in five bird species in Nepal is considered endangered, and over 100 species are nearing extinction [15].

Habitat degradation remains the dominant threat to avian populations in Nepal, driven primarily by deforestation, agricultural intensification, and urban expansion [16, 17]. Anthropogenic activities, including infrastructure development, road construction, and dam building in wetlands, along with pollution, habitat encroachment, and degradation caused by invasive species, have significantly impacted bird habitats in forests, wetlands, grasslands, and shrublands [18]. Furthermore, food and water scarcity, overgrazing, pesticide use, and pollution from household waste, industrial discharges, and agricultural runoff are severely degrading bird habitats, posing significant threats to bird populations in Nepal [19]. Similarly, the widespread use of veterinary pharmaceuticals, such as diclofenac, has led to catastrophic declines in vulture populations due to kidney failure from consuming contaminated carcasses [20].

Although Nepal has implemented significant legislative measures, including the National Parks and Wildlife Conservation Act of 1973, enforcement challenges, outdated policies, and gaps in research and public awareness persist [21]. These issues are particularly pronounced at the local level, where anthropogenic pressures and limited conservation resources exacerbate threats to avian populations.

Bhimdatta Municipality in far-western Nepal also suffer these challenges. Its diverse forest, wetland, and grassland habitats support a wide array of resident and migratory bird species. However, anthropogenic activities, such as livestock grazing, habitat encroachment, and unsustainable

agricultural practices, have significantly impacted bird diversity and community composition [6].

This study aims to assess the diversity, abundance, and threats to bird species in Bhimdatta Municipality, Kanchanpur. By integrating field-based observations with conservation frameworks, this research seeks to inform strategies that address local conservation challenges.

2. MATERIALS AND METHODS

2.1 Study area

The present study was conducted in three wards (Ward no. 15, 18 and 19) of Bhimdatta Municipality, located in Kanchanpur District, Nepal. The municipality lies between the latitudes of 28º32' to 29º08'N and the longitudes of 80º03' to 80º33'E, covering a total area of 171.24 km². Geographically, the municipality is situated in the Terai region, although the northern part of the district features elevated terrains, with the highest point reaching approximately 1,528 meters and the lowest at around 176 meters [22]

The climate of the study area is characterized by three distinct seasons: winter, summer, and monsoon. The winter season lasts from November to February, characterized by moderate daytime temperatures and very cold nights. The summer season extends from March to June, during which temperatures can soar to a maximum of 44ºC. The monsoon season occurs from July to September, bringing significant rainfall to the region. The climate of this area is humid subtropical, with seasonal temperatures typically ranging from 10°C in winter to 30°C in summer. Average maximum temperatures reach up to 43°C in summer and drop to a low of 24°C, while winter temperatures range from a high of 19°C to a low of 2°C [23]. The area's forests predominantly consist of low tropical Shorea robusta (Sal) along with mixed hardwood species. These forests exhibit strong natural regeneration and diverse tree composition, with moisture availability varying according to changes in slope and aspect [22].

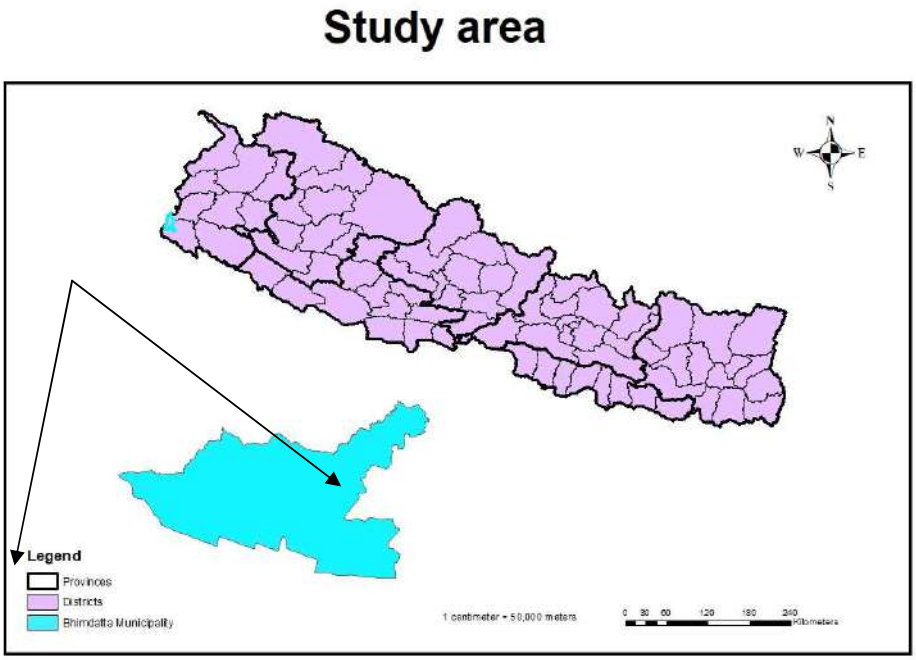

Fig. 1: Map of Bhimdatta Municipality.

2.2 Methodology

The avifaunal survey in Wards 15, 18, and 19 of Bhimdatta Municipality, Kanchanpur, Nepal, was conducted from February 2022 to May 2023 using the Point Count Method. This method involved observing and recording birds from fixed points within a 50-meter radius for 10 minutes per point, strategically covering diverse habitats like wetlands, forests, and urban areas to capture a comprehensive species inventory. Surveys were conducted in winter (February to April) and summer (May to September) to account for seasonal variations. Birds were identified with the assistance of ornithologists from Bird Conservation Nepal (BCN) and the revised edition of Birds of Nepal (2022), ensuring accurate identification. Data on species characteristics were recorded. Additionally, threats such as habitat loss, urban expansion, and poaching were identified through visual field observations that provided vital insights into the conservation needs of Bhimdatta Municipality.

2.3 Data Analysis

The data collected during the avifaunal survey was systematically entered into a Microsoft Excel spreadsheet. This process involved categorizing bird species based on their taxonomic order, family, and residential status, as well as their International Union for Conservation of Nature (IUCN) Red List status. The species composition was visualized through charts and graphs, which illustrated the proportion of species within each order and family, helping to identify the most and least dominant groups.

Qualitative data on threats from field observations were enlisted. This qualitative information was categorized into major threat types, such as habitat loss, poaching, urban development, and agricultural encroachment.

3. RESULTS AND DISCUSSION

3.1 Results: Bird Species Composition

In total, 250 individuals representing 29 bird species across 11 orders and 23 families were recorded in the study area. Among these, the order Passeriformes was the most dominant, comprising 15 species from 11 families. This was followed by four species each from the orders Galliformes and Coraciiformes, and three species from Anseriformes. In contrast, the least represented orders were Psittaciformes, Accipitriformes, Ciconiiformes, Pelecaniformes, and Strigiformes, each represented by a single species. At the family level, Passeriformes included the highest diversity, with 11 families, while Coraciiformes contributed three families. 26 of the birds were resident breeding birds, while the remaining three were winter migratory birds.

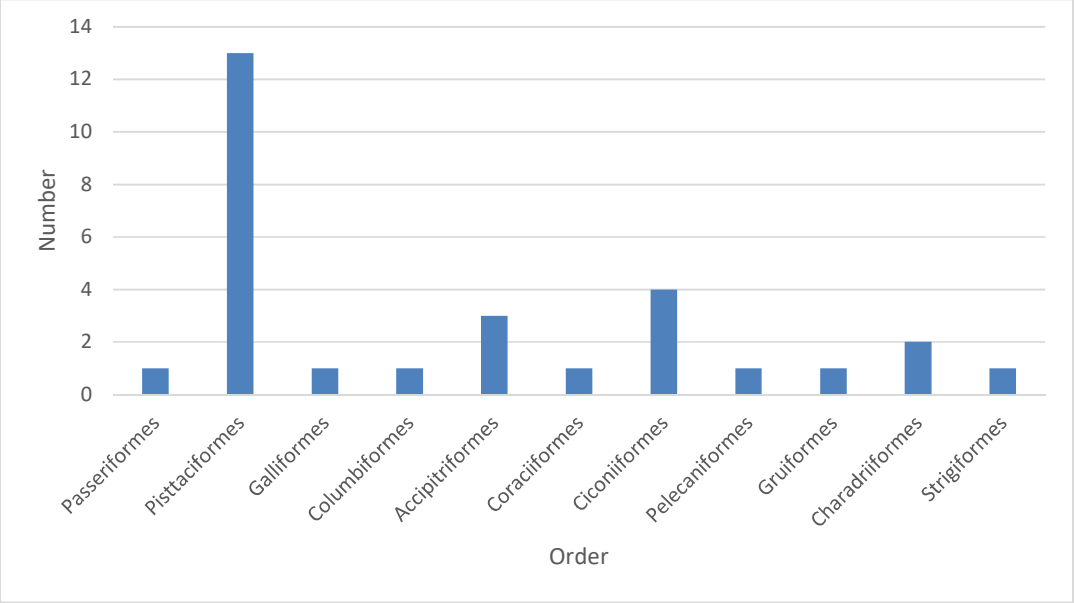

Fig. 2: Bird Species Composition based on Order

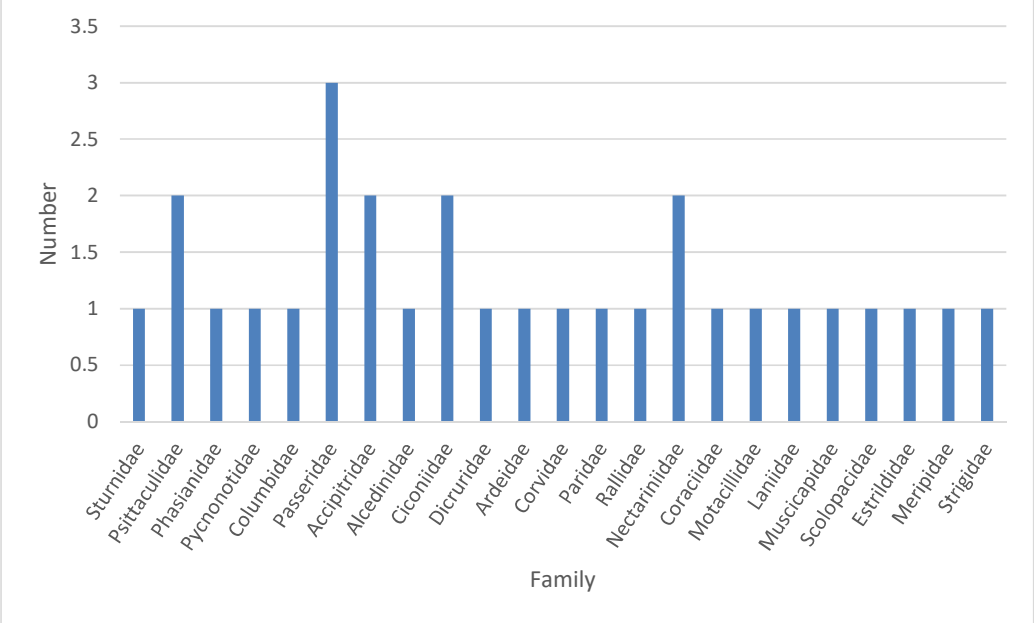

Fig. 3: Bird Species Composition based on Family.

Table 1: Checklist of birds of the Bhimdatta municipality, with their residential statusand IUCN Red List status.

SN	Name of birds	Scientific Name	Order	Family	IUCN Status	Status
1	Common Myna	*Acridotheres tristis*	Passeriformes	Sturnidae	LC	R
2	Rose-ringed parakeet	*Psittacula krameria*	Pisttaciformes	Psittaculidae	LC	R
3	Indian peafowl	*Pavo cristatus*	Galliformes	Phasianidae	LC	R
4	Red-vented bulbul	*Pycnonotuscafer*	Passeriformes	Pycnonotidae	LC	R
5	Indian pied myna/Asian pied Starling	*Gracupica contra*	Passeriformes	Sturnidae	LC	R
6	Spotted dove	*Spilopelia chinensis*	Columbiformes	Columbidae	LC	R
7	House sparrow	*Passer domesticus*	Passeriformes	Passeridae	LC	R
8	Black kite	*Milvus migrans*	Accipitriformes	Accipitridae	LC	r
9	White-throated Kingfisher	*Halcyon smyrnensis*	Coraciiformes	Alcedinidae	LC	R
10	Common pigeon	*Columba livia*	Columbiformes	Columbidae	LC	R
11	Black-necked stork	*Ephippiorhynchus asiaticus*	Ciconiiformes	Ciconiidae	NT	M
12	Black drongo	*Dicrurusmacrocercus*	Passeriformes	Dicruridae	LC	R
13	True sparrow/Eurasian sparrow tree	*Passer domesticus*	Passeriformes	Passeridae	LC	R
14	Cattle egret	*Egretta garzetta*	Pelecaniformes	Ardeidae	LC	R
15	House crow	*Corvus splendens*	Passeriformes	Corvidae	LC	R
16	Cinereous tit/ Great tit	*Parus cinereus*	Passeriformes	Paridae	LC	R
17	Common pigeon	*Columba livia*	Columbiformes	Columbidae	LC	R
18	White-breasted waterhen	*Amaurornisphoenicurus*	Gruiformes	Rallidae	LC	R
19	Purple sunbird	*Cinnyris asiaticus*	Passeriformes	Nectariniidae	LC	R
20	Pied Kingfisher	*Ceryle rudis*	Coraciiformes	Alcedinidae	LC	R
21	Indian roller	*Coracias benghalensis*	Coraciiformes	Coraciidae	LC	R
22	White wagtail	*Motacilla alba*	Passeriformes	Motacillidae	LC	M
23	Long-tailed shrike	*Lanius Schach*	Passeriformes	Laniidae	LC	R
24	Pied bush chat	*Saxicola caprata*	Passeriformes	Muscicapidae	LC	R
25	Green Sandpiper	*Tringaochropus*	Charadriiformes	Scolopacidae	LC	M
26	Scaly-breasted munia	*Lonchura punctulate*	Passeriformes	Estrildidae	LC	R
27	Grey-headed swamphen	*Porphyriopoliocephalus*	Gruiformes	Rallidae	LC	R
28	Green- Bee-eater	*Meropsorientalis*	Coraciiformes	Meripidae	LC	R
29	Spotted owlet	*Athene brama*	Strigiformes	Strigidae	LC	R

Remarks: LC= Least Concern, NT= Near threatened, R=Resident, M=Migratory

3.2 discussions

A total of 250 individual birds representing 29 species, 11 orders, and 23 families were recorded in the study area, with Passeriformes being the most abundant order. The diversity of bird species was attributed to the presence of various habitat types offering different nesting and foraging sites. The major threats to bird populations included habitat loss, deforestation, human disturbance, poaching, and land conversion for urban development.

Bird Species Composition

In this study, a total of 250 individual birds from 29 species, 11 orders, and 23 families were recorded in the study area. Passeriformes were the dominant order, both in terms of

species diversity and abundance, while Ciconiidae represented the lowest. These findings are consistent with [16], who also identified Passeriformes as the most diverse order. Similarly, Passeriformes was also found to be the dominant order in the Karra River Basin in Hetauda [8], Butwal [23], and Biratnagar [24] The dominance of Passeriformes in these areascan be attributed to similar landforms (lowlands). Passeriformes are known to frequent agricultural fields and open spaces where food sources, particularly grains, are abundant [23], and their large flocks often contribute to their success in such habitats.

The high species diversity in this region can likely be attributed to the variety of available habitats, which offer different nesting and foraging opportunities [25] Similar findings have been observed in the Khata Corridor Forest [26) and Sani Bheri Valley [27], where Passeriformes were also the dominant order. The consistent dominance of Passeriformes across these areas may be linked to similar climatic conditions and the availability of favourable breeding, feeding, and nesting sites.

Threats

The primary threats to bird populations in the study area include habitat loss, deforestation, human disturbance, hunting, poaching, and land loss due to urban development. These threats are consistent with those identified in other studies, such as those conducted in the Karra River Basin [6, 8] and Biratnagar [24] Habitat destruction, fragmentation, and degradation are particularly concerning, as they reduce the availability of critical resources for birds.

Human activities such as construction, land-use changes, and the depletion of wetlands further exacerbate these threats. However, unlike studies from the Barandabhar Corridor Forest in Chitwan [23], chemical pollution was not observed as a significant threat in the Bhimdatta municipality, possibly due to the absence of chemical industries. Despite this, disturbances from roads and other human activities have been shown to negatively impact bird diversity and abundance in similar lowland regions [28]

Moreover, factors like poaching, the overuse of pesticides, and the lack of public awareness about the importance of birds have contributed to the decline of bird populations in lowlands throughout Nepal [24]. Effective conservation efforts will need to address these threats through improved habitat protection, awareness programs, and stricter regulations on human activities that affect bird populations.

Therefore, our study strongly suggests that immediate and comprehensive conservation measures are essential to mitigate the threats to bird populations in Bhimdatta Municipality. These measures should include strengthening habitat protection, curbing deforestation, and reducing hunting and pesticide use, which are critical to ensuring the survival of local bird species. A detailed conservation action plan for these species must be developed and executed promptly. Additionally, further field-based scientific research is needed to gain a clearer understanding of the region's avifauna.

4. CONCLUSION

The exploration of bird diversity in Bhimdatta Municipality revealed that the order Passeriformes was the most dominant, followed by Galliformes and Coraciiformes. Conversely, Psittaciformes, Accipitriformes, Ciconiiformes, Pelecaniformes, and Strigiformes were the least represented. Out of the 29 bird species identified, 28 were classified as least concern according to the IUCN Red List, while only one species fell into the near-threatened category.

This study highlights the importance of understanding bird diversity and abundance in Bhimdatta Municipality, situated in the Kanchanpur District of Nepal. Despite significant conservation efforts in surrounding regions, such as Shuklaphanta National Park, there remains a notable gap in research regarding the local avian populations in semi-urban and urban areas. The research presented underscores the need for targeted studies on bird species in Bhimdatta, especially considering the ecological pressures stemming from habitat destruction, urbanisation, and climate change.

The findings contribute to the broader conservation landscape by addressing the challenges faced by threatened species in Nepal, where 38 bird species are globally threatened, and many others face local extinction risks. This study will aid local conservation authorities in better understanding the avian communities of Bhimdatta Municipality, ultimately supporting more effective management strategies and conservation actions tailored to the region's unique ecological contexts. Future research should prioritize continued monitoring, habitat restoration efforts, and the implementation of conservation measures to mitigate the threats faced by both endemic and migratory bird species in this vital part of Nepal.

AUTHOR CONTRIBUTIONS

All authors contributed to the study conception and design. Material preparation, data collection and analysis were performed by P. Joshi and S. Bista. The first draft of the manuscript was written by S. Bista and all authors commented on previous versions of the manuscript. All authors read and approved the final manuscript.

CONFLICT OF INTEREST

It is certified that all authors have contributed significantly, and all authors are in agreement with the content of the manuscript and have no conflicts of interest

ACKNOWLEDGMENTS

We express our gratitude to BCN for identification of birds**.**

REFERENCES

[1] I. Newton, (2003). Speciation and biogeography of birds. *Academic Press*, USA.

[2] J.A. Amat, A.J. Green, (2010). Waterbirds as bioindicators of environmental conditions. In C. Hurford, M. Schneider, I. Cowx (Eds.), Conservation monitoring in freshwater habitats (pp. 45–52). https://doi:10.1007/976-1-4020-9278-7_5.

[3] D. Bensizerara, H. Chenchouni, A.S. Bachir, M. Houhamdi, Ecological status interactions for assessing bird diversity in relation to a heterogeneous landscape structure. *Avian Biology Research*, **6(1)** (2013) 67–77. https://doi:10.3164/175815513X1357344603957.

[4] J.C. Morante-Filho D. Faria, An appraisal of bird-mediated ecological functions in a changing world. *Tropical Conservation Science*, **10** (2017). Doi:10.1177194008291770333 9

[5] S. Lama, Shrestha, A. Sherpa, M. Tamang, D. Ghale, Avifaunal diversity in important bird areas of western Nepal. eco.mont, **14** (2022). 70–77.

https://doi.org/10.1553/eco.mont-14-2s70.

[6] T.P. Begman, C.H. Sekercioglu, J.A. Tobias, Global patterns and predictors of bird species responses to forest fragmentation: Implications for ecosystem function and conservation. Biological Conservation, **169** (2014). 372–383. https://doi.org/10.1016/j.biocon.2013.11.024

[7] R. Napit, A. Poudel, S.M. Pradhan, P. Manandhar, S. Ghaju, A. N. Sharma, J. Joshi, S. Thapa, K. Dhital, U. Rajbhandari, A. Basnet, Schwind, R.M. Rajbhandari, D.B. Karmacharya, Newcastle disease burden in Nepal and efficacy of Tablet I2 vaccine in commercial and backyard poultry production. PLoS One, **18(3**) (2023). e0280688. https://doi.org/10.1371/journal.pone.0280688

[8] K. Parajuli, Assessment of bird diversity and abundance in Karra River Basin, Hetauda, Makawanpur. *International Research Journal of MMC*, **3(3)** (2022) 18–33. https://doi.org/10.3126/irjmmc.v3i3.48630

[9] H.S. Baral, C. Inskipp, Important bird areas in Nepal: Key sites for conservation. Bird Conservation Nepal & BirdLife International, Kathmandu & Cambridge, (2005).

[10] Y.R. Basnet, B.Tamang, B. Gautam, Bird diversity and their habitat status at Rajarani Community Forest, Bhogteny, Morang, Nepal, (2005).

[11] Bird Conservation Nepal & Department of National Parks and Wildlife Conservation (DNPWC). Birds of Nepal: An official checklist. Kathmandu, Nepal, (2022).

[12] P.K. Jha, C.K. Sharma, Status of migratory birds in Nepal: A case study of Chitwan National Park. *Journal of Indian Research*, **6(2)** (2018). 49–61.

[13] Bird Conservation Nepal (BCN). *Annual Report 2019*. Bird Conservation Nepal, Lazimpat, Kathmandu, Nepal, (2019).

[14] Bird Conservation Nepal & Department of National Parks and Wildlife Conservation (DNPWC). Birds of Nepal: An official checklist. Kathmandu, Nepal, (2018).

[15] Bird Conservation Nepal & Department of National Parks and Wildlife Conservation (DNPWC). The state of Nepal's birds 2010. Bird Conservation Nepal & Department of National Parks and Wildlife Conservation, Kathmandu, (2011).

[16] R. Grimmett, C. Inskipp, T. Inskipp, H.S. Baral, Birds of Nepal (Revised ed.). *Bloomsbury Publishing,* (2016).

[17] K. Gosai, A. Dhakal, K. Gosai, S.M Shrestha, First record of ashy minivet Pericrocotusdivaricatus in Kathmandu Valley, Nepal. *Nepalese Journal of Zoology*, **7(2)** (2023) 64–67. https://doi.org/10.3126/njz.v7i2.60812

[18] N. Pokharel, B. Bhandari, M.S. Miya, N. Phuyal, Avifaunal diversity inside and outside protected areas: A case of Sundarijal Forest and Changunarayan Forest, Kathmandu Valley, Nepal. *Nepalese Journal of Zoology*, **7(1)** (2023) 36–47. https://doi.org/10.3126/njz.v7i1.56309

[19] C. Inskipp, H.S. Baral, S. Phuyal, T.R. Bhatt, M. Khatiwada, T. Inskipp, The status of Nepal's birds: *The national red list series*. Zoological Society of London, UK, (2016). 628.

[20] T. Galligan, K. Bhusal, K. Paudel, D. Chapagain, A. Joshi, I. Chaudhary, A. Chaudhary, H.S. Baral, R. Cuthbert, R. GreenPartial recovery of critically endangered Gyps vulture populations in Nepal. Bird Conservation International**, 30** (2019) 1–16. https://doi.org/10.1017/S0959270919000169

[21] Bird Conservation Nepal & Department of National Parks and Wildlife Conservation (DNPWC). Birds of Nepal: An official checklist. Bird Conservation Nepal & Department of National Parks and Wildlife Conservation, Kathmandu, Nepal (2016).

[22] R.C. Sudhakar, S.P. Vazeed, K.V. Satish, K.R.L. Saranya, C.S. Jha, M. KrishnaQuantifying nationwide land cover and historical changes in forests of Nepal (1930-2014): Implications on forest fragmentation. *Biodiversity and Conservation*, **27** (2018) 91–107. https://doi.org/10.1007/s10531-017-1423-8

[23] J.N. Adhikari, B.P. Bhattarai, T.B. Thapa, Diversity and conservation threats of water birds in and around Barandabhar corridor forest, Chitwan, Nepal. *Journal of Natural History Museum*, **30** (2018) 164–179. https://doi.org/10.3126/jnhm.v30i0.27553

[24] P.K. Jha, B.R. Subba, Population status studies and anthropogenic impact on birds of Biratnagar Sub-Metropolis. *Our Nature*, **10(1)** (2012) 24–33.

[25] D. Adhikari, J. Adhikari, J. Khatiwada, B. Bhattarai, S. Ghimire, D. Rijal, Species composition and habitat associations of birds around Jhilmila Lake at Western Chure Landscape, Nepal. *Ornis Hungarica*, **31** (2023) 24–47. https://doi.org/10.2478/orhu-2023-0002

[26] U.K. Chaudhary, G. Kafle, H.S. Baral, Avifaunal diversity of Khata corridor forest. *Journal of Wetlands Ecology*, **2** (2009). 48–56.

[27] G. Shrestha, M.B.Shrestha, R.M. Byanju, A baseline study on the diversity of birds in the Sani Bheri River valley, Nepal. *Central Department of Environmental Science, Tribhuvan University*, Kathmandu, Nepal, **9(2)** (2021), 25–33.

[28] J. Alexander, D.A.E. Smith, Y.C. E. Smith, C.T. Downs, Drivers of fine-scale avian functional diversity with changing land use: An assessment of the effects of eco-estate housing development and management. Landscape Ecology, **34**(3) (2019) 537–549. https://doi.org/10.1007/s10980-019-00786-y

Community Knowledge, Perception and Conservation Challenges of Smooth-coated Otter (*Lutrogale perspicillata*) in Shuklaphanta National Park, Nepal

Balram Awasthi[1], Kusum Uprety[2], Purna Man Shrestha[3,4], Laxman Prasad Poudyal[5], Amar Kunwar [6]*

[1]Department of Zoology, Siddhanath Science Campus, Tribhuvan University, Mahendranagar, Nepal
[2]Central Department of Zoology, Institute of Science and Technology, Tribhuvan University, Kirtipur, Nepal
[3]Wildlife Research and Education Network, Kathmandu, Nepal
[4]IUCN Species Survival Commission, Otter Specialist Group, Rue Mauverney 28, 1196 Gland, Switzerland
[5] Nepalese Ornithological Union, Kathmandu
[6]Center for Integrative Conservation & Yunnan Key Laboratory for the Conservation on Tropical Rainforests and Asian Elephants, Xishuangbanna Tropical Botanical Garden, Chinese Academy of Sciences, Mengla, Yunnan 666303, China

Research Article

ISSN: 3059-9504 (online)
Doi: xxxx

Article History

Received: November 17, 2024
Revised: December 2, 2024
Accepted: December 8, 2024
Published: December 28, 2024

Keywords

Smooth-coated otter, buffer zones, community attitudes, conservation challenges, wetland management

***Corresponding author**

Email: amar.kwr@gmail.com (A. Kunwar)

ABSTRACT

Smooth-coated otters face increasing challenges from anthropogenic pressure, but research studies in human-dominated environments are sparse. This study aims to analyze residents' knowledge, attitudes, and practices about smooth-coated otters to guide sustainable conservation efforts and management decisions for implementing management interventions as well as policy intervention to safeguard the otter populations in the wetlands of Shuklaphanta National Park's buffer zone. Sixty-six locals from three user committees of Shuklaphanta National Park's buffer zone participated in semi-structured interviews to gain information on their livelihoods, resource consumption, awareness of otters, and conservation attitudes. Agriculture (78.7%) was the primary source of income, and a lack of information hampered conservation efforts. Fishing and livestock grazing were prominent river activities, despite concerns about declining fish populations due to overfishing and pollution. Socioeconomic challenges, such as low education levels, along with habitat degradation from overfishing, pollution, and riverbank construction, exacerbate the issues. Despite these challenges, 95% of participants supported otter conservation, considering awareness campaigns and habitat protection as their primary concerns. The community's support for otter protection is strong, but their lack of awareness of ecological complexities emphasizes the need for education. Human activities that have an impact on the river ecology demonstrate the importance of long-term management in conserving otter habitats and local resources. A strong community engagement in conservation provides a solid foundation for otter protection. Building on this positive attitude through focused education and sustainable resource management can lead to long-term conservation success for smooth-coated otters in buffer zones.

.

1. INTRODUCTION

Smooth-coated Otter, semi-aquatic mammals of the Mustelidae family, play an important role in maintaining a healthy ecosystem [1,2]. Thriving across diverse wetland habitats-rivers, ponds, marshes, and lakes—these adaptable animals contribute significantly to aquatic ecosystem stability as apex predators [3,4]. Their presence indicates a healthy, balanced ecosystem free of significant pollution [5,6]. Foraging primarily in freshwater and marine environments, otters consume a diverse diet of fish, frogs, crabs, and insects [7,8,9,10]. However, growing human encroachment has forced them to adopt nocturnal behaviors, shifting from their natural diurnal patterns to avoid human conflict [11,12]. This behavioral change reflects the pressures that human presence and activity exert on their population. Despite their resilience, otters are becoming more vulnerable to environmental changes, particularly those caused by human activity [13,2,8,14]. However, rapid infrastructure development, particularly dams and hydroelectric projects, has significantly altered their habitats. Pollution from industrial waste, including heavy metals and toxic chemicals, further threatens their survival [15,2]. Conflicts between otters and fishermen pose challenges to conservation, as otters are seen as competitors for fish, often leading to harm [16,17] (Trivedi & Variya, 2023; Shrestha et al., 2023). Overfishing and toxic fishing methods worsen food scarcity, intensifying these conflicts [1,15,16]. The smooth-coated otter is classified as Vulnerable on the IUCN Red List [18,19] and is listed under Appendix I of CITES [20]. Although it is not included in Nepal's National Park and Wildlife Conservation Act of 1973, the 2002 amendment to the Aquatic Life Protection Act enforces a nationwide ban on hunting [21]. The smooth-coated otter, once widespread in Nepal's Terai wetlands [5,6, 22], is now confined to fragmented habitats within protected areas like Koshi Tappu, Chitwan, Bardia, and Shuklaphanta. Its population has declined due to habitat loss, human disturbance, and limited protection, highlighting the urgent need for conservation efforts [5,23,24].

Local communities' knowledge of otters' behavior, habitat requirements, and ecological roles can offer valuable insights for conservation, while their perceptions—whether positive or negative—can directly influence conservation success [6, 15, 17, 23, 25,26]. Socio-economic factors largely shape local perceptions, which can range from viewing otters as valuable for ecotourism to regarding them as pests, complicating conservation efforts [27,23,15]. Despite legal protections under Nepal's Aquatic Life Protection Act (2002), minimal enforcement and illegal hunting for otter fur and body parts continue to threaten their populations [1,21].

This study builds upon [23], which offered essential insights into otter conservation in Shuklaphanta National Park. Expanding on their work, this research incorporates a more

comprehensive survey of public opinion to enhance understanding of local perceptions and uncover detailed conservation challenges, ultimately guiding more precise and effective conservation efforts This park is located amidst human settlements and agricultural areas, where human-wildlife conflict is a significant issue [28]. Although the park's rich wetland habitats are essential for otter survival, these areas are increasingly impacted by natural and human-induced threats [15,23,2]. Research in Nepal has provided valuable insights into otter conservation, but further exploration of local attitudes and socio-economic factors influencing habitat destruction and human-otter conflicts could deepen our understanding of these challenges [29,30,23]. This study explores threats to otters in Shuklaphanta and Nepal, analyzing local perceptions and socio-economic factors. It offers critical insights for policymakers, conservationists, and communities, aiding smooth-coated otter conservation amid environmental change.

2. METHODOLOGY

2.1 Study Site:Shuklaphanta National Park

Shuklaphanta National Park (hereafter - ShNP) in far western Nepal spans 305 km², encompassing grasslands, forests, wetlands, and riverbeds at elevations of 174–1,386 m (Figure 1). Renowned for its biodiversity, it supports species of conservation concern, including smooth-coated otters in areas like the Mahakali and Chaudhar rivers and wetlands such as Kalikich Tal and Rani Tal [23,15,2]. The 243 km² buffer zone of ShNP includes five urban municipalities—Bedkot, Belauri, Bhimdatta, Mahakali, and Shuklaphanta—and two rural municipalities, Beldandi and Laljhadi [28]. This study focuses on Bhimdatta, Bedkot, and Beldandi municipalities (Figure 1). The subtropical monsoonal climate features three seasons—cool-dry (September–February), hot-dry (February–June), and monsoon (June–September)—with an average annual rainfall of 1,579 mm [31]. ShNP is home to 665 plant species, 88 fish, 15 amphibians, 56 reptiles, 460 birds, and 57 mammals, including the greater one-horned rhino, fishing cat, and Asian elephant [32,33,31,2, 34].

2.2 Data Collection: Questionnaire Surveys

The survey was conducted from February to May 2022, using a mixed-methods approach that combined both qualitative and quantitative research techniques. Data were collected through a questionnaire survey. A purposive sampling method was followed since our main purpose was to elicit as much information as possible from informants [35]. A review of relevant literature, including published articles and scientific reports was done. The survey included 66 respondents, comprising residents, fishermen, and other stakeholders of the Shuklaphanta, Bedkot, and Kalikich users committee The questionnaire covered socio-economic and demographic details, river usage and fishing practices, otter sightings and ethnobiological knowledge, perceptions of otters, and potential threats based on observations. Participants were shown a picture of the Smooth-coated otter to ensure accurate identification and informed consent was obtained before the survey [17,23, 36].

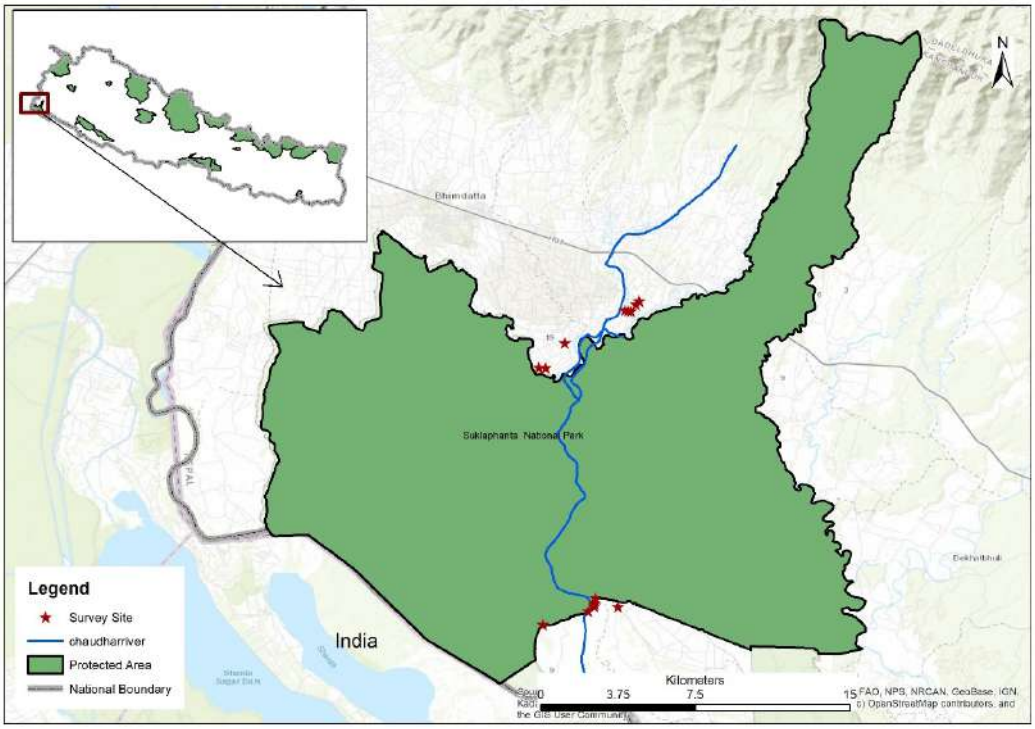

Fig. 1: Survey locations for interviews in the Buffer Zone of ShNP.

2.3 Key Informant Interview (KII) Surveys

Key Informant Interviews (KIIs) were conducted with 20 individuals deeply familiar with ShNP, including park officials, nature guides, mahouts, and National Trust for Nature Conservation (NTNC) staff offered detailed insights into wildlife behavior, conservation challenges, and management

effectiveness. Respondents highlighted issues like overfishing, human disturbance, and habitat degradation while also noting ecological changes such as shifts in biodiversity and vegetation. These insights are crucial for informed conservation planning.

Data Analysis

Data were analyzed descriptively. Additionally, logistic regression analysis to examine the relationship between age, education, and knowledge about otters was done in R version 4.4.1. The predictor variables included Age (categorized as 15-24, 25-54, 55-64, and 65+ years) and Education (treated as an ordinal variable ranging from illiterate to bachelor's degree or above).

3. RESULTS

3.1 Demographic and Socio-economic Profile of Respondents

The Shuklaphanta Buffer Zone is predominantly a farming community, with 78.78% of respondents engaged in agriculture (Table 1). The population is of Prime working age (68.18%), and educational attainment remains low, with just a small proportion completing secondary school or above. This profile depicts an urbanized area with a strong agricultural reliance and access to advanced education and diversified job options.

Table 1: Socio-demographic characteristics of the people in the Shuklaphanta Buffer Zone area.

Socio-demographic status	Category	Total	Percentage
Gender	Male	35	53.03
	Female	31	46.94
Age	Early working age (16 - 24)	7	10.60
	Prime working age (25 - 54)	45	68.18
	Mature working age (55 - 64)	3	4.54
	Elderly age group (≥ 65)	11	16.66
Occupation	Farmers	52	78.78
	Business	3	4.54
	Job	1	1.51
	Others (laborers)	7	10.60
	Students	3	4.54
Education	Illiterate (no formal education)	5	7.58
	Literate	31	46.97
	Primary level (≤ 8 class)	16	24.24
	Secondary level (9 - 12 class)	11	16.67
	Bachelor and above	3	4.54

Livelihood Dependence and Resource Use on the River Ecosystem in ShNP Buffer Zone

The river ecosystem supports the livelihoods of communities in the ShNP Buffer Zone, providing essential natural resources for livelihood. All respondents (n=66) reported that their family members visit the river for various purposes (Figure 2).

Fish Species Abundance and Taste Preferences

Fish species distribution and preferences indicate that certain species, like Rohu, are widely available and highly valued for taste, reflecting their cultural and dietary significance. Other species, while noted for abundance, are less favored for consumption, suggesting selective preferences shaped by culinary or cultural factors within the community (Table 2).

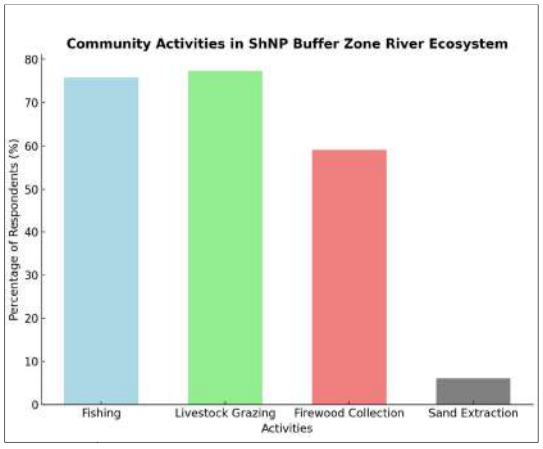

Fig. 2: Resource use in the ShNP Buffer Zone River Ecosystem

Table 2: Fish abundance and taste preferences among people in the ShNP Buffer Zone area (n= 66).

Common/Local Name	Scientific name	Abundant (%; N)	Not Abundant (%; N)	Taste Preference (%; N)	Inference
Rohu	*Labeo rohita*	66.67 (44)	33.33 (22)	48.48 (32)	Highly abundant and highly preferred
Spotted Snakehead/Geluwa	*Channa punctata*	50.00 (33)	50.00 (33)	7.56 (5)	Moderately abundant but less preferred for taste.
Spiny Eel/Bam	*Mastacembelus armatus*	33.33 (22)	66.67 (44)	-	Moderately abundant, not recognized for taste preference
Spotfin Swamp Barb/ Chocolate/Sidhra	*Puntius sophore*	30.56 (20)	69.44 (46)	-	Moderately abundant, limited culinary use
Baikha	*Pangasius pangasius*	-	100.00 (66)	12.12 (8)	Not abundant but has specific desirability
Giant freshwater prawn/Jhinge Maccha	Macrobrachium rosenbergii	-	100.00 (66)	10.60 (7)	Not abundant but has moderate appeal
Stinging Catfish/ Shingi	*Heteropneustes fossilis*	-	100.00 (66)	9.09 (6)	Not abundant but some appeal

The community employs a variety of fishing methods, with traditional techniques being widely practiced (Table 3). The major fishing methods include Hulka, Hand Catching, Pakhiya, Poison, Ghagi, Dhariya, Chiudi, Tapi, Khong, and Patta (Figure 3, Supplementary Table S1).

Table 3: Fishing methods used by respondents in the Shuklaphanta Buffer Zone area (n=66).

Fishing Methods responses	(%)
Hulka	45.45
Hand Catching	25.76
Pakhiya	25.76
Poison	7.58
Ghagi	6.06
Dhariya	4.55
Chiudi	3.03
Tapi	3.03
Khong	1.52
Patta	1.52

Over fishing and the occasional use of poison raises concerns about potential environmental impacts on river health (Table 4).

Table 4: Community-perceived challenges affecting the river ecosystem in the Shuklaphanta Buffer Zone Area (n=66).

Challenges	%
Poisoning from agricultural runoff and toxic substances	36.36
Overfishing	27.27
Pollution from washing/bathing	27.27
Habitat Degradation	24.24
Climate Factors	12.12

Fig. 3: (a) Fishing net Hulka, (b) Fishing net Tapi, (c) Fishing net Dhariya, (d) Fishing activity in the study area, (e) Animal grazing on the riverbank (f), Researcher (Ms. Kusum Uprety) with local respondents.

Community Knowledge and Perceptions of Otters

Respondents widely recognized Smooth-coated Otters, with 66.67% reporting sightings and 71.21% identifying fish as their primary diet (Table 5). Logistic regression analysis revealed that age significantly influenced otter food knowledge ($p = 0.022$). Participants in the 15-24 age group were notably less likely to possess otter food knowledge compared to the reference group (Estimate = -2.1439, $p = 0.0194$). Education, however, did not have a significant impact on otter knowledge ($p = 0.3513$).

Table 5: Respondents' perspective on smooth-coated otter ecology, cultural significance, and use (n=66).

Characteristics Question	Responses	Number	%
	Yes	40	60.60
Awareness of the otter habitats	No	13	19.69
	No Idea	13	19.71
	Decreased	31	46.96
	No response	14	21.21
Perceived status of otter population (last 10 years)	Stable	2	3.03
	No Idea	15	22.72
	Increased	4	6.06
	No	48	72.72
Identification of otter scats	Yes	6	9.09
	No response	12	18.18
	No	39	59.09
Cultural or traditional myths associated with otters	No Idea	19	28.78
	No response	8	12.12
	No	41	62.12
Medicinal value of otter body parts	No Idea	15	22.72
	No response	10	15.15
Knowledge of otter diet	Fish	47	71.21
	Insect	1	1.51
	No Idea	18	27.27

Knowledge of Otter conservation status and approaches

About Ninety-six percent of respondents expressed positive views on otters and supported their conservation, with 92 % of respondents prioritizing conservation efforts. Dynamite fishing was reported as minimal indicating limited use of this destructive practice (Table 6).

Table 6: Respondents' Perceptions of Otters (n=66): Their Role in Ecosystem Services and Conservation Significance.

Characteristic Questions	Opinion	Number	(%)
Do you appreciate the presence of otters?	Yes	63	95.46
	Neutral	3	4.55
Should efforts be made to conserve otters?	Yes	61	92.43
	Not sure	5	7.57
	No	0	0
Is dynamite fishing present in the area?	Yes	1	1.5
	No	45	68.18
	Not sure	12	18.18
	No response	8	12.12

Table 7. Key conservation challenges and suggested measures for otters based on respondents' opinions (n=66)

Conservation Challenges	**Number**	**(%)**
Road construction along the riverbank or nearby river	23	34.84
Livestock grazing	21	46.96
Extraction of sand and gravel	4	6.06
Natural habitat modifications	13	19.69
Pollution (Washing of clothes, bathing)	22	33.33
Low water in the dry season	11	16.66
Conservation Measures		
Conservation awareness	40	60.60
Habitat improvement	38	57.57
Stop poisoning and pollution	4	6.06
Stop hunting	16	24.24
Protect fish species	30	45.45
Don't know	8	12.12

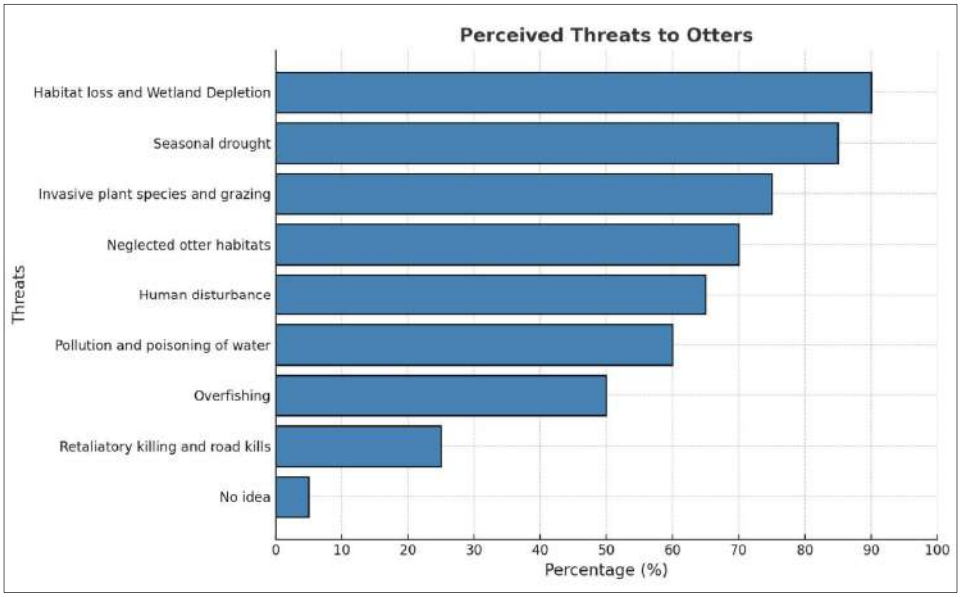

Fig. 4: Perceived Conservation Threats to Smooth-coated Otters in ShNP Buffer Zone Based on Respondent Perceptions

Conservation challenges for Smooth-coated otter

In addition to the challenges affecting the river ecosystem (Table 5), community members highlighted several challenges impacting otter conservation. Livestock grazing (46.96 %) along riverbanks appeared as the most significant threat, followed by road construction (34.84 %) near water sources and pollution (33.33 %) from washing and bathing activities (Table 7). Additional concerns include habitat modifications, seasonal water shortages, and sand and gravel extraction. A small percentage of respondents were unsure about specific conservation actions, indicating varied perspectives on effective strategies. These factors reflect human-driven pressures on otter habitats (Table 7).The major threats as identified by the community include habitat loss, wetland depletion, and seasonal water scarcity. In addition to them, invasive plant species, pollution, and several human disturbances further prioritize the importance of conservation measures (Figure 4).

3.3 DISCUSSION

The socio-demographic profile of respondents reveals communities heavily reliant on agriculture, with limited access to diverse job opportunities and advanced education, which may shape their environmental priorities. Low levels of formal education suggest low awareness of ecological issues, with the survey revealing gaps in knowledge about otters and their habitats, likely due to minimal educational background and interaction with river ecosystems. This knowledge gap could hinder effective conservation efforts, underscoring the need for targeted educational and awareness programs to enhance understanding of otter ecology and habitat requirements [7,30]. Despite these gaps, the community exhibits a strong positive attitude toward otter conservation, providing a solid foundation for conservation initiatives [23,37]. Addressing knowledge deficits and increasing awareness of otters' ecological roles will be essential for building on this goodwill and ensuring the long-term success of conservation efforts [23,37].

The river ecosystem plays a vital role in sustaining the livelihoods of the Shuklaphanta Buffer Zone community, with fishing and livestock grazing being the primary activities. This strong dependence on the river's resources for subsistence may impact both the environment and local wildlife, including otters, as increased human activity can lead to habitat degradation and resource competition [30]. Despite the community's heavy reliance on these resources, the survey revealed significant knowledge gaps regarding otters and their ecological roles [23, 38]. This limited understanding likely stems from low educational attainment and minimal exposure to environmental education, which could hinder effective conservation efforts [7,1,30].

While the community exhibits a positive attitude toward otters, our findings indicate a knowledge gap about otters among younger, more educated people, implying that ecological knowledge is not being efficiently passed down through generations [17]. Adults, particularly farmers who work closely with the environment, have better knowledge despite their lower education levels. This mismatch indicates a loss of species awareness as younger generations transition away from land-based livelihoods. To remedy this, incorporating ecological education into formal curriculum and encouraging intergenerational information exchange could assist in maintaining important conservation knowledge. Implementing educational programs to bridge these gaps could enhance the community's understanding of how their reliance on river resources intersects with otter conservation [7,30,17]. By fostering a deeper appreciation for otters' roles within the ecosystem, these initiatives could strengthen the community's support for conservation actions and encourage sustainable practices [30,17]. Leveraging the community's positive sentiment and promoting a better understanding of ecological balance will be crucial in building a foundation for sustainable resource use and successful otter conservation efforts [17,39]. The survey also identifies several environmental challenges that threaten otters. Livestock grazing and road construction along riverbanks are significant threats, as these activities can degrade otter habitats and disrupt their access to essential resources [15, 23]. Pollution from human activities further exacerbates these problems, indicating the need for improved land-use management and stricter regulations to protect river ecosystems [15].

The Shuklaphanta Buffer Zone community relies on traditional fishing methods like *Hulka* and hand-catching, which, while culturally significant, contribute to overfishing and declining fish populations, impacting both livelihoods and otter food sources [40,15]. Regional challenges, including agricultural runoff and toxic fishing practices, further threaten aquatic ecosystems [41, 42]. Low otter sightings in some areas highlight their vulnerability. Sustainable fishing, pollution control, and targeted conservation strategies are essential to protect both the river ecosystem and dependent species [43].

The results indicate that otters are a well-known fish-eating species in the ShNP Buffer Zone, with the majority of respondents reporting that they have either seen or heard about them however, poor knowledge of otter habitats and minimal cultural linkages with otters indicate a gap in our understanding of their ecological roles [44,15]. While most respondents understand that otters eat fish as their principal food source, many are unaware of other elements of otter behavior and importance. This underscores the importance of focused awareness programs to increase community knowledge and build a stronger relationship with otters as members of the local environment.

The community's strong positive attitude toward otter protection provides a solid foundation for conservation efforts [15, 23,45]. Almost all respondents showed admiration for otters, and the majority support conservation efforts, suggesting a willingness to participate in conservation operations [15]. The few reported instances of dynamite fishing, though limited, represent a highly destructive practice that adds further pressure on the environment. It is indiscriminate, harming not only fish populations but also the wider aquatic ecosystem while intensifying other threats such as pollution and habitat degradation. These positive views present an opportunity to conduct awareness campaigns that capitalize on the community's goodwill, further educate them about conservation concerns, and empower them to actively participate in safeguarding otters and their habitat [46,45].

Community members identified a variety of human-caused hazards to otter habitats, with livestock grazing and road building along riverbanks standing out as major concerns. Other issues, such as pollution from washing and bathing and habitat change, show the strain that human activities put on otter habitats. Suggested conservation methods, such as increasing habitat quality, raising awareness, and banning harmful practices, demonstrate a strong community

commitment to conservation efforts. For conservation strategies, respondents emphasized the importance of raising awareness about otter conservation and suggested habitat improvement as a key approach. Other recommendations include protecting the fishpopulation that otters depend on, enforcing hunting bans, and addressing pollution issues. These recommendations areonsistent with the need for a comprehensive conservation strategy that includes education habitat restoration, and sustainable resource management to effectively safeguard otters.

Overall, the survey highlights the importance of several approaches for otter conservation. These approaches should include efforts to restore and protect habitats, enhance community awareness and involvement in conservation activities, and enforce regulations to address environmental threats. By addressing these, it will be possible to improve the otter's habitats, safeguard fish populations, and support the long-term sustainability of local ecosystems.

4. CONCLUSION

This study highlights the complex relationship between traditional fishing practices, environmental disruptions, and human-wildlife conflicts in the region. While local communities have extensive fishing knowledge, their practices face threats from habitat degradation and illegal activities, impacting fish populations and dependent livelihoods. Addressing these issues requires integrated management strategies. The research also found low awareness of otter conservation, with key threats including overfishing, pollution, encroachment, invasive species, and illegal sand mining. Additionally, a common challenge in otter conservation is the misidentification of otters, which are often mistaken for mongooses by local communities. This confusion, coupled with negative perceptions from fish farmers, further complicates conservation efforts to support otter conservation, the study recommends habitat restoration, better riverine management, and targeted outreach to foster ommunity involvement. These efforts are essential for balancing wildlife protection with sustainable livelihoods.

ACKNOWLEDGMENT

We extend our gratitude to the Department of National Parks and Wildlife Conservation and ShNP for granting the necessary research permissions. Our appreciation also goes to Siddhanath Science Campus for their technical assistance during fieldwork. Balram Awasthi and Kusum Upreti would like to acknowledge the University Grants Commission, Nepal (SRDI-74/75-S&D-01), for funding this project. We are grateful for the invaluable support provided by Kavi Raj Bohara, and Bharat Awasthi, as well as the contributions of local respondents. Finally, we thank the reviewers for their constructive feedback, which significantly improved the manuscript.

REFERENCES

[1] P.M. Acharya, S.L. Rajbhandari, Distribution and conservation status of otters in Nepal, *Zoo Journal,* **2** (2011) 27–37.

[2] B. Awasthi, B. Banjade, N. Pandey, S. Joshi, M. Savage, P.M. Shrestha, Y.B. Rawat, P.R. Bhatt, The effects of biological water quality on the presence of the smooth-coated otter in far western Nepal, *IUCN Otter Specialist Group Bulletin,* **41** (2024).

[3] K.R. Anoop, S.A. Hussain, Factors affecting habitat selection by smooth-coated otters (*Lutra perspicillata*) in Kerala, India, *Journal of Zoology,* **263**(4) (2004) 417–423.

[4] S. Gwach, M. Koirala, P.M. Shrestha, Habitat status of the smooth-coated otter (*Lutrogale perspicillata*) in Geruwa-Khaurahi River, Bardia National Park, Nepal, *Nepal Journal of Environmental Science,* **11**(2) (2023) 23–33.

[5] P.M. Acharya, P. Lamsal, A survey for smooth-coated otter (*Lutrogale perspicillata*) on the River Narayani, Chitwan National Park, Nepal, *Hystrix, the Italian Journal of Mammology,* **21**(2) (2010) 203–207.

[6] P.M. Acharya, P. Thainiramit, K. Techato, S. Baral, N. Rimal, M. Savage, A. Campos-Arceiz, D. Neupane, Predicting the distribution and habitat suitability of the smooth-coated otter (*Lutrogale perspicillata*) in lowland Nepal, *Global Ecology and Conservation,* **46** (2023) e02578. https://doi.org/10.1016/j.gecco.2023.e02578.

[7] G. Kafle, A review on research and conservation of otters in Nepal, *IUCN Otter Specialist Group Bulletin,* **26**(1) (2009) 32–43.

[8] A. Nawab, S.A. Hussain, Factors affecting the occurrence of smooth-coated otter in aquatic systems of the Upper Gangetic Plains, India, *Aquatic Conservation: Marine and Freshwater Ecosystems,* **22**(5) (2012) 616–625. https://doi.org/10.1002/aqc.2269.

[9] M. Theng, N. Sivasothi, H.H. Tan, Diet of the smooth-coated otter (*Lutrogale perspicillata*) at natural and modified sites in Singapore, *Raffles Bulletin of Zoology,* **64** (2016) 290–301.

[10] N. Baskaran, R.S. Sundarraj, R. Sanil, Population, distribution, and diet composition of smooth-coated otter (*Lutrogale perspicillata* Geoffroy, 1826) in Hosur and Dharmapuri Forest Divisions, India, *Journal of Threatened Taxa,* **14**(1) (2022) 20469–20477.

[11] H. Kruuk, *Otters: Ecology, behavior and conservation,* Oxford University Press, 2006.

[12] S.A. Hussain, Activity pattern, behavioural activity and interspecific interaction of smooth-coated otter (*Lutrogale perspicillata*) in National Chambal Sanctuary, India, *IUCN Otter Specialist Group Bulletin,* **30**(1) (2013) 5–17.

[13] N. Tantipisanuh, W. Chutipong, A. Kamjing, U. Dachyosdee, D. Ngoprasert, Assessing effects of landscape modifications and identifying priority areas for two Asian otters in coastal wetlands, *Global Ecology and Conservation,* **48** (2023) e02760. https://doi.org/10.1016/j.gecco.2023.e02760.

[14] P. de Silva, W.A. Khan, B. Kanchanasaka, I. Reza Lubis, M.M. Feeroz, O.F. Al-Sheikhly, *Lutrogale perspicillata,* The IUCN Red List of Threatened Species 2015: e.T12427A21934884.

[15] G.K. Joshi, R. Joshi, B. Poudel, Distribution and threats to smooth-coated otters (*Lutrogale perspicillata*) in Shuklaphanta National Park, Nepal, *Journal of Threatened Taxa,* **13**(11) (2021) 19475–19483. https://doi.org/10.11609/jott.6535.13.11.19475-19483.

[16] K. Trivedi, M. Variya, Interactions between fishermen and smooth-coated otters (*Lutrogale perspicillata*) in the Tapti River of Surat District: A case study on conflict mitigation, *IUCN Otter Specialist Group Bulletin,* **40**(2) (2023) 64–71.

[17] P.M. Shrestha, S. Gwachha, S. Shrestha, A. Hamal, T.T. Tamang, B. Awasthi, S. Ghimire, R. Koju, People's perceptions of the Eurasian otter (*Lutra lutra*) conservation in Mugu District, Nepal, *OTTER, Journal of the International Otter Survival Fund,* **9**(1) (2023) 128–143.

[18] M. Khoo, S. Basak, N. Sivasothi, P.K. de Silva, I. Reza Lubis, *Lutrogale perspicillata,* The IUCN Red List of Threatened Species 2021: e.T12427A164579961. https://doi.org/10.2305/IUCN.UK.2021-3.RLTS.T12427A164579961.en.

[19] IUCN, The IUCN Red List of Threatened Species, Version 2023-1, Retrieved from https://www.iucnredlist.org.

[20] CITES, Convention on International Trade in Endangered Species of Wild Fauna and Flora, Retrieved from https://cites.org/sites/default/files/eng/app/2021/E-Appendices-2021-06-22.pdf.

[21] M. Savage, M. Shrestha, The illegal trade in otter pelts in Nepal, *TRAFFIC Bulletin,* **30**(2) (2018).

[22] P.M. Acharya, S.L. Rajbhandari, Study of smooth-coated otter (*Lutrogale perspicillata*) in Babai Valley of Bardia National Park, Report submitted to the International Otter Survival Fund (IOSF), UK, (2012) 13–19.

[23] P. Thapa, G.C.D. Bijaya, J. Bhandari, B.P. Devkota, T. Silwal, L. Can, Distribution, threats, and community perceptions of otters in Suklaphanta National Park, Nepal, *OTTER, Journal of the International Otter Survival Fund,* (2020) 128–142.

[24] R. Mishra, B.R. Lamichhane, B. Gautum, A.K. Ram, N. Subedi, Photographic evidence of smooth-coated otter (*Lutrogale perspicillata*) in Koshi Tappu Wildlife Reserve, Nepal, *IUCN Otter Specialist Group Bulletin,* **39**(4) (2022) 189–195.

[25] M.D.Y. Khoo, B.H. Lee, The urban smooth-coated otters (*Lutrogale perspicillata*) of Singapore: A review of the reasons for success, *International Zoo Yearbook,* **54**(1) (2020) 60–71. https://doi.org/10.1111/izy.12246.

[26] P.M. Acharya, Status of smooth-coated otters (*Lutrogale perspicillata* Geoffroy, 1826) in the Khauraha River of Bardia National Park, Nepal, *OTTER, The Journal of the International Otter Survival Fund,* **3** (2017) 23–37.

[27] M. Václavíková, T. Václavík, V. Kostkan, Otters vs. fishermen: Stakeholders' perceptions of otter predation and damage compensation in the Czech Republic, *Journal for Nature Conservation,* **19**(2) (2011) 95–102. https://doi.org/10.1016/j.jnc.2010.07.001.

[28] M. Bhatta, R. Joshi, Analysis of human-wildlife conflict in buffer zone area: A case study of Shuklaphanta National Park, Nepal, *Bhatta, M., & Joshi,* (2021) 28–45.

[29] A. Basnet, P. Ghimire, Y.P. Timilsina, B.S. Bist, Otter research in Asia: Trends, biases, and future directions, *Global Ecology and Conservation,* **24** (2020) e01391. https://doi.org/10.1016/j.gecco.2020.e01391.

[30] P.M. Acharya, S. Saeung, K. Techato, N. Rimal, S. Gyawali, D. Neupane, Review of environmental policies and otter conservation in Nepal, *IUCN Otter Specialist Group Bulletin,* **39**(1) (2022).

[31] L.P. Poudyal, Y.B. Rawat, D.K. Yadav, D.R. Joshi, K.R. Bohara, First report of Himalayan Goral from Nepal's Shuklaphanta National Park, *Mammal Tales,* **24** (2021) 36, 23–25.

[32] L.P. Poudyal, H. Chaudhary, Birds of Shuklaphanta National Park, *Shuklaphanta National Park Office and Nepalese Ornithological Union,* (2019).

[33] Y.B. Rawat, S. Bhattarai, L.P. Poudyal, N. Subedi, Herpetofauna of Shuklaphanta National Park, Nepal, *Journal of Threatened Taxa,* **12**(5) (2020) 15587–15611. https://doi.org/10.11609/jott.5733.12.5.15587-15611.

[34] L.R. Joshi, H.S. Baral, L.P. Poudyal, D.R. Joshi, R. Saud, C. Chand, Breeding of Indian Spotted Eagle and some new bird records for Shuklaphanta National Park, Nepal, *ZOO'S PRINT,* **39**(8) (2024) 17–20.

[35] M.D.C. Tongco, Purposive sampling as a tool for informant selection, *A Journal of Plants, People, and Applied Research,* **5** (2007) 147–158. http://hdl.handle.net/10125/227.

[36] S. Gwachha, M. Koirala, P.M. Shrestha, Habitat status of the Smooth-coated Otter (*Lutrogale perspicillata*) in Geruwa-Khaurahi River, Bardia National Park, Nepal, *Nepal Journal of Environmental Science,* **11**(2) (2023) 23–33.

[37] V. Jain, K.K. Karanth, Living alongside otters: Examining human-otter interactions and attitudes towards otters in Central India for conservation in shared landscapes, *Biodiversity and Conservation,* **32**(8) (2023) 3001–3020.

[38] S. Basak, B. Pandav, A.J. Johnson, S.A. Hussain, Resource utilisation by smooth-coated otters in the rivers of Himalayan foothills in Uttarakhand, India, *Global Ecology and Conservation,* **32** (2021) e01896.

[39] R. Kathariya, D.R. Pant, K.R. Gosai, R.P. Sapkota, M.B. Shrestha, Effects of habitat variables on the distribution of smooth-coated otters (*Lutrogale perspicillata*) along the Kauriala branch of the Karnali River, Nepal, *IUCN Otter Specialist Group Bulletin,* **40**(3) (2023).

[40] P.K. Singh, Traditional fishing gears and fishing methods used in the Koshi River Basin, *Research Journal on Multidisciplinary Issues,* **3**(1) (2021) 29–38.

[41] M.S.B. Aziz, N.A. Hasan, M.M.R. Mondol, M.M. Alam, M.M. Haque, Decline in fish species diversity due to climatic and anthropogenic factors in Hakaluki Haor, an ecologically critical wetland in northeast Bangladesh, *Heliyon,* **7**(1) (2021).

[42] T.B. Gurung, Native fish conservation in Nepal: Challenges and opportunities, *Nepalese Journal of Biosciences,* **2** (2012) 71–79.

[43] M. Meinam, Y.J. Singh, H. Bharati, T. Meinam, Importance of fish biodiversity conservation and management, *International Journal of Science and Research Archive,* **9**(2) (2023) 387–391.

[44] D. Freitas, J. Gomes, T.S. Luís, L. Madruga, C. Marques, G. Baptista, L.M. Rosalino, P. Antunes, R. Santos, M. Santos-Reis, Otters and fish farms in the Sado estuary: Ecological and socio-economic basis of a conflict, *Hydrobiologia,* **587** (2007) 51–62.

[45] A. Samal, S. Fullonton, R. Mahapatra, A. Rath, S. Pandey, K.K. Jena, First community-based conservation for smooth-coated otters in Puri, Odisha, India, *IUCN Otter Specialist Group Bulletin,* **39**(2) (2022) 59–72.

[46] S. Dey, S.K. Choudhary, S. Dey, K. Deshpande, N. Kelkar, Identifying potential causes of fish declines through local ecological knowledge of fishers in the Ganga River, eastern Bihar, India, *Fisheries Management and Ecology,* **27**(2) (2020) 140–154.

Computational evaluation on reactivity, stability, and Hirshfeld surface analysis of caffeine-maleic acid cocrystal: Insights into molecular interactions

Tirth Raj Paneru[a,b*], Basanti Bhandari[c]

[a]*Central Department of General Science, Far Western University, Kanchanpur, 10400, Nepal*
[b]*Central Department of Physics, Tribhuvan University, Kirtipur, Kathmandu, Nepal*
[c]*Baijnath Secondary School Mahendranagar Kanchanpur, Nepal*

Research Article

ISSN: 3059-9504 (online)
Doi: xxxx

Article History

Received: November 2, 2024
Revised: November 18, 2024
Accepted: November 20, 2024
Published: December 28, 2024

Keywords

Caffine-maleic acid, Cocrystal, Hirshfeld surface, Molecular electrostatic potential, QTAIM

***Corresponding author**

Email: tirthpaneru2015@gmail.com (T.R. Paneru)
Phone: +977-9845397970

ABSTRACT

This work presents a computational evaluation of the caffeine-maleic acid cocrystal using density functional theory at the B3LYP/6–311++G(d,p) level of theory to gain a comprehensive understanding of molecular interaction. The purpose of this study is to use quantum chemical calculations to assess the strength of intra- and intermolecular interactions between API caffeine and coformer maleic acid, as well as within cocrystal, to predict the superiority of chemical reactivity and stability over API caffeine. The cocrystal was optimized, and geometrical parameters were compared to those parameters of crystal structure, which showed good agreement except at the intermolecular hydrogen bonding sites. The QTAIM analysis indicated a strong intermolecular hydrogen bond H29...N8 between caffeine and maleic acid, with strength of –16.152 kcal/mol. This finding was also supported by the isosurface of the RDG scatter plot. The intermolecular hydrogen bonding interaction O...H was discovered to be significant in crystal packing, as evidenced by its 42.4% contribution to the Hirshfeld surface of the caffeine-maleic acid cocrystal. The electrostatic potential on the molecular surface of the cocrystal justified the sites H24 and O27 being proper for the nucleophilic and electrophilic attack with global maximum and minimum potential, which also support O...H intermolecular hydrogen bonding in the crystal packing of the caffeine-maleic acid cocrystal. The frontier molecular orbital energy gap in the caffeine-maleic acid cocrystal was found to be 4.018 eV, which is less than the energy gap in API caffeine, implying that the cocrystal is more reactive, polarizable, and kinetically less stable than caffeine.

1. INTRODUCTION

Cocrystals are a new type of crystalline material held together by non-ionic and non-covalent interactions and consist of two or more different molecules in a single crystal lattice in a specific ratio [1]. “Pharmaceutical cocrystals consist of at least one active pharmaceutical ingredient (API) and another non-toxic coformer that meets pharmaceutical approval” [2]. The use of pharmaceutical cocrystals in drug discovery is increasingly popular as it can enhance the stability, reactivity, bioavailability, solubility, dissolution profiles, and therapeutic effects of the drug [3]. Carboxylic acid functional groups are widely used as coformers during the formation of cocrystals in drug design discovery [4]. Conventional hydrogen bonds, including N–H…O, N–H…N, O–H…O, and O–H…N interactions, are responsible for the majority of pharmaceutical cocrystal formation [5]. Caffeine is a naturally occurring drug that stimulates the central nervous system and belongs to the methylxanthine class [6]. Caffeine is most commonly found in coffee, tea, cacao beans, dairy products, energy drinks, and chocolate [7]. Caffeine increases mental alertness, speeds up thought processes, reduces fatigue, delays sleep, and also alleviates headaches and pain [8]. Caffeine is unstable in humid environments and forms non-stoichiometric hydrates. Dicarboxylic acids were used as a cocrystal coformer to increase the stability of caffeine in the presence of humidity [9]. According to Trask *et al*., the caffeine-maleic acid cocrystal in 2:1 and 1:1 stoichiometric measurements made using solution precipitation and solid-state grinding exhibits stability concerning humidity. The binary and ternary phase diagrams of caffeine-maleic acid cocrystals in 1:1 and 2:1 ratios in solvent acetone can be used to validate stability [10]. Leyssens *et al.*, investigated the crystallization of caffeine-maleic acid in the solvent under suitable conditions through nucleation growth, resulting in the formation of a cocrystal that improved its physicochemical characteristics [11]. The study conducted by Aher *et al.* found that the molar ratio of the caffeine-maleic acid cocrystal component in solution is a crucial parameter for large solubility differences [12].

The literature reveals that researchers have reported the crystallographic structure and other experimental studies to enhance the physicochemical properties of caffeine-maleic cocrystals. The caffeine-maleic acid cocrystal is still of interest for a DFT study. Our study intends to investigate the superiority of the caffeine-maleic acid cocrystal over the active pharmaceutical ingredient (API) as caffeine and the coformer as maleic acid by performing a computational evaluation using density functional theory (DFT). This study provides insight into the intra- and intermolecular hydrogen bonding, reactive sites, reactivity, and stability of the caffeine cocrystal with maleic acid. Density functional theory is used to calculate the quantum chemical using the hybrid functional B3LYP in the basis set 6–311++G(d,p). QTAIM analysis is used to analyze the electronic structure of cocrystals using the topology of electron density. The non-covalent interactions in the molecules are visualized via RDG scatter plot. Hirshfeld surface analysis allows for the quantification of the percentage of different interactions in the molecule. The electrostatic potential surface provides a key understanding of the reactive sites of the molecule. The natural bond orbital (NBO) analysis provides a clear understanding of bonding and interactions. The energy gap between the highest occupied and lowest unoccupied molecular orbitals was used to

estimate the reactivity and stability of cocrystals over API caffeine.

2. MATERIALS AND METHODOLOGY

2.1 Computational details

The geometry optimization of the molecular structure has been done using density functional theory in the Gaussian 09 software package [13,14]. The basis set 6–311++G(d,p), which incorporates both polarization diffusion functions, was used with the hybrid functional B3LYP [15,16]. The optimized molecular structure and molecular orbitals, such as HOMO and LUMO, of the cocrystal were visualized using GaussView 05 [17]. The AIMALL software package was used to create a molecular graph depicting intra- and intermolecular interactions in the cocrystal [18]. Crystal Explorer software was used to conduct Hirshfeld surface analysis and plot fingerprints of interaction in the cocrystal [19]. The RDG plot and its isosurface in support of non-covalent interactions and electrostatic potential on the molecular surface were rendered from Multiwfn 8.0 and VMD 1.9.4 software [20,21]. The total density of state (DOS) was performed with GaussSum 3.0 software [22]. The natural bond orbital (NBO) analysis was employed for the evaluation of hyperconjugative charge transfer interactions by using the NBO 3.0 program included in the Gaussian 09 software [23].

3. RESULTS AND DISCUSSION

3.1 Geometry optimization

The crystal structure of the caffeine-maleic acid cocrystal (CCDC 272622) was obtained from the crystal structure database and optimized by using DFT in Gaussian software 09 with B3LYP/6–311++G(d,p) level of theory [24]. The optimized structure of the caffeine-maleic acid cocrystal is shown in Fig. 1. The nitrogen of the caffeine ring and the carboxylic group of maleic acid form an intermolecular hydrogen bond O–H…N to form the cocrystal of caffeine. The ground state energy of caffeine cocrystal was found to be –713143.319 kcal/mol. In contrast, the ground state energy of caffeine and maleic acid at the same level of theory were computed to be –427060.184 and –286067.634 kcal/mol, respectively. The interaction energy of the hydrogen bond was calculated by subtracting the energy sum of the cocrystal's constituents from its own energy, and it was found to be –15.501 kcal/mol. The calculated optimized structural parameters (bond lengths and bond angles) of the caffeine-maleic acid cocrystal, along with the corresponding parameters of the crystal structure, are presented in Table 1. The bond lengths C11-H12, C11-H13, C11-H14, C15-H16, C15-H17, C15-H18, C19-H20, C19-H21, C19-H22, C23-H24, C32-H33, and C34-H35 differ from the experimental value by 0.111, 0.110, 0.106, 0.111, 0.111, 0.107, 0.109, 0.109, 0.109, 0.129, 0.135, and 0.135 Å, respectively. The bond angles C1-C10-O3, N2-C19-H20, C4-N9-C11, N5-C15-H18, N9-C11-H14, H26-O25-C31, H29-O28-C36, C31-C32-H33, H33-C32-C34, and C32-C34-H35 differ from experimental values by 1.2, 1.2, 2.4, 1.9, 2.0, 1.7, 4.2, 4.2, 2.9, and 2.5˚, respectively. The main reason behind the variation of calculated data from the experimental value is that our calculation was performed in a gaseous medium. The intermolecular hydrogen bonding was not considered in gaseous medium, which plays a significant role in crystal packing.

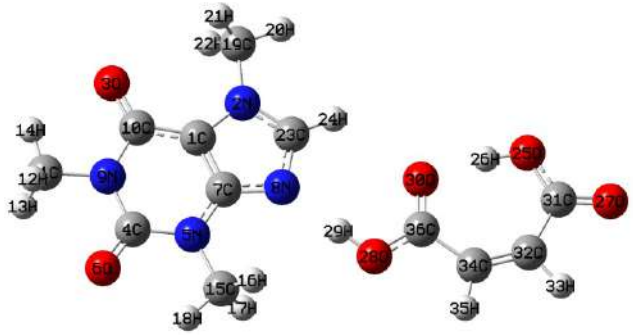

Fig. 1: The optimized structure of the caffeine-maleic acid cocrystal with numbering scheme.

Table 1. The optimized structure parameters (bond lengths and bond angles) of the caffeine-maleic acid cocrystal calculated at B3LYP/6–311++G(d,p) level of theory with the corresponding value of the experimental structure.

Bond Name	Bond length (Å)	Experimental[a]	Angle Name	Angle (^{0})	Experimental[a]
R(C1-N2)	1.388	1.390	A(N2-C1-C7)	105.5	105.7
R(C1-C7)	1.377	1.362	A(N2-C1-C10)	131.2	131.5
R(C1-C10)	1.434	1.424	A(C1-N2-C19)	126.8	127.0
R(N2-C19)	1.462	1.469	A(C1-N2-C23)	106.4	106.6
R(N2-C23)	1.345	1.327	A(C7-C1-C10)	123.2	122.7
R(O3-C10)	1.221	1.222	A(C1-C7-N5)	122.3	122.5
R(C4-N5)	1.398	1.380	A(C1-C7-N8)	110.7	110.6
R(C4-O6)	1.216	1.221	A(C1-C10-O3)	126.1	127.3
R(C4-N9)	1.407	1.399	A(C1-C10-N9)	111.2	111.6
R(N5-C7)	1.370	1.371	A(C19-N2-C23)	126.8	126.4

R(N5-C15)	1.465	1.473	A(N2-C19-H20)	108.3	109.5
R(C7-N8)	1.362	1.359	A(N2-C19-H21)	110.0	109.5
R(N8-C23)	1.336	1.342	A(N2-C19-H22)	110.0	109.5
R(N9-C10)	1.417	1.405	A(N2-C23-N8)	112.7	112.3
R(N9-C11)	1.470	1.470	A(N2-C23-H24)	123.8	123.8
R(C11-H12)	1.090	0.979	A(O3-C10-9)	122.6	121.1
R(C11-H13)	1.090	0.980	A(N5-C4-O6)	122.1	121.5
R(C11-H14)	1.086	0.980	A(N5-C4-N9)	116.9	116.8
R(C15-H16)	1.091	0.980	A(C4-N5-C7)	119.4	119.3
R(C15-H17)	1.091	0.980	A(C4-N5-C15)	119.8	119.9
R(C15-H18)	1.086	0.979	A(O6-C4-N9)	121.1	121.7
R(C19-H20)	1.089	0.980	A(C4-N9-C10)	127.0	127.0
R(C19-H21)	1.089	0.980	A(C4-N9-C11)	115.1	117.5
R(C19-H22)	1.089	0.980	A(C7-N5-C15)	120.9	120.9
R(C23-H24)	1.079	0.950	A(N5-C7-N8)	127.0	126.9
R(O25-H26)	0.991	0.987	A(N5-C15-H16)	110.1	109.5
R(O25-C31)	1.330	1.323	A(N5-C15-H17)	110.1	109.5
R(O27-C31)	1.209	1.212	A(N5-C15-H18)	107.6	109.5
R(O28-H29)	1.016	1.055	A(C7-N8-C23)	104.7	104.8
R(O28-C36)	1.317	1.286	A(N8-C23-H24)	123.5	123.9
R(O30-C36)	1.231	1.241	A(C10-N9-C11)	117.9	115.5
R(C31-C32)	1.509	1.488	A(N9-C11-H12)	109.9	109.4
R(C32-H33)	1.085	0.950	A(N9-C11-H13)	109.9	109.5
R(C32-C34)	1.343	1.329	A(N9-C11-H14)	107.5	109.5
R(C34-H35)	1.084	0.950	A(H12-C11-H13)	108.6	109.5
R(C34-C36)	1.483	1.485	A(H12-C11-H14)	110.5	109.5
R(N8-H29)	1.676	1.497	A(H13-C11-H14)	110.5	109.5
R(H26-O30)	1.626	1.529	A(H16-C15-H17)	109.2	109.5
			A(H16-C15-H18)	109.8	109.4
			A(H17-C15-H18)	109.8	109.5
			A(H20-C19-H21)	109.9	109.4
			A(H20-C19-H22)	109.9	109.5
			A(H21-C19-H22)	108.7	109.5
			A(H26-O25-C31)	111.6	109.9
			A(O25-C31-O27)	121.9	120.4
			A(O25-C31-C32)	120.2	120.0
			A(O27-C31-C32)	117.9	119.5
			A(H29-O28-C36)	110.8	115.0
			A(O28-C36-O30)	122.8	123.3
			A(O28-C36-C34)	112.1	113.4
			A(O30-C36-C34)	125.1	123.2
			A(C31-C32-H33)	109.6	113.8
			A(C31-C32-C34)	133.7	132.4
			A(H33-C32-C34)	116.7	113.8
			A(C32-C34-H35)	117.7	115.2
			A(C32-C34-C36)	128.9	129.5
			A(H35-C34-C36)	113.4	115.3

A(C7-N8-H29)	137.8	131.7
A(C23-N8-H29)	117.5	123.5
A(O25-H26-O30)	170.1	174.9
A(O28-H29-N8)	178.4	175.5
A(C36-O30-H26)	110.4	109.6

[a]Ref. [24]

3.2 QTAIM analysis

The quantum theory of atoms in molecules (QTAIM) is an analytical framework for understanding chemical bonds. It employs electron density to determine bond paths and their corresponding bond critical points [25]. The characteristics of the bond critical point (BCP) are analyzed from the electron density (ρ_{BCP}), Laplacian of electron density ($\nabla^2\rho_{BCP}$), and total electron density (H_{BCP}), the sum of kinetic electron energy density (G_{BCP}) and potential electron energy density (V_{BCP}) [26]. The interaction energy in the formation of intermolecular hydrogen bonds can also be evaluated by taking half of the potential electron energy density. The electron density from the calculation was found within the range (0.002–0.040) a.u., while the Laplacian electron density ranges (0.024–0.139) a.u., indicating that the bond critical point for the proton acceptor confirms the presence of the hydrogen bond [27]. The presence of a medium hydrogen bond that is partially covalent in nature was predicted by the Laplacian $\nabla^2\rho_{BCP} > 0$ and $H_{BCP} < 0$ values [28]. The molecular graph of the caffeine-maleic acid cocrystal with the visualization of hydrogen bond interactions is shown in Fig. 2. The topological parameters for the intra-molecular hydrogen bonds in the caffeine-maleic acid cocrystals and intermolecular hydrogen bond interactions between caffeine and maleic acid are presented in Table 2.

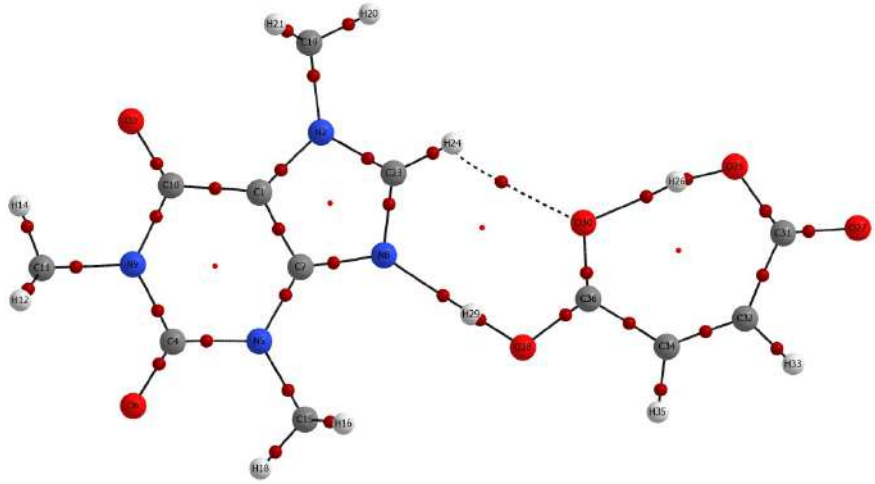

Fig. 2: The molecular graph showing intra- and intermolecular hydrogen bonding in the caffeine-maleic acid cocrystal.

Table 2. The topological parameters for the intra- and intermolecular hydrogen bonding in the caffeine-maleic acid cocrystal.

Interactions	Bond length (Å) (DFT)	Bond length (Å) in Crystal[a]	ρ_{BCP}	G_{BCP}	V_{BCP}	$\nabla^2\rho_{BCP}$	H_{BCP}	E_{int}	ε
H29…N8	1.676	1.485	0.05579	0.01307	–0.05148	0.10133	–0.03841	–16.152	0.0469
H24…O30	2.465	2.708	0.00986	–0.00131	–0.00598	0.03443	–0.00729	–1.876	0.0746
H26…O30	1.626	1.529	0.05487	0.00865	–0.05568	0.15347	–0.04703	–17.470	0.0304

ρ_{BCP}: Electron density at bond critical point (a.u), H_{BCP}: Total energy density (a.u), G_{BCP}: Kinetic energy density (a.u), E_{int}: Interaction energy (kcal/mol), V_{BCP}: Potential energy density (a.u), $\nabla^2\rho_{BCP}$: Laplacian of electron density (a.u), ε: Bond ellipticity, [a] Ref. [24]

In the caffeine-maleic acid cocrystal, two intermolecular hydrogen bonds, H29…N8 and H24…O34, were observed. The H29…N8 bond has interaction energy of –16.152 kcal/mol, indicating a strong hydrogen bond. The total interaction energy for intermolecular interaction in the formation of the caffeine-maleic acid cocrystal from QTAIM calculations was found to be –18.128 kcal/mol, which was found to be comparable to the interaction energy of –15.501 kcal/mol found from the energy difference. The strong intra-molecular hydrogen bond H26…O30 exists, which has a interaction energy of –17.470 kcal/mol. The bond length of the intermolecular hydrogen bond H29…N8 between caffeine and maleic acid calculated from DFT was 1.676 Å, and its length in crystal structure was 1.485 Å. The bond angle of the hydrogen bond from DFT calculation was found to be 178.4˚, and its corresponding value in crystal structure was 175.5˚, showing good agreement.

3.3 Non-covalent interaction

Non-covalent interactions that do not involve the exchange of electron pairs between atoms include hydrogen bonds, van der Waals forces, and electrostatic interactions in molecular complexes based on electron density and its derivatives [29]. In our study, the non-covalent interactions were visualized and illustrated with the aid of the RDG scatter plot and its isosurface. The value of RDG is determined by the following relation [30]:

$$RDG(r) = \frac{1}{2(3\pi^2)^{\frac{1}{3}}} \frac{|\nabla\rho(r)|}{\rho(r)^{\frac{4}{3}}}$$

In the relation, $\rho(r)$ is the electron density and $\nabla\rho(r)$ represents the gradient of electron density. The graph plotted between the RDG value and sign$\lambda_2(\rho)$ distinguishes different interactions, among them: green spikes stand for van der Waals interactions, red spikes for steric repulsion, and blue spikes represent hydrogen bond interactions [31]. The RDG scatter plot and its isosurface with the visualization of non-covalent interactions in caffeine-maleic acid cocrystals are shown in Fig. 3. (a) and (b) respectively. In the RDG scatter graph, blue color spikes are observed between –0.03 and –0.05 a.u. This indicates a strong intermolecular hydrogen bond between N8 and H29, as well as an intra-molecular hydrogen bond between H26 and O30. These bonds are also seen in the molecular graph from the AIM study. The red color spikes, which are indicative of steric repulsion and are particularly noticeable in the caffeine ring, appear between 0.02 and 0.05 a.u. The hydrogen of the methyl moieties and the oxygen of the caffeine ring were found to be attracted to each other by a weak van der Waals force.

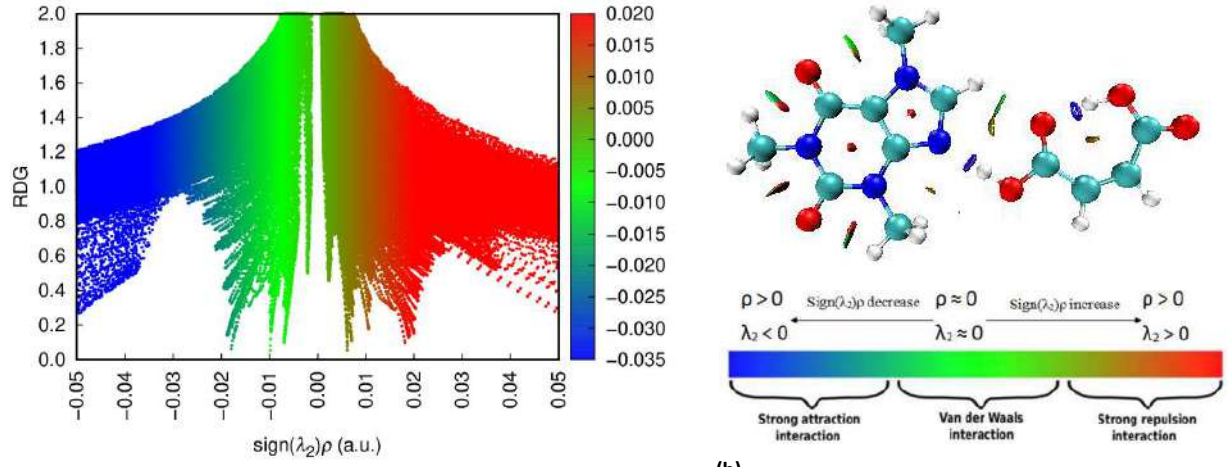

(a) (b)

Fig. 3: (a) The RDG scatter plot and (b) isosurface showing non-covalent interactions in the caffeine-maleic acid cocrystal.

3.4 Hirshfeld surface analysis

The intermolecular interactions within a crystal structure can be quantitatively described and visualized through Hirshfeld surface analysis [32]. To analyze intermolecular interactions, we used the Hirshfeld surface mapped over d_{norm} and two-dimensional finger plots. The distance between the Hirshfeld surface and the interior atom is di, and the distance between the Hirshfeld surface and the exterior atom is d_e. The normalized distance d_{norm} measures the proximity of an atom from the Hirshfeld surface to another atom in the crystal structure when compared to the sum of their van der Waals radii, which is given by the relation [33].

$$d_{norm} = \frac{d_{i-r_i^{vdw}}}{r_i^{vdw}} + \frac{d_{e-r_e^{vdw}}}{r_e^{vdw}}$$

Where, r_i^{vdw} and r_e^{vdw} stands for the van der Waals radii. HS plotted mapped over d_{norm} and shape-index of crystal surface is shown in Fig. 4 (a) and (b), respectively. If $d_{norm} < 0$, then the distance between surface points and nearby atoms is shorter than the sum of van der Waals radii; hence, they make strong intermolecular interactions represented by the red spots for the H-bond donors and acceptors on the Hirshfeld surface. The blue regions of the Hirshfeld surface show $d_{norm} > 0$, and white regions have $d_{norm} = 0$ [34]. Van der Waals interactions are indicated by the white regions of the Hirshfeld surface, while no interactions are observed in the blue regions. The red spot visualized in the HS of the molecule is for the strong intermolecular interaction C–H…O. The presence of red and blue triangles on the shape-indexed surface of the Hirshfeld surface indicates the presence of π–π stacking in the cocrystal [35]. There are noticeable peaks in the region of nearly 2.2 Å < d_e+d_i < 3.3 Å in the fingerprint plots shown in Fig. 5. The O…H interaction at d_e+d_i = 2.2 Å produced the most prominent long spikes, which provide the highest contribution of 42.4% to the total Hirsfeld surface. The wide and scattered large region of the finger plot covered by H…H interaction is due to the higher number of atoms, which contributed 31.8% to the Hirshfeld surface with tips at d_e+d_i = 2.4 Å. The C…C contact results from π–π stacking, with triangle-shaped tips at d_e+d_i = 3.3 Å, contributing 5.5% to the Hirshfeld surface. The contributions from C…H and N…H interactions to the Hirshfeld surface are 5.9% and 4.1%, respectively. This indicates that O…H interactions play a significant role in crystal packing.

3.5 Electrostatic potential (ESP) surface analysis

The electrostatic potential on the molecular surface provides insight into intermolecular interactions in conjunction with molecular properties, including biological activity [36]. It aids in the prediction of electrophiles and nucleophiles by identifying the molecule's reactive sites. The most positive potential region of the molecular surface, highlighted in blue corresponds to electrophile, while the most negative potential region, highlighted in red belongs to a nucleophile. The electrostatic potential rises in the order of red, orange, yellow, green, and blue [37]. On the molecular electrostatic potential surface, the blue dot corresponds to the lowest potential and the orange dot to the highest potential [38]. The electrostatic potential surface for the caffeine-maleic acid cocrystal is shown in Fig. 6. The hydrogen atom in the methyl group is in the blue color region and has a positive electrostatic potential, which allows it to act as an electrophile. In contrast, the oxygen atoms of maleic acid and caffeine are in the red color

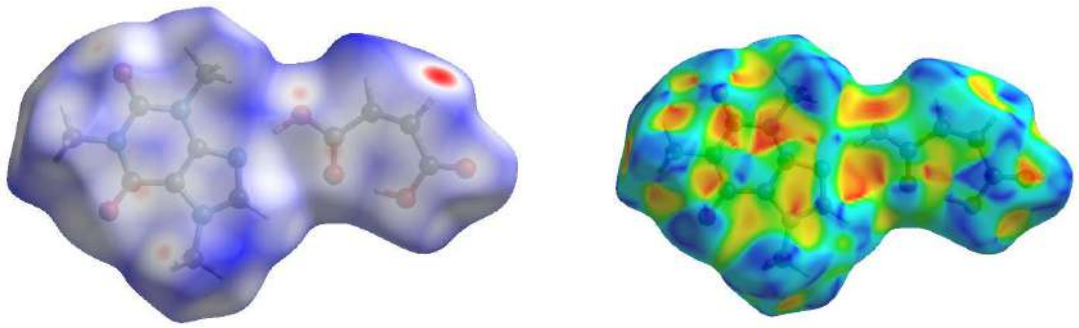

(a) d_{norm} **(b) Shape-index**

Fig. 4: Hirshfeld surfaces mapped with (a) d_{norm} and (b) shape-index

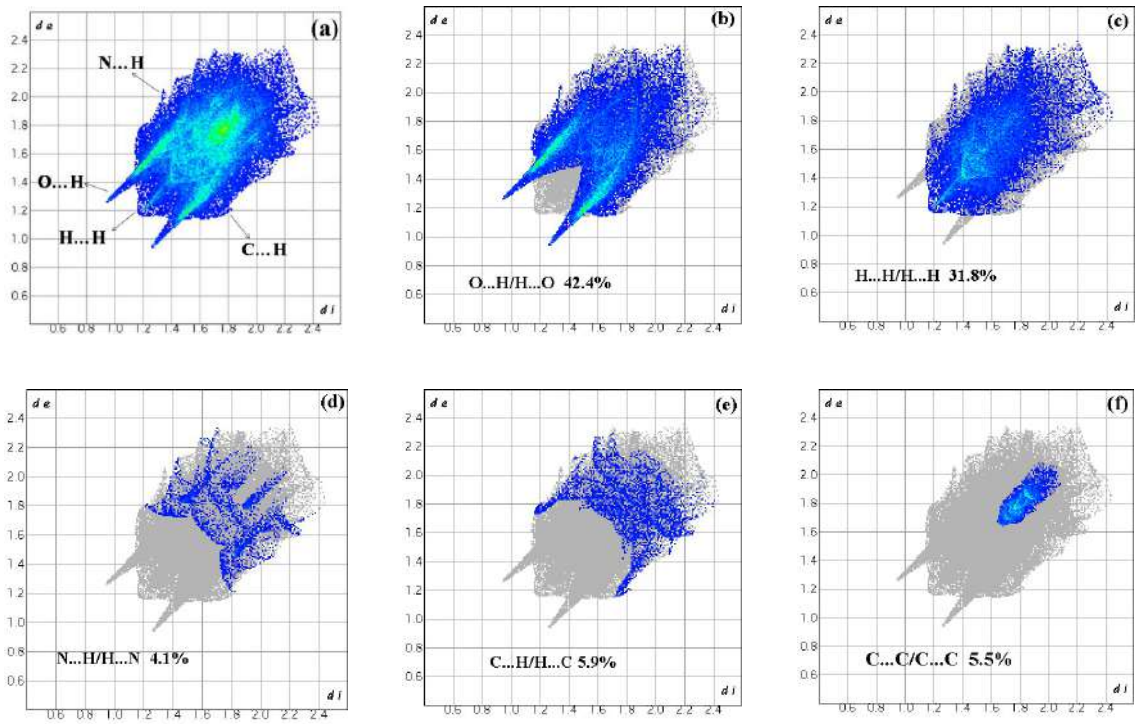

Fig. 5: The fingerprint plots: (a) For overall interactions, (b) For O…H/H…O interaction, (c) For H…H/H…H interaction (d) For N…H/H…N interaction, (e) For C…H/H…C interaction, and (e) For C…C/C…C interaction.

color region and possess a negative electrostatic potential, enabling them to function as nucleophiles. With negative potentials of –27.08, –30.15, and –44.85 kcal/mol, the atoms O3, O6, and O27 have been identified to be nucleophiles; O27 has the global minimum potential, indicating that it is the strong nucleophile. The hydrogen atoms H20, H22, H24, and H35 have positive electrostatic potentials of 26.03, 25.96, 37.63, and 25.65 kcal/mol, with H24 being the strongest electrophile among them, exhibiting the highest potential. The global minimum potential seen on O27 and maximum potential on H24 indicate that they are the probable sites of electrophilic and nucleophilic attack, respectively, which may form strong intermolecular hydrogen bonding for the crystal packing. This may lead to the conclusion that O...H interaction may be significant in the crystal packing of the caffeine-maleic acid cocrystal which was also revealed from the Hirshfeld surface analysis.

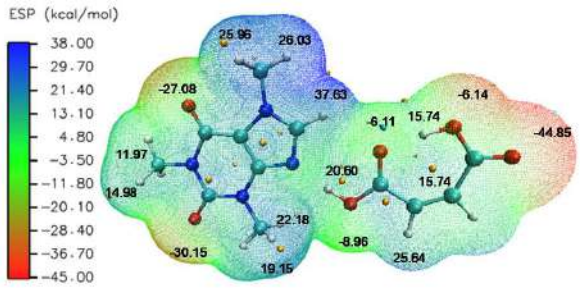

Fig.6. ESP mapped molecular vdW surface for the caffeine-maleic acid cocrystal.

3.6 Frontier molecular orbital and density of state

The frontier molecular orbital (FMO) model provides insight into the structure and reactivity of molecules by depicting the highest occupied molecular orbital (HOMO) and lowest unoccupied molecular orbital (LUMO) [39]. The energy gap

between HOMO and LUMO is used to predict molecular reactivity and kinetic stability. A molecule with a small energy gap is considered soft because it is more polarizable, which increases chemical reactivity [40]. The excitation of an electron from the valence band to the conduction band was revealed by a density of states. The HOMO–LUMO plot and DOS spectrum created with a full width at half maximum of 0.3 eV for the caffeine-maleic acid cocrystal are shown in Fig. 7. Caffeine-maleic acid cocrystals have an energy gap of 4.018 eV in gas and 3.670 eV in solvent water, indicating that it is more reactive and polarizable in solvent water than in gas. The HOMO–LUMO energy gap was found to be identical to the energy gap in the DOS spectrum. Rijal *et al.* calculated the energy gap between HOMO and LUMO for caffeine in the gaseous medium in solvent water at the B3LYP/6–311++G(d,p) level of theory. They found that the energy gap in the gaseous medium is 5.04 eV and 5.08 eV in solvent water [7]. From this observation, we conclude that the caffeine-maleic acid cocrystal is more reactive, and more polarizable but kinetically less stable than the active pharmaceutical ingredient (API) caffeine. This leads to the conclusion that the physicochemical properties of the caffeine-maleic acid cocrystal were superior to those of API caffeine in terms of reactivity. In the Density of States (DOS) spectrum, a high-intensity peak indicates the presence of multiple states at various energy levels. The red and blue lines are attributed to the lowest unoccupied molecular orbital (LUMO) and the highest occupied molecular orbital (HOMO), respectively. The virtual orbital is associated with the acceptor orbital, while the occupied orbitals are considered donor orbitals.

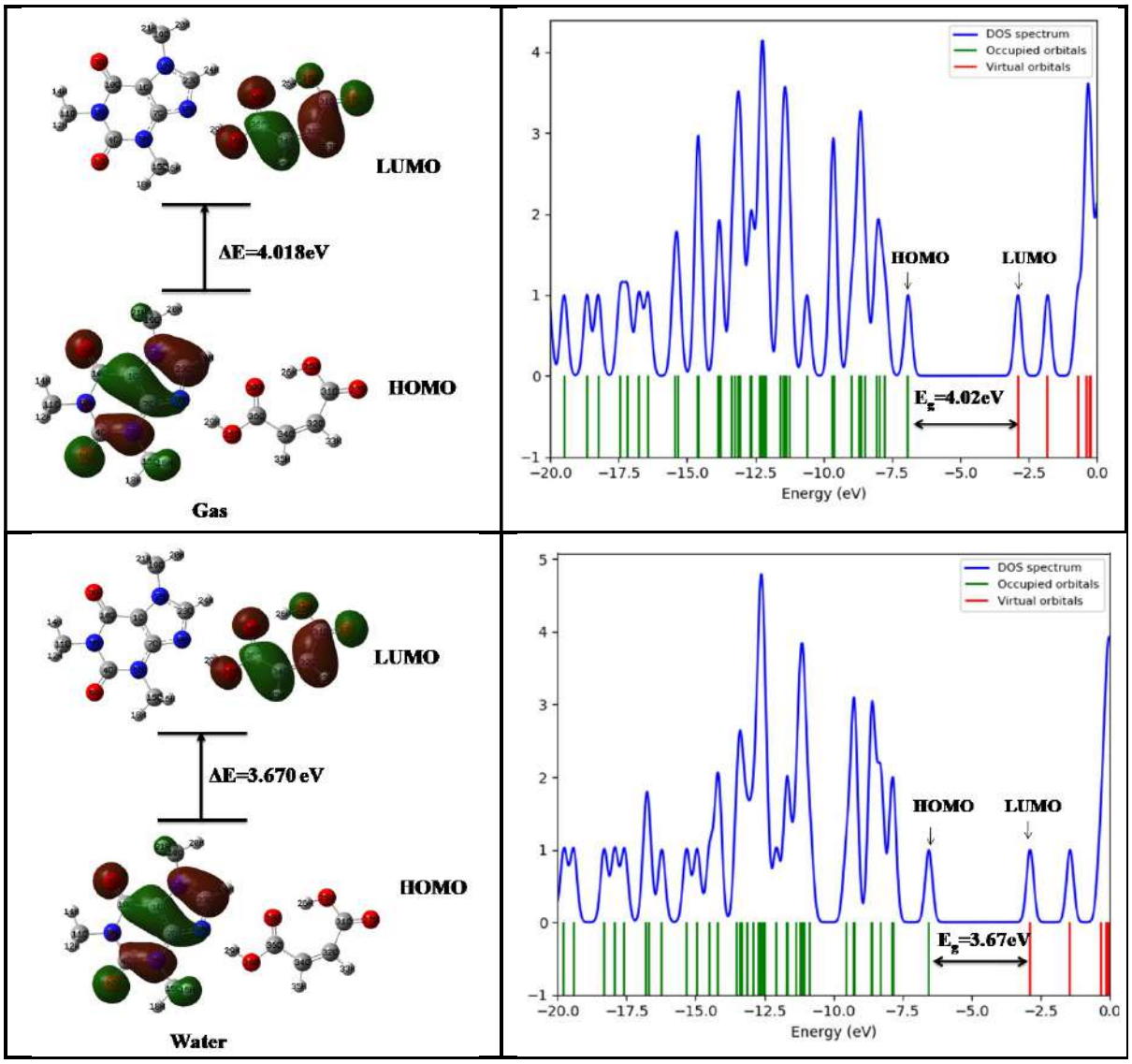

Fig. 7: HOMO–LUMO plots and DOS spectrum for the caffeine-maleic acid cocrystal in the gaseous medium and in solvent water.

3.7 Global reactivity descriptors

The global reactivity descriptors are chemical parameters used to predict chemical behavior, such as electrophilicity, nucleophilicity, reactivity, stability, and other reaction mechanism-related factors. The Koopman theorem suggests that the ionization potential is the energy associated with HOMO, while the electron affinity is the energy associated with LUMO [41]. The following relations provide the reactivity descriptors electronegativity (χ), chemical potential (μ), global hardness (η), softness (S), and electrophilicity index (ω)

in terms of ionization potential (I) and electron affinity (A) [42,43].

$$\text{Electronegativity } (\chi) = \frac{1}{2}(\mathrm{I} + \mathrm{A})$$

$$\text{Chemical Potential } (\mu) = -\chi = -\frac{1}{2}(\mathrm{I} + \mathrm{A})$$

$$\text{Global Hardness } (\eta) = \frac{1}{2}(\mathrm{I} - \mathrm{A})$$

$$\text{Softness}(\mathrm{S}) = \frac{1}{2\eta}$$

$$\text{Global Electrophilicity index}(\omega) = \frac{\mu^2}{2\eta}$$

The global reactivity descriptors for the caffeine-maleic acid cocrystal are displayed in Table 3. The electrophilicity index measures the tendency of a system to attract electrons from nucleophiles. The chemical potential and electrophilicity index of the caffeine-maleic acid cocrystal are higher in solvent water as compared to that in gaseous medium, indicating that it is a good electrophile in solvent. The ionization potential in the gaseous medium is higher than in solvent water, indicating that this cocrystal is a good electron acceptor in a gaseous medium. The global hardness in gaseous medium is higher and softness is lower as compared to that in solvent water, which confirms that caffeine-maleic acid cocrystal is softer, polarizable, and reactive in solvent as compared to that in gaseous medium. The energy gap of the caffeine-maleic acid cocrystal in solvent water was found to be lower than that in gaseous medium; due to this, it is easier to donate an electron from HOMO to LUMO in solvent, and its chemical reactivity increases in water. The reason for the increase in reactivity in solvent water is that water facilitates the flow of charge.

Table. 3: Global reactivity descriptors for the caffeine-maleic acid cocrystal.

Medium	I(eV)	A(eV)	(I– A)(eV)	χ(eV)	μ(eV)	η(eV)	S(eV^{-1})	ω(eV)	ΔNmax
Gaseous	6.9050	2.8870	4.0180	4.8960	–4.8960	2.0090	0.2489	5.9659	2.4370
Water	6.5440	2.8740	3.6700	4.7090	–4.7090	1.8350	0.2725	6.0421	2.5662

3.8 Natural bond orbital analysis

Natural bond orbital analysis is a reliable method for studying electron donor-acceptor charge transfer and conjugative interactions to gain insight into intra- and intermolecular bonding interactions [44]. The stabilization energy E(2) resulting from the interaction between electron donor and acceptor orbitals measures the intensity of that interaction. The donor and acceptor orbitals interact more strongly as the stabilizing energy increases [45]. In our study, NBO analysis was performed at the B3LYP/6–311++G(d,p) level of theory, and Table 4 shows the stabilization energy, as well as the donor and acceptor bonding interactions. The interactions LP(1)N2→π*(N8-C23), LP(1)N5→π*(C4-O6), LP(1)N9→π*(C4-O6), and LP(1)N9→π*(O3-C10) within caffeine have stabilization energies of 67.01, 55.32, 55.72, and 52.28 kcal/mol, and the interactions LP(2)O25→π*(O27-C31) and LP(2)O28→π*(O30-C36) within maleic acid have stabilization energies of 51.21 and 59.69 kcal/mol. These interactions indicate that the caffeine-maleic acid cocrystal has stabilized, as evidenced by higher stabilization energy values. The intermolecular interaction for the hydrogen bonding between API caffeine and coformer maleic acid is represented by the interaction LP(1)N8→π*(O28-H29), which exhibits strong hydrogen bonding with a stabilization energy of 37.25 kcal/mol.

Table 4. NBO of the caffeine-maleic acid cocrystal by the analysis of second-order perturbation theory analysis of Fock matrix calculated at B3LYP/6–311++G(d,p) level of theory.

Donor NBO(i)1	ED (i)/e	Acceptor NBO(j)2	ED(j)/e	E(2)[a] kcal/moln3	E(j)-E(i)[b]n4	Co F(i,j)[c]a.u
Within caffeine						
π(C1-C7)	1.730	π*(O3-C10)	0.351	28.00	0.30	0.083
π(C1-C7)	1.730	π*(N8-C23)	0.455	12.58	0.25	0.053
σ(N8-C23)	1.980	σ*(N5-C7)	0.037	7.09	1.29	0.086
π(N8-C23)	1.839	π*(C1-C7)	0.421	26.19	0.34	0.090
LP(1)N2	1.524	π*(N8-C23)	0.455	67.01	0.25	0.116
LP(1)N2	1.524	π*(C1-C7)	0.421	29.59	0.29	0.084
LP(2)O3	1.855	σ*(N9-C10)	0.097	28.53	0.64	0.122
LP(2)O3	1.855	σ*(C1-C10)	0.056	17.23	0.74	0.103
LP(1)N5	1.637	π*(C4-O6)	0.372	55.32	0.27	0.110
LP(1)N5	1.637	π*(C1-C7)	0.421	49.09	0.28	0.106
LP(2)O6	1.840	σ*(C4-N9)	0.084	26.10	0.64	0.118
LP(2)O6	1.840	σ*(C4-N5)	0.084	25.74	0.65	0.118
LP(1)N9	1.863	π*(C4-O6)	0.372	55.72	0.27	0.109
LP(1)N9	1.626	π*(O3-C10)	0.351	52.28	0.27	0.107
Caffeine to maleic acid						
LP(1)N8	1,863	σ*(O28-H29)		37.25	0.78	0.154

Within maleic acid						
π(O27-C31)	1.966	π*(C32-C34)	0.049	6.91	0.39	0.046
σ(C32-H33)	1.972	σ*(C34-C36)	0.058	6.99	0.93	0.072
π(C32-C34)	1.871	π*(O30-C36)	0.309	19.00	0.28	0.068
π(C32-C34)	1.871	π*(O27-C31)	0.246	12.04	0.32	0.057
LP(2)O27	1.860	σ*(C31-C32)	0.074	18.49	0.63	0.098
LP(2)O25	1.788	π*(O27-C31)	0.246	51.21	0.33	0.117
LP(2)O27	1.860	σ*(O25-C31)	0.084	29.06	0.65	0.124
LP(1)O28	1.967	σ*(O30-C36)	0.028	8.90	1.13	0.090
LP(2)O28	1.756	π*(O30-C36)	0.309	59.69	0.31	0.124
LP(2)O30	1.845	σ*(O28-C36)	0.067	25.37	0.72	0.123
LP(2)O30	1.845	σ*(O25-H26)	0.067	25.21	0.74	0.125
LP(2)O30	1.845	σ*(C34-C36)	0.058	11.41	0.73	0.083

[a]E(2) is the stabilization energy represented by hyper conjugative interaction .
[b]Energy difference between donor (i) and acceptor (j) NBO orbitals.
[c]F(i,j) is the element of the Fock matrix between NBO orbitals i and j.

4. CONCLUSION

This study sheds light on the molecular interactions in the caffeine-maleic acid cocrystal. The intermolecular hydrogen bonds between caffeine and maleic acid (O28-H29...N8) created the cocrystal. The interaction energy in the formation of cocrystals was found to be –15.501 kcal/mol, which is in agreement with the interaction energy evaluated from the QTAIM analysis. The optimized structure parameters of the cocrystal were evaluated and compared to those of the crystal structure. Caffeine and maleic acid showed two intermolecular hydrogen bonds and one intra-molecular hydrogen bond, which were supported by QTAIM analysis and the RDG scatter and its isosurface. With a greater contribution of 42.4% to the Hirshfeld surface, the intermolecular interaction caused by O...H demonstrates its critical role in the crystal packing of the cocrystal of caffeine and maleic acid. The global minimum electrostatic potential of –44.85 kcal/mol attributed to O27 and the highest positive potential of 37.63 kcal/mol attributed to H24 suggested the sites of intermolecular hydrogen bonding from ESP analysis in the packing of the crystal, which also support the fingerprint plot of Hirshfeld surface analysis. The energy gap of the caffeine-maleic acid cocrystal was found to be less compared to that of API caffeine, indicating that the cocrystal is more reactive and more polarizable. Compared to a gaseous medium, the caffeine-maleic acid cocrystal was found to be more reactive in solvent water. According to the natural bond orbital analysis, the interaction LP(1)N8→π*(O28-H29) is responsible for the intermolecular hydrogen bonding between API caffeine and coformer maleic acid, with a stabilization energy of 37.25 kcal/mol indicating a strong interaction.

AUTHOR CONTRIBUTIONS

T.R. Paneru: Conceptualization of research activity, investigation, data analysis, writing original draft; B. Bhandari: Reviewing, analysis of result, and proofreading.

ETHICAL ISSUE

The authors declare no ethical issues.

CONFLICT OF INTEREST

There are no conflicts to declare.

ACKNOWLEDGMENTS

T.R. Paneru acknowledges University Grants Commission (UGC), Nepal, for providing partial research support through the Research Fellowship (UGC Award No. PhD-079/80-ST-18), and he also acknowledges Far Western University, Mahendranagar, Nepal.

REFERENCES

[1] S.N. Wong, Y.C.S. Chen, B. Xuan, C.C. Sun, S.F. Chow, Cocrystal engineering of pharmaceutical solids: therapeutic potential and challenges, Cryst Eng Comm 23 (2021) 7005–7038. https://doi.org/10.1039/D1CE00825K.

[2] M. Guo, X. Sun, J. Chen, T. Cai, Pharmaceutical cocrystals: A review of preparations, physicochemical properties and applications, Acta Pharmaceutica Sinica B 11 (2021) 2537–2564. https://doi.org/10.1016/j.apsb.2021.03.030.

[3] T.R. Paneru, M.K. Chaudhary, B.D. Joshi, P. Tandon, Cocrystal screening of benznidazole based on electronic transition, molecular reactivity, hydrogen bonding, and stability, J Mol Model 30 (2024) 378. https://doi.org/10.1007/s00894-024-06146-1.

[4] T.R. Shattock, K.K. Arora, P. Vishweshwar, M.J. Zaworotko, Hierarchy of supramolecular synthons: persistent carboxylic acid···pyridine hydrogen bonds in cocrystals that also contain a hydroxyl moiety, Cryst. Growth Des. 8 (2008) 4533–4545. https://doi.org/10.1021/cg800565a.

[5] S. Aitipamula, R.B.H. Tan, 1. Pharmaceutical cocrystals: crystal engineering and applications, in: E. Tiekink, J. Zukerman (Eds.), Multi-Component Crystals, De Gruyter, 2017: pp. 1–31. https://doi.org/10.1515/9783110464955-001.

[6] J. Evans, J.R. Richards, A.S. Battisti, Caffeine, in: StatPearls, StatPearls Publishing, Treasure Island (FL), 2024. http://www.ncbi.nlm.nih.gov/books/NBK519490.

[7] R. Rijal, M. Sah, H.P. Lamichhane, H.S. Mallik, Quantum chemical calculations of nicotine and caffeine molecule in gas phase and solvent using DFT methods, Heliyon 8 (2022) e12494. https://doi.org/10.1016/j.heliyon.2022.e12494.

[8] B.F. Harland, Caffeine and nutrition, Nutrition 16 (2000) 522–526. https://doi.org/10.1016/S0899-9007(00)00369-5.
[9] A.V. Trask, W.D.S. Motherwell, W. Jones, Pharmaceutical cocrystallization: Engineering a remedy for caffeine hydration, Cryst Growth Des 5 (2005) 1013–1021. https://doi.org/10.1021/cg0496540.
[10] K. Guo, G. Sadiq, C. Seaton, R. Davey, Q. Yin, Cocrystallization in the Caffeine/Maleic Acid System: Lessons from Phase Equilibria, Cryst Growth Des 10 (2010) 268–273. https://doi.org/10.1021/cg900885n.
[11] T. Leyssens, G. Springuel, R. Montis, N. Candoni, S. Veesler, Importance of solvent selection for stoichiometrically diverse cocrystal cystems: Caffeine/maleic Acid 1:1 and 2:1 cocrystals, Cryst Growth Des 12 (2012) 1520–1530. https://doi.org/10.1021/cg201581z.
[12] S. Aher, R. Dhumal, K. Mahadik, A. Paradkar, P. York, Ultrasound assisted cocrystallization from solution (USSC) containing a non-congruently soluble cocrystal component pair: Caffeine/maleic acid, Eur J Pharm Sci 41 (2010) 597–602. https://doi.org/10.1016/j.ejps.2010.08.012.
[13] P. Hohenberg, W. Kohn, Inhomogeneous Electron Gas, Phys Rev 136 (1964) B864–B871. https://doi.org/10.1103/PhysRev.136.B864.
[14] M.J. Frisch, G.W. Trucks, H.B. Schlegel, G.E. Scuseria, M.A. Robb, J.R. Cheeseman, G. Scalmani, V. Barone, B. Mennucci, G.A. Petersson, H. Nakatsuji, M. Caricato, X. Li, H.P. Hratchian, A.F. Izmaylov, J. Bloino, G. Zheng, J.L. Sonnenberg, M. Hada, M. Ehara, K. Toyota, R. Fukuda, J. Hasegawa, M. Ishida, T. Nakajima, Y. Honda, O. Kitao, H. Nakai, T. Vreven, J.A. Montgomery, J.E. Peralta, F. Ogliaro, M. Bearpark, J.J. Heyd, E. Brothers, K.N. Kudin, V.N. Staroverov, R. Kobayashi, J. Normand, K. Raghavachari, A. Rendell, J.C. Burant, S.S. Iyengar, J. Tomasi, M. Cossi, N. Rega, J.M. Millam, M. Klene, J.E. Knox, J.B. Cross, V. Bakken, C. Adamo, J. Jaramillo, R. Gomperts, R.E. Stratmann, O. Yazyev, A.J. Austin, R. Cammi, C. Pomelli, J.W. Ochterski, R.L. Martin, K. Morokuma, V.G. Zakrzewski, G.A. Voth, P. Salvador, J.J. Dannenberg, S. Dapprich, A.D. Daniels, Ö. Farkas, J.B. Foresman, J.V. Ortiz, J. Cioslowski, D.J. Fox, Gaussian 9 Revision, Gaussian, Inc. Wallingford (2009).
[15] A.D. Becke, Density-functional thermochemistry. III. The role of exact exchange, J Chem Phys 98 (1993) 5648–5652. https://doi.org/10.1063/1.464913.
[16] T.H. Dunning, Gaussian basis sets for use in correlated molecular calculations. I. The atoms boron through neon and hydrogen, J Chem Phys 90 (1989) 1007–1023. https://doi.org/10.1063/1.456153.
[17] R. Dennington, T.A. Keith, Millam, M. John, GaussView 05 Semichem Inc., Shawnee Mission, KS (2009).
[18] T.A. Keith, AIMALL version (19.10.12) TK Gristmill Software, Overland Park KS. USA, (2019). http://aim@tkgristmill.com/.
[19] M. Turner, J. McKinnon, S. Wolff, D. Grimwood, P. Spackman, D. Jayatilaka, M. Spackman, CrystalExplorer17, (2017).
[20] T. Lu, F. Chen, Multiwfn: A multifunctional wavefunction analyzer, J Comput Chem 33 (2012) 580–592. https://doi.org/10.1002/jcc.22885.
[21] W. Humphrey, A. Dalke, K. Schulten, VMD: Visual molecular dynamics, J Mol Graph 14 (1996) 33–38. https://doi.org/10.1016/0263-7855(96)00018-5.
[22] N.M. O'boyle, A.L. Tenderholt, K.M. Langner, cclib: A library for package-independent computational chemistry algorithms, J Comput Chem 29 (2008) 839–845. https://doi.org/10.1002/jcc.20823.
[23] E.D. Glendening, A.E. Reed, J.E. Carpenter, F. Weinhold, NBO 3.0 Program manual, Theor Chem Inst, University of Wisconsin, Madison, WI (1996).
[24] A.V. Trask, W.D.S. Motherwell, W. Jones, CCDC 272622: Experimental Crystal Structure Determination, (2005). https://doi.org/10.5517/CC94P8C.
[25] R.F.W. Bader, S.G. Anderson, A.J. Duke, Quantum topology of molecular charge distributions. 1, J Am Chem Soc 101 (1979) 1389–1395. https://doi.org/10.1021/ja00500a006.
[26] S.J. Grabowski, Non-covalent interactions – QTAIM and NBO analysis, J Mol Model 19 (2013) 4713–4721. https://doi.org/10.1007/s00894-012-1463-7.
[27] U. Koch, P.L.A. Popelier, Characterization of C-H-O hydrogen bonds on the basis of the charge density, J Phys Chem 99 (1995) 9747–9754. https://doi.org/10.1021/j100024a016.
[28] I. Rozas, I. Alkorta, J. Elguero, Behavior of ylides containing N, O, and C atoms as hydrogen bond acceptors, J Am Chem Soc 122 (2000) 11154–11161. https://doi.org/10.1021/ja0017864.
[29] E.R. Johnson, S. Keinan, P. Mori-Sánchez, J. Contreras-García, A.J. Cohen, W. Yang, Revealing Noncovalent Interactions, J Am Chem Soc 132 (2010) 6498–6506. https://doi.org/10.1021/ja100936w.
[30] G. Saleh, C. Gatti, L. Lo Presti, Non-covalent interaction via the reduced density gradient: Independent atom model vs experimental multipolar electron densities, Comput Theor Chem 998 (2012) 148–163. https://doi.org/10.1016/j.comptc.2012.07.014.
[31] T.R. Paneru, M.K. Chaudhary, P. Tandon, T. Chaudhary, B.D. Joshi, Theoretical study on molecular stability, reactivity, and drug potential of cirsilineol from DFT and molecular docking methods, Chem Phys Impact 8 (2024) 100641. https://doi.org/10.1016/j.chphi.2024.100641.
[32] F.L. Hirshfeld, Bonded-atom fragments for describing molecular charge densities, Theor Chim. Acta 44 (1977) 129–138. https://doi.org/10.1007/BF00549096.
[33] P.R. Spackman, M.J. Turner, J.J. McKinnon, S.K. Wolff, D.J. Grimwood, D. Jayatilaka, M.A. Spackman, *CrystalExplorer* : a program for Hirshfeld surface analysis, visualization and quantitative analysis of molecular crystals, J Appl Crystallogr 54 (2021) 1006–1011. https://doi.org/10.1107/S1600576721002910.
[34] A. Khurshid, A. Saeed, T. Hökelek, U. Taslim, M. Irfan, S.U. Khan, A. Iqbal, H.R. El-Seedi, Experimental and Hirshfeld surface investigations for unexpected aminophenazone cocrystal formation under thiourea reaction conditions via possible enamine assisted rearrangement, Crystals 12 (2022) 608. https://doi.org/10.3390/cryst12050608.
[35] K.L. Jyothi, R. Gautam, D. Swain, T.N. Guru Row, N.K. Lokanath, Cocrystals of gallic acid with urea and propionamide: Supramolecular Structures, Hirshfeld surface analysis, and DFT studies, Cryst Res Tech 54 (2019) 1900016. https://doi.org/10.1002/crat.201900016.
[36] P.K. Weiner, R. Langridge, J.M. Blaney, R. Schaefer, P.A. Kollman, Electrostatic potential molecular surfaces., Proc Natl Acad Sci U.S.A. 79 (1982) 3754–3758.

https://doi.org/10.1073/pnas.79.12.3754.

[37] B.D. Joshi, Chemical Reactivity, Dipole Moment and First Hyperpolarizability of Aristolochic Acid I, J Inst Sci Tech 21 (2016) 1–9. https://doi.org/10.3126/jist.v21i1.16030.

[38] F.R. B., J.C. Prasana, S. Muthu, C.S. Abraham, Molecular docking studies, charge transfer excitation and wave function analyses (ESP, ELF, LOL) on valacyclovir : A potential antiviral drug, Comput Bio Chem 78 (2019) 9–17. https://doi.org/10.1016/j.compbiolchem.2018.11.014.

[39] J. Yu, N.Q. Su, W. Yang, Describing chemical reactivity with frontier molecular orbitalets, JACS Au 2 (2022) 1383–1394. https://doi.org/10.1021/jacsau.2c00085.

[40] H.A. Hussein, G.F. Fadhil, Theoretical investigation of *para* amino-dichloro chalcone isomers. part II: A DFT structure–stability study of the FMO and NLO properties, ACS Omega 8 (2023) 4937–4953. https://doi.org/10.1021/acsomega.2c07148.

[41] T. Koopmans, Über die zuordnung von wellenfunktionen und eigenwerten zu den einzelnen elektronen eines atoms, Physica 1 (1934) 104–113. https://doi.org/10.1016/S0031-8914(34)90011-2.

[42] R.G. Parr, R.G. Pearson, Absolute hardness: companion parameter to absolute electronegativity, J Am Chem Soc 105 (1983) 7512–7516. https://doi.org/10.1021/ja00364a005.

[43] R.G. Parr, L.V. Szentpály, S. Liu, Electrophilicity Index, J Am Chem Soc 121 (1999) 1922–1924. https://doi.org/10.1021/ja983494x.

[44] S. Sebastian, N. Sundaraganesan, The spectroscopic (FT-IR, FT-IR gas phase, FT-Raman and UV) and NBO analysis of 4-Hydroxypiperidine by density functional method, Spectrochim Acta A Mol Biomol Spectrosc 75 (2010) 941–952. https://doi.org/10.1016/j.saa.2009.11.030.

[45] F. Weinhold, C.R. Landis, Valency and Bonding: A Natural bond orbital donor-acceptor perspective, Cambridge University Press, 2005.

Simulation of Vibrational Spectra (IR and Raman), PED Analysis and Study of Solvation Effects on Electronic Properties of Methyldopa

Tarun Chaudhary[1], Bhawani Datt Joshi[2*]

[1]Department of Physics, Mid-WEST University, Bageshwary Multiple Campus, Kohalpur, Nepal
[2]Department of Physics, Tribhuvan University, Siddhanath Science Campus, Mahendranagar, 10400, Nepal

Research Article

ISSN: 3059-9504 (online)
Doi: xxxx

Article History

Received: November 2, 2024
Revised: November 25, 2024
Accepted: December 7, 2024
Published: December 28, 2024

Keywords

IR and Raman, PED, Atomic charge, Charge transfer

***Corresponding author**
Email: bhawani.joshi@snsc.tu.edu.np)
Orcid: 0000-0003-3276-9319 (BD Joshi)
Phone: + 977-9841580777

ABSTRACT

The properties like hydrogen bonding, partial atomic charges associated with atoms and intramolecular charge transfer characteristics of a drug are very crucial for its biological activity. In the paper, these electronic properties of antihypertensive drug methyldopa have been studied intensively, using Density Functional Theory (DFT). The simulated infrared (IR) and Raman spectra of monomer and dimer, Potential energy distribution (PED), Mullikan atomic charges and UV spectra have been analysed. In both IR and Raman spectra, the prominent stretching of the O-H group taking part in intermolecular hydrogen bonding was obtained at 2814.64 cm^{-1}. Furthermore, the most negative Mulliken charge was found to be associated with nitrogen, N5 and onygen. O4 the most positive with carbon atom C10 in momomer. The UV- Vis absorption spectra analysis has been performed in gaseous and solvent (EtOH) states. The present work precisely explains hydrogen bonding, reactive sites and possibility of intramolecular charge transfer.

1. INTRODUCTIONS

The structural and electronic properties of the molecule, which are important factors to determine the chemical and biological properties, have been for a well-known drug Methyldopa. Methyldops, (S)-2-amino-3-(3,4-dihydroxyphenyl)-2-methyl-propanoic acid is an antihypertensive drug that has been used since 1960 [1]. It is frequently used to treat preeclampsia and gestational hypertension [2] and preferred for breast-feeding women and often prescribed to heart, kidney, and diabetes patients [3,4]. Methyldopa is more soluble in dimethyl sulfoxide (DMSO) than in water [3].

Methyldopa, being one of the most important and popular medicines, has drawn considerable attention regarding its structural and chemical characteristics. In the last few years, a number of research projects have focused on its structural, thermal, chemical, and biological properties [6-10]. Noei et al. explored the different structure of molecules and their stability due to charge delocalisation in terms of natural bond orbitals (NBO) in different solvents [7]. The previous study shows that the molecule is thermodynamically stable and it exhibits significant non-linear optical properties [6,8]. The molecule shows charge-transfer characteristics with o-chloranil (O-ClN) [9]. Furthermore, Chaudhary et al. showed charge transfer due to excitation based on electron hole distribution [8]. Previously, Prabakaran et al. performed an experimental vibrational study. However, the stretching of frequency of O-H taking part in intermolecular hydrogen bonding remained undetermined. Recently, Chaudhary et al. investigated the structural and chemical properties of the monomer and dimer of methyldopa [10]. However, the analysis of IR and Raman spectra in the monomeric and dimeric forms has not been performed yet. In addition to this, the effects of solvents on their electronic properties are still the subject of interest. Thus, our study is aimed at calculating these properties. As Density Functional Theory (DFT) is an effective method to analyse the structural and electronic properties of the molecules [11], the overall calculations have been performed using DFT at B3LYP/6-31G(d,p) level of theory. In this paper, IR and Raman spectra of monomer and dimer structures have been simulated and comparatively studied to find out the vibrational shifts of the functional groups taking part in hydrogen bonding. To reproduce the nucleophilic and electrophilic active sites, partial atomic charges associated with the molecule have been calculated. The study of UV-Vis spectra in solvent has been conducted theoretically to get insight into its electronic properties. The present work provides the important information required to understand the molecular reactivity of the molecule more precisely. Fig. 1 depicts teh optimized structure of methyldopa dimer.

2. COMPUTATIONAL AND THEORETICAL BACKGROUND

The optimized structure of monomer and dimer of methyldopa were obtained based on previous work of Chaudhry et al. [10] and further calculations were performed using the Gaussian 09 package [12]. The density functional theory (DFT) method [13] with exchange hybrid functional Becke's 3-parameters (Local, nonlocal and Hartree-Fock) and correlation functional Lee–Yang–Parr, B3LYP/6-31G(d,p), was employed for calculations [14-17]. GaussView 05 [18] was used to visualize and analyse the results of Gaussian output. For the vibrational analysis, potential energy distribution (PED) for each of the vibrational modes is obtained using Gar2PED software package [19]. The Raman intensities were calculated utilizing the given equation [20,21]:

$$\frac{\partial\sigma_j}{\partial\Omega} = \left(\frac{2^4\pi^4}{45}\right)\left(\frac{(\nu_0-\nu_j)^4}{1-\exp\left[\frac{-hc\nu_j}{kT}\right]}\right)\left(\frac{h}{8\pi^2 c\nu_j}\right)S_j$$

where, $\frac{\partial\sigma_j}{\partial\Omega}$ = Raman scattering cross-section,
S_j = cattering activities, ν_j = estimated wavenumbers for j^{th} normal mode ν_0 =Wave number for the Raman-excited state *h*, *c*, and *k* represent the universal constants. More often, the calculated value of wave numbers is higher than the actual ones. Thus, the calculated values are adjusted using the WLS factor, $\nu_{observed} = (1.008700 - 0.0000163 \times \nu_{calculated})\ \nu_{calculated}$ [22].

Furthermore, Mulliken charges distribution in the molecule was visualized using GaussView. TD-DFT with integral equation formalism-polarized continuum (IEF-PCM) model was used to analyze UV-Vis spectra.

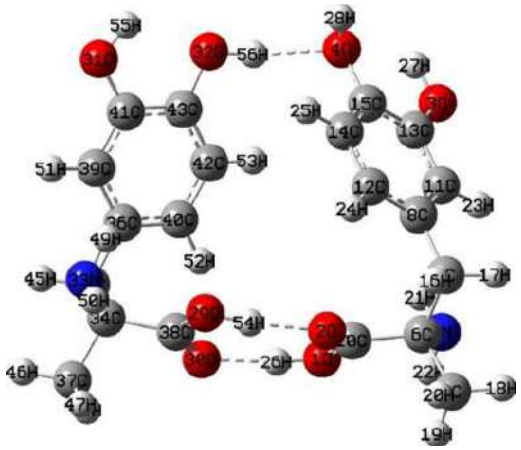

Fig. 1. Optimized structure of methyldopa dimer at B3LYP/6-311++G (d,p) [10]

3. RESULTS AND DISCUSSIONS

3.1 Vibrational modes

Methyldopa molecule consists of 28 atoms, so it exhibits 78 vibrational modes. The IR and Raman frequencies for the most stable monomer and dimer are represented in Figs. 2 and 3 respectively. The PED contributions of each of their vibrational modes are illustrated in Table 1. The different vibration modes [23] are explained below:

O-H vibration

Moreover, the stretching of O-H was calculated in between 3530–3645 cm^{-1} [24]. The simulated stretching of the non-bonded O-H group in monomer were observed at 3636.18 cm^{-1} for O4H28, 3583.47 cm^{-1} for O3H27 and 3549.67 cm^{-1} for O1H26. In the dimer, the two hydroxyl groups O4H28 and O3H27 have almost the same frequency as they have in the monomer. However, the stretching frequency of O1H26 was decreased to 2814.64 cm^{-1}. Also, the frequency of hydrogen bonded O-H group of the carboxylic group lies in the range of 3300–2500 cm^{-1} [24]. Hence, the red shift in the frequency of this hydroxyl group justifies the strong hydrogen-bond interaction in the dimer.

NH_2 vibration

The amine group possesses asymmetric and symmetric stretching frequency bands. Its asymmetric stretching was observed at 3403.87 cm^{-1} and symmetric stretching at 3330.73 cm^{-1} in the monomer. Similarly, in the dimer, the asymmetric stretching was obtained at 3399.56 cm^{-1} and symmetric at 3327.20 cm^{-1}. All calculated frequencies lie in the specified range, 3490–3310 cm^{-1} [24]. The strong bending vibration of NH_2 in a plane was determined at 1642.94 cm^{-1} in monomer and 1620.34 cm^{-1} in dimer, respectively. At 874.42 cm^{-1}, the waging of the monomer has the highest PED contribution.

C-H vibration

The calculated stretching frequency of C-H associated with the ring were obtained at 3071.16, 3065.59, 3030.41 cm^{-1} for the monomer and at 3068.16, 3019.16, 2994.82 cm^{-1} for the dimer structure. These calculated frequencies of C-H are within the range, 3100-3000 cm^{-1} [25, 26]. Furthermore, it's in plane bending vibration were obtained in the wide range of 1486.0-1127.89 cm^{-1} and out-of-plane bending in 918.49-810.00 cm^{-1}.

The asymmetric stretching of CH_2 was calculated at 2992.55 cm^{-1} and symmetric stretching at 2942.90 cm^{-1} in the monomer. Similarly, its symmetric stretching in dimer was obtained at 2945.81 cm^{-1}. These all calculated frequency bands fall under the given range, that is 3000-2900 cm^{-1} for asymmetric and 2900-2800 cm^{-1} for symmetric [25]. In addition to this, other vibrations occurred intensely at 1464.65 cm^{-1} (deformation), 863.90 cm^{-1} (rocking), 1351.18 cm^{-1} (waging) and 1259.53 cm^{-1} (scissoring).

The stretching of CH_3 was estimated at 2990.61 cm^{-1} (asymmetric), and at 2924.10 cm^{-1} (symmetric) in the monomer, and 2994.82 cm^{-1} (asymmetric) and 2921.27 (symmetric) in the dimer. The typical range of CH_3 stretching is 3000-2905 cm^{-1} for asymmetric vibrations and 2870-2860 cm^{-1} for symmetric vibrations [27,28]. The deformation of CH_3 with very high contribution PED contribution (87 percent) was calculated at 1393.39 and its rocking were generally obtained below 1127.89 cm^{-1}.

C=O, C-C vibration

The calculated stretching frequency band for C=O in monomer was observed at 1782.40 cm^{-1}, which is in the range, 1870-1550 cm^{-1} [29]. But, in dimer structure, it's frequency was observed at 1723.86 cm^{-1}. This fall in frequency of the carbonyl group, indicates that oxygen is involved in the hydrogen bonding.

The C-C stretching frequencies were almost the same in monomer and dimer. In the monomer, prominent stretching was discovered between 1644.87 cm^{-1} and 1040.80 cm^{-1}. Generally, the stretching frequency bands for C-C lie in between 1650 and 1100 cm^{-1} [30].

Ring vibration

The ring exhibited a variety of vibrations, includingpuckering, torsional vibration, and trigonal deformation. The considerable puckering of the Ring R was detected at 698.03 cm^{-1} and its asymmetric torsional vibration was found at a very low frequency, 156.03 cm^{-1}.

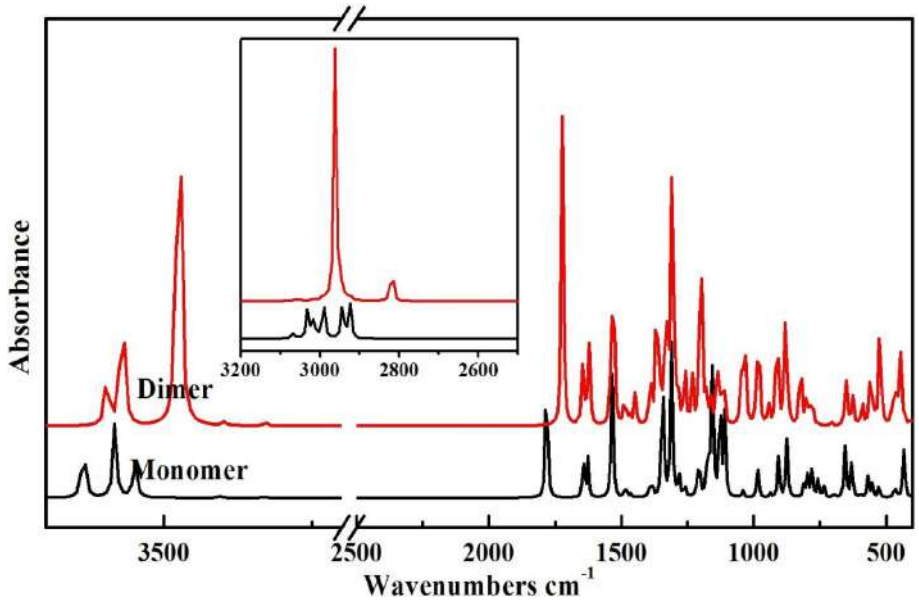

Fig. 2. Simulated IR spectra of methyldopa.

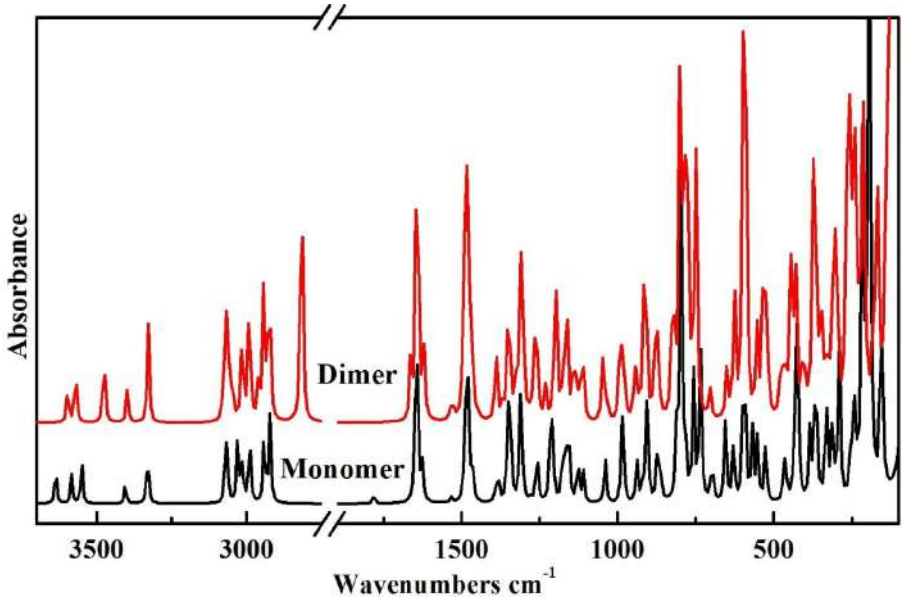

Fig. 3. Simulated Raman spectra of methyldopa.

Table 1. Potential energy distribution (PED) associated with vibrational frequency of methyldopa.

Unscaled frequency	Scaled frequency	IR intensity	Raman activity	PED distribution (≥ 5%)
3843.54	3636.18	69.34	138.30	ν(O4H28)(100)
3783.94	3583.47	88.34	84.77	ν(O3H27)(100)
3745.78	3549.67	48.49	128.48	ν(O1H26)(100)
3581.83	3403.87	2.31	48.09	$\nu_a(NH_2)$(100)
3499.95	3330.73	2.01	130.34	$\nu_s(NH_2)$(100)
3211.32	3071.16	1.92	76.14	R[ν(CH)](95)
3205.60	3065.99	2.01	57.86	R[ν(CH)](98)
3166.28	3030.41	19.00	98.02	R[ν(CH)](96)
3149.67	3015.37	12.75	63.38	ν(C9H20)(99)
3124.50	2992.55	5.61	31.26	$\nu_a(CH_2)$(98)
3122.36	2990.61	20.58	71.92	$\nu_a(CH_3)$(99)
3069.80	2942.90	22.49	94.36	$\nu_s(CH_2)$(98)

3049.12	2924.10	21.37	113.73	$\nu_s(CH_3)(99)$
1820.59	1782.40	181.88	2.75	ν (C=O)(80)+δ_{in}(C10H26)(6)
1676.08	1644.87	7.92	32.25	R[ν(CC)(45)+δ_a(10)]
1674.06	1642.94	41.57	17.45	$\delta_{in}(NH_2)(87)$
1656.47	1626.16	48.07	7.77	R[ν(CC)(56)+ δ_a'(9)]
1561.47	1535.31	168.99	1.16	R[ν(CC)(36)+δ_{in}(CH)(36)+ν(C15O)(9)+ν(C13O)(6)]
1514.41	1490.20	5.32	10.28	[δ_a(45)+δ_a'(20)+ρ(5)](CH_3)
1510.07	1486.04	2.81	9.14	[δ_a(18)+δ_a'(6)](CH_3)+R[δ_{in}(C12H)(11)+ν(CC)](30)]+δ(O3H)(11)
1502.99	1479.24	6.99	18.44	[δ_a'(57)+δ_a(23)+ρ'(6)](CH3)+$\delta(CH_2)$(9)
1487.79	1464.65	3.58	4.33	$\delta(CH_2)$(85)+δ_a'(CH3)(6)
1413.67	1393.39	11.55	1.22	δ(CH3)(87)
1403.66	1383.76	19.06	5.23	R[ν(CC)(60)]+δ(O3H)(9)+ $\delta(CH_2)$(10)
1369.85	1351.18	10.89	14.68	$\omega(CH_2)$(40)+$\rho(NH_2)$(10)+ν(C6C9)(6)+δ(C8C6C7)(6)
1365.08	1346.58	52.39	1.20	δ(C8C6C7)(10)+δ(O4H)(9)+ν(C10O)(8)+R[δ_{in}(CH)(15)]+ν(C6C10)(7)
1359.85	1341.54	96.07	7.07	δ(O3H)(16)+R[δ_{in}(CH)](19)+δ(O4H)(8)+δ(C8C6C7)(8)+ν(C10O)(6)+ω(CH2)(6)
1328.81	1311.59	189.62	14.22	R[ν(CC)(33)+ δ_{in}(CH)(7)+ν(C7C8)(6)+ ν(C13O)(21)+ν(C15O)(6)]+ $\rho(NH_2)$(8)
1322.28	1305.28	9.79	1.72	$\rho(NH_2)$(28)+$\omega(CH_2)$(19)+δ(C6C9N)(8)+$\delta'(CH_3)$(6)
1298.31	1282.13	33.22	0.62	R[ν(C15O)(17)+δ_{trig}(15)+δ_{in}(C12H)(17)+ν(C13O)(12)]+[γ(9)+ω(7)](CH_2)+δ(O3H)(8)
1274.93	1259.53	15.97	7.17	$\gamma(CH_2)$(24)+ν (N5C6)(15)
1227.59	1213.71	13.78	14.68	δ(C8C6C7)(10)+ν (N5C6)(10)+ν(C6C7)(9)+ν (C6C9)(8)+$\omega(CH_2)$(7)+$\rho(NH_2)$(6)
1219.71	1206.07	49.87	2.63	δ(O3H)(30)+R[ν(CC)(16)+δ_{in}(CH)(14)+ν(C15O)(6)]+δ(O4H)(5)
1187.41	1174.76	65.78	7.03	δ(O4H)(22)+R[δ_{in}(CH)(22)+ν(C8C12)(8)]+ν(C7C8)(18)
1174.20	1161.94	16.40	5.20	R[δ_{in}(CH)(36)+ν(CC)(19)]+δ(O4H)(13)+ν(C7C8)(9)
1168.26	1156.18	148.73	3.97	δ(C8C6C7)(23)+ν(C10O)(22)+γ(CH2)(14)+ν(N5C6)(8)
1139.13	1127.89	144.88	4.82	δ(O4H)(15)+ν(C10O)(11) –R[δ_{in}(CH)(10)+δ_{trig}(8)+ν(C15O)(7)]+$\rho(CH_3)$(8)
1120.54	1109.82	100.27	2.96	$\rho(CH_3)$(21)+ν(C10O)(11)+$\gamma(CH_2)$(9)+δ(O4H)(6)+ν(C8C11)(6)+R[δ_{trig}](6)
1049.63	1040.80	8.41	4.27	ν(C6C9)(25)+$\rho'(CH_3)$(22)+δ(NH2)(19)
992.71	985.28	25.16	6.16	$\rho'(CH_3)$(15)+ν(C6C7)(12)+ν(C6C9)(11)+R[ν(CC)](7)+ν(C7C8)(6)+$\omega(NH_2)$(6)
988.81	981.48	13.18	1.15	$\rho(CH_2)$(26)+$\rho'(CH_3)$(17)+$\rho(CH_3)$(11)+R[δ_{trig}](6)
945.22	938.88	5.43	3.12	$\omega(NH_2)$(17)+$\rho(CH_2)$(13)+ρ(CH3)(10)+ν(C6C9)(8)+R[ν(C8C12)(7)+δ_{trig}(7)]
924.38	918.49	0.98	1.73	R[oop(CH)(74)+τ_a'](6)
911.56	905.95	48.85	6.63	R[oop(CH)](35)+puck(6)]+ω(NH2)(20)+ν(C6C7)(12)
879.37	874.42	72.00	2.68	R[oop(CH)](36)+$\omega(NH_2)$(26)+ν(N5C6)(14)
868.64	863.90	2.33	2.80	ν (N5C6)(18)+$\rho(CH_2)$(16)+R[oop(CH)](14)+ν(C6C7)(12)+ν(C6C10)(9)+ ρ(CH3)(6)
813.71	810.00	19.35	5.21	R[oop(CH)](67)+R[τ_a](8)
799.84	796.37	25.84	18.80	R[ν(C15O)(23)+ν(CC)(28)+δ_{trig}(9)+δ_a(7)]
783.91	780.71	31.84	2.08	oop(C10O)(38)+τ(C10O)(13)+ν(C6C9)(11)+R[oop(C14H)](6)
760.38	757.57	20.88	6.34	R[δ_{trig}(16)+δ_a'(10)+ν(C7C8)(10)+puck(6)]+oop(C10O)(10)
737.43	734.98	14.29	7.90	ν(C6C10)(19)+δ_{in}(C10O)(14)+R[puck(13)+oop(C8C7)(7)]+ν(C10O)(9)
699.93	698.03	4.73	2.30	R[puck(56)+oop(C13O)(14)+oop(C15O)(14)+oop(C8C7)(5)]
656.53	655.22	61.93	3.19	τ(C10O)(28)+R[oop(C13O)(16)+τ_a(10)+oop(C15O)(10)+oop(C8C7)(6)]
630.29	629.30	48.46	2.38	τ(C10O)(26)+R[τ_a(18)+oop(C13O)(13)+oop(C8C7)(13)+oop(C15O)(8)]
596.02	595.41	4.02	6.38	R[δ'_a](38)+δ_{in}(C15O)(21)+ν(CC)(9)+δ_{in}(C13O)(6)+ν(C13O)(6)]
568.84	568.51	25.51	2.34	δ_{in}(C10O)(22)+δ_a(C6C9N)(12)+ν(C6C10)(9)+δ(C6C10O)(9)+R[δ_a](6)+ $\rho'(CH_3)$(6)
552.08	551.91	16.19	1.87	R[δ_a(12)+puck(9)+δ_{in}(C13O)(8)+τ_a(7)]+ρ(C6C9N)(9)
526.41	526.47	13.04	1.71	(C6C10O)(17)+δ(C6C9N)(14)+δ_{in}(C10O)(12)+δ_a'(C6C9N)(10)+R[puck(8)]

Types of vibration: ν(stretching), ν_a (asymmetric stretching), ν_s(symmetric stretching), δ (deformation and bending), oop(out of plane bending), ω(wagging), γ(twisting), ρ(rocking), τ(torsion).

3.2 Mulliken Charge

Atomic charges affect the electronic properties, such as non-linear optical properties and chemical and biological properties of the molecule [31,32]. In addition, it also influences the electronic structure, molecular reactivity, molecular electrostatic potential, etc. [44]. The Mulliken charge associated with each of the atoms is illustrated as shown in Fig. 4. All hydrogen atoms exhibit the positive charges, and all the oxygen and nitrogen atoms exhibit the negative charges. Some carbon exhibits the positive charge, and some of the carbons exhibit the negative charge. The highest positive charge is associated with carbon atoms C10 and also, the higher negative charges are mainly associated with atoms O4 and N5. The negativity of atom O4 and N5 are also well demonstrated by molecular electrostatic potential (MEP) map in the literature [10]. The positive atoms behave as an electrophilic sites and negative atoms as nucleophilic sites [10, 44]. Thus, these atoms have a crucial role for the non-covalent interactions.

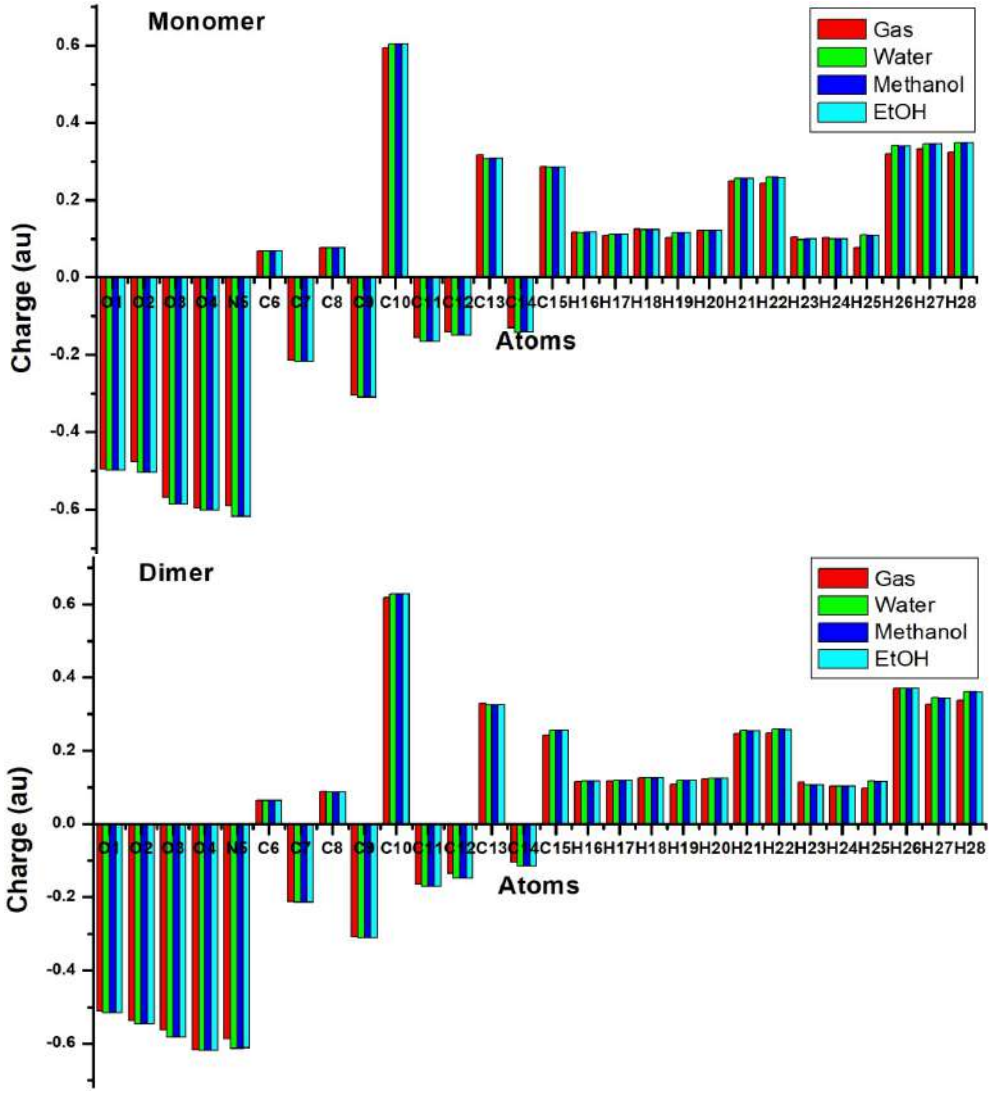

Fig. 4. Mulliken charges associated with each atoms of methyldopa.

Table 2. Mulliken charges of non-hydrogen atoms of methyldopa calculated at B3LYP/6-31G(d,p) level of theory.

		Monomer		
Atom	**Gaseous state**	**Water |e|**	**Methanol |e|**	**EtOH |e|**
O1	−0.4947	−0.4980	−0.4980	−0.4980
O2	−0.4777	−0.5050	−0.5042	−0.5038
O3	−0.5699	−0.5873	−0.5868	−0.5865
O4	−0.5957	−0.6021	−0.6019	−0.6018
N5	−0.5911	−0.6193	−0.6184	−0.6179
C6	0.0691	0.0696	0.0696	0.0696
C7	−0.2145	−0.2170	−0.2169	−0.217
C8	0.0770	0.0772	0.0772	0.0772
C9	−0.3054	−0.3093	−0.3093	−0.3093
C10	0.5933	0.6049	0.6045	0.6043
C11	−0.1565	−0.1656	−0.1653	−0.1652
C12	−0.1410	−0.1505	−0.1502	−0.1501
C13	0.3165	0.3070	0.3073	0.3074
C14	−0.1299	−0.1416	−0.1414	−0.1412
C15	0.2869	0.2848	0.2849	0.2850
		Dimer (first molecule)		
O1	−0.51149	−0.51602	−0.51591	−0.51585
O2	−0.53638	−0.5458	−0.54553	−0.54538
		72		

O3	−0.56245	−0.58205	−0.58148	−0.58118
O4	−0.61617	−0.61831	−0.61835	−0.61836
N5	−0.58676	−0.61375	−0.61284	−0.61237
C6	0.06329	0.06348	0.06348	0.06348
C7	−0.21135	−0.2132	−0.21317	−0.21315
C8	0.08841	0.08753	0.08753	0.08753
C9	−0.30834	−0.31138	−0.31134	−0.31132
C10	0.6186	0.6279	0.62763	0.62749
C11	−0.16531	−0.17131	−0.17112	−0.17103
C12	−0.13475	−0.14843	−0.14786	−0.14758
C13	0.3304	0.32474	0.32485	0.32491
C14	−0.10457	−0.11538	−0.11492	−0.11469
C15	0.24254	0.25723	0.25669	0.25642

3.3 UV-Vis Spectra

The electron transition from the highest occupied molecular orbital (HOMO) to the lowest unoccupied molecular orbital (LUMO) is the main factor that determines the accessibility of chemical reactions, and the energy gap indicates the feasibility of electron transfer [34,35]. In the previous paper [10], the chemical reactivity of the molecule on the basis of the HOMO-LUMO gap has already been discussed. However, the theoretical treatment of the UV-Vis characteristic of the in dimer has not been discussed yet.

The electronic absorption in the bulk of different solvents, TD-DFT with integral equation formalism-polarized continuum (IEF-PCM) model at the same level of theory, has been used for the computation. Fig. 5 depicts the UV-Vis spectra of methyldopa in a gaseous state and solvent (ethanol). The transitions of electrons in different solvents with their respective excitation energy (ΔE), absorption wavelength (λ) and oscillator strength (f) have been listed in Table 3. In the gaseous phase and in solvent (EtOH), two transition peaks were observed. In gaseous phase, transition peak corresponds to the wavelength 248.82 and 182.91nm (monomer); and 247.34 and 185.78 (dimer). The absorption in solvent, ethanol (EtOH) were observed at 249. 4 and 185.78 in monomer and 246.73 and 183.86 nm in dimer. These values were found to be closer to the experimental ones (279, 202 nm) in EtOH [6].

Table 3. Electronic transition properties of methyldopa in the gaseous phase and in solvent.

Gas phase and solvent (EtOH)	Absorption peaks (λ)nm	Oscillator strength (f)	Excitation energy (ΔE) eV	Excitation state
Gas phase	248.82	0.0444	4.9828	HOMO→LUMO
	182.91	0.6941	6.7784	HOMO−2 →LUMO+2
EtOH	249. 4	0.0591	4.9709	HOMO→LUMO
	185.78	0.7655	6.6736	HOMO−2 →LUMO+2
		Dimer		
Gas phase	247.34	0.0638	5.0127	HOMO−1→LUMO
	182.03	0.4951	6.8112	HOMO→LUMO+8
EtOH	246.73	0.0918	5.0252	HOMO−1 →LUMO
	183.86	1.1861	6.7434	HOMO−5 →LUMO+4

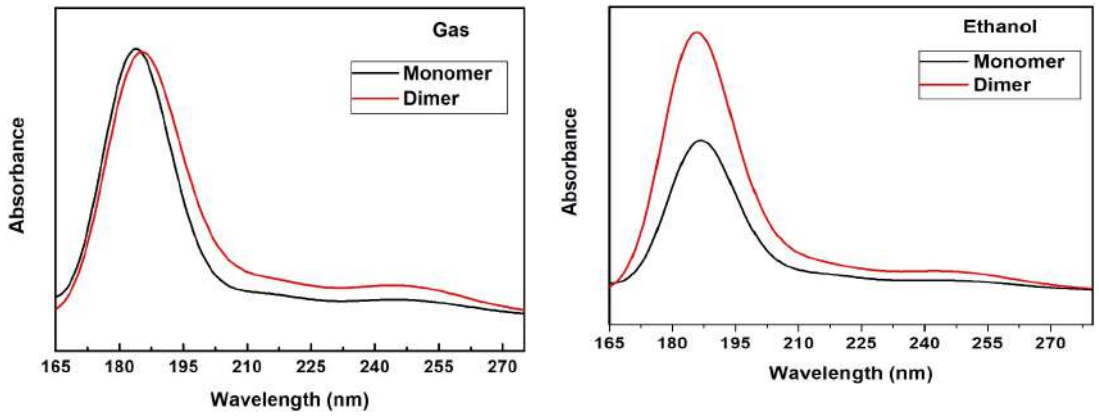

Fig. 5: Simulated UV-Vis absorption spectra for methyldopa in the gaseous phase and in solvent (ethanol).

4. CONCLUSION

The IR and Raman spectra, atomic charge and UV-Vis absorption spectra of methyldopa have been analysed in the present work. From IR and Raman analysis, functional group, O-H has been justified to from intermolecular hydrogen bonding. Due to the hydrogen bonding, the red shift occures in the stretching frequency of the O-H group. Thus, the stretching frequency of H-bonded O-H group was explored at 2814.64 cm^{-1}. The Mulliken charge for each of the atoms was calculated. Carbon atoms C10 exhibit the highest positive charge and atoms like O4, N5 exhibit the higher negative charge than others showing higher electrophilic and nucleophilic behavior, respectively. The UV-Vis absorption performed in gaseous phase and in the solvent shows the electronic transition. The intense transition peaks were calculated at 248.82 nm (monomer) and 247.34 nm in (dimer) in the gaseous state, whereas they were found at 249. 4 nm(monomer) and 246.73 nm (dimer) in EtOH. Ultimately, the present work provides fundamental and insightful knowledge regarding the intermolecular hydrogen bonding, intramolecular charge-transfer and possible reactive sites which are important for interaction with the target.

ACKNOWLEDGEMENT

We sincerely acknowledge Prof. Poonam Tandon, former HoD, Department of Physics, Lucknow University, India, for providing software facilities, including the Gaussian 09 program.

AUTHOR CONTRIBUTIONS

T. Chaudhary: Writing-original draft, investigation, analysis; and conceptualization; B.D. Joshi: Writing-review, validation and supervision.

CONFLICTS OF INTEREST

There are no conflicts to declare.

REFERENCES

[1] G. T., Mah, A. M., Tejani, V. M. Musini, Methyldopa for primary hypertension, *Cochrane Database of Systematic Reviews*, **4** (2009).

[2] M. Wicinski, B. Malinowski, O. Puk, M. Socha, M.´ Słupski, Methyldopa as an inductor of postpartum depression and maternal blues: A review, *Biomedicine & Pharmacotherapy*, **127** (2020). 110196. doi: 10.1016/j.biopha.2020 .110196

[3] F. H. Amro, H. N. Moussa, O. A., Ashimi, B. M. Sibai, Treatment options for hypertension in pregnancy and puerperium, *Expert Opinion on Drug Safety*, **15** (2016), 1635–1642. doi: 10.1080/14740338.2016.1237500

[4] M. Noei, M. Holoosadi, H. Anaraki-Ardakani 2017, Design of methyldopa structure and calculation of its properties by quantum mechanics, *Arabian Journal of Chemistry*, **10** (2017) S1923–S1937. doi: 10.1016/j.arabjc.2013.07.021

[5] K. Sharma, S. Sharma, S. Lahiri, Spectrophotometric, fourier transform infrared spectroscopic and theoretical studies of the charge–transfer complexes between methyldopa [(s)-2 amino-3-(3, 4-dihydroxyphenyl)-2-methyl propanoic acid] and the acceptors (chloranilic acid, o-chloranil and dichlorodicyanobenzoquinone) in acetonitrile and their thermodynamic properties, *Spectrochimica Acta Part A: Molecular and Biomolecular Spectroscopy*, **92** (2012) 212–224. doi: 10.1016/j.saa.2012.02.072

[6] A. Prabakaran, S. Muthu, Normal coordinate analysis and vibrational spectroscopy (FT-IR and FT-Raman) studies of (2S)-2-amino-3-(3, 4-dihydroxyphenyl)-2-methylpropanoic acid using ab initio HF and DFT method, *Spectrochima Acta A Molecular and Biomolecular Spectroscopy,* **99** (2012) 90-96. https://doi.org/10.1016/j.saa.2012.09.014

[7] M. Noei, M. Holoosadi, H. Anaraki-Ardakani, Design of methyldopa structure and calculation of its properties by quantum mechanics, *Arabian Journal of Chemistry*, **10** (2017) S1923-S1937. https://doi.org/10.1016/j.arabjc.2013.07.021

[8] T. Chaudhary, M. K. Chaudhary, B. D. Joshi, A theoretical study on charge transfer and hyperpolarizability of (s)-2-amino-3-(3, 4-dihydroxyphenyl)-2methyl-propanoic acid, *Journal of Nepal Physical Society*, **8** (2022), 16–21. doi:10.3126/jnphyssoc.v8i1.48280

[9] D. A. Ostrov, A. Alkanani, K. A. McDaniel, S. Case, E. E. Baschal, L. Pyle, . . . others, Methyldopa blocks MHC class II binding to disease-specific antigens in autoimmune diabetes, *The Journal of clinical investigation*, **128** (2018), 1888– 1902. doi: 10.1172/jci97739

[10] T. Chaudhary, T. Karthick, M. K. Chaudhary, P. Tandon, B. D. Joshi, Computational evaluation on molecular stability and binding affinity of methyldopa against lysine-specific demethylase 4d enzyme through quantum chemical computations and molecular docking analysis, *Journal of Molecular Structure*, **1286** (2023) 135518. doi: 10.1016/j.molstruc.2023.135518

[11] T. Chaudhary, M. K. Chaudhary, S. Jain, P. Tandon, B. D. Joshi, The experimental and theoretical spectroscopic elucidation of molecular structure, electronic properties, thermal analysis, biological evaluation, and molecular docking studies of isococculidine, *Journal of Molecular Liquids*, **391** (2023) 123212. https://doi.org/10.1016/j.molliq.2023.123212

[12] M.J. Frisch, G.W. Trucks, H.B. Schlegel. G.E. Scuseria, J.R. Cheeseman, M.A. Robb, G. Scalmani, V. Barone, B. Mennucci, G.A. Petersson, H. Nakatsuji, M. Caricato, X. Li, H.P. Hratchian, A.F. Izmzylov, J. Bloino, G. Zheng, J.L. Sonnenberg, M. Hada, M. Ehara, K. Toyota, R. Fukuda, J. Ishida, M. Hasegawa, T. Nakajima, Y. Honda, O. Kitao, H. Nakai, T. Vreven, J.A. Montgomery Jr., J.E. Peralta, F. Ogliaro, M. Bearpark, J.J. Heyd, E. Brothers, K.N. Kudin, V.N. Staroverov, R. Kobayashi, J. Normand, A. Raghavachari, A. Rendell, J.C. Burant, S.S. Iyengar, J. Tomasi, M. Cossi, N. Rega, J.M. Millan, M. Klene, J.E. Knox, J.B. Cross, V. Bakken, C. Adamo, J. Jaramillo, R. Gomperts, R.E. Stratmann, O. Yazyev, A.J. Austin, R. Cammi, C. Pomelli, J.W. Ochterski, R.L. Martin, K. Morokuma, V.G. Zakrzewski, G.A. Voth, P. Salvador, J.J. Dannerberg, S. Dapprich, A.D. Daniels, J. Farkas, B. Foresman, J.V. Ortiz, J. Cioslowski, D.J. Fox, Gaussian 09, Revision, Gaussian, Inc., Wallingford CT, 2009.

[13] P. Hohenberg, W. Kohn, Inhomogeneous Electron Gas, *Physical Review B*, **136** (1964) 864–871.

[14] C. Lee, W. Yang, R.G. Parr, Development of the Colle-Salvetti correlation-energy formula into a functional of the electron density, *Physical Review B*, **37** (1998) 785-789. https://doi.org/10.1103/PhysRevB.37.785-789

[15] R.G. Parr, W. Yang, Density Functional Theory of Atoms and Molecules, Oxford University Press, New York, 1989 1-325.

[16] A.D. Becke, Densityfunctional thermochemistry III, The role of exact exchange, *The Journal of Chemical Physics*, **98** (1993) 5648–5652. http://dx.doi.org/10.1063/1.464913

[17] T.H. Dunning Jr, Gaussian basis sets for use in correlated molecular calculations. I. The atoms boron through neon and hydrogen, *The Journal of Chemical Physics*, **90** (1989) 1007–1023. https://doi.org/10.1063/1.456153

[18] A. Frisch, A.B. Nielson, A.J. Holder, GaussView User Manual, Gaussian Inc, Pittsburgh, PA (2005).

[19] J.M.L. Martin, C. Van Alsenoy, Gar2ped, "Gar2ped software." University of Antwerp (1995).

[20] P. L. Polavarapu, Ab initio vibrational Raman and Raman optical activity spectra, *The Journal of Physical Chemistry*, 94 (1990) 8106–8112. doi: 10.1021/j100384a024

[21] Guirgis, G. A., Klaboe, P., Shen, S., Powell, D. L., Gruodis, A., Aleksa, V., . . . Durig, J. R. (2003). Spectra and structure of silicon-containing compounds. xxxvi—raman and infrared spectra, conformational stability, ab initio calculations and vibrational assignment of ethyldibromosilane, *Journal of Raman Spectroscopy*, **34** (2003), 322–336. doi: 10.1002/jrs.989

[22] H. Yoshida, K. Takeda, J. Okamura, A. Ehara, H. Matsurra, A new approach to vibrational analysis of large molecules by density functional theory: wavenumber-linear scaling method, *The Journal of Physical Chemistry A*, **106** (2002) 3580– 3586, doi: 10.1021/jp013084m .

[23] Chaudhary T., Structural and spectroscopic studies on cefalexin and methyldopa using quantum mechanical methods (Unpublished Ph.D. Thesis, Central department of Physics, Tribhuvan University, Nepal) 2024.

[24] J. Coates, Interpretation of infrared spectra, a practical approach, *Encyclopedia of analytical chemistry*, **12** (2006), 815–10. doi: 10.1002/9780470027318.a5606

[25] S. Muthu, J. U. Maheswari, Quantum mechanical study and spectroscopic (FT-IR, FT-Raman, 13C, 1H, UV) study, first order hyperpolarizability, NBO analysis, HOMO and LUMO analysis of 4-[(4-aminobenzene) sulfonyl] aniline by ab initio HF and density functional method, *Spectrochimica Acta Part A: Molecular and Biomolecular Spectroscopy*, 92 (2012)154–163. doi: 10.1016/j.saa.2012.02.056

[26] S. Sevvanthi, S. Muthu, M. Raja, Quantum mechanical, spectroscopic studies and molecular docking analysis on 5, 5-diphenylimidazolidine-2, 4-dione, *Journal of Molecular Structure*, **1149** (2017) 487–498. doi: 10.1016/j.molstruc.2017 .08.015

[27] C. Liu, R. Alfano, W. Sha, H. Zhu, D. Akins, J. Cleary, . . . E. Cellmer, Human breast tissues studied by ir fourier-transform raman spectroscopy, *In Conference on lasers and electro-optics* (1991) p. CWF51. https://opg.optica.org/abstract.cfm?uri=cleo-1991-CWF51

[28] N.L. Alpert, W. E. Keiser, H.A. Szymanski, N.L. Alpert, W.E. Keiser, H.A. Szymanski, Instruments, *IR: Theory and Practice of Infrared Spectroscopy*, (1979) 9–64. doi: 10.1007/978-1-4684-8160-0_2

[29] G. Socrates, *Infrared and raman characteristic group frequencies: tables and charts*, John Wiley & Sons, 2004. Retrieved from http://surl.li/lkfpl

[30] A. Srivastava, T. Karthick, B.D. Joshi, R. Mishra, P. Tandon, A. Ayala, J. Ellena, Spectroscopic (far or terahertz, mid-infrared and raman) investigation, thermal analysis and biological activity of piplartine. *Spectrochimica Acta Part A: Molecular and Biomolecular Spectroscopy,* **184** (2017) *368–381.doi: 10.1016/ j.saa.2017.05.007*

[31] P.L. Polavarapu, Ab initio vibrational raman and raman optical activity spectra, Journal of Physical Chemistry, 94 (1990) 8106–8112, https://doi.org/10.1021/j100384a024.

[32] S. Muthu, J.U. Maheswari, Quantum mechanical study and spectroscopic (FT-IR, FT-Raman, 13C, 1H, UV) study, first order hyperpolarizability, NBO analysis, HOMO and LUMO analysis of 4-[(4-aminobenzene) sulfonyl] aniline by ab initio HF and density functional method, *Spectrochima Acta A Molecular and Biomolecular Spectroscopy*, **92** (2012) 154–163, https://doi.org/10.1016/j.saa.2012.02.056.

[33] G.A. Guirgis, P. Klaboe, S. Shen, D.L. Powell, A. Gruodis, V. Aleksa, C.J. Nielsen, J. Tao, C. Zheng, J.R. Durig, Spectra and structure of silicon-containing compounds. XXXVI—Raman and infrared spectra, conformational stability, ab initio calculations and vibrational assignment of ethyldibromosilane, *Journal of Raman Spectroscopy*, **34** (2003) 322–336, https://doi.org/10.1002/jrs.989.

[34] B.D. Joshi, A. Srivastava, P. Tandon, S. Jain, A.P. Ayala, A combined experimental (IR, Raman and UV–Vis) and quantum chemical study of canadine, *Spectrochima Acta A: Molecular and Biomolecular Spectroscopy* **191** (2018) 249-258. https://doi.org/10.1016/j.saa.2017.10.008

[35] N. N. Ayare, V. K. Shukla, N. Sekar, Charge transfer and nonlinear optical properties of anthraquinone D-π-A dyes in relation with the DFT based molecular descriptors and perturbational potential, *Computational and Theoretical Chemistry*, **1174** (2020) 112712. https://doi.org/10.1016/j.comptc.2020.112712

On Some Properties of A_p Weights

Jayadev Nath[1]

[1]Siddhanath Science Campus, Mahendranagar, Kanchanpur

Research Article

ISSN: 3059-9504 (online)
Doi: xxxx

Article History

Received: October 25, 2024
Revised: November 18, 2024
Accepted: November 22, 2024
Published: December 28, 2024

Keywords

Weighted inequality, Jones factorization theorem, Hardy-Littlewood maximal function

***Corresponding author**

Email: nathjayadev@gmail.com (J.D. Nath), Phone: +977- 9848879766

ABSTRACT

We provide a survey of the literature on the issue of weighted inequalities of operators in harmonic analysis. Some features of A_p weight functions are discussed and elaborated in this note that will assist in the comprehensive study on the theory of weights.

1. NTRODUCTION

1.1 Background and Literature Review

The concept of A_p weight was introduced by Muckenhoupt [1] in 1972. Weighted inequalities deals with boundedness features of an operator T on weighted Lebesgue space $L^p(w)$, where T is commonly maximal function, square function and other classical operators of harmonic analysis. Basically strong and weak-type estimates of the form

$\int_{\mathbb{R}^n}|Tf(x)|^p\, u(x)dx \le c\int_{\mathbb{R}^n}|f(x)|^p\, v(x)dx$ and $u(\{x \in \mathbb{R}^n : |Tf(x)| > \lambda\}) \le \frac{c}{\lambda^p}\int_{\mathbb{R}^n}|f(x)|^p\, v(x)dx$ are included in the study of weighted norm inequalities. Either a single weight $(u = v = w)$ or a pair of weights (u, v) could be the issue [2].

Muckenhoupt [1] first proved that both the weighted strong and weak type estimates for Hardy-Littlewood maximal function M holds if and only if w satisfies the A_p condition. The same class of weights also characterizes the boundedness of the Hilbert transform on $L^p(w)$, was proved by Hunt, Muckenhoupt and Wheeden [4] shortly after. In 1974, Coifman and Fefferman [5] proved that the general Calderón-Zygmund operators and their analogues are bounded on $L^p(w)$ whenever w satisfies the A_p condition. In addition, the proof of the boundedness of maximal operators and singular integral operators on weighted spaces were built on the foundation of A_∞ condition, the reverse Hölder's inequality and A_p implies $A_{p-\varepsilon}$ that are based on A_p condition.

Discussing and elaborating on certain aspects of A_p weight functions that could improve knowledge of weight theory is the primary goal of this work.

Analytical methods and basic analysis tools are used to present the work on the spirit of close to the books [9, 10].

1.2 Weighted Norm Inequalities

For the past three decades, mathematicians have studied the connection between the so-called A_p characteristic of the weight and the norm of certain operators for singular integrals in a weighted space in the strong type (p, p) inequality.

The Jones factorization theorem and the Rubio de Francia Extrapolation theorem are two essential and closely connected findings in the study of weighted norm inequalities. Jones factorization theorem resembles with the property 3.4.

The study of optimal quantitative estimates for the norm, $\|T\|_{L^p(w)}$, whenever $w \in A_p$ is a crucial topic in theory of weighted norm inequalities.

Buckley [6] first studied the question for the Hardy-Littlewood maximal operator M, and proved the estimate

$\|Mf\|_{L^p(w)} \le C_{n,p}[w]_{A_p}^{1/p-1}||f||_{L^p(w)}$.

For the chronology of the linear estimate of the type $\|Tf\|_{L^2(w)} \le C[w]_{A_2}\|f\|_{L^2(w)}$ we refer, page 173 in [7].

1.3 Significance of the Study

Weighted estimates holds significant importance in several domains, including Fourier analysis, complex analysis, approximation theory, partial differential equations, theory of quasi-conformal mappings, operator theory, regularity theory of Beltrami equations [7]. The idea of $A_p$weight is fundamental to weight theory and serves as a stepping stone. For more detail of weight theory, we refer [8, 9, 10, 11, 12].

2 . BASIC NOTATIONS AND DEFINITIONS

The necessary notations and definitions used in this work are as follows.

2.1 Notations

- $\mathrm{w(E)} = \int_{\mathrm{E}} \mathrm{w(x)\,dx}$ denotes the w-measure of the set E
- $|Q|$ is Lebesgue measure of the set Q
- $\langle w\rangle_Q = \frac{1}{|Q|}\int_Q w(x)dx$
- $L^p(\mathbb{R}^n, w)$ or simply $L^p(w) := \{f : \|f\|_{L^p(\mathbb{R}^n,w)} < \infty$ denotes the weighted Lp space, where $\|f\|_{L^p(\mathbb{R}^n,w)} := \left(\int_{\mathbb{R}^n}|f(x)|^p w(x)\,dx\right)^{\frac{1}{p}}$.

2.2 Definitions

Definition 2.2.1

A weight is locally integrable function on $\mathbb{R}^n$ that takes values

in the interval $(0,\infty)$ almost everywhere. So by definition a weight function can be zero or infinity only on a set whose Lebesgue measure is zero and w-measure of the measurable set E is defined as
$w(E)=\int_E w(x)\,dx$ [9, 10].

Definition 2.2.2
Let, $1\le p<\infty$. A weight, $w\in L^1_{loc}(\mathbb{R}^n)$, with $w(x)\ge 0$ for almost every $x\in\mathbb{R}^n$ is said to be an A_p weight if there exists a constant C, independent of Q, such that
$\frac{1}{|Q|}\int_Q w(x)dx\left(\frac{1}{|Q|}\int_Q w(x)^{-\frac{1}{p-1}}dx\right)\le C$ for every $Q\in\mathbb{R}^n$.
The Muckenhoupt characteristic constant or simply A_p constant of w represented by $[w]_{A_p}$ is the smallest constant C for which the inequality is true, where the supremum is taken over all the cubes whose sides are parallel to coordinate axes. Thus
$[w]_{A_p}:=Sup_{Qin\,\mathbb{R}^n}\left(\frac{1}{|Q|}\int_Q w(x)\,dx\right)\left(\frac{1}{|Q|}\int_Q w(x)^{-\frac{1}{p-1}}dx\right)^{p-1}$.
w is said to be in A_p class and we denote $w\in A_p$ [7, 9, 10, 11, 12, 13].

Definition 2.2.3
A finite, strictly positive and locally integrable function w is said to be an A_1 weight or in A_1 class if there exists a constant $C>0$ such that $Mw(x)=Cw(x)$ for $x\in\mathbb{R}^n$ a.e. and M is uncentered Hardy Littlewood maximal function. $[w]_{A_1}$ is the minimum of C satisfying the inequality [9, 10, 13].

Definition 2.2.4
Given a locally integrable function f on $\mathbb{R}^n$ the Hardy-Littlewood maximal function Mf of f is defined by $Mf(x):=Sup_{x\in Q}\frac{1}{|Q|}\int_Q|f(y)|\,dy, x\in\mathbb{R}^n$, where the supremum is taken over all cubes containing x. The operator, $M:f\to Mf$ is called Hardy-Littlewood maximal operator [8, 10, 11].

3. PROPERTIES [9, 10]

Property 3.1
$[\tau^z(w)]_{A_p}=[w]_{A_p}$, where $\tau^z(w)(x)=w(x-z), z\in\mathbb{R}^n$.
Proof: We have by definition,
$$[\tau^z(w)]_{A_p}=$$
$$Sup_{Q\text{ in }\mathbb{R}^n}\left(\frac{1}{|Q|}\int_Q\tau^z(w)\,dx\right)\left(\frac{1}{|Q|}\int_Q\tau^z(w)^{-\frac{1}{p-1}}dx\right)^{p-1}.$$
$$\Rightarrow [\tau^z(w)]_{A_p}=Sup_{Q\text{ in }\mathbb{R}^n}\left(\frac{1}{|Q|}\int_Q w(x-z)\,dx\right)\left(\frac{1}{|Q|}\int_Q w(x-z)^{-\frac{1}{p-1}}dx\right)^{p-1}$$
Put, $x-z=y\Rightarrow dx=dy$
$$\therefore\ [\tau^z(w)]_{A_p}$$
$$=Sup_{Q\text{ in }\mathbb{R}^n}\left(\frac{1}{|Q|}\int_Q w(y)\,dy\right)\left(\frac{1}{|Q|}\int_Q w(y)^{-\frac{1}{p-1}}dy\right)^{p-1}$$
$$=[w]_{A_p}.$$

Property 3.2
If $w\in A_p$, then the function $\lambda w\in A_p$. Moreover, $[\lambda w]_{A_p}=[w]_{A_p}$.
Proof: We have,
$$[\lambda w]_{A_p}=Sup_{Q\,in\,\mathbb{R}^n}\left(\frac{1}{|Q|}\int_Q(\lambda w)\,dx\right)\left((\lambda w)^{-\frac{1}{p-1}}dx\right)^{p-1}$$
$$\Rightarrow [\lambda w]_{A_p}$$
$$=Sup_{Q\,in\,\mathbb{R}^n}\frac{1}{\lambda}\left(\frac{1}{|Q|}\int_Q w(x)\,dx\right)\lambda^{-1}\left(w(x)^{-\frac{1}{p-1}}dx\right)^{p-1}$$
$$\Rightarrow [\lambda w]_{A_p}=Sup_{Q\,in\,\mathbb{R}^n}\left(\frac{1}{|Q|}\int_Q w(x)\,dx\right)\left(w(x)^{-\frac{1}{p-1}}\right)^{p-1}$$
$$\Rightarrow [\lambda w]_{A_p}=[w]_{A_p}.$$

Property 3.3
If $\in A_p$, for some $1\le p<\infty$ and non-negative measurable function k such that k, k^{-1} are in $L^\infty(\mathbb{R}^n)$ then $kw\in A_p$.
Proof: We have,
$$\left(\frac{1}{|Q|}\int_Q(kw)(x)\,dx\right)\left(\frac{1}{|Q|}\int_Q(kw)\,(x)^{-\frac{1}{p-1}}dx\right)^{p-1}$$
$$=\left(\frac{1}{|Q|}\int_Q k(x)(w)(x)\,dx\right)\left(\frac{1}{|Q|}\int_Q k(x)^{-\frac{1}{p-1}}(w)\,(x)^{-\frac{1}{p-1}}dx\right)^{p-1}$$
$$\le\left(\frac{1}{|Q|}\int_Q\|k\|_{L^\infty}w(x)\,dx\right)\left(\frac{1}{|Q|}\int_Q\|k^{-1}\|_{L_\infty}^{\frac{1}{p-1}}w(x)^{-\frac{1}{p-1}}dx\right)^{p-1}$$
$$\le\|k\|_{L^\infty}\|k^{-1}\|_{L^\infty}[w]_{A_p}<\infty$$
$$\Rightarrow\ Sup_{Q\,in\,\mathbb{R}^n}\left(\frac{1}{|Q|}\int_Q(kw)(x)\,dx\right)\left(\frac{1}{|Q|}\int_Q(kw)\,(x)^{-\frac{1}{p-1}}dx\right)^{p-1}$$
$$<\infty.$$

Property 3.4
If $w_1,\ w_2\in A_1,$ then $w_1w_2^{1-p}\in A_p$.
Proof: Let, $w_1,w_2\in A_1$. Then by definition there exists a constant C such that
$Mw_i(x)\le Cw_i(x),\ i=1,2.$
$$\Rightarrow\frac{1}{|Q|}\int_Q w_i(x)\,dx\le[w_i]_{A_1}w_i(x)\Rightarrow\frac{1}{w_i(x)}\le[w_i]_{A_1}\frac{|Q|}{\int_Q w_i(x)\,dx}$$
$i.e.\ \frac{1}{w_i(x)}\le[w_i]_{A_1}\frac{|Q|}{w_i(Q)}$ for $x\in\mathbb{R}^n$ $a.e.$
Now, $\frac{1}{|Q|}\int_Q w_1(x)\,w_2(x)^{1-p}dx=\frac{1}{|Q|}\int_Q w_1(x)\left(\frac{1}{w_2(x)}\right)^{p-1}dx$
$$\le[w_2]_{A_1}^{p-1}\left(\frac{|Q|}{w_2(Q)}\right)^{p-1}\frac{1}{|Q|}\int_Q w_1(x)\,dx$$
$$=[w_2]_{A_1}^{p-1}\left(\frac{|Q|}{w_2(Q)}\right)^{p-1}\frac{w_1(Q)}{|Q|}$$
Also,
$$\left(\frac{1}{|Q|}\int_Q(w_1(x)w_2(x)^{1-p})^{-\frac{1}{p-1}}dx\right)^{p-1}$$
$$=\left(\frac{1}{|Q|}\int_Q w_1(x)^{-\frac{1}{p-1}}w_2(x)\,dx\right)^{p-1}$$
$$=\left(\frac{1}{|Q|}\int_Q\left(\frac{1}{w_1(x)}\right)^{\frac{1}{p-1}}w_2(x)\,dx\right)^{p-1}$$
$$\le[w_1]_{A_1}\frac{|Q|}{w_1(Q)}\left(\frac{1}{|Q|}\int_Q w_2(x)\,dx\right)^{p-1}$$
$$=[w_1]_{A_1}\frac{|Q|}{w_1(Q)}\left(\frac{w_2(Q)}{|Q|}\right)^{p-1}$$
Thus we have,

$\left(\frac{1}{|Q|}\int_Q w_1(x)\,w_2(x)^{1-p}dx\right)\left(\frac{1}{|Q|}\int_Q(w_1(x)w_2(x)^{1-p})^{-\frac{1}{p-1}}dx\right)^{p-1}\le[w_1]_{A_1}[w_2]_{A_1}^{p-1}<\infty.$

Property 3.5

If $w \in A_p$ and $a \in \mathbb{R}, a \neq 0$, then the function $\delta_a w \in A_p$, where $\delta_a w(x) = w(ax)$. Moreover, $[w]_{A_p} = [\delta_a w]_{A_p}$.

Proof: We have,

$$Sup_{Q\ in\ \mathbb{R}^n}\left(\frac{1}{|Q|}\int_Q w(ax)\,dx\right)\left(\frac{1}{|Q|}\int_Q w(ax)^{-\frac{1}{p-1}}\,dx\right)^{p-1}$$
$$= Sup_{Q\ in\ \mathbb{R}^n}\left(\frac{1}{|Q|}\int_Q w(y)\frac{dy}{a}\right)\left(\frac{1}{|Q|}\int_Q w(y)^{-\frac{1}{p-1}}\,dy/a^{-\frac{1}{p-1}}\right)^{p-1}$$
$$= Sup_{Q\ in\ \mathbb{R}^n}\left(\frac{1}{|Q|}\int_Q w(x)\,dx\right)\left(\frac{1}{|Q|}\int_Q w(x)^{-\frac{1}{p-1}}\,dx\right)^{p-1}$$

Hence the property follows.

Property 3.6

$$\left[w^{-\frac{1}{p-1}}\right]_{A_{p'}} = [w]_{A_p}^{\frac{1}{p-1}}.$$

Proof: We have,

$$[w]_{A_p}^{\frac{1}{p-1}} = \left[Sup_Q\langle w\rangle_Q\left\langle w^{-\frac{1}{p-1}}\right\rangle_Q^{p-1}\right]^{\frac{1}{p-1}}$$
$$= Sup_Q\langle w\rangle_Q^{\frac{1}{p-1}}\left\langle w^{-\frac{1}{p-1}}\right\rangle_Q$$
$$= Sup_Q\left\langle w^{-\frac{1}{p-1}}\right\rangle_Q\left\langle\left(w^{-\frac{1}{p-1}}\right)^{-\frac{1}{p'-1}}\right\rangle_Q^{p'-1}$$
$$\Rightarrow [w]_{A_p}^{\frac{1}{p-1}} = \left[w^{-\frac{1}{p-1}}\right]_{A_{p'}}$$

Property 3.7

$[w]_{A_p} \geq 1$ for all $w \in A_p$. Equality holds if and only if w is a constant.

Proof: We have,

$$|Q| = \int_Q w(x)^{\frac{1}{p}}\left(\frac{1}{w(x)}\right)^{\frac{1}{p}}dx$$

$|Q| \leq \left(\int_Q w(x)^{\frac{1}{p}p}\,dx\right)^{\frac{1}{p}}\left(\int_Q\left(\frac{1}{w(x)}\right)^{\frac{1}{p}p'}dx\right)^{\frac{1}{p'}}$, using Hölder's inequality, we have

$$= \left(\int_Q w(x)\,dx\right)^{\frac{1}{p}}\left(\int_Q\left(\frac{1}{w(x)}\right)^{\frac{1}{p-1}}dx\right)^{\frac{1}{p'}}$$
$$\Rightarrow 1 \leq \left(\frac{1}{|Q|}\int_Q w(x)\,dx\right)^{\frac{1}{p}}\left(\frac{1}{|Q|}\int_Q (w(x))^{-\frac{1}{p-1}}dx\right)^{\frac{1}{p'}}$$
$$\Rightarrow 1 \leq Sup_Q\left(\frac{1}{|Q|}\int_Q w(x)\,dx\right)\left(\frac{1}{|Q|}\int_Q w(x)^{-\frac{1}{p-1}}dx\right)^{\frac{p}{p'}}$$
$$\Rightarrow 1 \leq Sup_Q\left(\frac{1}{|Q|}\int_Q w(x)\,dx\right)\left(\frac{1}{|Q|}\int_Q w(x)^{-\frac{1}{p-1}}dx\right)^{p-1}$$

Hence, $[w]_{A_p} \geq 1$.

Again we have, $1 = \frac{1}{|Q|}\int_Q dx$

$$\Rightarrow 1 = \frac{1}{|Q|}\int_Q w(x)^{\frac{1}{p}}w(x)^{-\frac{1}{p}}dx$$

Equality holds in Hölder's inequality only when $\alpha|f|^p = \beta|g|^{p'}$ for any constants α, β.

$$\Leftrightarrow \alpha\left|w^{\frac{1}{p}}\right|^p = \left|w^{-\frac{1}{p}}\right|^{p'}$$
$$\Leftrightarrow \alpha w = \beta w^{-\frac{p'}{p}}$$
$$\Leftrightarrow w = \left(\frac{\beta}{\alpha}\right)^{\frac{p}{p+p'}},$$ which is a constant.

Property 3.8

The classes A_p are increasing as p increases; precisely for $1 \leq p < \infty$ we have $A_p \subset A_q$, and $[w]_{A_q} \leq [w]_{A_p}$.

Proof: We have, $1 \leq p < q < \infty$. Since, $p < q \Rightarrow 1 - \frac{1}{p} < 1 - \frac{1}{q} \Rightarrow \frac{1}{p'} < \frac{1}{q'} \Rightarrow q' < p' \Rightarrow q' - 1 < p' - 1$.

$$\Rightarrow \|w^{-1}\|_{L^{q'-1}\left(Q,\frac{dx}{|Q|}\right)} \leq \|w^{-1}\|_{L^{p'-1}\left(Q,\frac{dx}{|Q|}\right)}$$
$$\Rightarrow \left(\int_Q (w^{-1})^{q'-1}\frac{dx}{|Q|}\right)^{\frac{1}{q'-1}} \leq \left(\int_Q (w^{-1})^{p'-1}\frac{dx}{|Q|}\right)^{\frac{1}{p'-1}}$$
$$\Rightarrow \left(\frac{1}{|Q|}\int_Q (w^{-1})^{q'-1}dx\right)^{\frac{1}{q'-1}} \leq \left(\frac{1}{|Q|}\int_Q (w^{-1})^{p'-1}dx\right)^{\frac{1}{p'-1}}$$
$$\Rightarrow \left(\frac{1}{|Q|}\int_Q (w^{-1})^{\frac{1}{q-1}}dx\right)^{q-1} \leq \left(\frac{1}{|Q|}\int_Q (w^{-1})^{\frac{1}{p-1}}dx\right)^{p-1}$$

Which implies,

$$Sup_{Q\ in\ \mathbb{R}^n}\left(\frac{1}{|Q|}\int_Q w(x)\,dx\right)\left(\frac{1}{|Q|}\int_Q (w^{-1})^{\frac{1}{q-1}}dx\right)^{q-1}$$
$$\leq Sup_{Q\ in\ \mathbb{R}^n}\left(\frac{1}{|Q|}\int_Q w(x)\,dx\right)\left(\frac{1}{|Q|}\int_Q (w^{-1})^{\frac{1}{p-1}}dx\right)^{p-1}$$
$$\therefore [w]_{A_q} \leq [w]_{A_p}.$$

Property 3.9

If $p > 1$ then $w \in A_p$ if and only if $w^{1-p'} \in A_{p'}$, where p' is the conjugate exponent of p such that $\frac{1}{p} + \frac{1}{p'} = 1$.

Proof: " ⇒ " We have,

$$\left(\frac{1}{|Q|}\int_Q w(x)^{1-p'}dx\right)\left(\frac{1}{|Q|}\int_Q \left(w(x)^{1-p'}\right)^{-\frac{1}{p'-1}}dx\right)^{p'-1}$$
$$= \left(\frac{1}{|Q|}\int_Q w(x)^{-\frac{1}{p-1}}dx\right)\left(\frac{1}{|Q|}\int_Q w(x)\,dx\right)^{\frac{1}{p-1}}$$
$$= \left[\left(\frac{1}{|Q|}\int_Q w(x)^{-\frac{1}{p-1}}dx\right)^{p-1}\left(\frac{1}{|Q|}\int_Q w(x)\,dx\right)\right]^{\frac{1}{p-1}}$$
$$\leq \left[Sup_Q\left(\frac{1}{|Q|}\int_Q w(x)^{-\frac{1}{p-1}}dx\right)^{p-1}\left(\frac{1}{|Q|}\int_Q w(x)\,dx\right)\right]^{\frac{1}{p-1}}$$
$$= \left([w]_{A_p}\right)^{\frac{1}{p-1}}$$

This shows that $w(x)^{1-p'} \in A_{p'}$.

" ⇐ " Conversely assume that $w(x)^{1-p'} \in A_{p'}$ with $1 < p < \infty$. We have,

$$\left[\left(\frac{1}{|Q|}\int_Q w(x)\,dx\right)\left(\frac{1}{|Q|}\int_Q w(x)^{-\frac{1}{p-1}}dx\right)^{p-1}\right]^{\frac{1}{p-1}}$$

$$= \left(\frac{1}{|Q|}\int_Q w(x)\,dx\right)^{\frac{1}{p-1}}\left(\frac{1}{|Q|}\int_Q w(x)^{-\frac{1}{p-1}}\,dx\right)$$
$$= \left(\frac{1}{|Q|}\int_Q w(x)\,dx\right)^{p'-1}\left(\frac{1}{|Q|}\int_Q (w(x))^{1-p'}\,dx\right)$$
$$= \left[\frac{1}{|Q|}\int_Q \left(w(x)^{1-p'}\right)^{-\frac{1}{p'-1}}dx\right]^{p'-1}\left(\frac{1}{|Q|}\int_Q w(x)^{1-p'}\,dx\right)$$
$$\leq Sup_Q\left(\frac{1}{|Q|}\int_Q w(x)^{1-p'}\,dx\right)\left[\frac{1}{|Q|}\int_Q \left(w(x)^{1-p'}\right)^{-\frac{1}{p'-1}}dx\right]^{p'-1}$$
$$= \left[w(x)^{1-p'}\right]_{A_{p'}} \Rightarrow w \in A_p$$

Property 3.10

Let, $v,\ w \in A_p$ for $1 < p < \infty$. Then, $max\{v(x), w(x)\} \in A_p$.

Proof: Since, $v,\ w \in A_p, max\{v(x), w(x)\}$ is a weight. We have,

$$\frac{1}{|Q|}\int_Q max\{v(x), w(x)\}\,dx \leq \frac{1}{|Q|}\int_Q v(x)\,dx + \frac{1}{|Q|}\int_Q w(x)\,dx$$
$$= \frac{1}{|Q|}\int_Q v(x)\,dx\left(\frac{1}{|Q|}\int_Q v(x)^{-\frac{1}{p-1}}dx\right)^{p-1}\left(\frac{1}{|Q|}\int_Q v(x)^{-\frac{1}{p-1}}dx\right)^{1-p}$$
$$+\frac{1}{|Q|}\int_Q w(x)\,dx\left(\frac{1}{|Q|}\int_Q w(x)^{-\frac{1}{p-1}}dx\right)^{p-1}\left(\frac{1}{|Q|}\int_Q w(x)^{-\frac{1}{p-1}}dx\right)^{1-p}$$
$$\leq [v]_{A_p}\left(\frac{1}{|Q|}\int_Q v(x)^{-\frac{1}{p-1}}dx\right)^{1-p}$$
$$+\,[w]_{A_p}\left(\frac{1}{|Q|}\int_Q w(x)^{-\frac{1}{p-1}}dx\right)^{1-p}$$
$$\leq \left([v]_{A_p} + [w]_{A_p}\right)\left(\frac{1}{|Q|}\int_Q max\{v(x), w(x)\}^{-\frac{1}{p-1}}dx\right)^{1-p}$$
$$\Rightarrow \frac{1}{|Q|}\int_Q max\{v(x), w(x)\}\,dx\left(\frac{1}{|Q|}\int_Q max\{v(x), w(x)\}^{-\frac{1}{p-1}}\right)^{p-1}$$
$$\leq [v]_{A_p} + [w]_{A_p}$$

Thus, $max\{v(x), w(x)\} \in A_p$.

Property 3.11.

$\lim_{q\to 1+}[w]_{A_q} = [w]_{A_1}$ if $w \in A_1$.

Proof: A weight w is said to be of class A_q if

$$[w]_{A_q}$$
$$:= Sup_{Q\ in\ \mathbb{R}^n}\left(\frac{1}{|Q|}\int_Q w(x)\,dx\right)\left(\frac{1}{|Q|}\int_Q w(x)^{-\frac{1}{q-1}}dx\right)^{q-1}$$
$$< \infty$$
$$\Rightarrow [w]_{A_q}$$
$$= Sup_{Q\ in\ \mathbb{R}^n}\left(\frac{1}{|Q|}\int_Q w(x)\,dx\right)\frac{1}{|Q|^{q-1}}\left(\int_Q w(x)^{-\frac{1}{q-1}}dx\right)^{q-1}$$
$$\Rightarrow [w]_{A_q}$$
$$= Sup_Q\left(\frac{1}{|Q|}\int_Q w(x)\,dx\right)\frac{1}{|Q|^{q-1}}\left(\int_Q (w(x)^{-1})^{\frac{1}{q-1}}dx\right)^{q-1}$$
$$\Rightarrow [w]_{A_q} = Sup_Q\left(\frac{1}{|Q|}\int_Q w(x)\,dx\right)\frac{1}{|Q|^{q-1}}\|w^{-1}\|_{L^{\frac{1}{q-1}}(Q,dx)}$$

When $q \to 1+$, we have

$$[w]_{A_q} = Sup_Q\left(\frac{1}{|Q|}\int_Q w(x)\,dx\right)\frac{1}{|Q|^{q-1}}\|w^{-1}\|_{L^{\infty}(Q,dx)}$$
$$\therefore \lim_{q\to 1+}[w]_{A_q} = [w]_{A_1}.$$

Property 3.12.

An equivalent characterization of A_p constant of w is

$$[w]_{A_p} = Sup_{Q\ in\ \mathbb{R}^n}Sup_{f\ in\ L^p(Q,wdx),|f|>0\ a.e.on\ Q}\left\{\frac{\left(\frac{1}{|Q|}\int_Q|f(t)|dt\right)^p}{\frac{1}{w(Q)}\int_Q|f(t)|^p w(t)dt}\right\}.$$

Proof: We have,

$$\left(\frac{1}{|Q|}\int_Q|f(x)|\,dx\right)^p = \left(\frac{1}{|Q|}\int_Q|f(x)|w(x)^{\frac{1}{p}}w(x)^{-\frac{1}{p}}dx\right)^p$$

Applying Hölder's inequality for the functions $|f(x)|^p w(x)^{\frac{1}{p}}$ and $w(x)^{-\frac{1}{p}}$ with conjugate exponents $p,\ p'$,

$$\left(\frac{1}{|Q|}\int_Q|f(x)|\,dx\right)^p$$
$$\leq \frac{1}{|Q|^p}\left[\left(\int_Q\left(|f(x)|w(x)^{\frac{1}{p}}\right)^p dx\right)^{\frac{1}{p}}\left(\int_Q\left(w(x)^{-\frac{1}{p}}\right)^{p'}dx\right)^{\frac{1}{p'}}\right]^p$$
$$= \frac{1}{|Q|^p}\left(\int_Q|f(x)|^p\,w(x)dx\right)\left(\int_Q w(x)^{-\frac{p'}{p}}dx\right)^{\frac{p}{p'}}$$
$$= \frac{1}{|Q|^p}\left(\int_Q|f(x)|^p\,w(x)dx\right)\left(\int_Q w(x)^{-\frac{1}{p-1}}dx\right)^{p-1}$$
$$\left(\frac{1}{|Q|}\int_Q|f(x)|\,dx\right)^p$$
$$\leq \left(\frac{1}{w(Q)}\int_Q|f(x)|^p\,w(x)dx\right)\left(\frac{1}{|Q|}\int_Q w(x)\,dx\right)$$
$$\left(\frac{1}{|Q|}\int_Q w(x)^{-\frac{1}{p-1}}dx\right)^{p-1} \leq \frac{1}{w(Q)}\int_Q|f(x)|^p w(x)\,dx\,[w]_{A_p}$$
$$\Rightarrow \frac{\left(\frac{1}{|Q|}\int_Q|f(x)|\,dx\right)^p}{\frac{1}{w(Q)}\int_Q|f(x)|^p\,w(x)dx} \leq [w]_{A_p} \quad \dots\ \dots\ (1)$$

Also set $f = (w+\varepsilon)^{-\frac{p'}{p}}$ in $Sup_{Q\ in\ \mathbb{R}^n}Sup_{f\ in\ L^p(Q,wdx),|f|>0\ a.e.on\ Q}\left\{\frac{\left(\frac{1}{|Q|}\int_Q|f(t)|dt\right)^p}{\frac{1}{w(Q)}\int_Q|f(t)|^p w(t)dt}\right\}$, we have

$$Sup_{Q\ in\ \mathbb{R}^n}Sup_{f\ in\ L^p(Q,wdx),|f|>0\ a.e.on\ Q}\left\{\frac{\left(\frac{1}{|Q|}\int_Q(w+\varepsilon)(t)^{-\frac{p'}{p}}dt\right)^p}{\frac{1}{w(Q)}\int_Q(w+\varepsilon)(t)^{-p'}w(t)\,dt}\right\}$$
$$= Sup_{Q\ in\ \mathbb{R}^n}Sup_{f\ in\ L^p(Q,wdx),|f|>0\ a.e.on\ Q}\frac{1}{|Q|}w(Q)\left(\frac{1}{|Q|}\int_Q(w+\varepsilon)^{-\frac{p'}{p}}(t)\,dt\right)^p\left(\frac{1}{|Q|}\int_Q\frac{w(t)}{(w+\varepsilon)(t)^{p'}}dt\right)^{-1}$$
$$\geq Sup_{Q\ in\ \mathbb{R}^n}Sup_{f\ in\ L^p(Q,wdx),|f|>0\ a.e.on\ Q}\frac{1}{|Q|}w(Q)\left(\frac{1}{|Q|}\int_Q(w+\varepsilon)^{-\frac{p'}{p}}(t)\,dt\right)^p\left(\frac{1}{|Q|}\int_Q\frac{(w+\varepsilon)(t)}{(w+\varepsilon)(t)^{p'}}dt\right)^{-1}$$
$$= Sup_{Q\ in\ \mathbb{R}^n}Sup_{f\ in\ L^p(Q,wdx),|f|>0\ a.e.on\ Q}\frac{1}{|Q|}w(Q)\left(\frac{1}{|Q|}\int_Q(w+\varepsilon)(t)^{-\frac{p'}{p}}dt\right)^p\left(\frac{1}{|Q|}\int_Q(w+\varepsilon)(t)^{1-p'}dt\right)^{-1}$$
$$= Sup_{Q\ in\ \mathbb{R}^n}Sup_{f\ in\ L^p(Q,wdx),|f|>0\ a.e.on\ Q}\frac{1}{|Q|}\int_Q w(t)\,dt\left(\frac{1}{|Q|}\int_Q(w+\varepsilon)(t)^{-\frac{1}{p-1}}dt\right)^{p-1}$$
$$= [w]_{A_p}, \text{ when } \varepsilon \to 0.$$

$$\Rightarrow Sup_{Q\ in\ \mathbb{R}^n} Sup_{f\ in\ L^p(Q,wdx),|f|>0\ a.e.on\ Q} \left\{ \frac{\left(\frac{1}{|Q|}\int_Q (w+\varepsilon)(t)^{-\frac{p'}{p}}\,dt\right)^p}{\frac{1}{w(Q)}\int_Q (w+\varepsilon)(t)^{-p'}w(t)\,dt} \right\} \geq [w]_{A_p} \quad \ldots\ \ldots \quad (2)$$

From inequality (1) and (2) the property follows.

Property 3.13

The measure $w(x)dx$ is doubling, precisely for all $\lambda > 1$ and all cubes Q we have $w(\lambda Q) \leq \lambda^{np}[w]_{A_p} w(Q)$.

Proof: Set $f = \chi_Q$ and λQ for Q in the inequality

$$\frac{\left(\frac{1}{|Q|}\int_Q |f(t)|\,dt\right)^p}{\frac{1}{w(Q)}\int_Q |f(t)|^p w(t)\,dt} \leq [w]_{A_p}$$

we have $\frac{\left(\frac{1}{|\lambda Q|}\int_Q \chi_Q dt\right)^p}{\frac{1}{w(\lambda Q)}\int_Q \lambda_Q w(t)\,dt} \leq [w]_{A_p}$

$$\Rightarrow \frac{\frac{1}{|\lambda Q|^p}\left(\int_Q \chi_Q\,dt\right)^p}{\frac{1}{w(\lambda Q)}\int_Q \lambda_Q w(t)\,dt} \leq [w]_{A_p} \Rightarrow \frac{w(\lambda Q)\left(\int_Q \chi_Q\,dt\right)^p}{\int_Q \chi_Q w(t)\,dt}$$

$$\leq [w]_{A_p}|\lambda Q|^p \Rightarrow w(\lambda Q)|Q|^p$$
$$\leq [w]_{A_p}|\lambda Q|^p w(Q) \Rightarrow w(\lambda Q)|Q|^p$$
$$\leq [w]_{A_p}\lambda^{np}|Q|^p w(Q) \Rightarrow w(\lambda Q)$$
$$\leq [w]_{A_p}\lambda^{np} w(Q).$$

4. CONCLUSION

We revisit the literature on weighted inequalities and discuss some properties of A_p weight functions with proof that will enhance the understanding of weight theory and set the course for further study and research in this domain.

CONFLICT OF INTEREST

No any conflict 0f interest.

ACKNOWLEDGMENTS

I would like to express my due gratitude and sincerethank to my Ph. D. supervisor and co-supervisor Prof. Dr. Chet Raj Bhatta (HoD at CDM, IoST, TU) and Assoc. Prof. Dr. Ishwari Jang Kunwar (FVSU,USA) respectively for their invaluable motivation, feedback, guidance and suggestion. In addition I am also in debit of the following institutions: (a) Siddhanath Science Campus, Mahendranagar (b) Central Department of Mathematics, Kirtipur (c) Institute of Science and Technology, Kirtipur (d) University Grant Commission, Sanothimi, Bhaktapur for providing financial assistance through PhD fellowship award (PhD-7980-S&T-12)

REFERENCES

[1] B. Muckenhoupt, Weighted norm inequalities for the maximal function, *Transactions of the American Mathematical Society*, **165** (1972) 207-256. https://www.ams.org/journals/tran/1972-165-00/S0002-9947-1972-0293384-6/S0002-9947-1972-0293384-6.pdf

[2] E.M. Dyn'kin, B.P. Osilenker, Weighted estimates of singular intgrals and their applications, *Journal of Soviet Mathematics,* **30** (1985) 2094-2154. https://link.springer.com/article/10.1007/BF02105397

[3] D. Cruz-Uribe, OFS, Matrix weights, singular integrals, Jones factorization and Rubio de Francia extrapolation (202). htt ps://doi.org/10.48550/arXiv.2304.03887

[4] H. Richard, B. Muckenhoupt, R. Wheeden, Weighted norm inequalities for the conjugate function and Hilbert transform, *Transactions of American Mathematical Society*, **176** (1973) 227-251. https://www.ams.org/tran/1973-176-00/S0002-9947-1973-0312139-8/

[5] R. Coifman, C. Fefferman, Weighted norm inequalities for maximal functions and singular integrals, *Studia* Mathematica, **51** (1974), 241-250. https://eudml.org/doc/217916

[6] S.M. Buckley, Estimates for operator norms on weighted spaces and reverse Jensen inequality, *Transaction of American Mathematical Society,* (1993) 253-272. https://www.ams.org/tran/1993-340-01/S0002-9947-1993-1124164-0/

[7] M.C. Pereyra, New Trends in Applied Harmonic Analysis, **2** (2019) 159-239. http://mate.dm.uba.ar/~hafg/papers/book-2.pdf

[8] J.G. Cuerva, J.R.D. Francia, Weighted norm inequalities and related topics, New York, (1985) 385-464. https://books.google.com/books/about/Weighted_Norm_Inequalities_and_Related_T.html?id=AFErOJHeLQoC

[9] L. Grafakos, Modern Fourier Analysis, Columbia Missouri, (2009) 279-335. https://www.academia.edu/117844414/Modern_Fourier_Analysis

[10] J. Kinnunen, Harmonic Analysis, 2022. (pp. 57-84) https://math.aalto.fi/~jkkinnun/files/harmonic_analysis.pdf

[11] E.M. Stein, T.S. Murphy, Harmonic Analysis: Real variable methods, orthogonality, and oscillatory integrals, Princetor University Press Princeton, New Jersey, **(1993)** 193-218. https://doi.org/10.1515/9781400883929

[12] J.D. Zuazo, Fourier Analysis, Providence, Rhode Island, (2001) 133-147. https://www.scribd.com/document/726164945/Duoandikoetxea-J-Fourier-analysis-AMS-2001

[13] I. Kunwar, Multilinear dyadic operators and their commutators, *ANNALI DELL'UNIVERSITA'DE FERRARA*, **64** (2018), 111-144. https://arxiv.org/abs/1512.03865 or https://doi.org/10.48550/arXiv.1512.03865

Analysis of Metaheuristic Solutions to the Response Time Variability Problem

Rajendra Prasad joshi[1*]

[1]Department of Computer Science & Information Technology, Siddhanath Science Campus, Tribhuvan University, Mahendranagar, Nepal

Research Article

ISSN: 3059-9504 (online)
Doi: xxxx

Article History

Received: November 12, 2024
Revised: November 28, 2024
Accepted: December 12, 2024
Published: December 25, 2024

Keywords

Greedy Search, Multi-Start, Optimization, Response Time Variability

***Corresponding author**
Email: rajendra.joshi@snsc.tu.edu.np
Phone: +977-9849555467

ABSTRACT

The problem of variation in the response time is known as response time variability problem (RTVP). It is combinatorial NP-hard problem which has a broad range of real-life applications. The RTVP arises whenever events, jobs, clients or products need to be sequenced so as to minimize the variability of the time they wait for their next turn in obtaining the resources they need to advance. In RTVP the concern is to find out near optimal sequence of jobs with objective of minimizing the response time variability. The metaheuristic approaches to solve the RTVP are: Multi-start (MS), Greedy Randomized Adaptive Search Procedure (GRASP) and Particle Swarm Optimization (PSO). In this paper, the computational result of MS and GRASP will be analyzed.

1. INTRODUCTION

The Response Time Variability Problem (RTVP) is a sequence optimization problem [1]. It was first reported in 1994 and first time solved by using a method called lottery scheduling [2]. It occurs in real-life situations in which jobs, clients, products or events need to be sequenced in order to minimize the variability in the time between two successive points at which they receive their necessary resources. The fair sequence concept has emerged from scheduling problem in different environments [1]. The common aim of scheduling problem is to minimize an objective function. The objective is to minimize the response time variability metric value of the solutions. The RTVP has been proved to be NP-hard [1]. Thus, this problem has been mostly solved by means of heuristic and metaheuristic methods [3].

The response time variability problem is formulated in [4]. Let n be the number of symbols (jobs), d_i the number of copies to be scheduled of symbol *i* (*i*=1…n) and D the total number of copies (equal to $\sum_{1\ldots d_i}$)

Consider a sequence $S=S_1S_2\ldots..S_D$ of length D where *i* (a client, a product, or a task) occurs exactly d_i times. Such a sequence is called feasible. Here s_j is the copy sequenced in position *j* of sequence *S* and S_1 immediately follows S_D. For any two consecutive occurrences of *i,* we define distance *t* between them as the number of positions that separate them plus 1. So there are d_i distances $t_1^i \ldots\ldots t_{d_i}^i$ for i.

So we have, $t_1^i \ldots\ldots t_{d_i}^i$ =D.

The average distance $t_i^{'}$ between the i's equals D/d_i

The response time variability for *i* is defined as

$$RTV_i = \sum_{1\le j\le d_i} (t_i^{'} - t_i^{'})^2$$

The total response time variability is defined as

$$RTV = \sum_{i=1}^{n} RTV_i = \sum_{i=1}^{n}\sum_{j=1}^{d_i} (t_j^i - t_i^{'})^2$$

An input to the total response time variability problem is a list of *n* positive integers $d_1 \le d_2 \le d_3 \le\ldots\ldots..\le d_n$ (the number of copies of each job). The solution to RTVP is a sequence S of jobs and the objective is to minimize the value of RTV obtained above.

Example:

Let n=3 with symbols A, B, C. Also consider d_A=2, d_B=2 and d_C=4. Thus D=8, t_A^i=4, t_B^i=4 and t_c^i=2. Then the sequence C A C B C B A C is a solution and has

RTV = $((5-4)^2 + (3-4)^2) + ((2-4)^2 + (6-4)^2) + ((2-2)^2 + (3-2)^2) = 12$

2. METAHEURISTIC METHODS

This section discusses the complexity of RTVP and introduces the metaheuristic methods for solving RTVP.

Complexity

The RTVP is difficult to be solved optimally. It has been proved to be NP-hard [5]. Many algorithms are proposed to find the near to optimal solution [6]. Some of the solutions based on metaheuristic procedures are: MS, GRASP and PSO.

Multi –Start (MS) Method

The multi-start is metaheuristic procedure for solving the RTVP [7]. It is a general scheme that consists of two phases. In the first phase obtains an initial solution and in the second phase improves the obtained initial solution by using the local optimization methods and select the best of one. The pseudo code of the adaptation of the multi-start methodis:

Let the value of the best solution found b $\bar{z} = \infty$.

1. While (actual time<execution time) do:
2. Get a random initial solution X.
3. Apply the local optimization to X and get X'.
4. If value (X') < $\bar{Z}$, then $\bar{Z}$ = value (X').

Random solutions are generated as follows. For each position from 1 to D in the solution, is randomly obtain, which product will be sequenced with a probability equal to the number of units of that type of product that remains to be sequenced divided by the total number of units that remains to be sequenced. A local optimization is performed iteratively in a neighborhood that is generated by interchanging each pair of

two consecutive units of the sequence that represent the current solution. The best solution in the neighborhood is chosen, the optimization ends when no neighboring solution is better than current solution.

The Greedy Randomized Adaptive Search Procedure (GRASP) Methods

The GRASP can be considered as a multi-start variant [8]. But the generation of initial solution is obtained by greedy method. In which random steps are added and choice of elements to be included in the sequence is adaptive. The probability of each job is proportional to the value of an associated index. The job to be sequenced is randomly selected from the list with a probability proportion to the value of its Webster index [9].

Let X_{ik} be the number of units of job i, that have been already sequenced in the sequence of length k, k=0, 1,……,d_i the number of units of the job i and D the total number of units; the value of the Webster index of product i to be sequenced position k+1 is $d_i/X_{ik}+\delta$.

Here δ is the Webster's parametric metrics, δ=1/2.

In the Jefferson's sequence the parametric matrices δ=1 used [10]. This parameter affects the relative priority of low decreased jobs and their position in the sequence. When δ is near to 0, low demand jobs will be positioned earlier in the solution but when δ is near to 1, low demand jobs will be positioned later in the solution.

Another form of GRASP algorithm can be obtained by using the insertion sequence as the initial sequence [8]. In insertion sequence, for more than two products, the problem is reduced in to two-product case [6]. Let the demands are $d_1 \leq \ldots\ldots\ldots\leq dn$. consider n-1 two case problem.

$$\boldsymbol{p_{n-1}} = (\boldsymbol{d_{n-1}}, \boldsymbol{d_n}), \qquad \boldsymbol{p_{n-2}} = \left(\boldsymbol{d_{n-2}}, \sum_{\boldsymbol{j=n-1}}^{\boldsymbol{n}} \boldsymbol{d_j}\right), \ldots, \boldsymbol{p_1} = \left(\boldsymbol{d_1}, \sum_{\boldsymbol{j=2}}^{\boldsymbol{n}} \boldsymbol{d_j}\right)$$

In each of the problem the first product is the original and second product will be the assumed product, and denoted by the *. Let the sequences s_{n-1}, s_{n-2} , ……. , s_1. be the optimal solution. For the given problems they can be obtained by using the two case problem. The solution is made up of the product j and *. The sequence of the original problem is built recursively by first replacing * in S_1 by S_2 to obtain $s_1^{'}$. Next * are replaced by S_3 in $s_1^{'}$ to obtain the solution S_1''.Sequence S_{n-1} replaces all the remaining * and obtain the final solution. This method is called insertion method [11].

3. RESULTS AND DISCUSSION

The metaheuristic algorithms have been run for 882 different instances, which are grouped into four different categories. Formation of category is based on [12]. Category 1 includes 162, category 2 includes 192, category 3 includes 282 and category 4 includes 246 instances. The corresponding instances are same for every category of different algorithms. The instances of first category CATEGORY 1 were generated using a random value of D between 25 and 50, and random value of n between 3 and 15. For the second category CATEGORY 2, D was between 50 and 100 and number of demands n between 3 and 30; for the third category CATEGORY 3 D was from 100 to 200 and n between 3 and 65; and finally for the forth class CATEGORY 4 number of copies are between 200 and 500 and number of demands are between 3 and 150. The instances have been generated by first fixing the total number of copies D and the number of demands n. For all instances and for each type of product i= 1,……, n, a random value of d_i is between 1 and D. The program has been executed to obtain the output of demands among which some of them were executed for several minutes.

The average initial RTV values(AIRTV), the average optimized values (AORTV) and the average number of iterations required to obtained the optimized sequence using in multi-start, $GRASP_{we}$ (GRASP use Wester's sequence as initial solution) and $GRASP_{je}$ (GRASP with use of Jeffersion's sequence as initial solution) metaheuristic algorithms [13]. The computational result is tabulated as:

Table 1: Computational result of MS method.

Category	Average initial RTV	Average optimal RTV	No. of iterations
Global	137515.75	326	1402
CAT 1	890	25	58
CAT 2	4837	57	192
CAT 3	34050	232	781
CAT 4	510286	990	4577

Table 2: Computational result of $GRASP_{we}$ method.

Category	Average initial RTV	Average optimal RTV	No. of iterations
Global	21352.50	292.5	929.25
CAT 1	144	38	22
CAT 2	1056	80	119
CAT 3	5114	315	726
CAT 4	79096	737	2850

Table 3: Computational result of GRASP method.

Category	Average initial RTV	Average optimal RTV	No. of iterations
Global	18698.25	244	629
CAT 1	143	29	21
CAT 2	941	63	95
CAT 3	4537	219	322
CAT 4	69172	665	2078

By analyzing these tables, for all instances in initial value of RTV the $GRASP_{je}$ is 12.43% better than $GRASP_{we}$ and 86.40% better than multi-start. In optimized RTV value $GRASP_{je}$ is 16.58% better than $GRASP_{we}$ and 25.15% better than multi-start. $GRASP_{je}$ also take the less number of iterations for obtaining the optimized solution i.e. it is faster than other two methods. The multi-start algorithm obtains the good averages for small instances (category 1 and category 2) but, poor average results for large instances (category 4). $GRASP_{je}$ and $GRASP_{we}$ gives the better result than MS method for large instances (category 4).

4. CONCLUSION

In the RTVP, the aim is to minimize variability in the distance between any two consecutive copies of the same symbol. i. e. to distribute the symbols as regular as possible. It is an NP-hard problem so metaheuristic methods are needed for solving real life problems. A computational experiment was done and its results show that on average the $GRASP_{je}$ is better than $GRASP_{we}$ and multi-start for small instances, multi-start is better metaheuristic method for solving RTVP. The $GRASP_{je}$ method has a stable behavior for small, medium and large instances**.**

DECLARATION OF COMPLETING INTEREST

The authors declare that they have no known competing interests or personal relationships that could have appeared to influence the work reported in this paper.

ACKNOWLEDGEMENT

Author would like to thanks Shiv Raj Pant for his encouragement and support.

REFERENCES

[1] A. Corominas, K. Wieslaw, N.M. Palli. "Response time variability." *Journal of Scheduling,* **10** (2007) 97-110. https://doi.org/10.1007/s10951-006-0002-8

[2] C.A. Waldspurger W.E. Weihl. Lottery Scheduling: Flexible Proportional-Share Resource Management. *First USENIX Symposium on Operating System Design and Implementation* (1994).

[3] A. Corominas, A. Garcia-Villoria, R. Pastor. Metaheuristic algorithmms hybridized with variable neighborhood search for solving response time variability problem. *Institute of Industrial and Control Engineering* (IOC),*U*niversitat Politecnuca de Catalunga (UPC*)*, Barcelona, Spain(2011). https://doi.org/10.1007/s11750-011-0175-y

[4] A. Corominas. Mathematical Programming Modeling of the Response Time Variability Problem. *European Journal of Operational Research,* **200** (2010) 347-357. https://doi.org/10.1016/j.ejor.2009.01.014

[5] A. Corominas W. Kubik,and N. M. Palli. Response time variability, IOC-DT-2004- 08. N.

[6] A. Garcia-Villoria, S. Salhi, A. Corominas, R. Pastor.. Hyper-Heuristic approaches for the response time variability problem. *European Journal of Operational Research*, **211** (2011) 160-169. https://doi.org/10.1016/j.ejor.2010.12.005

[7] A. Corominas, A. Garcia-Villoria, R. Pastor. A new metaheuristic procedure for improving the solution of the response time variability problem. *Scheduling and Sequencing* (2010)

[8] A. Corominas, W. Kubiak, R. Pastor. Heuristics for the response time variability problem. *Institute of industrial and control engineering* (2009). IOC-DT-P-2009-03.

[9] A. Garcia-Villoria, A. Corominas, X. Delorme, A. Dolgui, W. Kubiak,R. Pastor. A branch and bound algorithm for the Response time variability problem. *Journal of Scheduling,* (2012). https://doi.org/10.1007/s10951-012-0277-x

[10] A. Garcia-Villoria, R. Pastor. Solving the Response Time Variability Problem by Means of a Genetic Algorithm. *European Journal of Operational Research,* **202** (2010) 320-327. https://doi.org/10.1016/j.ejor.2009.05.024

[11] Moreno. Solving the Product Rate Variation Problem of Large Dimensions as an Assignment Problem. Doctoral Thesis (2004), DOE, UPC.

[12] J.W. Herrmann. Using Aggregation to Reduce Response Time Variability in Cycle Fair Sequences. *Tech. Rep. University of Maryland, USA*. (2008). https://doi.org/10.1007/s10951-009-0127-7

[13] S. Salhi, A. Garcia-Villoria. An adaptive search for the Response Time Variability Problem. *Journal of the Operational Research Society,* **10** (2011) 1-9. https://doi.org/10.1057/jors.2011.46

Hydrogen Bonding and Reactivity Behavior of Guanosine-5' -Diphosphate from DFT and Molecular Docking Approach

Manoj Kumar Chaudhary[1]*, Bhupendra Maharjan[1], Gulab Singh Verma[2], Rajesh Kumar Shukla[2]

[1]*Department of Physics, Tribhuvan University, Amrit Campus, Institute of Science and Technology, Kathmandu 44600, Nepal*
[2]*Department of Physics, University of Lucknow, Lucknow-226007, India*

Research Article

ISSN: 3059-9504 (online)
Doi: xxxx

Article History

Received: November 28, 2024
Revised: December 15, 2024
Accepted: December 17, 2024
Published: December 28, 2024

Keywords

Guanosine-5' -Diphosphate (GDP), MEP, DFT, Molecular Docking, Global Reactivity Descriptor

***Corresponding author**
Email: manoj.chaudhary@ac.tu.edu.np, manojkc054@gmail.com
Orcid: 0000-0002-49351827 (M.K. Chaudhary)
Phone: + 977-9841436728

ABSTRACT

Minimum energy structure of Guanosine-5' -Diphosphate (GDP) has been obtained from DFT-B3LYP/6-311++G(d,p) level of theory. The entermolecular hydrogen bonding possibility of GDP has been predicted from optimized parameters, MEP surface analysis and molecular docking approach. The hyper conjugation interaction energy has been analyzed from NBO approach and the significant interaction energy for stability of the molecule is the delocalization of lone pair electron η (1) C21→ π*(N18–C30) and yields 271.82 kcal/mol energy. For the ligand protein interaction, the protein Cdc42 is predicted for the ligand GDP and the three PDB codes 1ANO, 1A4R and 1DOA has been taken into consideration. The Inhibition constant for 1DOA is least which emphases the most binding energy -7.2 kcal/mol. The MEP surface analysis exhibits the most negative potential across O31 and N20 whereas the positive potential cloud is seen across the hydroxyl groups (O8-H9, O3-H4, O35-H36) and amine groups (N26-H_2, N23-H). These regions have significant roles in hydrogen bonding which is satisfied from the molecular docking approach.

1. INTRODUCTION

Guanosine-5' -Diphosphate (GDP) is a nucleoside diphosphate which consists of a pyrophosphate group, a pentose sugar ribose and the nucleobase guanine [1]. The chemical formula of GDP is $C_{10}H_{15}N_5O_{11}P_2$. It is prepared from condensation of the hydroxy group at the 5' position of quanosine with pyrophosphoric acid. GDP is the uncoupling inhibitor as well as Escherichia coli metabolite and mouse metabolite. According to its biological activity it lies in Homo sapiens, Escherichia coli and other organism [2-4]. The anti-bacterial activity of Guvermectin (GV) with Guanosine-5' -Monophosphate (GMP) was studied from molecular docking, genetic and biochemical approach [5]. Guanosine-5' -Triphosphate (GTP) exhibit the good binding behavior with the many proteins like: NS3, NS4A and NS5 by analyzing from AutoDockVina [6].

The geometry optimization, binding sites and molecular docking with Cell division control protein 42 homolog (Cdc42) of GDP have not been performed in the literature. In this manuscript we have focused on these properties of GDP from density functional theory (DFT) and molecular docking approach.

2. METHODS AND METHODOLOGY

The geometry optimization has been carried out from quantum chemical calculation by using Gaussian 16 software [7] from DFT approach by using the hybrid functional B3LYP [8-11] with 6-311++G(d,p) basis set [12]. The GausssView 06 [13] software is implemented to visualize the optimized parameter to study the distribution of charge around the molecule from molecular electrostatic potential (MEP) surface and charge on the orbital lob in highest occupied molecular orbital (HOMO) and lowest unoccupied molecular orbital (LUMO). The natural bond orbital (NBO) analysis is studied from NBO 3.1 which is included in Gaussian 16 software [14]. The binding activity of GDP with the protein codes 1ANO, 1A4R and 1DOA have been examined from AutoDock Tools and Discovery Studio Visualizer 4.5 [15, 16].

3. RESULTS AND DISCUSSION

3.1 Geometry Optimization

The compound GDP has been optimized from DFT/B3LYP/6-311++G(d,p) and the 3D least energy structure with atoms labeling of GDP is presented in Figure 1. The minimum energy was calculated as 1364642.78 kcal/mol. The optimized parameters of GDP such as: bond length and bond angles are depicted in Table 1. The least value of bond length has been obtained across O35-H36, O3-H4, and O8-H9 and their respective values are 0.962, 0.966 and 0.966 Å. This least values of bond length are due to high positive potential analyzed from MEP and these regions have prominent role in hydrogen bonding. Similarly, the longest bond length was found across O5-P6 and its value is 1.647 Å. This is due to intra molecular hydrogen bonding across O2-H11. The least value of angle was obtained across O3-P1-O12 and its value is 99.815° this is also due to intera molecular hydrogen bonding across O2-H11. The highest bond angle is obtained across C21-C22-O31 and its value is 131.379°, this is due to high negative potential across O31 and it takes part in intermolecular hydrogen bonding which is satisfied by molecular docking and MEP surface analysis.

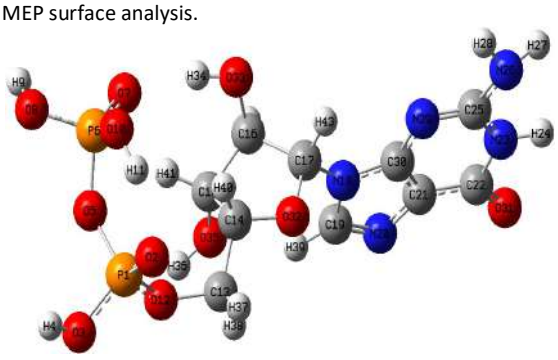

Fig. 1: 3D optimized structure of Guanosine-5' -Diphosphate with atoms numbering from B3LYP/6-311++G(d,p).

Table 1: Optimized parameters (bond length and bond angle) of Guanosine-5' -Diphosphate from B3LYP/6-311++G(d,p).

Bond Length	**(Å)**
R(P1–O2)	1.486
R(P1–O3)	1.590
R(P1–O5)	1.628
R(P1–O12)	1.577
R(O3–H4)	0.966
R(O5–P6)	1.647
R(P6–O7)	1.477
R(P6–O8)	1.595
R(P6–10)	1.578
R(O8–H9)	0.966
R(O10–H11)	0.988
R(O12–C13)	1.467
R(C13–C14)	1.518
R(C13–H37)	1.089
R(C13–H38)	1.087
R(C14–C15)	1.538
R(C14–O32)	1.424
R(C14–H40)	1.099
R(C15–C16)	1.535
R(C15–O35)	1.425
R(C15–H41)	1.090
R(C16–C17)	1.553
R(C16–O33)	1.419
R(C16–H42)	1.093
R(C17–N18)	1.445
R(C17–O32)	1.441
R(C17-H43)	1.090
R(N18–C19)	1.394
R(N18–C30)	1.378
R(C19–N20)	1.304
R(C19–H39)	1.078
R(N20–C21)	1.381
R(C21–C22)	1.437
R(C21–C30)	1.391
R(C22–N23)	1.440
R(C22–O31)	1.215
R(N23–H24)	1.012
R(N23–C25)	1.369
R(C25–N26)	1.377
R(C25–N29)	1.308
R(N26–H27)	1.009
R(N26–H28)	1.010
R(N29–C30)	1.356
R(O33–H34)	0.970
R(O35–H36)	0.962
Bond Angle (°)	
A(O2–P1–O3)	118.465
A(O2–P1–O5)	109.874
A(O2–P1–O12)	117.830
A(O3–P1–O5)	103.112
A(O3–P1–O12)	99.815
A(O5–P1–O12)	106.069
A(P1–O3–H4)	114.487
A(P1–O5–P6)	131.209
A(O5–P6–O7)	111.642
A(O5–P6–O8)	102.479
A(O5–P6–10)	104.429
A(O7–P6–O8)	114.210
A(O7–P6–10)	119.290
A(O8–P6–10)	102.986
A(P6–O8–H9)	112.482
A(P6–10–H11)	114.386
A(P1–O12–C13)	124.021
A(O12–C13–C14)	109.827
A(O12–C13–H37)	109.392
A(O12–C13–H38)	104.751
A(C14–C13–H37)	111.460
A(C14–C13–H38)	111.077
A(37–C13–H38)	110.114
A(C13–C14–C15)	116.134
A(C13–C14–O32)	107.658
A(C13–C14–H40)	109.588
A(C15–C14–O32)	105.214
A(C15–C14–H40)	108.474
A(O32–C14–H40)	109.574
A(C14–C15–C16)	99.942
A(C14–C15–O35)	112.890
A(C14–C15–H41)	112.728
A(C16–C15–O35)	109.057
A(C16–C15–H41)	110.858
A(O35–C15–H41)	110.846
A(C15–C16–C17)	103.642
A(C15–C16–O33)	111.260
A(C15–C16–H42)	111.554
A(C17–C16–O33)	106.217
A(C17–C16–H42)	112.172
A(O33–C16–H42)	111.613
A(C16–C17–N18)	116.410
A(C16–C17–O32)	105.998
A(C16–C17–H43)	108.813
A(N18–C17–O32)	109.563
A(N18–C17–H43)	106.355
A(O32–C17–H43)	109.618
A(C17–N18–C19)	129.319
A(C17–N18–C30)	124.843
A(C19–N18–C30)	105.744
A(N18–C19–N20)	112.965
A(N18–C19–H39)	120.728
A(N20–C19–H39)	126.306
A(C19–N20–C21)	105.007
A(N20–C21–C22)	130.438
A(N20–C21–C30)	110.667
A(C22–C21–C30)	118.892
A(C21–C22–N23)	109.520
A(C21–C22–O31)	131.379
A(N23–C22–O31)	119.100
A(C22–N23–H24)	113.548
A(C22–N23–C25)	126.344
A(H24–N23–C25)	119.984
A(N23–C25–N26)	116.999
A(N23–C25–N29)	123.328
A(N26–C25–N29)	119.629
A(C25–N26–H27)	117.881
A(C25–N26–H28)	113.448
A(H27–N26–H28)	114.438
A(C25–N29–C30)	113.100
A(N18–C30–C21)	105.613
A(N18–C30–N29)	125.575
A(C21–C30–N29)	128.803
A(C14–O32–C17)	109.305
A(C16–O33–H34)	110.931
A(C15–O35–H36)	109.010

3.2 Molecular Electrostatic Potential (MEP) Surface Analysis

The distribution of charge in the molecular system is not uniform and its presence around the compound is visualized in terms of pictorial presentation by using MEP surface analysis. The color codes identify the potential due to charge. The red region for most negative potential, green one for zero potential whereas the blue one for positive potential. The potential increases in terms of color as red > yellow > green > blue. The molecular electrostatic potential due to combined effect of electrons and protons in the molecular system is given by the formula [17,18].

$$V(r) = \sum_A \frac{Z_A}{\left|\overrightarrow{R_A} - \vec{r}\right|} - \int \frac{\rho\left(\overrightarrow{r'}\right)}{\left|\overrightarrow{r'} - \vec{r}\right|}$$

Where $\rho(r')$ stands for negative concentration and Z_A is the positive charge concentration on nucleus A, present at R_A.

The MEP surface of GDP is presented in Figure 2. The most negative potential in GDP was found across O31 and N20 after that certain negative cloud was seen across O2, O7, O32 and O33. These reasons have prominent participation in hydrogen bonding as well as reactive sites.

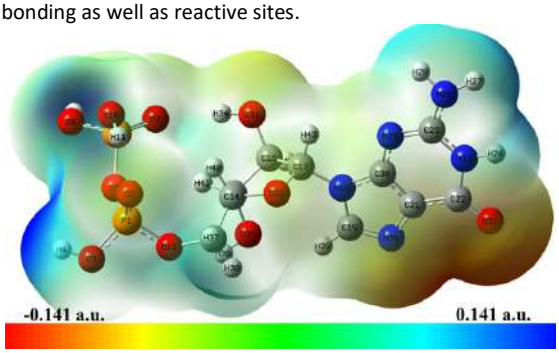

Figure2: MEP surface of Guanosine-5' -Diphosphate.

This is verified by molecular docking in section 3.5. Similarly, the positive cloud has been fond across the hydroxyl groups (O8-H9, O3-H4, O35-H36) and amine groups (N26-H_2, N23-H). These functional groups has wide role to take part in chemical reaction as well as in hydrogen bonding. This is also satisfied by molecular docking analysis, explained in molecular docking in section 3.5.

3.3 Natural Bond Orbital (NBO) Analysis

NBO analysis is the significant tool to study the stability of compound in terms of delocalization of charge from donor (i) to acceptor (j) orbitals. The concentration of charge in the donor orbital ED(i)/e is more than the concentration of charge in acceptor orbital ED(j)/e. The electron in the molecular system delocalized from higher concentration to lower concentration and gains the stability. The stability is measured in terms of stabilization energy E(2) and is given by the formula [19,20]

$$E(2) = E(i,j) = -q_i\left[\frac{F_{i,j}^2}{E_i - E_j}\right]$$

Where E_i is the energy of (i) orbital and E_j is the energy of (j) orbital, $F_{i,j}$ is the off-diagonal element of Fock matrix and q_i is the occupancy of NBO.

The stabilization energy E(2) when the electron delocalized from donor (i) to acceptor (j) orbital along with electron density of donor and acceptor orbital for GDP is presented in Table 2. The stability of GDP is due to delocalization of charge from □→□*, π→ π* and from LP orbital η→π* and □*.The delocalization of charge from η(1) C21→ π*(N18-C30) and π*(C22-O31) stabilizes the GDP significantly with respective stabilization energy 271.82 and 89.23 kcal/mol. Similarly, the others prominent transitions are π (C25-N29) → π*(N18-C30) and π (N18-C30) → π*(C19-N20) with stabilization energy 32.62 and 23.47 kcal/mol respectively. The remaining transitions are presented in Table 2.

Table 2: Stabilization energy E(2), electron density of donor ED(i)/e and acceptor ED(j)/e orbitals of GDP from B3LYP/6-311++G(d,p) level of theory.

Donor NBO (i)	ED(i)/e	Acceptor NBO (j)	ED(j)/e	E(2) kcal/mol	E(j)-E(i) a.u.	F(i,j) a.u.
σ(N29–C30)	1.97757	σ*(C25–N26)	0.03056	5.41	1.24	0.073
σ(N26–H28)	1.98642	σ*(N23–C25)	0.04918	5.27	1.11	0.069
σ(C25–N29)	1.97916	σ*(N18–C30)	0.04158	5.17	1.32	0.074
σ(C21–C30)	1.97244	σ *(C17–N18)	0.04858	5.39	1.05	0.067
σ(C19–N20)	1.98322	σ *(C21–C22)	0.06324	5.00	1.34	0.074
σ(N18– C19)	1.98426	σ *(N29–C30)	0.01977	5.07	1.29	0.072
σ(C17– H43)	1.97543	σ *(N18–C19)	0.04370	5.69	0.94	0.066
π (C25–N29)	1.83879	π*(N18–C30)	0.71341	32.63	0.29	0.102
π (C19–N20)	1.89207	π*(N18–C30)	0.71341	6.26	0.26	0.043
π (N18–C30)	1.84422	σ*(C17–O32)	0.04765	8.65	0.60	0.066
π (N18–C30)	1.84422	π*(C19–N20)	0.29151	23.47	0.36	0.085
η (3) O 7	1.80654	σ*(O5–P6)	0.20849	25.87	0.46	0.097
η (3) O 7	1.80654	σ(P6–O10)	0.15182	10.67	0.53	0.068
η (3) O 2	1.80720	σ*(P1–O3)	0.15661	20.47	0.51	0.092
η (3) O 2	1.80720	σ*(P1–O12)	0.15707	14.59	0.52	0.079
η (2) O10	1.90864	σ*(P6–O7)	0.09341	10.97	0.71	0.079

η (2) O10	1.90864	σ*(P6–O8)	0.15436	7.12	0.57	0.058
η (2) O 8	1.91490	σ*(O5–P6)	0.20849	12.15	0.53	0.074
η (2) O 7	1.81388	σ*(P6–O8)	0.15436	22.77	0.51	0.097
η (2) O 7	1.81388	σ*(P6–O10)	0.15182	11.17	0.53	0.069
η (2) O 5	1.90273	σ*(P1–O12)	0.15707	8.35	0.61	0.065
η (2) O 5	1.90273	σ*(P6–O7)	0.09341	6.96	0.75	0.064
η (2) O 3	1.91712	σ*(P1–O2)	0.09512	7.41	0.71	0.065
η (2) O 3	1.91712	σ*(P1–O5)	0.20259	10.24	0.55	0.069
η (2) O 2	1.81301	σ*(P1–O5)	0.20259	25.01	0.49	0.099
η (2) O 2	1.81301	σ*(P1–O12)	0.15707	8.80	0.53	0.062
η (2) O 2	1.81301	σ*(O10–H11)	0.03570	11.28	0.70	0.083
η (2) O35	1.95584	σ*(C14–C15)	0.04816	8.37	0.67	0.067
η (2) O33	1.94855	σ*(C16–H42)	0.03294	8.60	0.70	0.069
η (2) O32	1.91580	σ*(C14–H40)	0.03590	8.06	0.69	0.067
η (2) O32	1.91580	σ*(C17–N18)	0.04858	5.64	0.66	0.055
η (2) O32	1.91580	σ*(C17–H43)	0.02719	5.49	0.72	0.057
η (2) O31	1.84655	σ*(C21–C22)	0.06324	16.98	0.74	0.102
η (2) O31	1.84655	σ*(C22–N23)	0.09970	32.16	0.60	0.126
η (2) O12	1.89372	σ*(P1–O5)	0.20259	13.13	0.54	0.077
η (1) O 8	1.96615	σ*(P6–O7)	0.09341	5.23	1.01	0.066
η (1) O 5	1.93975	σ*(P1–O2)	0.09512	5.19	0.92	0.062
η (1) N29	1.89453	σ*(C21–C30)	0.03940	8.54	0.93	0.081
η (1) N29	1.89453	σ*(N23–C25)	0.04918	12.83	0.80	0.092
η (1) N26	1.82065	π*(C25–N29)	0.40604	36.51	0.31	0.101
η (1) N23	1.64915	π*(C22–O31)	0.33643	40.24	0.30	0.099
η (1) N23	1.64915	π*(C25–N29)	0.40604	61.09	0.27	0.116
η (1) C21	1.13946	π*(N18–C30)	0.71341	271.82	0.07	0.128
η (1) C21	1.13946	π*(C19–N20)	0.29151	48.48	0.13	0.084
η (1) C21	1.13946	π*(C22–O31)	0.33643	89.23	0.14	0.115
η (1) N20	1.92308	*(N18–C19)	0.04370	8.32	0.77	0.072
η (1) N20	1.92308	*(C21–C30)	0.03940	5.61	0.92	0.065
η (1) O12	1.94323	*(P1–O2)	0.09512	7.36	0.92	0.074

3.4 Frontier Molecular Orbital (FMO's) and Global Reactivity Descriptor

The FMO's have the prominent role to take part in chemical reaction in the molecular system. The highest occupied molecular orbital (HOMO) has the major role to donate the electrons whereas the lowest unoccupied molecular orbital (LUMO) has significant role to absorb the electrons. The HOMO-LUMO energy (ΔE_{L-H}) determines the stability of the compound. Higher the value of (ΔE_{L-H}) more the stability of the compound and less the value of ΔE_{L-H}.the compound is more reactive. The HOMO-LUMO plot of GDP with TD-B3LYP/6-311++G(d,P) is presented in Figure 3. In HOMO the concentration of charge is found across amine group $N26H_2$, imidazole as well as benzene rings, but in LUMO this charges is diverges to carbonyl group C22=O31 and to the benzene and imidazole rings. These regions have significant role in hydrogen bonding as well as ligand protein binding interaction which is also justified in Section 3.5.

The HOMO energy (E_L), LUMO energy (E_H), the value (ΔE_{L-H} electronegativity (χ) softness (S), hardness (η), electrofilicity index (ω), value of chemical potential (μ) for GDP is depicted in Table 3. These values is calculated in terms of E_H and E_L and is given by the formulae [17,21].

$$\chi = -\frac{1}{2}(E_H + E_L)$$

$$\mu = -\chi = \frac{1}{2}(E_H + E_L)$$

$$\eta = \frac{1}{2}(E_L - E_H)$$

$$S = \frac{1}{2\eta}$$

$$\omega = \frac{\mu^2}{2\eta}$$

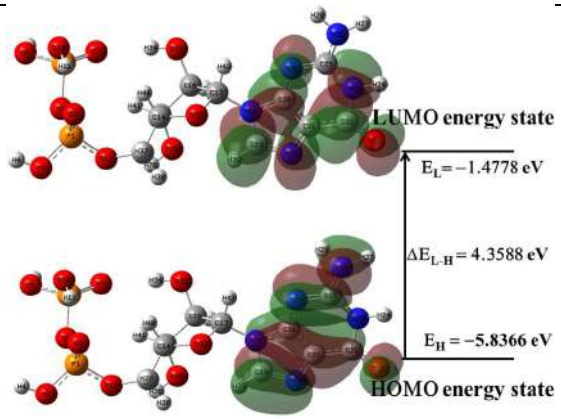

Fig. 3: HOMO -LUMO plot of Guanosine-5′ -Diphosphate.

Table 3: Calculated values of E_H, E_L(ΔE_{L-H}, χ, S, η, ω, μ from B3LYP/6-311++G(d,p) of Guanosine-5′ -Diphosphate.

E_H (eV)	E_L(eV)	(E_L– E_H) (eV)	χ(eV)	μ(eV)	η(eV)	S(eV^{-1})	ω(eV)	ΔNmax
-5.8366	-1.4778	4.3588	3.6572	-3.6572	2.1794	0.2294	3.0685	1.6781

3.5 Molecular Docking

Molecular docking is the essential tool to identify the binding of ligand with predicted target protein. The target protein of GDP which is unique ligand of Cell division control protein 42 homolog (Cdc42) is predicted from the Swiss Target Prediction [22]. The three PDB codes 1ANO, 1A4R and 1DOA have been downloaded from the RCSB data bank [23] and proteins have been cleaned by removing the water molecules and docked ligand by using Discovery Studio Visualizer 4.5 [16]. After that the docking has been performed by AutoDock Tools and the docked conformers have been visualized from Discovery Studio Visualizer 4.5. Out of the many docked conformer the only best conformers are presented in Figure 4 and the 2-D structure of docked conformers is depicted in Figure 5. The conventional hydrogen bond, inhibition constant, ligand efficiency and the binding atoms of GDP is presented in Table 4. Generally the atoms O2,O3,O5,O7,O33, O35, H4,H11, H24, H28, and H34 binds with residue of protein Cdc42. These atoms are also predicted in geometry optimization and MEP surface analysis in Sections 3.1 and 3.2. Out of three PDB codes the 1DOA has highest binding energy -7.2 kcal/mol. The protein Cdc42 shows the good inhibitor for GDP.

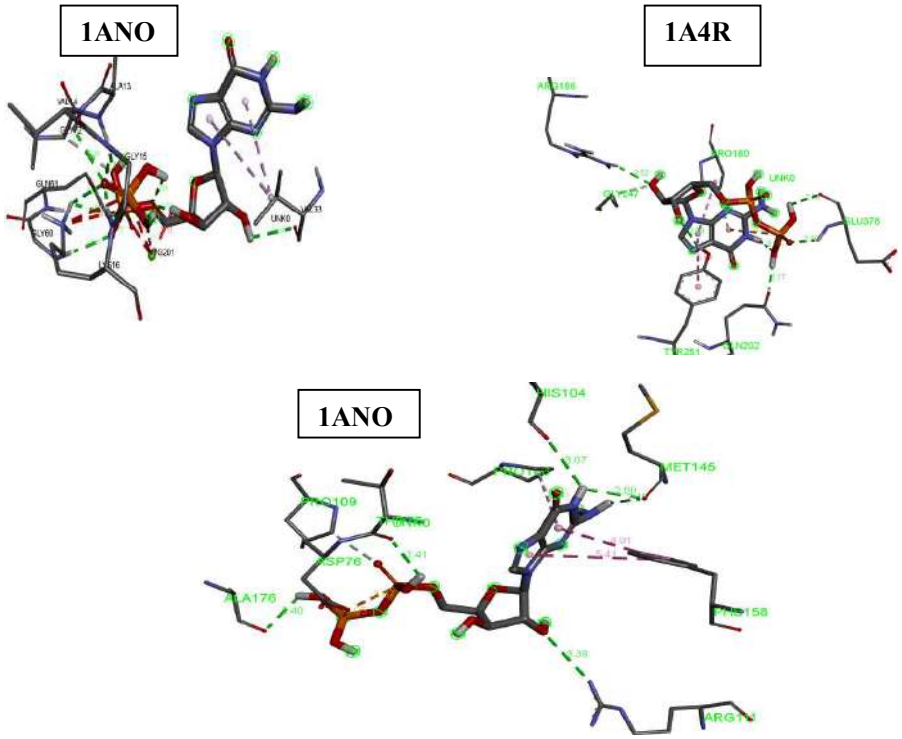

Fig. 4: Residues of amino acids with ligand Guanosine-5′-Diphosphate.

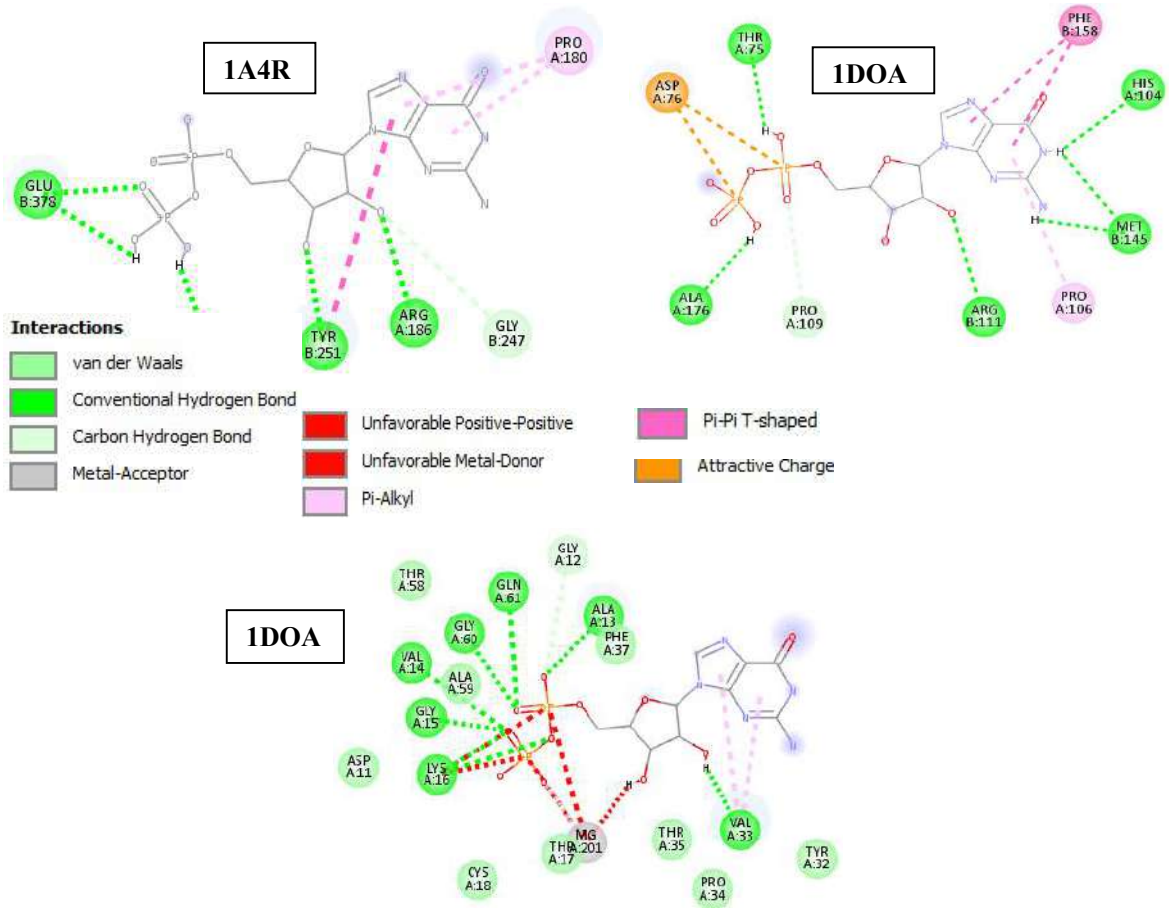

Fig. 5: 2 D structures of docked conformers with ligand Guanosine-5′ -Diphosphate.

Table 4. Molecular docking parameters of Guanosine-5′ -Diphosphate with protein code 1ANO, 1A4R and 1DOA of Cell division control protein 42 homolog.

Ligand	Protein	PDB code	Bond length (Å)	Binding Atoms	Amino acid	Binding energy (kcal/mol)	Inhibition constant (μM)	Ligand efficiency
GDP	Cdc42	1ANO	2.50	H34	VAL A:33	– 6.6	14.35	−0.24
			2.68	O3	ALA A:13			
			2.68	O2	GLN A:61			
			2.41	O2	GLY A:60			
			2.41	O7	VAL A:14			
			2.15	O7	GLY A:15			
			2.13	O7,O5	LYS A:16			
		1A4R	2.52	O33	ARG A:186	−6.6	14.35	−0.24
			2.50	O35	TIR B:251			
			2.17	H11	GLN B:202			
			2.36	O7	GLU B:378			
			2.76	H9	GLU B:378			
			3.07	H24	HIS A:104			
		1DOA	2.60	H24	MET B:145	−7.2	5.21	−0.26
			2.18	H28	MET B:145			
			3.38	O33	ARG B:111			
			2.41	H4	THR A:75			
			2.40	H11	ALA A:176			

4. CONCLUSIONS

The three dimensional optimized structure of GDP has been obtained from DFT-B3LYP/6-311++G(d,p) and the optimized energy is calculated as 1364642.78 kcal/mol. The least bond length is calculated as 0.962 and 0.966 Å across (O35-H36) and (O3-H4). These moieties will take part in iner molecular hydrogen bonding. The longest bond length is calculated as 1.647 Å across (O5-P6). This is due to intra molecular hydrogen bonding across (O2-H11). MEP analysis conformed that the concentration of negative charge is more across O2, O7, O32 and O33. These moieties have prominent role to take part in hydrogen bonding as well as reactive sites in molecular docking. Moreover, the positive concentration of charge in GDP is most across the hydroxyl groups (O8-H9, O3-H4, O35-H36) and amine groups (N26-H_2, N23-H). These regions have maximum possibility to take part in hydrogen bonding which is justified by molecular docking. The HOO-LUMO energy gap is obtained as 4.3588 eV, chemical potential is obtained as -3.6572 eV. The highest binding energy -7.2 kcal/mol is found across PDB code of 1DOA of protein Cdc42. The atoms which bind with residue of amino acid are O2, O3, O5, O7, O33, O35, H4, H11, H24, H28, and H34 which is also justified from geometry optimization and MEP analysis.

AUTHOR CONTRIBUTION

M.K. Chaudhary: Conceptualization of research activity, data analysis and manuscript writing; B. Maharjan: Analysis, and drafting; G. S. Verma: Data calculation R. K. Shukla: supervision and editing.

DECLARATIONS CONFLICT OF INTEREST

The authors declare no competing interests.

REFERENCES

[1] L.E. Bettio, J. Gil-Mohapel, A.L. Rodrigues. “Guanosine and its role in neuropathologies. Purinergic Signal” 2016 Sep;12(3):411-26. Epub 2016 Mar 22. PMID: 27002712; PMCID: PMC5023624. https://doi.org/10.1007/s11302-016-9509-4

[2] National Center for Biotechnology Information. "PubChem Compound Summary for CID 135398619, Guanosine Diphosphate *PubChem*, https://pubchem.ncbi.nlm.nih.gov/compound/Guanosine-Diphosphate. Accessed 1 December, 2024.

[3] M.F., Carlier. "Guanosine-5′-triphosphate hydrolysis and tubulin polymerization." *Molecular and cellular biochemistry* 47 (1982): 97-113. https://doi.org/10.1007/BF00234410

[4] N. Nemoto, S. Baba, G. Kawai, and G.Sampei. "Crystal structure of guanosine 5′-monophosphate synthetase from the thermophilic bacterium Thermus thermophilus HB8." *Structural Biology and Crystallization Communications* 80, no. 10 (2024). doi.org/10.1107/S2053230X2400877X

[5] M. Zhang, L. Lei, L. Cheng, M. Aifang, L. Junzhou, Y. Chenyu, C. Xujun. "Natural product guvermectin inhibits guanosine 5′-monophosphate synthetase and confers broad-spectrum antibacterial activity." *International Journal of Biological Macromolecules* 267 (2024): 131510. https://doi.org/10.1016/j.ijbiomac.2024.131510

[6] D. K. Shill, J. Shafina, M. A. Mohammad Mamun, B. L. Hasan, M. Alam, Z. Rahman, and M. Rahman. S-Adenosyl-l-homocysteine exhibits potential antiviral activity against dengue virus serotype-3 (DENV-3) in Bangladesh: a viroinformatics-based approach. *Bioinformatics and Biology Insights* 17 (2023): 11779322231158249. https://doi.org/10.1177/11779322231158249

[7] M.J. Frisch, G.W. Trucks, H.B. Schlegel, G.E. Scuseria, M.A. Robb, J.R. Cheeseman, G. Scalmani, V. Barone, B. Mennucci, G.A. Petersson, H. Nakatsuji, M. Caricato, X. Li, H.P. Hratchian, A.F. Izmaylov, J. Bloino, G. Zheng, J.L. Sonnenberg, M. Hada, M. Ehara, K. Toyota, R. Fukuda, J. Hasegawa, M. Ishida, T. Nakajima, Y. Honda, O. Kitao, H. Nakai, T. Vreven, J.A. Montgomery, J.E. Peralta, F. Ogliaro, M. Bearpark, J.J. Heyd, E. Brothers, K.N. Kudin, V.N. Staroverov, R. Kobayashi, J. Normand, K. Raghavachari, A. Rendell, J.C. Burant, S.S. Iyengar, J. Tomasi, M. Cossi, N. Rega, J.M. Millam, M. Klene, J.E. Knox, J.B. Cross, V. Bakken, C. Adamo, J. Jaramillo, R. Gomperts, R.E. Stratmann, O. Yazyev, A.J. Austin, R. Cammi, C. Pomelli, J.W. Ochterski, R.L. Martin, K. Morokuma, V.G. Zakrzewski, G.A. Voth, P. Salvador, J.J. Dannenberg, S. Dapprich, A.D. Daniels, Ö. Farkas, J.B. Foresman, J.V. Ortiz, J. Cioslowski, D.J. Fox, Gaussian 16 Revision, Gaussian, Inc. Wallingford (2016).

[8] P. Hohenberg, W. Kohn, Inhomogeneous Electron Gas, Phys. Rev. 136 (1964) B864–B871. https://doi.org/10.1103/PhysRev.136.B864.

[9] C. Lee, W. Yang, R.G. Parr, Development of the Colle-Salvetti correlation-energy formula into a functional of the electron density, Phys. Rev. B 37 (1988) 785–789. https://doi.org/10.1103/PhysRevB.37.785.

[10] R.G. Parr, W. Yang, Density-functional theory of atoms and molecules, 1. iss. as ... paperback, Oxford Univ. Press, New York, NY, 1994.

[11] A.D. Becke, Density-functional thermochemistry. III. The role of exact exchange, J. Chem. Phys. 98 (1993) 5648–5652. https://doi.org/10.1063/1.464913.

[12] T.H. Dunning, Gaussian basis sets for use in correlated molecular calculations. I. The atoms boron through neon and hydrogen, J. Chem. Phys. **90** (1989) 1007–1023. https://doi.org/10.1063/1.456153.

[13] R. Dennington, T.A. Keith, Millam, M. John, GaussView 06 Semichem Inc., Shawnee Mission, KS (2016).

[14] E.D. Glendening, A.E. Reed, J.E. Carpenter, F. Weinhold, NBO 3.1 Gaussian Inc., Pittsburgh (2003).

[15] M.K. Chaudhary, A. Srivastava, K.K. Singh, P. Tandon, and B.D. Joshi. "Computational evaluation on molecular stability, reactivity, and drug potential of frovatriptan from DFT and molecular docking approach. *Computational and Theoretical Chemistry,* **1191** (2020): 113031.https://doi.org/10.1016/j.comptc.2020.113031

[16] P.K. Weiner, R. Langridge, J.M. Blaney, R. Schaefer, P.A. Kollman, Electrostatic potential molecular surfaces, Proc. Natl. Acad. Sci. U.S.A.79 (1982) 3754–3758. https://doi.org/10.1073/pnas.79.12.3754

[17] A.E. Reed, L.A. Curtis, F.A. Weinhold, Intermolecular interactions from a natural bond orbital, donor-acceptor viewpoint, Chem. Rev. 88 (1988) 899–926. https://doi.org/10.1021/cr00088a005

[18] P. Geerlings, F.D. Proft, W. Langenaeker, Conceptual density functional theory, Chem. Rev. 103 (2003) 1793−1874. https://doi.org/10.1021/cr990029p

[19] R.G. Parr, L. Szentpaly, S. Liu, Electrophilicity index, J. Am. Chem. Soc. 121 (1999) 1922−1924.

https://doi.org/10.1021/ja983494x

[20] A. Daina, O. Michielin, V. Zoete, SwissTargetPrediction: updated data and new features for efficient prediction of protein targets of small molecules, Nucleic Acids Res. 47 (2019) W357–W364. https://doi.org/10.1093/nar/gkz382.

[21] P.W. Rose, B. Beran, C. Bi, W.F. Bluhm, D. Dimitropoulos, D.S. Goodsell, A. Prlic, M. Quesada, G.B. Quinn, J.D. Westbrook, J. Young, B. Yukich, C. Zardecki, H.M. Berman, P.E. Bourne, The RCSB Protein Data Bank: redesigned web site and web services, Nucleic Acids Res. 39 (2011) D392–D401. https://doi.org/10.1093/nar/gkq1021.